The internal kinematics of globular clusters

An intimate view, from models to observations

Paolo Bianchini
Max-Planck-Institut für Astronomie

Heidelberg 2016

Dissertation in Astronomy
submitted to the
Combined Faculties of the Natural Sciences and Mathematics
of the Ruperto-Carola-University of Heidelberg, Germany,
for the degree of
Doctor of Natural Sciences

Put forward by
Paolo Bianchini
born in Milan, Italy

Oral examination: 19.07.2016

The internal kinematics of globular clusters

An intimate view, from models to observations

Paolo Bianchini
Max-Planck-Institut für Astronomie

Referees: Dr. Glenn van de Ven
Prof. Dr. Rainer Spurzem

To Schengen

Abstract

Globular clusters (GCs) were long believed to be simple, non-rotating, isotropic and spherical stellar systems with all of their stars formed approximately 13 Gyr ago. However, their origin in the early epochs of galaxy formation is still debated. Growing evidence is now showing a larger degree of complexity in their structure, morphology, stellar populations and internal dynamics. The goal of this Thesis is to unveil the complexity of their current dynamical properties and to connect it to their formation and subsequent dynamical evolution.

As a first step, I show that the study of the morphology alone is not enough in order to disentangle the formation of GCs, in particular to distinguish clusters that formed in-situ from clusters that were accreted. This motivated the detailed exploration of their internal kinematics, that provides a long lasting "fossil record" of the dynamical processes that a GC has experience during its long-term evolution. Using a combination of state-of-the-art kinematic observations and dynamical modeling, I carry out the study of the kinematic effects connected to the presence of intermediate-mass black holes, binary stars and the onset of energy equipartition. In particular, I focus on the understanding of the systematics and biases present in the integrated-light kinematic observations and Hubble Space Telescope proper motion samples, making use of mock observations constructed directly from the dynamical models. This strategy gives the direct advantage of achieving a sound interpretation of the observations and of the physical processes described by the models. Having reached a deeper understanding of the data, I set up a first step to trace the evolution of GCs, based on their current kinematics. I show that the degree of energy equipartition attained by a GC can be connected to its dynamical state and therefore used as an indicator of its formation or peculiar dynamical evolution.

My work indicates that the synergy between models, observations and the study of the internal kinematics of GCs is the key to unveil their dynamical state. This will be the starting point for exploiting at full power the comprehensive amount of data that will be delivered by the Gaia mission and in the approaching era of Extremely Large Telescopes.

Zusammenfassung

Kugelsternhaufen galten lange Zeit als simple, nicht-rotierende, isotrope und sphärisch symmetrische stellare Systeme, deren Sterne alle in einer Zeit vor ungefähr 13 Gyr entstanden sind. Dennoch steht ihr Ursprung in den Frühzeiten der Galaxienenstehung immer noch zur Debatte. Mit zunehmender Sicherheit zeigt sich ein höherer Grad an Komplexität in der Struktur, der Morphologie, den stellaren Populationen und der internen Dynamik von Kugelsternhaufen. Das Ziel dieser Doktorarbeit ist es, die Komplexität der gegenwärtigen dynamischen Eigenschaften zu enthüllen und diese mit dem Entstehungsprozess und der nachfolgenden Entwicklung zu verbinden.

In einem ersten Schritt zeige ich, dass das Studium der Morphologie allein nicht ausreicht um das Entstehungsgewirr von Kugelsternhaufen zu entflechten, insbesondere nicht um Sternhaufen, die in-situ entstanden sind, von denen, die akkretiert wurden, zu unterscheiden. Dies begründete die detaillierte Erforschung der internen Kinematik von Kugelsternhaufen, die eine langlebige „fossile Aufzeichnung“ der dynamischen Prozesse, die ein Kugelsternhaufen während seiner langfristigen Evolution erfahren hat, darstellt. Unter Zuhilfenahme von modernsten kinematischen Beobachtungen und dynamischen Modellen studiere ich die kinematischen Effekte, ausgelöst durch das Vorhandensein von mittel schweren schwarzen Löchern, Doppelsternen und Energie-Äquipartition. Ich konzentriere mich dabei speziell auf das Verständnis der Systematiken und der Messeffekte in den IFU kinematischen Beobachtungen und den *HST* proper motion Samples, indem ich Gebrauch von Scheinbeobachtungen, direkt gewonnen aus den dynamischen Modellen, mache. Diese Strategie besitzt den direkten Vorteil einer zuverlässigen Interpretation der Beobachtungen und der physikalischen Prozesse, die durch die Modelle beschrieben werden. Nachdem ein tieferes Verständnis der Daten erreicht wurde, beginne ich mit dem ersten Schritt um die Evolution von Kugelsternhaufen, basierend auf ihrer gegenwärtigen Dynamik, zu verfolgen. Ich zeige, dass der Grad an Energie-Äquipartition in einem Kugelsternhaufen in Verbindung gesetzt werden kann mit seinem dynamischen Zustand und daher als Indikator seiner Entstehung oder seiner besonderen dynamischen Entwicklung benutzt werden kann.

Meine Arbeit weist darauf hin, dass die Synergie zwischen Modellen, Beobachtungen und der Untersuchung der internen Kinematik von Kugelsternhaufen der Schlüssel zum Verständnis ihres dynamischen Zustandes ist. Dies wird der Ausgangspunkt sein um im vollen Maße die umfangreichen Datenmengen, die von der Gaia Mission und in Zeiten des Extremely Large Telescopes geliefert werden, auszunutzen.

Contents

Chapter 1

Introduction

"If one cannot see gravitation acting here, he has no soul".
Richard Feynman

Globular clusters (GCs) are amongst the oldest stellar systems in the Universe, formed by a collection of up to a few million stars kept together by gravity only, in an approximately spherical shape. The Milly Way (MW) hosts $\simeq$160 of them; but GCs are a common features in most galaxies. As an example, massive elliptical galaxies can host up a few ten thousand of them, and dwarf galaxies typically only a few of them. GCs are gas, dust and dark matter free systems, solely formed of stars with approximately the same age ($\simeq$13 Gyr) and chemical composition, and have a typical size of a few parsec and a mass of $10^4 - 10^6\ M_\odot$. These features set them in the transition region between open star cluster and dwarf galaxies.

Taking a system of GCs as a whole, its properties can be used to trace the formation and evolution of its host galaxy, since the GCs are the stellar relicts of the earliest epochs of galaxy formation. Taken as individual objects, GCs are ideal for studies of stellar populations and stellar evolution, and are at the same time ideal laboratories for the study of stellar dynamics and gravitational interactions between stars.

Despite their apparent simplicity and the many dedicated studies, the origin of GCs in the early Universe still remains an open issue. The problem we are facing is the one to unveil the formation mechanism of GCs exploiting the observational information of their current properties, namely $\simeq$13 Gyr after their formation. This is extremely challenging since the current properties of GCs are the result of their >10 Gyr evolution driven by the complex interplay between gravitational encounters, both dynamical two-body interactions between stars as well as interactions with the host galaxy, and internal stellar astrophysical processes. Reaching a deep understanding of all of these evolutionary ingredients is the key to interpret their current internal properties and ultimately to reveal their formation during the earliest epochs of galaxy formation.

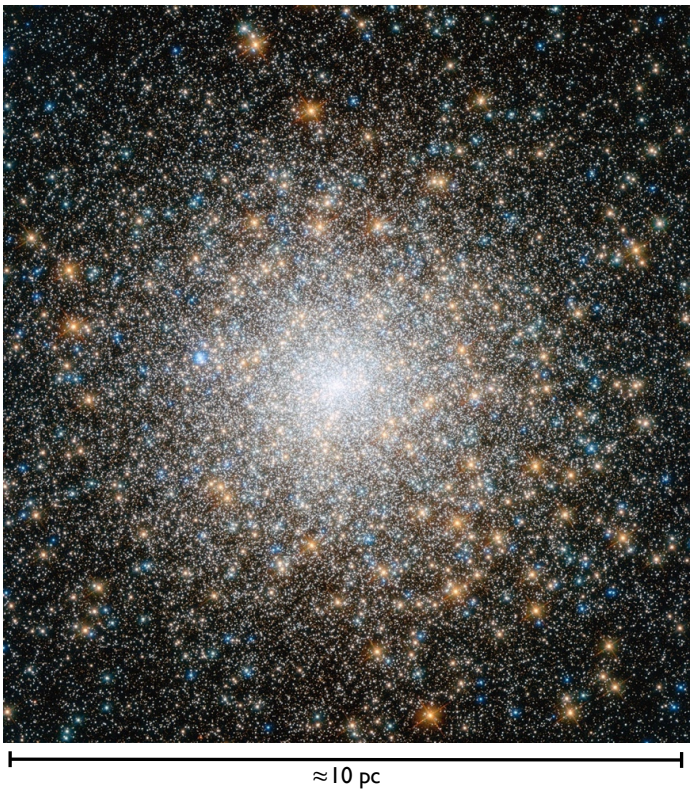

Figure 1.1: Hubble Space Telescope image of the globular cluster NGC 7078/M15. Credit: NASA, ESA, `http://www.spacetelescope.org/images/heic1321a`.

Since single stars can be resolved, Galactic GCs are the unique environment where detailed studies of the internal properties can be carried out, allowing to disentangle the effects of the long-term dynamical evolution and the one of the initial conditions of their formation. The goal of this Thesis is to *develop a deeper understanding of the dynamical properties of Galactic GCs*, with particular emphasis to their internal kinematic properties, to unveil how these relate to their dynamical history.

In the following Section, I will introduce the current understanding of Galactic GC properties and outline the major open issues connected to their origin (Sections 1.1 and 1.2). I will delineate the strategy to assess these problems (Section 1.3), based in particular to the combined use of dynamical modeling techniques and kinematic observations, which represent the methodology used throughout this work. Finally, in Section 1.4 and 1.5, I will briefly review the state-of-the-art dynamical modeling and kinematic observations for GCs.

1.1 Properties of a standard Galactic globular cluster

GCs were long believed to be simple, non-rotating, isotropic and spherical stellar systems with all of their stars formed in a single burst of star formation approximately

Poperty	mean value
d_{GC}	12.16 kpc
d_{Sun}	15.17 kpc
M_v	-7.27 mag
R_c	1.14 pc
R_h	2.21 pc
R_t	21.85 pc
C	1.57
ρ_0	$2.32\times\ 10^3\ L_\odot\ pc^{-3}$
t_{rh}	10^9 yr
t_{rc}	10^8 yr
σ	5.5 km s^{-1}

Table 1.1: Mean properties of Galactic globular clusters extracted from Harris (2010). From top to bottom: Galactocentric distance d_{GC}, distance to the Sun d_{Sun}, absolute v-band magnitude M_v, projected core radius R_c, projected half-light radius R_h, projected tidal radius R_t, concentration parameter $C = \log(R_t/R_c)$, central luminosity density ρ_0, half-light relaxation time t_{rh}, core radius relaxation time t_{rc}, central velocity dispersion σ.

13 Gyr ago. This simplistic picture is however wrong and growing evidence is now clearly showing a larger degree of complexity in their structure, morphology, internal kinematics and stellar populations.

Because of their typical old age and the lack of recent episodes of star formations, GCs are generally metal poor stellar systems, with a metal content from [Fe/H]$\simeq-2.5$ to -0.5 and are composed of old low-mass stars as the result of stellar evolution (with the brightest and most massive stars having a mass of $\simeq 0.8-0.9\ M_\odot$). GCs observed in external galaxies are characterized by a bimodality, metal-poor/blue and metal-rich/red clusters, taken as the indication of the presence of two distinct families of GCs (e.g., Peng et al., 2006; Usher et al., 2012; see also Section 1.2.2). Some of typical properties of the MW GCs are reported in Table 1.1.

From a stellar population point of view, GCs are now known to host multiple stellar populations (see e.g., Gratton et al., 2012), all with similar age and iron abundance, but differing in the light element abundances (see Section 1.2.3). This phenomenon is a peculiar feature of GCs only; however, it remains poorly understood. In addition, some of the most massive GCs show a spread in the iron abundance (Da Costa, 2015).

From the morphological point of view, GCs exhibit small, yet significant, deviations from spherical symmetry that can be measured in quantitative detail (Geyer et al., 1983; White & Shawl, 1987; Chen & Chen, 2010). The maximum observed ellipticity[1] of a Galactic GC is $e \approx 0.3$. The flattening of GCs is usually ascribed to the presence of internal rotation (see e.g., Fiestas et al., 2006; Bianchini et al., 2013), but the additional effects of pressure anisotropy and of the host galaxy's tidal field can also cooperate in

[1]The ellipticity is defined as $e = 1 - b/a$, with a and b major and minor axes, respectively.

shaping the overall structure of the clusters (see e.g., van den Bergh, 2008). Further highlighting the complex interplay between clusters and their host galaxies are the observations of tidal tails in the outskirts of many GCs (e.g., Jordi & Grebel, 2010).

From the kinematic point of view, GCs are pressure supported systems with typical velocity dispersions σ of about $\simeq 5$ km s^{-1} (Harris, 2010). However, a non-negligible amount of internal rotation has been measured in many GCs (see e.g., Bellazzini et al., 2012; Fabricius et al., 2014; Kacharov et al., 2014; Lardo et al., 2015). The typical amount of internal rotation is of only a few km s^{-1}, making these measurements challenging and requiring high-precision data. The typical ratio between the rotation velocity peak V and the central velocity dispersion σ is $V/\sigma \lesssim 0.2$, with the exception of ω Cen, the most massive GC in the MW, suspected to be a stripped nucleus of a dwarf galaxy (see Section 1.2.2), characterized by a higher $V/\sigma \simeq 0.4$ (see e.g., Bianchini et al., 2013).

Another important kinematical feature of GCs is the presence of anisotropy in velocity space. Moderate radial anisotropy is commonly measured in the intermediate regions of clusters while quasi-isotropy is observed in the core regions (Watkins et al., 2015a). This can be taken as a tracer of the earliest phases of clusters formation and evolution (e.g., violent relaxation, Lynden-Bell, 1967) that induce radial anisotropy to the systems. However, it is also the natural result of the relaxation processes that shape the long-term evolution of GCs towards isotropy in the more dense regions (Zocchi et al., 2012). Moreover, the presence of a tidal field can also play a role in shaping the anisotropy especially in the outer regions of GCs, where the system can become isotropic or mildly tangential (e.g., van de Ven et al., 2006; Vesperini et al., 2014; Tiongco et al., 2016).

Additional elements of complexity in the internal kinematics of GCs are the effects due to energy equipartition. Since GCs are old stellar systems where the fundamental dynamical processes take place on a time scale shorter than their age (see Section 1.4), two-body interactions between stars are efficient in shaping their internal structure. In particular, one of the effects of two-body interactions is to bring a system towards a state of thermalization, where stars with different masses approach the same energy (Spitzer, 1987). This is known as energy equipartition: massive stars lose kinematic energy sinking into the center of the cluster, while, vice versa, low-mass stars gain kinetic energy and move to the outer regions. Even if GCs are not expected to reach full energy equipartition (e.g., Spitzer, 1969; Trenti & van der Marel, 2013) this still produces a mass dependence of the kinematics.

Moreover, the stellar populations of GCs is characterized by the presence of binary stars, formed both primordially and as the result of dynamical interactions between stars. The typical observed binary fractions of GCs is $\simeq 5 - 20\%$, lower than the one of field stars (see e.g., Milone et al., 2012). However, binary stars are a fundamental ingredient for the understanding of the evolution of GCs, as their formation and destruction can significantly contribute in the overall energy budget of the clusters and their presence can introduce significant biases to the kinematic measurements (Meylan & Heggie, 1997).

Finally, GCs host a series of exotic stellar objects such as blue stragglers stars, cataclysmic variables and stellar remnants such as pulsars, neutron stars, and stellar

mass black holes (as a natural outcome of stellar evolution). Recent attention has also been devoted to the hunt for intermediate-mass black holes (IMBHs) in the centers of GCs. The existence of black-holes with mass of $10^3 - 10^4\ M_\odot$, intermediate between the regime of stellar mass black holes and supermassive black holes, could be the missing link to explain the formation of the supermassive black holes found in the center of nearly all galaxies. IMBHs have been postulated to exists at the center of GCs from the extrapolation of the $M_\bullet - \sigma$ relation for galaxies, linking the mass of the central back hole to the velocity dispersion of the host stellar system (Ferrarese & Merritt, 2000; Magorrian et al., 1998).

However the kinematic detection of IMBHs in Galactic GCs has so far been elusive, with different observational methods giving conflicting results (e.g., Gebhardt et al., 2000; van den Bosch et al., 2006; Noyola et al., 2010; van der Marel & Anderson, 2010; Lanzoni et al., 2013; Lützgendorf et al., 2013; den Brok et al., 2014). The difficulty consists on one side in detecting a rise of the velocity dispersion in the central very crowded few arcsecs of a cluster, where obtaining data is extremely challenging; on the other side, to disentangle the possible signature of an IMBH from those caused by other dynamical effects (e.g., radial anisotropy or presence of a subsystem of stellar remnants). Additionally, the detection of radio and X-ray emission due to the accretion of gas onto the black hole also proved to be difficult because of the highly inefficient gas poor environment of Galactic GCs (e.g., Strader et al., 2012). So far, no sound detection of an IMBH in a Galactic GC has been reported.

1.2 The formation of globular clusters: a 13 Gyr old problem

In the previous Section, I have highlighted the basic structural properties of MW GCs as observed today. In this Section, I will discuss the open issues connected to the understanding of their origin. On one side, the similarities and differences with other low-luminosity stellar systems (such as faint dwarf galaxies) has opened up the debate of what is the distinction between a star cluster and a faint dwarf galaxy. On the other side, the discovery of chemical inhomogeneity in stars in GCs (e.g., the presence of multiple stellar populations) has posed an additional puzzle in the understanding of their formation.

1.2.1 The link between globular clusters and dwarf galaxies

Nearly all galaxies host a variety of low-luminosity stellar systems with different masses and morphologies (Norris et al., 2014). Beside GCs, the presence of ultra-compact dwarfs and dwarf galaxies is rather common (Misgeld & Hilker, 2011; Brodie et al., 2011). Dwarf galaxies have always been thought to be well distinct from stellar clusters, since they are $1-2$ orders of magnitude larger in size, have complex stellar populations indicating extended or multiple star formation episodes, and are known to be the most dark matter dominated systems in the universe. This classical sharp distinction between dwarf galaxies and globular clusters is well depicted in Figure 1.2, where the two different classes of stellar systems occupy different areas in the luminosity-size diagram.

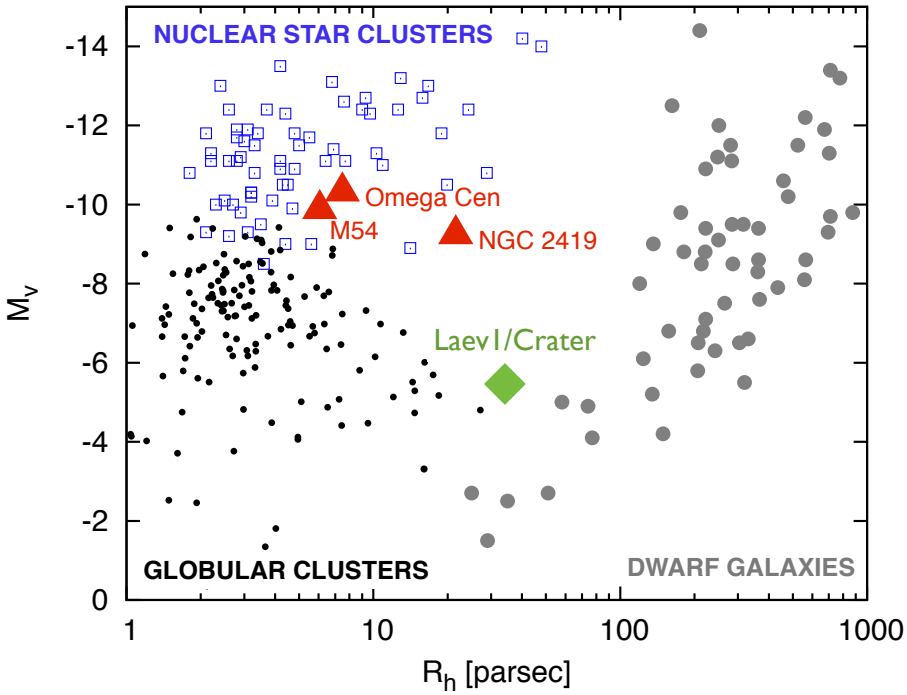

Figure 1.2: Observed low-luminosity stellar systems. The y-axis represents the luminosity in V-band magnitudes, M_v, while the x-axis shows their characteristic size, the half-light radius R_h in parsecs. The black dots indicate Galactic globular clusters, while the grey points are dwarf galaxies associated with the MW. The blue squares represent nuclear star clusters, found in the centers of galaxies. A population of objects in the intermediate region between star clusters and dwarf galaxies is visible (between 10−100 pc; e.g. Laevens1/Crater), as well as a clear overlap between the most massive globular clusters and nuclear star clusters. The red triangles indicates objects suspected to be stripped nuclei of dwarf galaxies (ω Cen, M54, NGC 2419), due to their size, luminosity and chemical properties. Data from Norris et al. (2014).

However, in recent years, a number of low-luminosity stellar systems were discovered around galaxies populating the transition region between low-luminosity dwarf spheroidal galaxies and GCs (see e.g., Laevens et al., 2015, Bechtol et al., 2015, Koposov et al., 2015). In particular, deviating from the standard definitions of GC and dwarf galaxy, we find two classes of objects (see Figure 1.2): i) MW GCs more massive than the average (e.g. Omega Cen, M54, NGC 2419), resembling in size, luminosity and possibly stellar populations, the nuclear star clusters found in the center of galaxies (Georgiev et al., 2009) and ii) GCs more extended than the average, so called extended clusters (e.g., Laevens1/Crater, Laevens et al., 2014, Belokurov et al., 2014), similar to ultra-faint dwarf galaxies. These latter stellar systems, with a luminosity between -6 $< M_v <$ −2 and a half-light radii of about 20−30 pc, are preferentially found in the outer halos of galaxies and are characterized by a more diffuse structure than typical GCs of similar luminosity (Brodie & Larsen, 2002; Mackey et al., 2013; Huxor et al.,

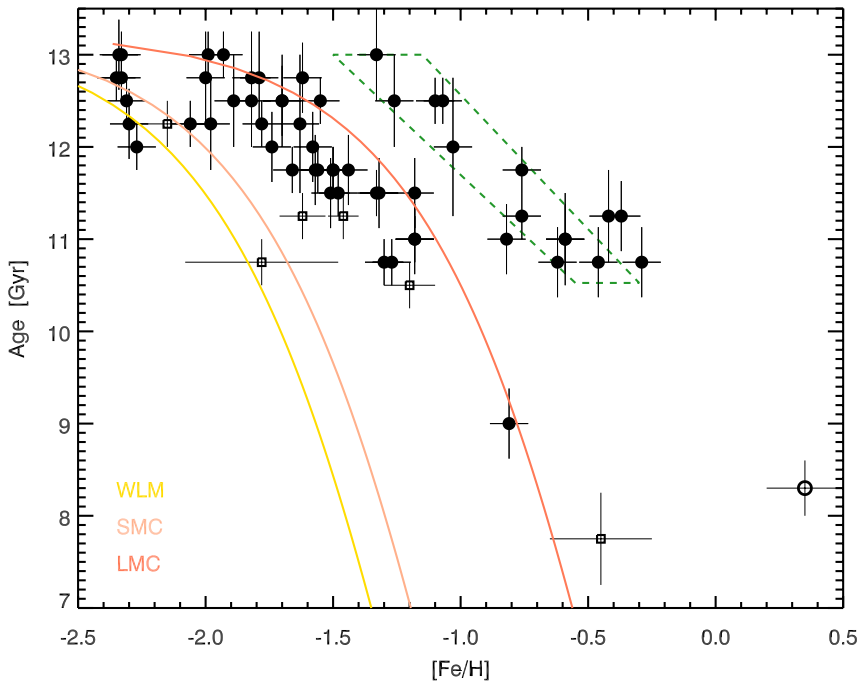

Figure 1.3: Age-metallicity relation for Milky Way globular clusters. A bifurcation is visible: the branch at higher metallicity, given an age, is indicative of the presence of globular clusters formed in-situ in the Milky Way (≈1/3 of the clusters) and display orbital properties consistent with the Milky Way disk, and the other branch (formed by ≈2/3 of the clusters) is composed by clusters suspected to be accreted systems, with age-metallicity relation possibly consistent with the one of dwarf galaxies (e.g., the Large Magellanic Cloud). Figure from Leaman et al. (2013).

2014). Therefore, their intermediate size, between the regime of dwarf galaxies and the bulk of GCs, makes them intriguing objects and extremely difficult to classify as either star clusters or faint dwarf galaxies.

The blurring of the traditional distinction between GCs and dwarf galaxies, has strengthened the idea that some GCs actually formed originally in more massive dwarf galaxies, even possibly as their nuclei, and subsequently were stripped and accreted onto the MW (Freeman, 1993; Meylan et al., 2001; Bekki & Freeman, 2003; Pfeffer & Baumgardt, 2013). In the next Section, I discuss in more details the lines of evidence for a possible accreted origin of GCs .

1.2.2 In-situ versus accreted globular cluster formation

In recent years, evidence has accumulated that the GC population of the MW (and other massive galaxies) was assembled in a two-step process. In this picture one population of GCs was formed in-situ during the violent, dissipative, early epoch of galaxy formation and subsequently, a second population of GCs was accreted from dwarf galaxies (e.g.

Marín-Franch et al., 2009; Forbes & Bridges, 2010; Keller et al., 2012). The accreted origin of a fraction of Galactic GCs has been partially motivated by the observations of ongoing stripping of dwarf galaxies, the presence of stellar streams both in the MW and in external galaxies, and the spatial coincidence of outer halo GCs with stellar streams and overdensities (e.g., Mackey & Gilmore, 2004; Mackey et al., 2010; Jennings et al., 2015). An example is the ongoing stripping process of the Sagittarius dwarf galaxy in the MW with GCs being accreted from it (see e.g. the GC M54, Ibata et al., 1995).

Additional evidence of the dichotomy of accreted vs. in-situ clusters, comes from the analysis of the age-metallicity relation for the Galactic GCs, that shows a bifurcation, often taken as the evidence for the presence of two distinct groups of clusters (see Figure 1.3). One group ($\approx$1/3 of the clusters) forms an offset sequence that, for a given age, is more metal rich (Leaman et al., 2013). These clusters show orbital properties consistent with the one of the MW disk and are believed to have formed in-situ. The other cluster sequence follows an age-metallicity relation consistent with the one for dwarf galaxies of masses $10^7 - 10^8$ $M_\odot$ and is associated with clusters suspected to have formed in low-mass dwarf galaxies later accreted onto the MW. These results are in agreements with studies of external galaxies, where the kinematics of the metal-rich/red GCs are coupled with the stellar kinematics of the host galaxies, while the metal-poor/blue GCs are instead characterized by random motions (Pota et al., 2013). This has been interpreted as the natural outcome of hierarchical merging of galaxies in simulations as well (Tonini, 2013).

Not only some GCs are suspected to be accreted systems, but there is also evidence that small subsets of them are actually stripped nuclei of dwarf galaxies. Figure 1.2, shows that the most massive GCs overlap in properties with nuclear star clusters found in the center of galaxies. These clusters (in particular M54 and ω Cen, but also, M2, M22, Terzan 5, NGC 5824) also show complex stellar populations characterized by a spread in metal content, typically observed in nuclear star clusters or dwarf galaxies (Da Costa, 2015) and at variance with the standard single-metallicity GCs (Leaman, 2012). This is illustrated in Figure 1.4, where ω Cen and M54 (the former nucleus of the Sagittarius dwarf spheroidal) are located on the metallicity relation typical of dwarf galaxies and not on the standard GC sequence.

If the stripped-nucleus scenario is correct, a series of peculiar properties should be detectable in these GCs, similarly to the properties observed in nuclear star clusters or ultra-compact dwarfs (e.g., Seth et al., 2014; Jennings et al., 2015; Norris et al., 2015):

- complex stellar populations, with metal spread indicative of multiple or extended star formation;
- complex kinematics related to the formation of the different populations (e.g., disk-like structures);
- strong signature of internal rotation in agreement with the higher rotational support typical of nuclear star clusters;
- presence of an IMBH in the center;
- presence of residual dark matter observable in the outskirts, as a left over of the dark halo typical of dwarf galaxies.

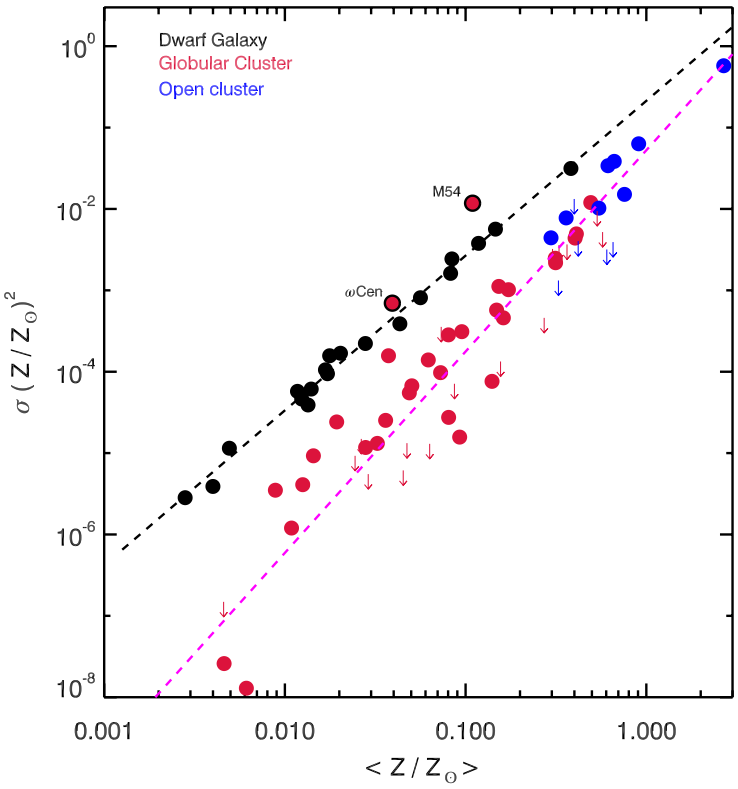

Figure 1.4: Metallicity spread versus metallicity for a collection of star clusters and dwarf galaxies. Star clusters are characterized by a single-metallicity value with very low spread, while dwarf galaxies shows a systematically higher spread in metals. Globular clusters suspected to be stripped nuclei of dwarf galaxies (M54 and ω Cen) are located along the dwarf galaxy sequence. Figure from Leaman (2012).

However, the combinations of all the above properties have not yet been confirmed in any of the Galactic GCs suspected to be stripped nuclei. Understanding the exact proportion of GCs that formed in-situ and the one accreted onto the Galaxy is fundamental, since it can provide a direct probe of the accretion history of the MW and therefore an estimate of the stellar mass accreted onto the Galactic halo. Indeed, if GCs are the final product of stripped dwarf galaxies, they are the "living fossil" of the consecutive merger events of galaxies that built up the MW through cosmological time and provide a crucial tool to understand the past of our galaxy.

1.2.3 An additional puzzle: the formation of multiple stellar populations

GCs have for long been thought to be made of a single stellar population with all stars having the same age and chemical composition. However, it is now well established that GCs actually harbour multiple stellar populations, characterized by the same metal content and same age (within few 100 Myr). This phenomenon is ubiquitously seen in GCs and it differs from the evidence of a metal spread observed instead only for few

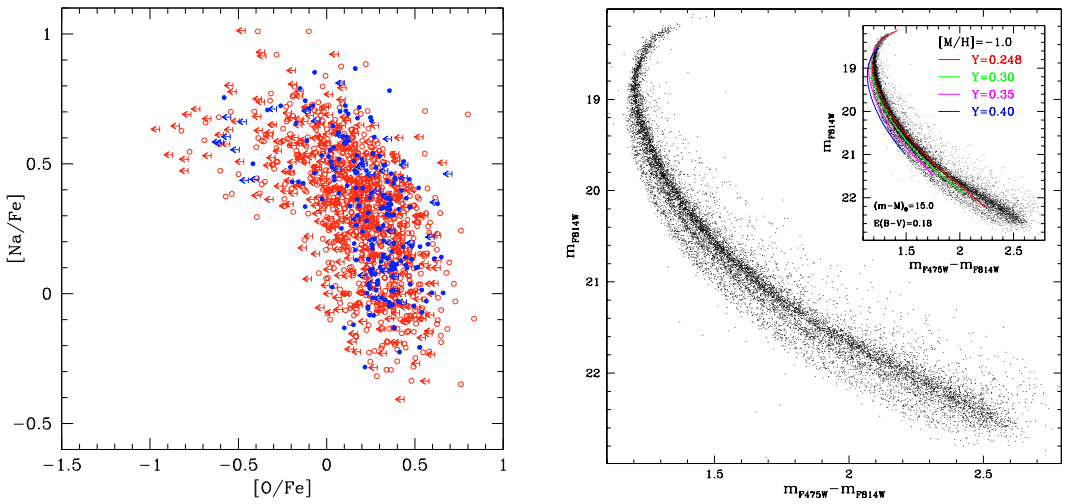

Figure 1.5: Multiple stellar populations in Galactic globular clusters. The left panel shows the inhomogeneity of the light-element abundances in GC stars (Carretta et al., 2009). At a given metallicity, both O-rich/Na-depleted stars and O-depleted/Na-rich stars are observed in a given GC. The right panel shows the photometric counterpart, where different populations of stars are located in different discrete sequences in the color-magnitude diagram (Piotto et al., 2007) that can be explained assuming different helium content for the different populations.

massive GCs (e.g., ω Cen). Multiple stellar populations are detectable spectroscopically through light element abundance variations (such as helium, nitrogen, carbon, sodium, oxygen, aluminum), within the same GCs (Kraft, 1994; Cannon et al., 1998; Carretta et al., 2009), and photometrically through the detection of multiple discrete sequences (or spread) in the color-magnitude diagram (Bedin et al., 2004; Piotto et al., 2007; Gratton et al., 2012). Figure 1.5 summarizes the typical spectroscopic and photometric evidence for the presence of multiple stellar populations in Galactic GCs.

Stars that are enriched in He, Na, N and Al while being depleted in C and O are often referred to as second generation stars (or enriched stars), while the other stars are referred to as first generation stars (or primordial population) and have the same abundance patterns of halo field stars (Bastian et al., 2015a).

The scenarios that attempt to explain these chemical features can be divided into two classes:

1. Multiple events of star formation, where the enriched populations formed from gas polluted by processed material of the primordial population (ejected by AGB stars, fast rotating stars, or very massive stars, e.g., Decressin et al., 2007; D'Ercole et al., 2008);

2. Primordial enrichment, where slower low-mass forming stars with protoplanetary disks accrete enriched material processed by faster-forming rotating massive stars

or interacting binaries, not requiring a multiple bursts of star formation (early disk accretion scenario, Bastian et al., 2013).

However, the detailed comparison with observations, including the evidence that young massive star clusters observed today do not show multiple epochs of star formation, leads to the conclusion that both the scenarios are not sufficient to comprehensively explain the multiple population phenomenon (Bastian et al., 2015b). Additional hints on their formation could come from the detailed study of the kinematic behavior of the different populations (Richer et al., 2013; Hénault-Brunet et al., 2015; Bellini et al., 2015) as seen today, after the long-term evolution of GCs. Thus, so far, the presence of multiple populations remains an unsolved puzzle that questions our understanding of the formation of GCs and of the first few 100 Myr of their life.

1.3 Unveiling the formation of globular clusters using their internal kinematics

The necessary first step to find a definite answer to the questions related to the formation of GCs is to understand in a comprehensive way their current internal properties and to link these to their dynamical evolution. The dynamical description of a GC is indeed fundamental to interpret their current internal properties (both morphological and kinematic) and to reveal their formation during the earliest epochs of galaxy formation. In fact, their >10 Gyr evolution was driven by the combined effects of dynamical processes (namely two-body interactions between stars and interactions with the host galaxy) and internal astrophysical processes (such as stellar evolution). Dynamics is therefore the suitable and necessary tool to understand the complex interplay between these processes.

In this Thesis, I will focus in particular on the investigation of the internal kinematics of GCs, a field that in the recent years has seen a boost in both quality and quantity (see Section 1.5). The study of kinematics provides an important piece of information to understand and interpret the current dynamical state of a GC and provides the "fossil record" of the processes that shaped these systems. The novel strategy that I will adopt consists in the *combined use of both state-of-the-art dynamical modeling and comprehensive kinematic observations*. In the field of GC related sciences, theoretical and observational studies have often not been sufficiently connected; therefore, it is crucial to bridge the gap between theory and observations.

The primary procedure to link dynamical models and observations will be by simulating mock observations. For this purpose, I have developed a tool to directly translating realistic dynamical simulations of GCs in observational-like samples (e.g., line-of-sight velocity or proper motion data sets), including errors and systematics that naturally arise from observations (see in particular Chapter 3). This brings a number of advantages:

1. estimating the limitations of the observations, in particular concerning potential biases in the data sets,

2. investigating the actual observability of kinematic fingerprints to test directly predictions from the dynamical models,

3. reaching a comprehensive interpretation of the observations,

4. understanding the limitations of the models.

Keeping this strategy in mind, in the remainder of this Chapter, I will introduce the main dynamical modeling techniques used for GCs throughout their long-term evolution and the state-of-the-art kinematic observations necessary for a thorough comparison with the models.

1.4 Dynamical modeling of globular clusters

As already mentioned, a GC can be described as a compact, bound, self-gravitating stellar systems where the stars interact gravitationally one with another (two-body encounters). In such a context it is useful to define some fundamental timescales to describe the effects of such gravitational interactions (Spitzer, 1987), in particular the relaxation time and the dynamical time of a cluster. The relaxation time $t_{\rm rel}$ can be defined as the timescale in which two-body interactions have a non-negligible effect on the dynamics of the system. As a function of the distance to the center of a cluster it is described as $t_{\rm rel}(r) \propto \sigma^3(r)/n(r)$, with σ the local velocity dispersion and n the stellar density of the system. For a typical cluster with 10^5-10^6 stars, the relaxation time is of the order of 10^7-10^9 years.[2]

Defining the dynamical time, $t_{\rm dyn}$, as the typical time of a particle to cross the stellar system (ratio between the characteristic size of a cluster R_h and the typical velocity of the stars, R_h/σ), one can show that (Spitzer, 1987)

$$\frac{t_{\rm rel}}{t_{\rm dyn}} \propto \frac{N}{\ln(0.4N)}, \tag{1.1}$$

where N is the number of stars in the cluster. This equation shows that the dynamical time of a typical cluster is always shorter than its relaxation time, that in turn is shorter than the age of the cluster, $t_{\rm dyn} \ll t_{\rm rel} < T_{\rm age}$. This illustrates how GCs can be considered as relaxed, quasi-collisional stellar systems, since they have lived long enough for two-body interactions to be effective in shaping their internal structure.

Two main goals can be reached with dynamical modeling: 1) understanding the dynamical evolution of a system of N particles interacting gravitationally, 2) describing the current dynamical state of such a system. These goals can be achieved using dynamical simulations of GCs (direct N-body, Monte Carlo, Fokker-Planck simulations) that follow the long-term dynamical evolution of a stellar systems. Moreover, a dynamical description of the current state of a cluster can be achieved also using dynamical models based on a steady-state solution of the Boltzmann collisionless equation (see e.g., Chapter 8 in Bertin, 2014), where the evolution due to stellar encounters is ignored[3].

[2]Note that these quantities are local quantities and therefore depend on the position considered in the cluster, typically implying shorter timescales in the central regions.

[3]This description is justified by the fact that the relaxation time of a cluster is larger than its dynamical time.

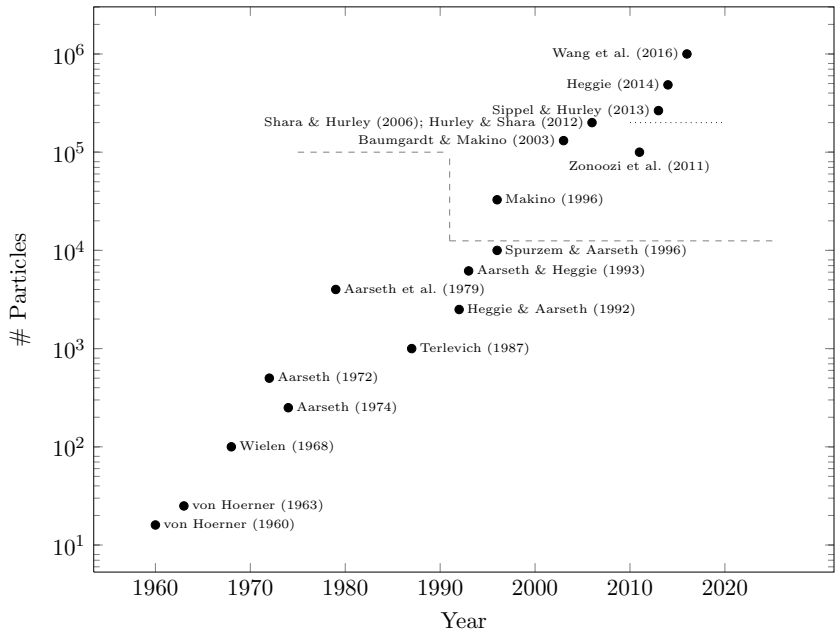

Figure 1.6: Selected milestones in increasing the number of particles used in direct N-body simulations, adapted by Anna Sippel from Heggie & Hut (2003); Hut (2010); Heggie (2011). The transition to special purpose computers, for example GRAPE (Makino et al., 2003), is indicated with a dashed line. The dotted line at $N \approx 2 \times 10^5$ particles indicates the transition to graphics processing units (GPUs).

In this Section, I will briefly introduce the main dynamical modeling techniques used for the description of GCs.

1.4.1 Globular cluster simulations

There exist different modeling techniques for studying the evolution of a system of N mass particles interacting gravitationally. The challenge consists in simulating a long-term evolution for a realistic number of particles (10^6 particles, a million-body problem) including all the relevant physical ingredients: stellar mass function, stellar evolution, binary stars, external potential of a host galaxy (Heggie & Hut, 2003).

The most direct approach consists in the direct summation of the gravitational force due to all the N particles in the system, to solve their equation of motion (e.g., Aarseth, 1999; Spurzem, 1999). Direct N-body simulations are computationally expensive, as they scale with the number of particles to the order of N^2. Figure 1.6 summarizes some important milestones in this computational challenge, showing the evolution of the number of particles used in a direct N-body simulation as a function of the year.

The development of special purpose hardware has been essential to complete simulations with a realist number of particles, in particular the GRAPE computers (GRavity PipE, see Makino et al., 2003) and GPUs (Graphic Processing Units, see Gaburov et al.,

2009; Nitadori & Aarseth, 2012). Today, the highlight of these efforts has cumulated in the state-of-the-art direct N-body simulations for one million stars of the DRAGON project (Wang et al., 2016), computed using a GPU parallelized version of `NBODY6` (Aarseth, 2003), called `NBODY6++GPU` (Wang et al., 2015).

As an alternative to direct N-body simulations, approximated methods could be regarded as an optimal compromise to have a realistic treatment of the relevant physical ingredients at a low computational cost. A possibility is the direct integration of the Fokker-Planck equation (e.g., Cohn, 1980; Einsel & Spurzem, 1999), where the time evolution of distribution functions is computed. An alternative, are the Monte Carlo methods (based on the early work of Hénon, 1971), where a statistical treatment to solve the Fokker-Planck equation is introduced. The basic assumptions of this method are 1) spherical symmetry, 2) proportionality of the time step at each position to the local relaxation time. This allows this method to be computationally fast. However, as a draw back, this method cannot follow any physical processes with time scales shorter than the local relaxation time, or consider deviations from spherical symmetry, for example due to internal rotation or external tidal fields. As an example of a Monte Carlo code, the `MOCCA` code (Giersz et al., 2013; Hypki & Giersz, 2013; Giersz et al., 2015) has provided in the recent years a high number of cluster simulations sampling a large range of parameter space, implementing most of the relevant physical processes, and it has been extensively tested against direct N-body simulations (see e.g., Giersz et al., 2013).

1.4.2 Distribution-function based models

Although not used here, for completeness I briefly discuss the use of physically motivated distribution-function models, as a useful tool to describe the current dynamical state of a GC. These self-consistent models are the steady-state solution of the Boltzmann collisionless equation, coupled with the Poisson equation. The use of the Boltzmann collisionless equation is justified by the fact that the relaxation time of a cluster is much larger than its dynamical time and therefore it can be assumed that the clusters reach rapidly a quasi-stationary state and that the time evolution due to collisions can be ignored.

A classical zeroth-order dynamical description is given by spherical, isotropic, non-rotating models, with a spatial truncation (physically motivated by the presence of the tidal field of the host galaxy) and with a single mass component. In this context, the most successful models used to describe the basic structural and dynamical properties of GCs are the King (1966) models and the spherical Wilson (1975) models (see e.g., McLaughlin & van der Marel, 2005).

The restrictive assumptions of sphericity and isotropy can be relaxed, taking into account the additional physical ingredients of internal rotation. This can be done considering the dependence of the distribution function to the z-component of the angular momentum, in addition to the dependence to the energy. An example of axisymmetric models that have been successful in reproducing the dynamical and structural properties of clusters are the rotational King models from Einsel & Spurzem (1999), the rotating Wilson (1975) models (Sollima et al., 2009), and the differential rotating models

from Varri & Bertin (2012). These models include deviations from spherical symmetry, presence of the differential rotation, and mild radial anisotropy (e.g., Bianchini et al., 2013 and reference therein).

An additional step towards a realistic description of a GC, consists in taking into account the presence of multiple mass components (that in a GC are represented by stars with a range of masses). An example are the multi-mass generalization of the King models (Da Costa & Freeman, 1976), the recently developed anisotropic two-component $f_T^{(\nu)}$ models (de Vita et al., 2016), and the family of multi-mass, truncated and anisotropic models by Gieles & Zocchi (2015). The latter models provide a flexible tool able to describe the phase-space density of star clusters at all stages of their life, including the effects connected to mass segregation.

Finally, there are other modeling techniques suitable to describe the current internal dynamical state of a GC: for example, the asymmetric Jeans modeling (based on the moments of the Boltzmann collisionless equation, e.g., Watkins et al., 2013; den Brok et al., 2014), or orbit-based methods, such as Schwarzschild modeling (e.g., van de Ven et al., 2006; van den Bosch et al., 2006). All these different modeling efforts have lead to a much deeper understanding of the internal dynamics of GCs from a theoretical point of view.

1.5 State-of-the-art kinematic observations

Kinematic measurements are necessary for a detailed comparison between observations and dynamical models. Galactic GCs are the ideal environment where detailed kinematic observations can be carried out, since their stellar population can be resolved with the available instrumentation, with the exception of the most crowded central regions of GCs. The studies of the internal kinematics of Galactic GCs have experienced a fast growth in the rent years, thanks to the development of a number of observational techniques delivering complementary kinematic measurements. Until recently, only of the order of 15 MW GCs had a sufficient number of stars (few hundred) with accurate enough velocity measurements (velocity errors of a few km s^{-1}) to carry out a dynamical analysis (see e.g., Zocchi et al., 2012). For this reason the study of the kinematics has been partially neglected, with more weight given to photometric studies. Today, thanks to the combination of large programs (like HSTPROMO collaboration[4], Gaia-ESO Survey[5], and the Gaia mission[6]) and dedicated investigations on single clusters, we can now make use of unprecedented kinematic measurements for a larger set of clusters. For the best studied cases (e.g., ω Cen), those cover the spatial extent from the outskirts to the very central few arcseconds. This delivers measurements for the two components of the velocity vector on the plane of the sky for over 100 000 stars and for the third component along the line-of-sight for a few thousands stars (see following paragraphs).

In this Section, I briefly review the main observational strategies that deliver us the state-of-the-art velocity measurements. A deep understanding of these data sets,

[4] http://www.stsci.edu/~marel/hstpromo.html
[5] https://www.gaia-eso.eu
[6] http://sci.esa.int/gaia

from an observational perspective, is fundamental to be aware of the limitations and advantages that different types of data offer, in view of the kinematic investigations presented throughout this Thesis.

1.5.1 Line-of-sight velocities

Traditional kinematic data sets of Galactic GCs are based on line-of-sight velocity measurements obtained with ground based spectroscopy. Two main strategies are usually adopted to acquire these velocities: 1) resolved kinematics, by measuring discrete velocities of individual stars, or 2) unresolved kinematics by measuring the velocity dispersion from line broadening of integrated-light spectra with either integral field units (IFUs) or slit spectroscopy.

The two different strategies sample two different spatial regions in a typical GC: discrete kinematics is best suited for the intermediate region around the half-light radius of a cluster (e.g., Lardo et al., 2015), while unresolved kinematics from integrated-light spectroscopy is suitable for the crowded center (e.g., Lützgendorf et al., 2013) where the stars in a GC are partially unresolved. An additional approach used for the central regions consists in extracting discrete measurements form adaptive optics corrected IFUs (e.g., Lanzoni et al., 2013). However, unsettlingly, these complementary methods seem to give discrepant results for the central measurements in many clusters (e.g., Lanzoni et al., 2013; Lützgendorf et al., 2015). An extensive investigation of the biases that can arise using IFU instruments to measure the kinematics of partially-resolved stellar systems is the focus of Chapter 3 of this Thesis.

Some intrinsic limitations in line-of-sight kinematic measurements are always present. First of all, since (time consuming) spectroscopy is needed, only the brightest sources can be observed. These correspond to the bright giant stars, in the mass range $0.8-0.9$ $M_{\odot}$. Moreover, the typical number of stars for which line-of-sight velocities are measured is relatively small, usually up to only a few hundred. However, the combination of IFU instruments with large field-of-views (such as MUSE at the Very Large Telescope) and deconvolution techniques to extract spectra of resolved stars, have very recently enabled the collection of $\approx 10\,000$ stars for a given cluster (see e.g., Kamann et al., 2016). Finally, line-of-sight measurements are limited to sampling only one component of the velocity vector, requiring assumptions when modeling the three-dimensional structure of a cluster (causing e.g., the mass-anisotropy degeneracy, Binney & Mamon, 1982).

1.5.2 Proper motions

A significant improvement in the quality of the kinematic data was recently possible thanks to the high-precision Hubble Space Telescope (*HST*) proper motions. Measuring accurate proper motions (with velocity errors of a few km s^{-1}) from ground based facilities is a very difficult task, since it requires to measure very small spatial displacement of stars in images taken at different epochs (e.g., van Leeuwen et al., 2000; Bellini et al., 2009). However, with the diffraction-limited resolution and the stability of *HST*, such an astrometric task is now possible. As an example, the astrometric precision reachable using *HST* is ~ 0.01 pixel per single exposure of a bright source (Bellini et al., 2014), which allows to measure velocity displacements for a typical GC (at the

distance of 5 kpc) of the order of ≈ 1 km s^{-1} using a time baseline of ≈ 10 yr. This make *HST* proper motion ideal for internal kinematic studies of GCs (with internal velocity dispersion of ≈ 10 km s^{-1}).

The largest proper motion data sets available come from the HSTPROMO collaboration[7] (Bellini et al., 2014; Watkins et al., 2015a,b), providing velocity measurements on the plane of the sky for 22 GCs, with a median of ∼60,000 stars per cluster (see Chapter 4 of this Thesis). Moreover, other dedicated works provided proper-motion samples to single GCs (e.g., McLaughlin et al., 2006; Richer et al., 2013 for NGC 104, McNamara et al., 2003 for NGC 7078, McNamara & McKeever, 2011; McNamara et al., 2012 for NGC 6266, and Anderson & van der Marel, 2010 for NGC 5139).

Proper motion samples provide many advantages over line-of-sight velocity samples. First of all, the motions of both bright and faint stars are measured, giving therefore the possibility to explore the kinematics for stars with different masses (down to $\approx 0.3-0.4$ $M_{\odot}$). This is of particular interests for studies related to energy equipartition in GCs (see Chapter 6 of this Thesis). Moreover, they provide data sets a factor of $10-100$ larger than typical line-of-sight samples, enabling a better statistics and to reach low levels of random errors. Finally, two components of the velocity-vector are measured, providing a direct constraint on the anisotropy in the velocity space and removing therefore the mass-anisotropy degeneracy of the dynamical modeling.

A disadvantage of *HST* proper motions is that the movement of each star is commonly computed relative to the movement of all the other stars. This is necessary due to the lack of an absolute reference frame in the GCs crowded fields, and results in the elimination of any solid body rotation possibly present in the clusters. Note however, that in specific cases, the internal rotation can then be fully recovered (for example for 47 Tuc, using background stars of the Small Magellanic Cloud as absolute reference frame, Anderson & King, 2003).

Finally, the typical field-of-view sampled by proper motion studies is around a few half-light radii around the center of a cluster. However, because of crowding, proper motions are not measurable in the inner ~ 10 arcsec (corresponding to 0.5 pc at the distance of 10 kpc) for those clusters with very high central concentration (e.g. M15, Bellini et al., 2014).

1.5.3 The advantages of three-dimensional kinematics

As discussed above, line-of-sight velocity samples and proper motion samples provide a complimentary kinematic view of a GC. Therefore, the combination of the two, gives us the unique opportunity to exploit their potential, constructing a comprehensive three-dimensional view of the internal kinematics of a cluster. The unprecedented quality of the available data sets allows us already to tackle a series of fundamental topics, some of them discussed in more details in the following of this Thesis:

1. **Intermediate-mass black holes:** measuring the central velocity dispersion of GCs within a few arcsecs from the center, to detect a cusp indicative of the presence a massive point source (see Chapter 3 of this Thesis).

[7] `http://www.stsci.edu/~marel/hstpromo.html`

2. **Energy equipartition:** measuring how efficiently stars with different masses have exchanged energy via two-body encounters, developing a mass-dependent velocity dispersion (see Chapter 6 of this Thesis).

3. **Binary stars:** measuring directly the kinematic behavior of binary stars (or other exotic stellar objects, such as blue stragglers stars, Baldwin et al., subm.) to asses their role in shaping the current state and the dynamical evolution of a cluster (see Chapter 5 of this Thesis).

4. **Multiple stellar populations:** coupling the kinematic information with chemical or stellar color information, to determine if different stellar populations display different kinematic behaviors as a "fossil record" of their formation and subsequent evolution in a cluster (see Chapter 5 of this Thesis, Bellini et al., 2015; Richer et al., 2013).

5. **Velocity anisotropy:** directly measuring the anisotropy in the velocity space using the three separate velocity vector components, fundamental to break the mass-anisotropy degeneracy in dynamical modeling (e.g., Bellini et al., 2014; Watkins et al., 2015a) or to assess the dynamical history of a cluster.

6. **Internal rotation:** measure the amount of internal rotation, indicative of the clusters' initial conditions and responsible in shaping their long-therm dynamical evolution (e.g., Kacharov et al., 2014; Fabricius et al., 2014; Bianchini et al., 2013; Bellazzini et al., 2012; Anderson & King, 2003).

7. **Comprehensive dynamical modeling:** exploiting the 5-dimensional phase space information (three-dimensional velocity and two-dimensional spatial coordinates) to assess the intrinsic properties of a cluster, such as three-dimensional shape, dynamical mass, mass-to-light ratio and dynamical distance.

In addition to the already available data sets, we are now entering the era of groundbreaking kinematic measurements thanks to the upcoming data from the Gaia mission[8]. This will first provide accurate membership information useful to discern cluster members from non-member stars, and then proper motions for the outer parts of GCs. This will be particularly useful to further study the effects of the interaction of clusters with the MW and their stripping process due to tidal interactions.

1.6 Research program

The particular goal of this Thesis is to *unveil the current dynamical properties of GCs and to connect these to their formation and subsequent dynamical evolution.* As a starting point, in Chapter 2, I address the question of an accreted versus in-situ formation of GCs, considering in particular the case of extended star clusters. I will show that morphological studies alone are not sufficient to disentangle the two categories of clusters. This hints to the need to investigate the complexity of the internal kinematics of GCs in detail, to look for tracers of particular evolution and formation mechanisms. The

[8]First data release scheduled for end of summer 2016, `http://sci.esa.int/gaia`.

main question that I wish to answer is: "Can we exploit the complexity of the internal kinematics to unveil the formation and dynamical evolution of globular clusters?".

Therefore, as a next step, in Chapters 3−5, I investigate two observational strategies used to assess the internal kinematics of GCs, primarily using simulated mock observations: integrated-light spectroscopy for line-of-sight velocity measurements and proper motion observations. The understanding of the limitations and advantages of these two strategies is fundamental to answer questions related to the presence of IMBHs in the centers of GCs, the effect of binary stars in the kinematics, the effects of energy equipartition due to two-body interactions, and the kinematics of multiple stellar populations. Finally, given our deeper understudying of the data, in Chapter 6, I will set the first step to link the dynamical state of a cluster to its peculiar dynamical history, using a set of dynamical simulations and investigating the phenomenon of energy equipartition in GCs from a kinematic point of view. The main questions that motivate my work can be summarized as follows:

- **Chapter 2: Accretion of globular clusters onto the Milky Way.** Are extended star clusters accreted systems? Can we distinguish on the basis of morphology alone between accreted star clusters and those that formed in-situ?
- **Chapter 3: Intermediate-mass black holes in globular clusters.** How robust are the kinematic observations used to detect intermediate-mass black holes? Do we understand the data? How can we obtain reliable data?
- **Chapter 4 and 5: State-of-the-art HST proper motions of globular clusters.** How are proper motions measured? What are the biases and systematics in the datas sets? What is the effect of unresolved binaries in proper motion samples?
- **Chapter 6: Energy equipartition in globular clusters.** How can we quantify the degree of energy equipartition reached by a cluster using state-of-the-art kinematic data? Can we find a way to connect the current dynamical properties of a cluster to its dynamical history and evolution?

The answers to these questions will be provided by the combination of a variety of modeling and observational techniques that will be the basis for revolutionizing our current understanding of the formation and evolution of GCs.

Chapter 2

The possible accreted origin of globular clusters: the case of extended star clusters

"*The inefficiency of satellite accretion in forming extended star clusters*"
Bianchini, Paolo; Renaud, Florent; Gieles, Mark; Varri, Anna Lisa
Monthly Notices of the Royal Astronomical Society: Letters, Volume 447, Issue 1, p.L40-L44
http://adsabs.harvard.edu/abs/2015MNRAS.447L..40B

This Chapter addresses the possible accreted origin of extended star clusters. These systems are characterized by a diffuse structure and overlap in properties with both standard GCs and faint dwarf galaxies. Their extended morphology suggests they could have originally formed compact and later expanded due a peculiar dynamical evolution, for example due to accretion onto the MW. Using N-body simulations, I test the accretion scenario and show that clusters originally formed as compact do not experience a sufficient expansion during the accretion event to explain their observed extended morphology. Therefore, these clusters were likely already extended at formation. Moreover, the simulations show that morphology alone is not enough in order to differentiate clusters with an accreted origin from clusters that formed in-situ in the host galaxy. From this arises the urge to study in details the internal kinematics of GCs in order to characterize their dynamical state and detect fingerprints of their formation, as will be done in the following Chapters.

Monthly Notices of the ROYAL ASTRONOMICAL SOCIETY

MNRAS **447,** L40–L44 (2015) doi:10.1093/mnrasl/slu177

The inefficiency of satellite accretion in forming extended star clusters

Paolo Bianchini,[1]★† Florent Renaud,[2,3] Mark Gieles[2] and Anna Lisa Varri[4]

[1]*Max-Planck Institute for Astronomy, Koenigstuhl 17, D-69117 Heidelberg, Germany*
[2]*Department of Physics, University of Surrey, Guildford GU2 7XH, UK*
[3]*Laboratoire AIM Paris-Saclay, CEA/IRFU/SAp, Université Paris Diderot, F-91191 Gif-sur-Yvette Cedex, France*
[4]*School of Mathematics and Maxwell Institute of Mathematical Sciences, University of Edinburgh, King's Buildings, Edinburgh EH9 3JZ, UK*

Accepted 2014 November 4. Received 2014 November 3; in original form 2014 October 15

ABSTRACT

The distinction between globular clusters and dwarf galaxies has been progressively blurred by the recent discoveries of several extended star clusters, with size (20–30 pc) and luminosity ($-6 < M_v < -2$) comparable to the one of the faint dwarf spheroidals. In order to explain their sparse structure, it has been suggested that they formed as star clusters in dwarf galaxy satellites that later accreted on to the Milky Way. If these clusters form in the centre of dwarf galaxies, they evolve in a tidally compressive environment where the contribution of the tides to the virial balance can become significant, and lead to a supervirial state and subsequent expansion of the cluster, once removed. Using *N*-body simulations, we show that a cluster formed in such an extreme environment undergoes a sizable expansion, during the drastic variation of the external tidal field due to the accretion process. However, we show that the expansion due to the removal of the compressive tides is not enough to explain the observed extended structure, since the stellar systems resulting from this process are always more compact than the corresponding clusters that expand in isolation due to two-body relaxation. We conclude that an accreted origin of extended globular clusters is unlikely to explain their large spatial extent, and rather favour the hypothesis that such clusters are already extended at the stage of their formation.

Key words: methods: numerical – globular clusters: general.

1 INTRODUCTION

In recent years, a number of low-luminosity stellar systems were discovered around galaxies populating the transition region between low-luminosity dwarf spheroidal galaxies (dSphs) and globular clusters (GCs) in the luminosity–size parameter space. These stellar systems, with a luminosity between $-6 < M_v < -2$ and a half-light radius of about ≈20–30 pc, are often referred to as extended clusters. In the Milky Way (MW), the known objects are Pal 4, Pal 14, AM 1 (Mackey & van den Bergh 2005; Harris 2010), and several extragalactic ones (Brodie & Larsen 2002; Huxor et al. 2014; Mackey et al. 2013). They are preferentially found in the outer haloes of galaxies and are characterized by a more diffuse structure than typical GCs of similar luminosity. Therefore, their intermediate size, between the regime of dSphs galaxies and the bulk of GCs, makes them intriguing objects, crucial for the understanding of the differences and similarities of the formation of low-mass stellar systems.

★E-mail: bianchini@mpia.de
†Member of the International Max Planck Research School for Astronomy, and Cosmic Physics at the University of Heidelberg, IMPRS-HD, Germany.

Extended clusters have half-mass relaxation times slightly larger than their age, which makes it difficult to explain their sizes by expansion driven by two-body relaxation (Gieles, Heggie & Zhao 2011). The debate on the nature of these objects was recently enhanced by the discovery of the peculiar MW extended stellar system Laevens1/Crater (half-light radius between 20 and 30 pc), whose classification as a GC or a dSph is still debated (Belokurov et al. 2014; Laevens et al. 2014). Moreover, the complexity of their internal dynamics is not fully understood yet. Frank, Grebel & Küpper (2014) found the surprising evidence of mass segregation in Pal 14. The current relaxation time of this extended cluster exceeds the Hubble time and therefore is too long to explain the settling of segregation only through dynamical evolution. The combined effect of primordial mass segregation and dynamical evolution could explain the structure of this cluster (Haghi et al. 2014). Therefore, further studies of the internal properties of such stellar systems are indeed crucial to unveil their origin.

The presumed origin of such extended clusters includes three main mechanisms: (1) they genuinely formed extended (this requires a formation environment with a high Mach number, which is appropriate to dwarf galaxies; Elmegreen 2008); (2) they formed through the merging of two or more star clusters (Fellhauer & Kroupa 2002; Assmann et al. 2011); (3) they were born as compact

star clusters and later expanded due their peculiar environmental-driven evolution; this hypothesis will be tested in this study. Evolutionary processes that are often assumed to cause an expansion are strong tidal shocks (Spitzer 1958; Ostriker, Spitzer & Chevalier 1972) or accretion process on to the MW halo (Mackey & Gilmore 2004; Miholics, Webb & Sills 2014). The latter mechanism assumes that these clusters formed in dwarf-like satellite galaxies that later were stripped and accreted on to the halo of the host galaxy. We note that accretion of dwarf galaxies is a process commonly used to explain the structural properties of GC systems. In fact, there is growing evidence that a significant fraction of MW GCs are accreted systems, while the remaining formed in situ in the early phase of galaxy formation (Marín-Franch et al. 2009; Forbes & Bridges 2010; Leaman, VandenBerg & Mendel 2013). This is further supported by the spatial coincidence of outer halo GCs with stellar streams and overdensities (Mackey et al. 2010).

In this work, we focus on the possibility that extended clusters formed in the context of an accretion event, testing if their observed extended sizes can be explained by the structural adjustment of the clusters to the time-dependent tidal field. We evaluate this hypothesis using *N*-body simulations considering the case of a cluster formed in the central regions of dwarf-like galaxies, where it experiences a compressive tidal field, which is then switched off to mimic the accretion of the cluster on to a MW-like galaxy. Compressive tides provide an extreme environment that enables the cluster to acquire an excess of kinetic energy with respect to its potential energy. A complementary approach has been followed by Webb et al. (2014) and Miholics et al. (2014) for the study of the evolution of the size of clusters embedded in less extreme (non-tidally compressive) environments.

The Letter is organized as follows: first, we introduce the compressive tidal environment typical of cored regions of galaxies and show with analytical calculations that an accretion event causes an expansion of stellar systems. Then, in Section 3, we present our *N*-body simulations and we discuss our results. Finally, we report our conclusions in Section 4.

2 EXPANSION OF CLUSTERS DUE TO SATELLITE ACCRETION

2.1 Compressive tides in galaxy cores

Let us consider a gravitational potential ϕ embedding a star cluster. The associated tidal tensor can be written as the second space derivative of the potential (Renaud et al. 2008)

$$T^{ij} = -\partial^i \partial^j \phi. \tag{1}$$

The tides are fully compressive if all eigenvalues λ_i of this tensor are negative, and extensive if at least one eigenvalue is positive. One typical environment of compressive tides is the central region of galaxies with cored density profiles. For dwarf galaxies, recent studies show that cored profiles are favoured over cuspy ones (e.g. Walker & Peñarrubia 2011). In the case of a Plummer potential with characteristic radius r_0, fully compressive tides are found in the central region, delimited by $r < r_0/\sqrt{2}$ (Renaud 2010).

2.2 Proof of the principle

We wish to describe the expansion of a stellar system due to a time-varying tidal field. We consider a GC initially embedded in an isotropic compressive tidal field that is then instantaneously removed (impulsive approximation; Spitzer 1958) to mimic the accretion event of the satellite that hosts the cluster in its centre. In this section, we follow the procedure outlined in Hills (1980).

Let us consider an isotropic tidal field such that the eigenvalues of the tidal tensor are equal, $\lambda_i = \lambda$, and negative (fully compressive tides). The initial energy of the cluster embedded in such field is (Renaud 2010, his equation E.12)

$$E_0 = \frac{1}{2} M_{\rm c} \sigma^2 - \frac{G M_{\rm c}^2}{2 r_{\rm v}} - \frac{1}{2} \lambda \alpha M_{\rm c} r_t^2, \tag{2}$$

where the last term describes the energy due to the compressive tides, $M_{\rm c}$ the total mass of the cluster, σ its velocity dispersion, $r_{\rm v}$ the virial radius, r_t the radius where the density of the cluster drops to zero, and α depends on the mass profile of the cluster and is defined as $\alpha = 1/(M_{\rm c}\, r_t^2) \int_0^{M_{\rm c}} r^2 \, {\rm d}m$. We assume that the system is virialized before the compressive tides are removed (Renaud 2010, his equation E.13)

$$M_{\rm c}\sigma^2 - \frac{G M_{\rm c}^2}{2 r_{\rm v}} + \lambda \alpha M_{\rm c} r_t^2 = 0. \tag{3}$$

Since λ is negative, we see that the velocity dispersion of the cluster is higher than what expected from a no-tide case.

In the impulsive approximation, we assume that both velocity dispersion and the radii of the cluster remain unchanged when the tidal field is instantaneously removed. This approximation is justified by the fact that the time-scale in which the stripping of a dwarf galaxy occurs is small compared to its internal dynamical time-scale. The new energy of the system is therefore

$$E_1 = \frac{1}{2} M_{\rm c} \sigma^2 - \frac{G M_{\rm c}^2}{2 r_{\rm v}} \tag{4}$$

and, by using equation (3), we get

$$E_1 = -\lambda \alpha M_{\rm c} r_t^2 - \frac{1}{2} M_{\rm c} \sigma^2. \tag{5}$$

The cluster remains bound ($E1 < 0$) for

$$\lambda > -\frac{1}{2} \frac{\sigma^2}{\alpha r_t^2}. \tag{6}$$

Therefore, if the system is embedded in too strong compressive tides (very negative values of λ), its energy exceeds the reference level which would allow it to remain bound after the impulsive change. The cluster is then 'supervirialized' and is unbound when the tides are switched off. We here consider unbound when the total energy is positive, in reality the core can remain bound and stars in the outer part escape with velocities larger than the escape velocity.

After turning off the tidal field, the cluster settles in a new equilibrium state on a dynamical time-scale, with a new radius $r_{\rm v}'$ and a new velocity dispersion σ'. Neglecting any mass-loss (i.e. constant $M_{\rm c}$ over a dynamical time), the final state is described by the virial equation

$$M_{\rm c}\sigma'^2 - \frac{G M_{\rm c}^2}{2 r_{\rm v}'} = 0, \tag{7}$$

and a total energy

$$E = -\frac{G M_{\rm c}^2}{4 r_{\rm v}'}. \tag{8}$$

Using equations (3), (4), and (8) we obtain a relation between the virial radius $r_{\rm v}'$ at the final state and the initial radius $r_{\rm v}$

$$r_{\rm v}' = r_{\rm v} \left(1 + \frac{2 \lambda \alpha r_t^2 r_{\rm v}}{G M_{\rm c}} \right)^{-1}. \tag{9}$$

In the case of compressive tides (i.e. $\lambda < 0$), the final virial radius r_v' is always larger than the initial r_v. The cluster therefore expands after the tidal field has been switched off.

In a realistic case, we would expect that the expansion would affect more the stars in the outer part of the cluster. These stars will escape with non-zero velocities, taking away a large fraction of the energy gained during the compressive phase. This could indeed reduce the expansion. Therefore, we discuss more detailed simulations in the next section.

3 *N*-BODY SIMULATIONS

We now study the problem with *N*-body simulations, using NBODY6TT (Renaud, Gieles & Boily 2011) based on NBODY6 (Aarseth 2003). NBODY6TT gives the possibility to add to the regular forces the effect of an arbitrary time-dependent tidal field. We use the graphics processing unit (GPU) enabled version of Nitadori & Aarseth (2012) and compute the simulations using the GPU cluster at the University of Surrey.

Our fiducial initial conditions for the cluster consist of 4096 particles drawn from a Plummer sphere. Since our investigation focuses specifically on the effects of an abrupt variation of the tidal environment of the star cluster, we consider exclusively equal-mass models, in the absence of stellar evolution. The compressive tides are given by the central region of another Plummer potential, mimicking the cored potential well in the centre of a dwarf galaxy (see Section 2.1). The tidal tensor is computed analytically and fed to NBODY6TT. The tides are switched off to simulate the stripping of the dwarf galaxy as a consequence of the accretion process on to the MW. For simplicity, the potential of the MW is not considered: the clusters experience the tides from the dwarf galaxy alone, which are then fully removed.[1]

In the following sections, we present the results of the long-term dynamical evolution of the cluster, considering different initial densities, tidal field strengths, transitions between compressive tides and isolation (impulsive or adiabatic transitions), and in orbit inside the dwarf galaxy potential. We consider as bound stars those with $E < 0$ (Renaud et al. 2011), where the energy is given by the sum of the potential and kinetic energy, E=W+K.

3.1 Evolution in the centre of a compressive tidal potential

The first case we explore consists in a cluster with virial radius $r_v = 1$ pc. We aim to study the dependence of the cluster's evolution on the strength of the tidal field. For this reason, we place the cluster with no orbital motion in the centre of a dwarf galaxy with total mass $M = 10^8 M_\odot$ and scale radius $r_0 = 1000, 500, 100$ pc (typical values for dwarf galaxies masses and characteristic radii; McConnachie 2012). The tidal field experienced is thus compressive, constant, and isotropic. We label these three compressive tidal fields as weak, intermediate, and strong. The compressive tides are switched off at 8 Gyr. At this time, the clusters have already undergone core collapse and have expanded to their maximum extent (see Fig. 1).

[1] We note that our low-*N* cluster evolves to lower densities than real clusters. This is because in the expansion phase clusters evolve to a constant ratio of relaxation time over age, such that the clusters density is proportional to N^2. From equation (9), we see that the expansion factor is smaller for cluster with higher density. This means that more massive clusters are less affected by the removal of the tides than the clusters in our *N*-body models.

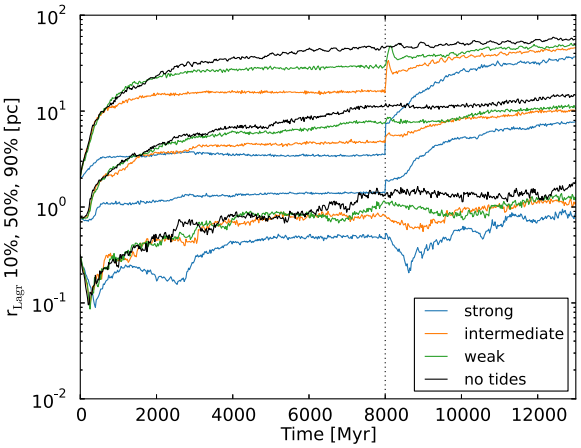

Figure 1. Time evolution of the Lagrangian radii (enclosing 10, 50, and 90 per cent of the total bound mass) of a cluster in three compressive tidal fields, labelled as weak (green lines), intermediate (orange lines), and strong (blue lines) tidal field. When the compressive tides are switched off at 8 Gyr (vertical line), the cluster expands. However, the expansion is not enough to generate objects more extended than the one evolved in isolation (black lines).

In Fig. 1, we show the time evolution of the 10, 50, and 90 per cent Lagrangian radii of the cluster (i.e. the radii containing 10, 50, and 90 per cent of the bound mass, respectively) for the strong, intermediate, and weak compressive tidal fields. The evolution of the tidally perturbed model is compared to the one of an isolated cluster. While the compressive tides are present, the spatial extent of the cluster depends on the strength of the tidal field: the stronger the field, the more compact the cluster is. The initial setup of the clusters ensures equipartition between kinetic and internal potential energies, and neglects the tidal term ($K/W = -0.5$). During the first phase, the negative energy brought by the compressive tides is balanced by an excess of kinetic energy with respect to the sole internal potential ($K/W < -0.5$). The time evolution of the ratio K/W is depicted in Fig. 2.

When the compressive tidal field is switched off (8 Gyr), the cluster experiences an expansion, that is larger for stronger tides. We note that the expansion is significant for the 50 and 90 per cent Lagrangian radii, while is negligible for the inner 10 per cent Lagrangian radius, confirming that tides only affect the outer regions of clusters. We compare the spatial structure of the clusters evolved in compressive tides with the corresponding clusters evolved in isolation. From Fig. 1, it is clear that the expansion due to the abrupt variation of the tidal environment fails to produce objects that are more extended than the isolated cluster. We test this conclusion using a wide range of initial conditions including different initial cluster densities (initial virial radius of $r_v = 0.4, 1, 2.5$ pc, initial number of particles $N = 4096, 8192$) and circular orbits for the cluster inside the compressive tidal region. None the less, all star clusters that underwent such a process are always less extended than the one evolved in isolation (a summary of the runs is reported in Table 1).

3.2 Impulsive versus adiabatic tidal change

So far, we considered the case of an impulsive transition between the regime of compressive tidal field and no tidal field. We explore the effect of an adiabatic transition, occurring over a

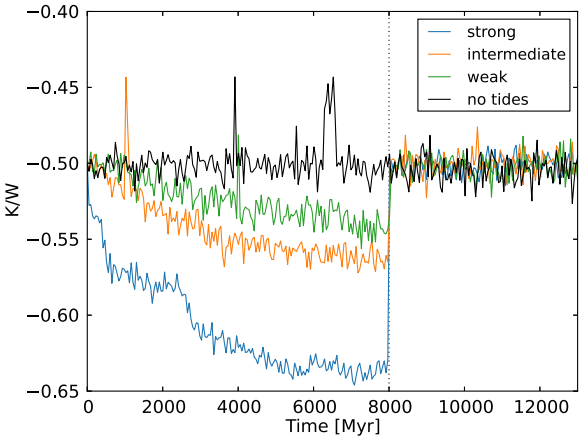

Figure 2. Time evolution of the ratio of kinetic and potential energy K/W of the runs presented in Fig. 1. The clusters are initialized with $K/W = -0.5$, i.e. neglecting the tides, but subsequently adjust quickly to it (see especially the case with strong tides). When compressive tides are switched off, the cluster is in a 'supervirialized' state and tends to retrieve a virialized one by expanding. The peaks correspond to the formation of binaries.

Table 1. Ratios, $\mathcal{R}_{10,50,90}$, of the 10, 50, and 90 per cent Lagrangian radii at 10 Gyr of a cluster evolved in compressive tides and then released to isolation at 8 Gyr and the corresponding one evolved in isolation. The names of the simulations indicate the strength of the compressive tidal field (W, I, S, for weak, intermediate, or strong; see Section 3.1) or a circular orbit at 250 pc from the dwarf galaxy centre, indicated with C. The initial number of particles N and virial radius r_v are reported. For I_4k_ad, the transition between the regime of compressive tides and isolation is adiabatic (see Section 3.2). Clusters evolved in compressive tides are always less extended than the one evolved in isolation.

Model	N	r_v	$\mathcal{R}_{10\,\mathrm{per\,cent}}$	$\mathcal{R}_{50\,\mathrm{per\,cent}}$	$\mathcal{R}_{90\,\mathrm{per\,cent}}$
W_4k	4096	1 pc	0.53	0.75	0.80
I_4k	4096	1 pc	0.68	0.74	0.76
S_4k	4096	1 pc	0.40	0.46	0.56
I_8k	8192	1 pc	1.01	0.90	0.83
C_4k	4096	0.4 pc	1.01	0.65	0.52
C_4k_1	4096	1 pc	0.92	0.77	0.69
C_4k_2	4096	2.5 pc	0.66	0.60	0.84
I_4k_ad	4096	1 pc	0.63	0.72	0.72

time-scale of 600 Myr.[2] Fig. 3 shows the evolution of the 90 per cent Lagrangian radius in the transition region only, for both an impulsive and adiabatic transition. The eigenvalues λ associated with the time-dependent tidal tensors are shown in the lower sub-panel. Both simulations converge to the same radial extent in a few dynamical times, and no significant differences are present 1 Gyr after the transition (see also Table 1, model I_4k and I_4k_ad).

3.3 Observational surface density and velocity dispersion profiles

A further confirmation of the inefficiency of satellite accretion events in forming extended stellar systems, is given by the detailed

[2] This time-scale is the other extreme (compared to the impulsive transition), lasting longer than a typical accretion event.

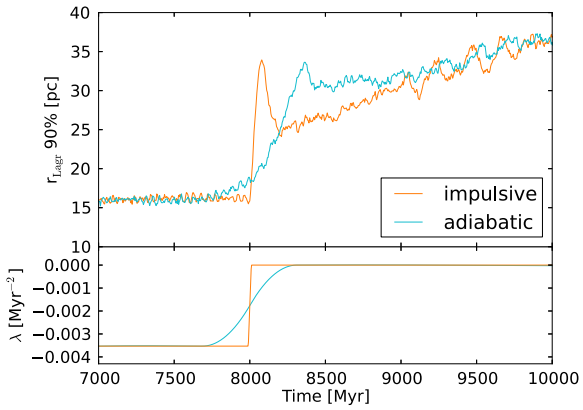

Figure 3. Time evolution of the 90 per cent Lagrangian radius for a simulation with an impulsive transition between compressive tidal field and isolation (orange line) and one with an adiabatic transition lasting 600 Myr (cyan line). An intermediate strength of the compressive tidal field is used (see Fig. 1) and the corresponding eigenvalues λ are shown in the lower sub-panel. The 90 per cent Lagrangian radii converge in short time to the same value.

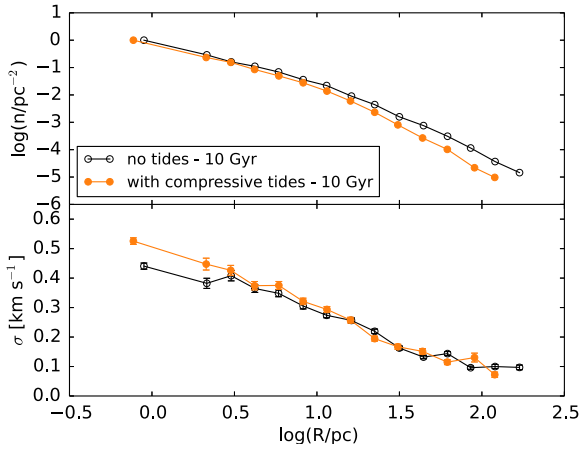

Figure 4. Surface density profile (top panel) and line-of-sight velocity dispersion profile (bottom panel) at 10 Gyr of a cluster evolved in isolation (black line) and one evolved in intermediate-strength compressive tides (orange line) and released to isolation at $t = 8$ Gyr. No significant structural differences are observable.

analysis of the morphology and kinematics of our simulations. Fig. 4 displays the surface density profiles and the line-of-sight velocity dispersion profile as a function of the projected radius R of snapshots at 10 Gyr of a cluster evolved completely in isolation and a cluster evolved initially in intermediate-strength compressive tides.[3] Despite the expansion imprinted by the time-dependent tidal field, the observational profiles do not show significant differences.[4]

[3] The profiles are constructed by stacking three snapshots around 10 Gyr, assuring to have a number of stars >100 per radial bin.

[4] Note that the number of particles of the two clusters at 10 Gyr is comparable ($N_{\mathrm{isolated}} = 1619$ and $N_{\mathrm{tides}} = 1413$) and the measured half-mass radii are $r_m = 11.49$ and 8.16 pc, for isolated and compressive tides case, respectively.

4 CONCLUSIONS

We tested the possibility that extended clusters form originally in the dense central regions of dwarf galaxies and later expand due to a time-variation of the tidal field induced by the accretion of the host dwarf galaxy. In the core regions of dwarf galaxies, the clusters experience a regime of compressive tides that produces an excess of kinetic energy with respect to the internal potential energy. When the dwarf galaxy is accreted on to the MW, the clusters are released in the outer halo and expand due to this excess of energy.

We find that the expansion imprinted to the clusters does not give origin to objects that are more spatially extended than systems that have always evolved in isolation. We tested our conclusion exploring different initial densities for the clusters, orbits inside the core of the dwarf galaxy, strengths of the compressive tides and time variations of the transition from the regime of compressive tides to isolation.

We note here that our result can be considered as conservative. In fact, we tested the most extreme case in which the cluster originally resides in the central compressive region of a dwarf galaxy and is then released in isolation due to the accretion event. In a more realistic case, the accretion process of the dwarf galaxy would bring the cluster in the (extensive) tidal potential of the host galaxy. This would set a natural boundary for the spatial extent of the cluster (Lagrange surface), that would further limit its expansion. Moreover, by setting compressive tides, we push further the results of Miholics et al. (2014) who found that the (less extreme) case of tidally extensive tides does not lead to accreted clusters more extended than those in isolation.

We conclude that an accreted origin of outer halo extended clusters is unlikely to explain their large spatial extent. For this reason, these stellar systems could have genuinely formed extended or could have experienced an enhanced expansion due to some internal dynamical mechanism (e.g. the interplay of primordial mass segregation and dynamical relaxation; Haghi et al. 2014). Alternatively, observations of the radius of extended clusters could be biased by unbound stars that have already been stripped, and wonder in its vicinity along its orbit (Küpper et al. 2010).

ACKNOWLEDGEMENTS

This work was carried out as part of the ISIMA programme on Gravitational Dynamics held in 2014 July at CITA, Toronto. We acknowledge Pascale Garaud for the organization, the financial support, and for the stimulating environment provided by all the participants. PB acknowledges support from Heidelberg Graduate School for Fundamental Physics. FR acknowledges support from the European Research Council (ERC) through grant ERC-StG-257720. MG acknowledges financial support from the Royal Society in the form of a University Research Fellowship (URF) and an equipment grant used for the GPU cluster in Surrey. MG and FR acknowledge support from the ERC (ERC-StG-335936, CLUSTERS) and ALV from RCE1851. Finally, all authors thank Sverre Aarseth and Keigo Nitadori for making the GPU version of NBODY6 available, and Dave Munro for the hardware support at the University of Surrey.

REFERENCES

Aarseth S. J., 2003, Gravitational N-Body Simulations. Cambridge Univ. Press, Cambridge
Assmann P., Wilkinson M. I., Fellhauer M., Smith R., 2011, MNRAS, 413, 2606
Belokurov V., Irwin M. J., Koposov S. E., Evans N. W., Gonzalez-Solares E., Metcalfe N., Shanks T., 2014, MNRAS, 441, 2124
Brodie J. P., Larsen S. S., 2002, AJ, 124, 1410
Elmegreen B. G., 2008, ApJ, 672, 1006
Fellhauer M., Kroupa P., 2002, AJ, 124, 2006
Forbes D. A., Bridges T., 2010, MNRAS, 404, 1203
Frank M. J., Grebel E. K., Küpper A. H. W., 2014, MNRAS, 443, 815
Gieles M., Heggie D. C., Zhao H., 2011, MNRAS, 413, 2509
Haghi H., Hoseini-Rad S. M., Zonoozi A. H., Küpper A. H. W., 2014, MNRAS, 444, 3699
Harris W. E., 2010, preprint (arXiv:1012.3224)
Hills J. G., 1980, ApJ, 235, 986
Huxor A. P. et al., 2014, MNRAS, 442, 2165
Küpper A. H. W., Kroupa P., Baumgardt H., Heggie D. C., 2010, MNRAS, 407, 2241
Laevens B. P. M. et al., 2014, ApJ, 786, L3
Leaman R., VandenBerg D. A., Mendel J. T., 2013, MNRAS, 436, 122
McConnachie A. W., 2012, AJ, 144, 4
Mackey A. D., Gilmore G. F., 2004, MNRAS, 355, 504
Mackey A. D., van den Bergh S., 2005, MNRAS, 360, 631
Mackey A. D. et al., 2010, ApJ, 717, L11
Mackey A. D. et al., 2013, ApJ, 770, L17
Marín-Franch A. et al., 2009, ApJ, 694, 1498
Miholics M., Webb J. J., Sills A., 2014, MNRAS, 445, 2872
Nitadori K., Aarseth S. J., 2012, MNRAS, 424, 545
Ostriker J. P., Spitzer L., Jr, Chevalier R. A., 1972, ApJ, 176, L51
Renaud F., 2010, PhD thesis, Universität Wien, Université de Strasbourg
Renaud F., Boily C. M., Fleck J.-J., Naab T., Theis C., 2008, MNRAS, 391, L98
Renaud F., Gieles M., Boily C. M., 2011, MNRAS, 418, 759
Spitzer L., Jr1958, ApJ, 127, 17
Walker M. G., Peñarrubia J., 2011, ApJ, 742, 20
Webb J. J., Leigh N., Sills A., Harris W. E., Hurley J. R., 2014, MNRAS, 442, 1569

This paper has been typeset from a TEX/LATEX file prepared by the author.

Chapter 3

Simulating integrated-light kinematic observations of globular clusters

"*Understanding the central kinematics of globular clusters with simulated integrated-light IFU observations*"
Bianchini, Paolo; Norris, Mark A.; van de Ven, Glenn; Schinnerer, Eva
Monthly Notices of the Royal Astronomical Society, Volume 453, Issue 1, p.365-376
http://adsabs.harvard.edu/abs/2015MNRAS.453..365B

The deep understanding of the biases and systematics of the available kinematic data sets is the key to assess and interpret kinematic fingerprints of the formation and evolution of GCs. A growing disagreement has recently emerged in the interpretation of the kinematic data in the very central regions of GCs, casting doubts on claims of the detection of intermediate-mass black holes. The goal of this Chapter is to approach the problem of the search for intermediate-mass black holes from a different perspective, investigating first our understanding of the data. In this Chapter, I present the code `SISCO` (Simulating IFU Star Clusters Observations), which I specifically developed for simulating integrated-light kinematic observations of the centers of GCs. The details of the code are given in the Appendix. `SISCO` is used to translate state-of-the-art dynamical simulations of star clusters into mock observations, from which an analysis of the biases and systematics is carried out thoroughly. This work shows that integrated-light kinematics can be strongly biased by the presence of a few bright stars that can lead to the misinterpretation of the presence/absence of an intermediate-mass black hole. Procedures to mitigate the observed biases are presented.

Monthly Notices of the ROYAL ASTRONOMICAL SOCIETY
MNRAS **453,** 365–376 (2015) doi:10.1093/mnras/stv1651

Understanding the central kinematics of globular clusters with simulated integrated-light IFU observations

Paolo Bianchini,★† Mark A. Norris, Glenn van de Ven and Eva Schinnerer
Max-Planck Institute for Astronomy, Koenigstuhl 17, D-69117 Heidelberg, Germany

Accepted 2015 July 20. Received 2015 July 20; in original form 2015 February 13

ABSTRACT

The detection of intermediate-mass black holes in the centres of globular clusters is highly controversial, as complementary observational methods often deliver significantly different results. In order to understand these discrepancies, we develop a procedure to simulate integral field unit (IFU) observations of globular clusters: Simulating IFU Star Cluster Observations (SISCO). The inputs of our software are realistic dynamical models of globular clusters that are then converted in a spectral data cube. We apply SISCO to Monte Carlo cluster simulations with a realistic number of stars and concentrations. Using independent realizations of a given simulation we are able to quantify the stochasticity intrinsic to the problem of observing a partially resolved stellar population with integrated-light spectroscopy. We show that the luminosity-weighted IFU observations can be strongly biased by the presence of a few bright stars that introduce a scatter in the velocity dispersion measurements up to $\simeq$40 per cent around the expected value, preventing any sound assessment of the central kinematic and a sensible interpretation of the presence/absence of an intermediate-mass black hole. Moreover, we illustrate that, in our mock IFU observations, the average kinematic tracer has a mass of $\simeq$0.75 $M_\odot$, only slightly lower than the mass of the typical stars examined in studies of resolved line-of-sight velocities of giant stars. Finally, in order to recover unbiased kinematic measurements we test different masking techniques that allow us to remove the spaxels dominated by bright stars, bringing the scatter down to a level of only a few per cent. The application of SISCO will allow us to investigate state-of-the-art simulations as realistic observations.

Key words: black hole physics – instrumentation: spectrographs – stars: kinematics and dynamics – globular clusters: general.

1 INTRODUCTION

The study of the internal kinematics of globular clusters (GCs) offers the possibility of unveiling the complexity of the stellar systems, previously regarded as simple, spherical and isotropic. In fact, kinematic measurements are key to understand the formation and dynamical evolution of GCs, providing insights into the role of ingredients such as internal rotation, velocity anisotropy, presence of intermediate-mass black holes (IMBHs) in the centre of GCs, fundamental in shaping their internal structure.

In particular, significant effort has been devoted to the search for IMBHs, postulated to have a mass intermediate between those of stellar mass black holes ($M_\bullet < 100$ $M_\odot$) and those of the supermassive black holes (SMBH; $M_\bullet > 10^5$ $M_\odot$) found at the centres of galaxies. These putative IMBHs have proven elusive, with disputed evidence for their presence in Galactic GCs (Gebhardt et al. 2000; van den Bosch et al. 2006; Noyola et al. 2010; van der Marel & Anderson 2010; Lanzoni et al. 2013; Lützgendorf et al. 2013; den Brok et al. 2014) and extragalactic ultra-luminous X-ray sources (e.g. Matsumoto et al. 2001; Fabbiano, Zezas & Murray 2001). The search for the existence of IMBHs within GCs has partially been motivated by the observation that the extrapolation of the $M_\bullet$–σ relation for galaxies, linking the mass of the central back hole to the velocity dispersion of the host stellar system (Ferrarese & Merritt 2000; Magorrian et al. 1998), suggests that GCs are ideal environments to find central IMBHs with masses of 10^3–10^4 $M_\odot$.

The search for IMBHs reported in the literature is based primarily on two channels: detection of radio and X-ray emission (Miller & Hamilton 2002; Maccarone & Servillat 2008; Kirsten & Vlemmings 2012; Strader et al. 2012), and detection of kinematic signatures in the central region of GCs, such as the rise of the central velocity dispersion (e.g. Bahcall & Wolf 1976; Lützgendorf et al. 2013). The detectability of the black hole by the former method is dependent on

★E-mail: bianchini@mpia.de
†Member of the International Max Planck Research School for Astronomy and Cosmic Physics at the University of Heidelberg, IMPRS-HD, Germany.

Table 1. Structural properties of the Monte Carlo cluster simulations used in this work for a snapshot at 13 Gyr.

Simulation properties		Simulation A	Simulation B	Simulation C
Number of particles	N	1.8×10^6	4.1×10^5	1.8×10^6
Total mass	$M_{\rm tot}$	6.7×10^5 M$_\odot$	1.5×10^5 M$_\odot$	6.7×10^5 M$_\odot$
Distance	d	10 kpc	10 kpc	20 kpc
Half-light radius	$R_{\rm h}$	2.8 pc/57.8 arcsec	2.24 pc/46.2 arcsec	2.8 pc/28.9 arcsec
Core radius	$R_{\rm c}$	1.3 pc/26.8 arcsec	0.39 pc/8.0 arcsec	1.3 pc/13.4 arcsec
Concentration	$C = \log(R_{\rm t}/R_{\rm c})$	1.6	2.3	1.6
Central luminosity density	l_0	64.4 L$_\odot$ arcsec^{-2}	37.5 L$_\odot$ arcsec^{-2}	234.7 L$_\odot$ arcsec^{-2}
Binary fraction	f_b	4 per cent	4 per cent	4 per cent
Metallicity	[Fe/H]	−1.3	−1.3	−1.3

the feeding of the black hole with gas, an event that is inefficient in the extremely gas poor environment of most GCs. The latter method requires instead very precise velocity measurements (accuracy of the order of 1 km s^{-1} to reliably measure central velocity dispersions of $\simeq$10 km s^{-1}) with high spatial resolution of the very crowded central region of GCs (central few arcsec).

Two main strategies are generally used to acquire the necessary kinematic information of the central region of GCs: (1) resolved kinematics, by measuring discrete velocities of individual stars (using line-of-sight velocities or proper motions) and (2) unresolved kinematics, by measuring the velocity dispersion from line broadening of integrated-light spectra with either integral field units (IFUs) or slit spectroscopy (e.g. Dubath, Meylan & Mayor 1997). Unsettlingly, these apparently complementary methods can give significantly different observational outcomes when applied to the same object, making the detection of IMBHs highly ambiguous.

In particular, integrated-light spectroscopy seems to measure rising central velocity dispersions, favouring the presence of IMBHs (see e.g. Noyola et al. 2010 for ω Cen; Lützgendorf et al. 2011, 2015 for NGC 6388), while resolved stellar kinematics do not confirm the presence of this signature (see van der Marel & Anderson 2010 for proper motion measurements of ω Cen; Lanzoni et al. 2013 for individual line-of-sight measurements in NGC 6388).

Therefore, understanding the possible sources of biases affecting the different methods is an essential first step to undertake before interpreting any kinematic signatures possibly connected to the presence of IMBHs. The difference between the techniques can arise because unresolved measurements give intrinsically luminosity-weighted kinematic information, whereas in resolved kinematic studies the kinematic profiles are constructed assigning to each discrete measurement the same weight. Progress in understanding how this difference could influence the measurements has been made, for example, in understanding that unresolved kinematics can be strongly biased by the presence of a few bright stars dominating the integrated spectra, increasing the shot noise of the velocity dispersion (e.g. see Dubath et al. 1997; Noyola et al. 2010; Lanzoni et al. 2013). Moreover, Lützgendorf et al. (2015) recently showed that measurements of velocity dispersions from discrete velocities of individual stars can also be biased towards lower values of velocity dispersions.

In order to undertake an exploration of the issues that emerge from applying integrated-light spectroscopy to systems with a (partially) resolved stellar population, like Galactic GCs, we develop a new procedure to simulate IFU observations of GCs: Simulating IFU Star Cluster Observations (SISCO). Starting from realistic Monte Carlo cluster simulations from Downing et al. (2010) (for details on the Monte Carlo code, see Giersz 1998; Giersz et al. 2013; Hypki & Giersz 2013), the output of our simulation is a data cube with spectra for every pixel in a selected field of view (FoV). Our work is motivated by the growing use of such techniques to study the general kinematic properties of Galactic GCs (see e.g. the study of internal rotation by Fabricius et al. 2014 in addition to the applications related to IMBHs mentioned above). We focus in particular on investigating the bias due to stochastic effects and shot noise introduced by a few bright stars, and explore possible physical interpretations (e.g. mass segregation) of the discrepancies reported in the literature (e.g. those relative to NGC 6388; Lützgendorf et al. 2011; Lanzoni et al. 2013).

The paper is organized as follows. In Section 2, we introduce the properties of the Monte Carlo cluster simulations that we will use in the rest of our work. In Section 3, we describe the method we have developed to construct IFU mock observations starting from a general cluster simulation. In Section 4, we analyse the kinematics of our mock observations and investigate the possible biases intrinsic to luminosity-weighted kinematic measurements. In Section 5, we outline and thoroughly test masking techniques to minimize stochastic scatter and to recover unbiased velocity dispersion measurements. Finally, in Section 6, we present our conclusions and future prospectives.

2 SIMULATIONS OF GLOBULAR CLUSTERS

The starting point of our work are Monte Carlo cluster simulations, developed by Downing et al. (2010) with the Mocca Monte Carlo code (Giersz 1998; Hypki & Giersz 2013). These simulations were not originally designed for our study. However, they provide the realistic long-term dynamical evolution of GCs with a single stellar population, in which ingredients such as stellar mass function, stellar evolution, initial binary fraction are taken into consideration, and therefore are suitable to test the performance of our tool SISCO (see Section 3).

The main set of simulations (labelled as Simulation A in Table 1) starts with 2×10^6 particles drawn from a Plummer (1911) model, with a Kroupa (2001) initial mass function, 10 per cent primordial binary fraction, metallicity [Fe/H] = −1.3, and they are evolved in isolation.[1] The simulations have no central IMBH and internal rotation is not considered (note however that internal rotation is observed in several GCs; e.g. Bianchini et al. 2013; Fabricius et al. 2014; Kacharov et al. 2014; Lardo et al. 2015). Five different independent realizations of the same simulation are available, and we will use them to analyse stochastic effects. At 13 Gyr,

[1] The assumption of isolation is not a limitation since we are only interested in the central region of clusters, where any effect of an external tidal field on a GC would be negligible.

the simulations are characterized by $N \simeq 1\,800\,000$ particles (both single and binary stars), $\simeq$4 per cent binary fraction, total mass of $M_{\rm tot} \simeq 6.7 \times 10^5$ M$_\odot$, projected half light radius of $R_{\rm h} \simeq 2.8$ pc, core radius of $R_{\rm c} \simeq 1.3$ pc and concentration $C = \log(R_{\rm t}/R_{\rm c}) \simeq 1.6$, with $R_{\rm t}$ tidal radius of the cluster. Moreover, the resulting clusters are isotropic in the central regions and mildly radially anisotropic in the outer parts. Having included a stellar mass function, they are also characterized by dynamical mass segregation as described in Section 4.2 (no initial mass segregation is assumed). For a summary of the structural properties, see Table 1.

We place the simulated GCs at 10 kpc from the observer with a global systemic line-of-sight velocity of 300 km s^{-1} to match the typical properties of a Galactic GC. The data from the Monte Carlo simulations that we will need are: the spatial coordinates of the stars in the plane of the sky, the velocity of each star along the line of sight, the stellar parameters of each star (effective temperature $T_{\rm eff}$, mass $m_\star$, luminosity $l_\star$) and the metallicity of the cluster. Any other GC simulation providing this information can also be used in the software package that we have developed.

We further consider two additional sets of simulations: (i) a more concentrated simulation (labelled Simulation B), with $N \simeq 410\,000$ stars, concentration c = 2.3, core radius $R_{\rm c} = 8$ arcsec, observed at 10 kpc, (ii) and a more crowded simulation (labelled Simulation C), obtained placing Simulation A at a distance of 20 kpc. The former simulation, even if more centrally concentrated, does not represent a more crowded case, since Simulation B is performed with fewer stars than Simulation A. The latter simulation has a higher number of giant stars in the FoV, making the crowding approximately four times higher than Simulation A (see the central luminosity density in Table 1). In the following section we will consider Simulation A, and we will discuss the results connected to Simulations B and C in Section 5.

3 SIMULATIONS OF IFU OBSERVATIONS

In this section we describe step-by-step our procedure, Simulating IFU Star Cluster Observations (SISCO), to build a mock IFU observation of a GC, starting from the Monte Carlo cluster simulations described in the previous section. The final product will consist of IFU simulations in the Calcium triplet wavelength range (8400–8800 Å) with spectra associated with every spaxel. From this, we will build kinematic maps and kinematic profiles in the same manner as observers.

3.1 From stellar parameters to stellar spectra

The first step in building an IFU mock observation consists in associating a stellar spectrum to each star in a GC simulation. We do this in two steps: first we associate to each star a low-resolution spectrum, covering a broad-wavelength, using the GALEV evolutionary synthesis model (Kotulla et al. 2009). GALEV is based on the BaSeL library of model atmospheres (Lejeune, Cuisinier & Buser 1997, 1998a,b) and gives stellar spectra from the extreme ultraviolet to the far-infrared (9–160 000 nm) with variable resolution ranging from 2 to 400 Å (20 Å in the optical). In order to associate to each simulated star a stellar spectrum, the effective temperature $T_{\rm eff}$, mass $m_\star$, luminosity $l_\star$, and metallicity Z outputs from the Monte Carlo simulations are matched to the appropriate GALEV spectrum. The computed spectra, in units of erg cm^{-2} s^{-1} Å^{-1}, can then be convolved with filter transmission curves to obtain the colour and magnitude information for every star (to build, for example, a colour–magnitude diagram in the desired filters; see Fig. 5).

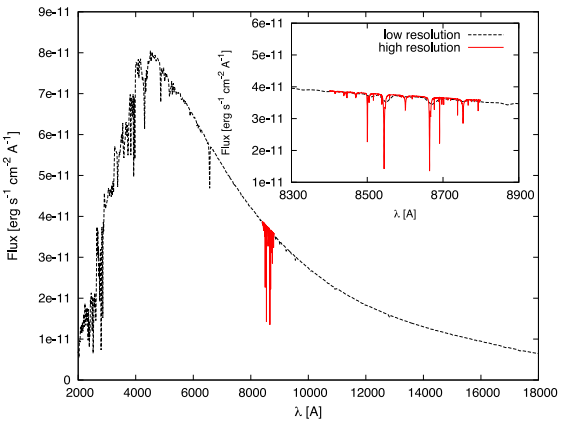

Figure 1. Stellar spectrum associated with a main-sequence star with $T_{\rm eff} = 5815$, $m_\star = 0.72$ M$_\odot$ and $l_\star = 0.66$ L$_\odot$ using the GALEV evolutionary synthesis model. The corresponding high-resolution synthetic spectrum (from the MARCS synthetic stellar library) in the region of the Ca II-triplet is shown with the red line. With a resolving power of $R = 20\,000$, these spectra are ideal for measurements of the internal kinematics of GCs.

The second step consists of associating an additional high-resolution spectrum in the wavelength range that will be used in our mock observations. These further spectra are necessary in order to have high enough spectral resolution to measure the internal kinematics of GCs with typical velocity dispersions of 10 km s^{-1}. We select the wavelength range around the Calcium triplet (8400–8800 Å) typically used to measure the kinematics in GCs, for example through spectroscopy with VLT/FLAMES.[2] The high-resolution spectra are taken from the MARCS synthetic stellar library (Gustafsson et al. 2008) and provide a constant resolving power $R = \lambda/\Delta\lambda = 20\,000$, corresponding to a velocity dispersion of 15 km s^{-1} around the Calcium triplet.

Once a high-resolution spectrum is associated with each star according to the stellar parameters, it is rescaled to match the flux of the low-resolution spectrum. Fig. 1 shows both the low- and high-resolution spectra for a main-sequence star with $T_{\rm eff} = 5\,815$, $m_\star = 0.72$ M$_\odot$ and $l_\star = 0.66$ L$_\odot$. The correctly rescaled high-resolution spectra will be used in the rest of our simulations. We finally proceed to Doppler-shift the single-star spectra using the line-of-sight velocity given by our Monte Carlo cluster simulation. In the case of binary systems, we apply a Doppler shift using the line-of-sight velocity of the barycentre.

3.2 From single-star spectra to an IFU data cube

The next step is to define the observational setup of the simulated IFU instrument, in order to obtain the three-dimensional data cube of our observation. We design an instrument with a FoV of 20×20 arcsec^2 and a spaxel scale of 0.25 arcsec, similar to the properties of FLAMES@VLT in ARGUS mode (pixel scale of 0.3 arcsec, FoV $\sim 7 \times 4$ arcsec^2, resolving power $R = 10\,000$, in the visible range with spectral coverage of 600–1000 Å; Pasquini et al. 2002). Note that these properties can be changed in order to match other instruments, for example, Gemini/GMOS. The covered

[2] Note that, in principle, any other wavelength range can be used.

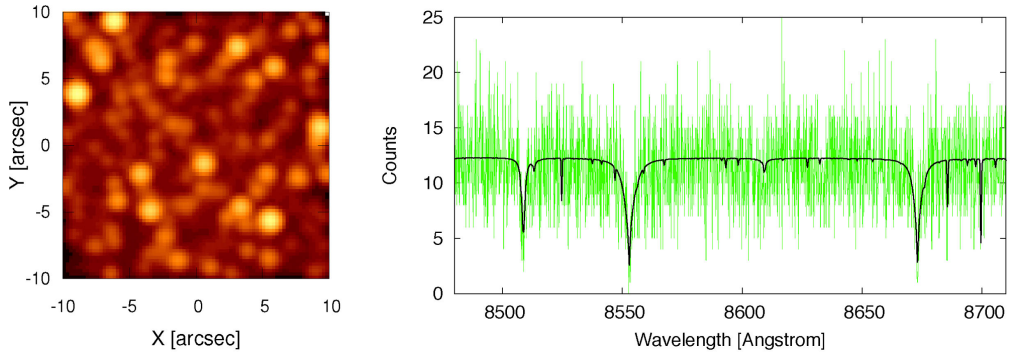

Figure 2. Left panel: luminosity map in logarithmic scale of the central 20 × 20 arcsec^2 region of our simulated GC (Simulation A) placed at 10 kpc and observed with a seeing of 1 arcsec and an average S/N of ≃10 per Å. The luminosity map is constructed summing up all the flux from the spectra within each spaxel, in the 8400–8800 Å range. Right panel: typical spectrum of a spaxel, obtained summing all the Doppler-shifted spectra falling in the spaxel, properly weighted by their PSF. The black line indicates the spectrum without noise, while the green line indicates the case of an observation with S/N ≃ 10 per Å.

wavelength range will be 8400–8800 Å, with a spectral sampling of 0.1 Å pixel^{-1}. In this particular example, when we place the simulated GC at 10 kpc (Simulation A), a total of ≈40 000 stars fall within the FoV of the simulation.

We also need to define a point spread function (PSF) for our observation. We implement a Gaussian PSF, but we will test later the effect of a different PSF shape (Moffat PSF; see Section 5.3). We set the seeing conditions assigning a full width at half maximum (FWHM) of the PSF of 1 arcsec, typical of ground-based non-adaptive optics assisted observations. After convolving each star with the resulting PSF, we sum the Doppler-shifted spectra of all the stars falling in each spaxel, properly weighted by their PSF. In this way for each spaxel we have a spectrum and the corresponding luminosity information (obtained by summing up all the flux within each spaxel).

Finally, we add Poisson noise to the final spectra in order to match the desired signal-to-noise ratio (S/N). The typical S/N values that we consider are S/N ≃ 5, 10, 20 per Å.[3] In practice, the chosen S/N does not significantly affect the final results, since we will construct the binned radial profiles such that the delivered S/N in each bin is approximately constant (i.e. the size of each bin is chosen to have a fixed S/N).

In the left panel of Fig. 2 we show the luminosity map of the GC at 10 kpc, observed with seeing of 1 arcsec and S/N ≃ 10 per Å. The luminosity map is constructed summing up all the flux from the spectra within each spaxel, like for real observational data. In the right panel we show the typical spectrum of a single spaxel (both with and without noise).

Note that we do not include any sky lines in addition to the synthetic spectra, since sky subtraction in the Calcium triplet wavelength region is efficiently performed in observational studies (Hanuschik 2003).

3.3 Measuring the kinematics

After producing the data cube of our IFU observation, we can proceed with the measurement of the kinematics from the spectra. In common with many observational studies, we use the penalized pixel-fitting (pPXF) program of Cappellari & Emsellem (2004) to determine the integrated kinematic properties of each spectrum. This software allows us to obtain the mean velocity and the velocity dispersion from the measured spectra, from the shift and from the broadening of the spectral lines.[4] One of the principal strengths of the pPXF method is the ability to reduce the often significant effects of template mismatch (i.e. the use of template spectra that do not adequately reflect the observed spectra) on the determined kinematics. In order to ensure that template mismatch is negligible we use a total of 16 high-resolution synthetic spectra taken from our simulation (i.e. the original MARCS library spectra before Doppler shifting), making sure they sufficiently cover the parameter space displayed by the stellar types present in our GC simulations. We select representative stars along the colour–magnitude diagram: five main-sequence stars, eight giant stars and three horizontal branch stars.

With the measured kinematics we are able to construct the mean line-of-sight velocity map and the associated velocity dispersion map. We will refer to these maps as the observed maps. They can be directly compared with the model maps. The model map is obtained by calculating for each spaxel the luminosity/PSF-weighted kinematics directly from the Monte Carlo simulation. Fig. 3 shows in the first row the model mean velocity map, the observed mean velocity map and the relative residuals between the two. In the second row, the corresponding velocity dispersion maps are shown. The figure clearly indicates that our measuring routine successfully recovers the average velocity map of the cluster, since our observed maps are consistent with the model ones.

Fig. 3 also shows that problems in recovering the internal kinematics of the cluster arise in correspondence to the brightest stars (see for comparison the luminosity map in Fig. 2). In these spaxels, the spectra are completely dominated by the contribution of one or few bright stars, therefore the measured kinematics is biased. For example, the measured velocity dispersion in these bright spaxels approaches zero, since by definition the spectrum of one star has no velocity dispersion (other than that caused by internal line

[3] The S/N reported is the average value per spaxel in the FoV; for an average S/N ≃ 10, the faintest spaxel has a S/N ≃ 3 and the brightest S/N ≃ 30.

[4] Note that pPXF is also capable of measuring higher order moments of the line-of-sight velocity distribution, i.e. h_3 and h_4. After verifying that the measurements of these higher moments are consistent with zero (as expected for quasi-isotropic stellar systems with no internal rotation), we decided to limit pPXF to fit only for the first two moments, that is the mean velocity and the velocity dispersion.

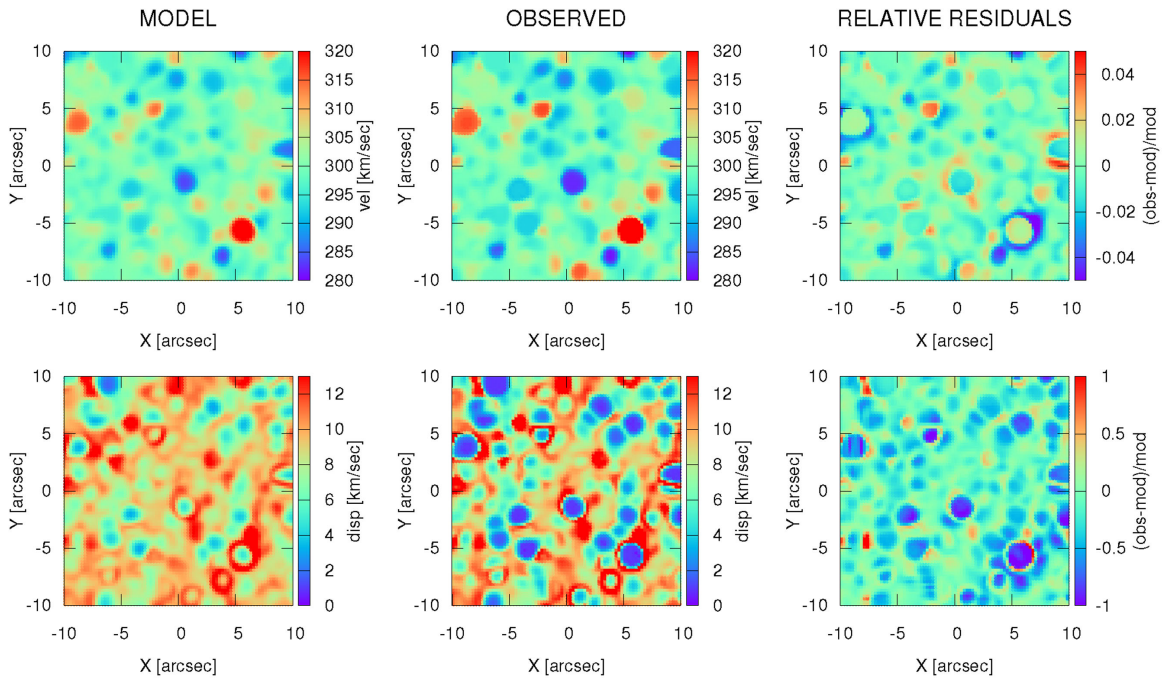

Figure 3. Top row: mean velocity map for one of our IFU mock observations relative to Simulation A with 1 arcsec seeing. The left panel shows the map computed directly from the model, the central panel the map recovered from the mock observation using pPXF to extract the kinematics, and the right panel the relative residuals between observed and model map. Bottom row: velocity dispersion maps of the model and observed GC, and map of the relative residuals of the two. This mock observation is carried out without considering noise in the measurements, to highlight the intrinsic biases possibly present in our procedure. Our measuring routine allows us to recover the kinematics of the model. The larger discrepancies between model and observations are found in the proximity of the brightest stars for the velocity dispersion measurements (note different plotting ranges for mean velocity and velocity dispersion maps).

broadening). We will discuss in Section 5 how to minimize this biasing effect introduced by the presence of bright stars.

Finally, we are able to extract from our data one-dimensional velocity dispersion profiles. We divide our FoV in annular bins and sum all the spectra in each bin. With pPXF we measure the velocity dispersion from the broadening of the lines of the summed spectra. The advantage of constructing profiles lies in the fact that a higher S/N per radial bin is reachable, making the velocity dispersion measurements more reliable and less affected by stochastic spaxel-to-spaxel noise. The radial size for the annular bins is such that every bin contains the same S/N. We use as the radial position of a bin the radial value at which half of the total number of counts is reached. Note that no error bars are shown in the figures, since the formal errors from pPXF are smaller than the symbols in the graphs. Additionally, we assume the centre of the cluster to be the one given by the Monte Carlo cluster simulation and test in Section 5.3 the effects introduced by a misidentification of the centre.

4 LUMINOSITY-WEIGHTED VERSUS DISCRETE KINEMATICS

In this section we will investigate the observational biases present in integrated-light spectroscopic observations. First, we remind the reader that the kinematic information delivered by integrated-light spectroscopy observation is intrinsically luminosity weighted. However, the physical ingredient we are ultimately interested in is not the luminosity, but the mass.

Therefore, using luminosity-weighted kinematics requires some additional caution, since it automatically biases the measured kinematics towards the properties of the brightest stars that dominate the spectra, typically red giant branch stars in old stellar systems such as GCs. This can generate two problems: (1) adding a stochastic uncertainty, due to the fact that only few bright stars are present in the FoV; and (2) introducing a systematic bias if stars with different luminosities (and different masses) have different kinematics because of mass segregation. We address both of these issues in the following, using the IFU mock observations of the five independent random realizations of our GC (Simulation A), with a fixed seeing condition of 1 arcsec and an average S/N of $\simeq$10 per Å. From these, we extract the velocity dispersion profiles as described in Section 3.3.

4.1 Role of stochasticity

We illustrate the problem connected to stochasticity in Fig. 4, in which we show the velocity dispersion profile of our model GC constructed using giant stars only (as is typically the case in studies which use measurements of resolved stars). We construct the profile in two different ways: first with discrete data, neglecting the luminosity information (the standard procedure used when discrete line-of-sight velocity measurements are available), then constructing a corresponding luminosity-weighted velocity dispersion profile. While for the former only one model is shown, for the latter we plot the profiles of the five different independent realizations

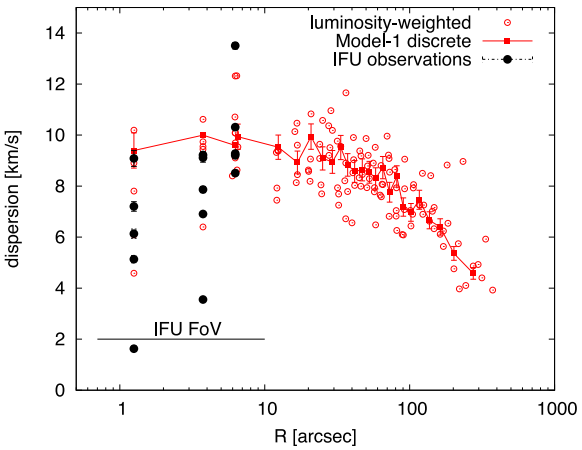

Figure 4. Velocity dispersion profiles of the giant stars in our GC model (Simulation A). The open red circles represent the luminosity-weighted velocity dispersion of the five independent realizations of our model (the bins vary slightly due to stochastic variation); the red squares joined by the red line are the discrete measurements of the velocity dispersion constructed without considering the luminosity information of the stars. Each bin contains 200 stars. The black points are instead the measured kinematics from our mock IFU observations of the five realizations, with the horizontal bar indicating the FoV. An intrinsic scatter due to the star-to-star variation of the luminosity is present in the luminosity-weighted profile of our model and this scatter is reflected in the mock observations.

of our GC simulation.[5] Both profiles are built with bins containing 200 stars each.

The plot clearly shows that, already in the GC model itself, the luminosity-weighted kinematic profiles are influenced by stochastic scatter due to the luminosity differences between stars. Note that, in fact, while all stars in the giant branch have approximately the same mass ($\simeq$0.85 $M_\odot$), their luminosity can vary over 6 magnitudes. This intrinsic stochasticity in the model is then transferred to the profiles measured from our mock IFU observations that show a similar amount of scatter. This scatter is high enough to prevent us from obtaining any sound measurement of the velocity dispersion in the central region of the cluster, if we were to use the uncorrected data. We therefore need a way to correctly estimate and minimize this stochasticity present in luminosity-weighted data before attempting any dynamical interpretation of our data. We will quantify the intrinsic scatter and describe the proposed strategy to minimize it in Section 5.

4.2 The true kinematic tracer

Here we investigate which stars are carrying the kinematic information in our IFU observations, that is, for which stars we are able to measure the kinematics. We remind the reader that our GC model incorporates the dynamical effects of mass segregation that acts to bring the clusters towards (partial) energy equipartition (Trenti & van der Marel 2013). This means that the most massive stars in the cluster sink towards the centre while losing energy, while less massive stars gain energy and are preferentially found in the outer regions of the cluster. As a result, higher-mass stars have a lower velocity dispersion with respect to lower-mass stars. This effect is aggravated in the central part of a cluster where mass segregation takes place more efficiently because of the higher density and the shorter relaxation time.

It is therefore necessary to know which stars act as the kinematic tracers that we are observing, before interpreting the resulting velocity dispersion measurements. We therefore construct a luminosity- and PSF-weighted mass map from our mock observations to understand what is the typical value of the stellar mass of the tracers carrying the kinematic information in each spaxel. We present the mass map in the top-right panel of Fig. 5 and the colour–magnitude diagram of the stars in the FoV of our simulation (left panel). We show that the average mass of the kinematic tracers is $\simeq$0.75 $M_\odot$ with little scatter (0.65 $\lesssim m_\star \lesssim$ 0.85 $M_\odot$). In the bottom-right panel of Fig. 5 we show the interpolated velocity dispersion profiles constructed using the discrete velocities of our GC model for eight different stellar mass bins (from 0.25 $M_\odot$ to 0.95 $M_\odot$). We also overplot the points corresponding to the five realizations of our model for the mass bin traced by the IFU observation (0.75 $M_\odot$) in the central region of the cluster corresponding to our IFU FoV.

From this analysis we show that the central velocity dispersion strongly depends on which kinematic tracer we are actually measuring, with lower mass stars displaying higher velocity dispersion. In our IFU observations the average stellar mass involved is 0.75 $M_\odot$, slightly lower than the typical giant stars mass of 0.85 $M_\odot$.[6] The small difference in mass between the red giant stars and the kinematic tracer of our IFU simulation produces a difference in the velocity dispersion profiles that is $<$1 km s^{-1}. However, we caution that mass segregation and energy equipartition strongly depend on the evolutionary history of the specific cluster considered.

In the following analysis, when referring to the model velocity dispersion profile we will consider only the profiles built from stars in the mass bin 0.7–0.8 $M_\odot$, since this is the proper kinematic tracer in our IFU observations.

5 ANALYSIS OF IFU SIMULATIONS

We now describe a procedure to analyse the IFU mock data in order to efficiently recover kinematic information consistent with the actual kinematic tracer involved in the observations, and to minimize stochastic scatter in the luminosity-weighted data. In order to do so, it is critical to mask the information conveyed by the bright stars. The masking procedure that we devise allows us to discard from the analysis those spaxels considered to be significantly contaminated by the light of a single or a few stars. This is a commonly used strategy (e.g. Lützgendorf et al. 2011) and here we intend to adequately understand its efficiency, comparing the results directly with the true model cluster. In this section, we will use all three sets of simulations (Simulations A, B and C; see Section 2) in order to test the validity of our analysis for clusters with different concentration and crowding. We use a fixed seeing of 1 arcsec and S/N $\simeq$ 10 per Å. In Section 5.3, we investigate the effect of bad seeing conditions, changing the shape of the PSF and the presumed centre of the cluster.

[5] Little scatter is present in a discrete non-luminosity weighted profile.

[6] Note that an additional dependence can be introduced by the wavelength range and the specific spectroscopic features that are used to measure the kinematics; for example, spectral features like CO bands will be preferentially sensitive to giant stars (Lanzoni et al. 2013).

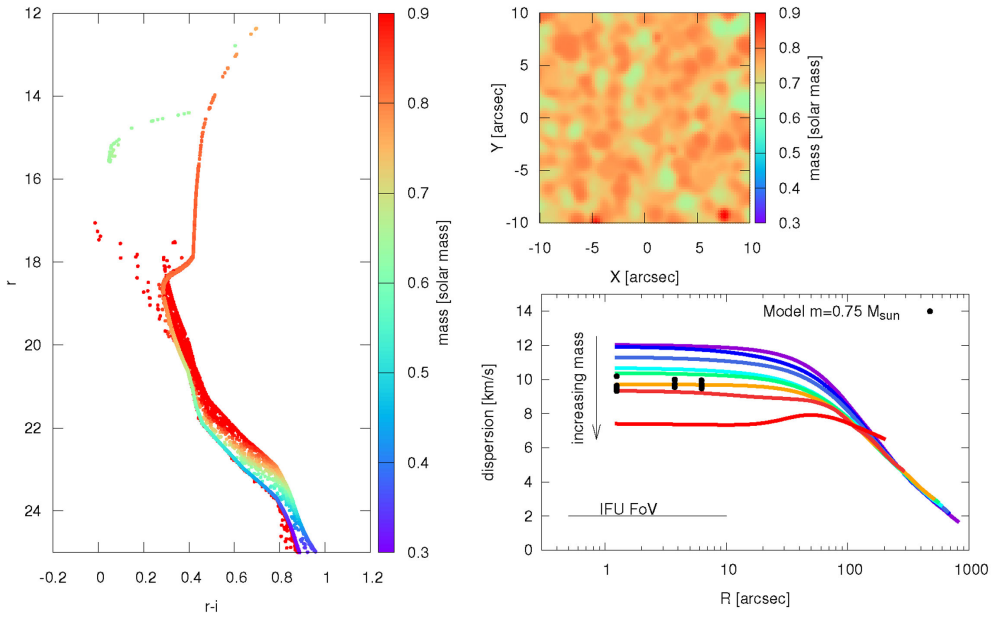

Figure 5. Left panel: colour–magnitude diagram of the stars in the FoV of our IFU simulation (Simulation A) colour-coded by stellar mass. Objects with masses >0.9 $M_{\odot}$ are either stellar binaries or blue stragglers stars. Top-right panel: luminosity-weighted map of the stellar mass distribution probed by the FoV of our IFU simulation. The typical stellar mass of the kinematic tracers that contribute to the spectra in each spaxel is 0.75 $M_{\odot}$. Bottom-right panel: velocity dispersion profiles as a function of the projected radius R for stars with increasing mass (from top to bottom). The profiles correspond to eight stellar mass bins of 0.1 $M_{\odot}$ width each, with an average stellar mass of $\simeq$0.25, 0.35, 0.45, 0.55, 0.65, 0.75, 0.85, 0.95 $M_{\odot}$, respectively. The colour scale of the lines is the same as that displayed in the left panel. Stars with lower mass display higher velocity dispersion due to mass segregation and partial energy equipartition. The black dots are the discrete velocity dispersions of the five realizations of our model in the FoV of our IFU observation, for stars with mass 0.70–0.80 $M_{\odot}$.

5.1 Masking of the observations

To define a masking strategy, we first need to specify what is a 'bad spaxel' that is contaminating our data. If we consider that the brightest stars are responsible for biasing our measurements of the integrated kinematics, then the brightest spaxels in our FoV can be defined as the 'bad spaxels'. We will refer to this simple masking as Masking A. As an alternative, one could define as 'bad spaxels' those spaxels whose light comes preferentially from a single bright star. We will refer to this alternative masking as Masking B. Note that the two definitions of 'bad spaxels' do not strictly coincide, for example a spaxel could be simply very bright because several stars are contributing to its luminosity; it would therefore be considered 'bad spaxels' in masking A but not in masking B.

We first consider Masking A and discard from the kinematic analysis the brightest 10 per cent, 20 per cent, and 30 per cent spaxels. We refer to these maskings as weak, intermediate, and strong masking, respectively, and we apply them to each of the five IFU mock observations of our model clusters. The result, for only one of the realizations of Simulation A, is shown in Fig. 6. The left panel shows the luminosity map superimposed with the 'bad spaxels' for the three different maskings. The right panel presents the velocity dispersion profiles in the FoV of the IFU observation, after the masking has been applied, compared to the profile obtained with no masking, as well as the profile expected directly from the model (see Section 4.2 and Fig. 5). The figure shows how a progressively stronger masking ensures recovery of the true model velocity dispersion profile, eliminating the stochastic fluctuations due to bright stars.

Incidentally, we note that, while masking eliminates the brightest spaxels, it does not introduce any bias on the average mass of the kinematic tracers contributing to the remaining spaxels. The average luminosity-weighted mass per spaxel remains constant at $\simeq$0.75 $M_{\odot}$ even after masking.

In the top row of Fig. 7 we compare the velocity dispersion profiles obtained without masking and the one after applying strong masking to the five realizations of the IFU Simulation A. In each panel the velocity dispersion profiles for the five independent realizations are shown. The unmasked profiles are strongly affected by scatter both in the values of velocity dispersion and in the values of radial position. We quantify the scatter in velocity dispersion calculating the biweight standard deviation of all the data points of the velocity dispersion profiles. The initial stochastic scatter is $\simeq$38 per cent around the central velocity dispersion and is reduced by an order of magnitude when masking is applied, reaching the value of $\simeq$3 per cent. Applying the masking we are able to both accurately recover the values of velocity dispersion expected from the model (see Section 4.2) and to considerably reduce the scatter.

We apply the same analysis also to Simulation B and Simulation C, the former providing a higher concentration cluster and the latter a FoV with higher crowding (see Section 2). As shown in the middle row (Simulation B) and bottom row (Simulation C) of Fig. 7, in both cases the masking procedure allows us to recover the values of velocity dispersion expected from the models and significantly reduce the scatter. Note, in particular, that for the high-crowding Simulation C, the initial stochastic scatter is $\simeq$21 per cent less severe than in the corresponding case of Simulation A and B. This can be explained by the higher number of stars in the FoV of our

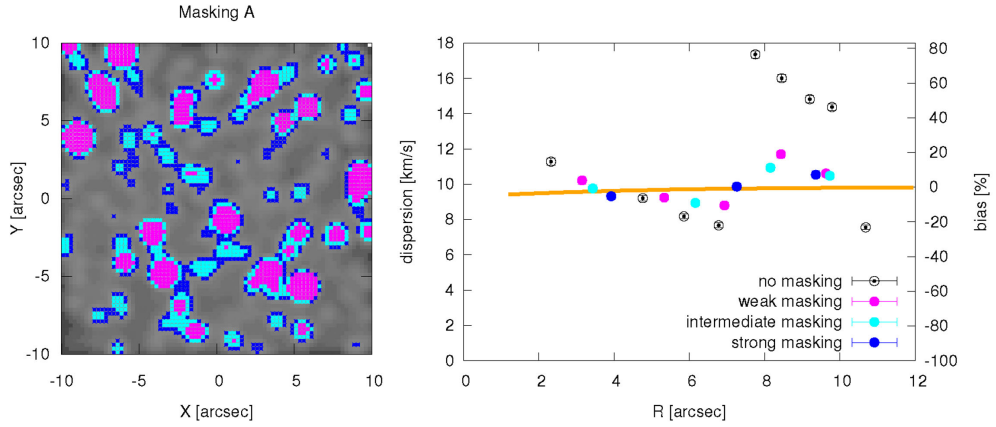

Figure 6. Left panel: luminosity map in logarithmic scale of one of our IFU mock observations (Simulation A, 1 arcsec seeing, S/N $\simeq$ 10 per Å) with the masked spaxels (masking procedure A) indicated by colours. Magenta spaxels refer to weak masking, cyan to intermediate masking, and blue to strong masking, discarding 10 per cent, 20 per cent, and 30 per cent of the brightest spaxels, respectively. Right panel: velocity dispersion profiles in the FoV of the IFU observation for the three maskings of the simulation shown in the left panel. The black open circles are the velocity dispersions computed without masking, while the orange line indicates the expected model velocity dispersion profile (see Fig. 5). The vertical axis on the right indicates the bias with respect to the expected velocity dispersion, in percentage. Stronger masking leads to a velocity dispersion profile that progressively approaches the true profile by reducing the scatter due to bright stars. The profiles are constructed as described in Section 3.3 keeping a constant S/N per radial bin.

IFU mock observations, connected to the higher central luminosity density of the simulated cluster (approximately four times more stars than in Simulation A, consistent with the fact that Simulation C is Simulation A observed at twice the distance, 20 kpc). This reduces the shot noise due to low number statistics in agreement with that reported in Dubath et al. (1997) for integrated-light slit spectroscopy. After masking is applied, the scatter reaches a value of $\simeq$4 per cent, comparable to the value reported for the case of the less dense Simulation A.

In the same way as described above, we test the masking strategy B. We discard those spaxels for which at least one single star contributes more than 50 per cent, 40 per cent, 30 per cent of the luminosity. We refer to these maskings as weak, intermediate, and strong masking, respectively. In Fig. 8 we compare the results of the two different masking strategies applied to Simulation A. The panels to the left show the luminosity map with the masked spaxels indicated in blue and in green, for Masking A and Masking B, respectively. In this figure we consider only the strongest masking flavours: in the case of Masking A, exactly 30 per cent of spaxels are discarded, while for Masking B approximately 40 per cent of spaxels are removed. Note however that, in this case, the two masking strategies agree with each other, since they both remove nearly the same 'bad spaxels'. Moreover, the right panel of the figure shows that the resulting velocity dispersion profiles for the five IFU observations obtained using the two masking strategies are fully consistent with each other.

A quantitatively similar result is obtained when comparing the two masking techniques applied to the higher concentration Simulation B. For the high-crowding Simulation C, although the two masking approaches lead to quantitatively comparable velocity dispersion profiles, Masking B proves more efficient (i.e. it removes less spaxels, $\approx$20 per cent instead of 30 per cent in Masking A). This can be explained by the fact that Masking A eliminates also those spaxels that are bright due to the contribution of many stars, which are therefore misidentified as 'bad spaxels'.

In the following section we summarize the main limitations of the two masking techniques discussed here.

5.2 Limitations of the masking approach

We showed in the previous section that, in the cases tested here, masking allows the reliable recovery of the expected unresolved kinematics. However, this procedure rejects from the analysis a fairly large amount of bright and high S/N spaxels. It is therefore important to highlight the main limitations of masking and in particular those connected to the two masking strategies used in this work.

(i) Masking enforces a loss of spatial resolution, since a relatively high number of 'bad spaxels' are removed. Therefore, some information on the central kinematic properties of a cluster is unavoidably not recoverable (note that in Figs 6–8 the masked profiles do not sample the inner $\lesssim$4 arcsec, corresponding to $\approx$3–4 PSF elements around the centre).

(ii) Masking A removes only the brightest spaxels in the FoV, leaving in the analysis spaxels that are still dominated by the light of a single star, but that are not bright. This drawback is not particularly severe if velocity dispersion profiles are constructed (i.e. the FoV is divided in annular bins and a summed spectrum is calculated for each bin). In fact, since these spaxels are faint, their relative contribution to the summed spectra is low. However, discarding these spaxels is crucial if a spaxel-by-spaxel kinematic map needs to be constructed. Moreover, in a very crowded FoV, Masking A would misidentify as 'bad spaxels' also those spaxels that are very bright due to the contribution of the light of many less bright stars.

(iii) Masking B properly identifies the spaxels dominated by a single star only. However, it requires additional observational information (e.g. distribution of the stars in the FoV and the modelling of the PSFs) to determine the relative contribution of the stars in each spaxel.

(iv) We showed that in the case of a less crowded FoV (Simulation A), Masking A performs more efficiently than Masking B (i.e. it delivers the expected velocity dispersion profiles, while removing a lower number of spaxels). For a more crowded FoV (Simulation C) Masking B is more efficient.

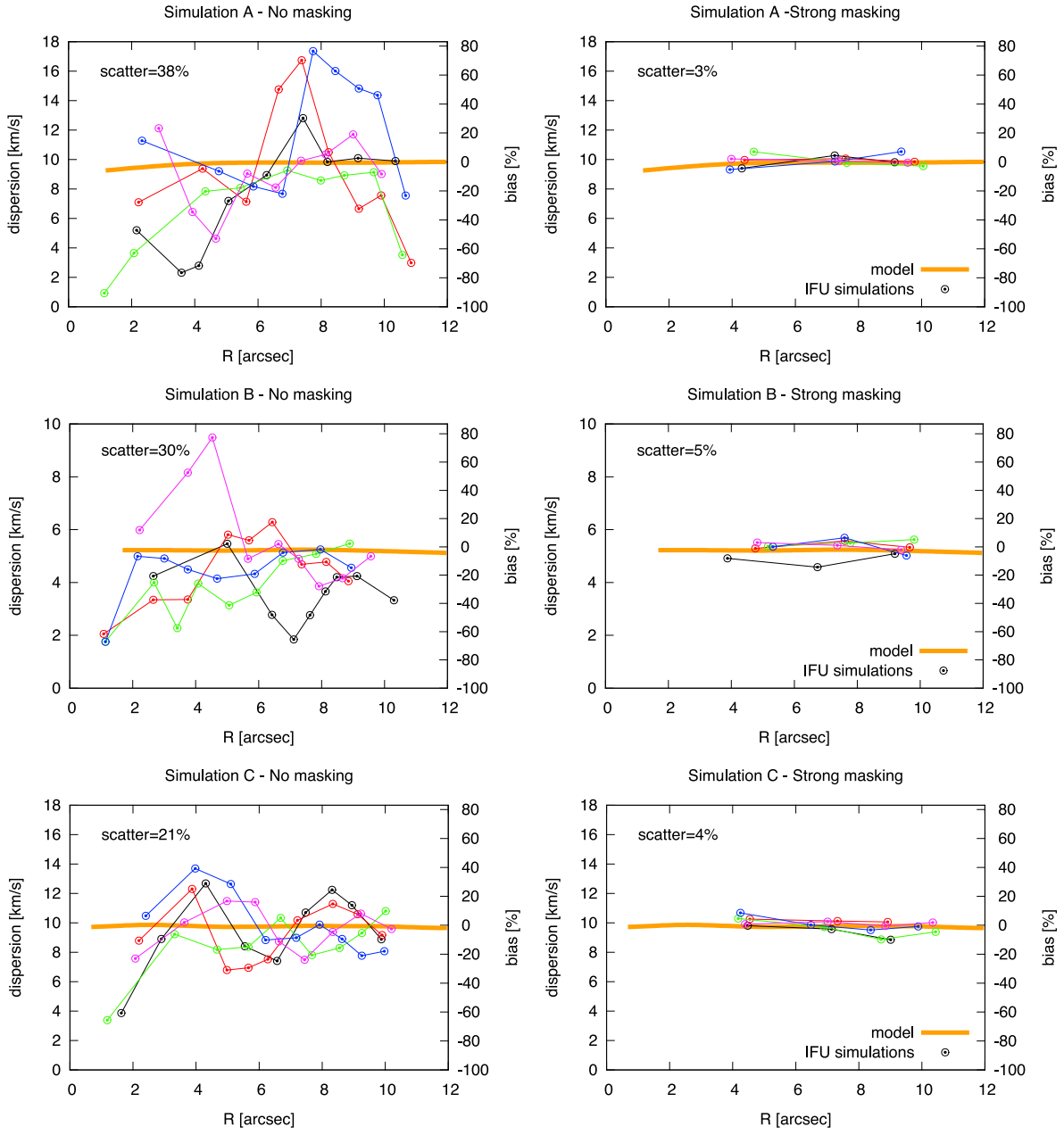

Figure 7. Comparison of masked and non-masked velocity dispersion profiles obtained for the three sets of IFU simulated observations (Simulation A, B and C; five independent realizations each) with 1 arcsec seeing and S/N $\simeq$ 10 per Å. The profiles have been constructed as described in Section 3.3, keeping a constant S/N per radial bin. The orange lines indicate the expected model velocity dispersions (see Fig. 5) and the vertical axes on the right indicate the bias with respect to the expected velocity dispersion, in percentage. Left panels: non-masked velocity dispersion profiles showing a strong scatter in velocity dispersion (with respect to the central velocity dispersion) of $\simeq$38, 30, 21 per cent, for Simulations A, B and C, respectively. Note that in the high-crowding Simulation C, the stochastic scatter of the non-masked profiles is lower than in the case of Simulations A and B, because of the higher number of stars (approximately four times larger) in the FoV. Right panels: velocity dispersion profiles corresponding to those in the left panels to which strong masking has been applied (masking A, eliminating 30 per cent of the brightest spaxels in the FoV; see Section 5). After masking, the profiles accurately reproduce the models and the scatter around the expected values of velocity dispersion is reduced to a few per cent.

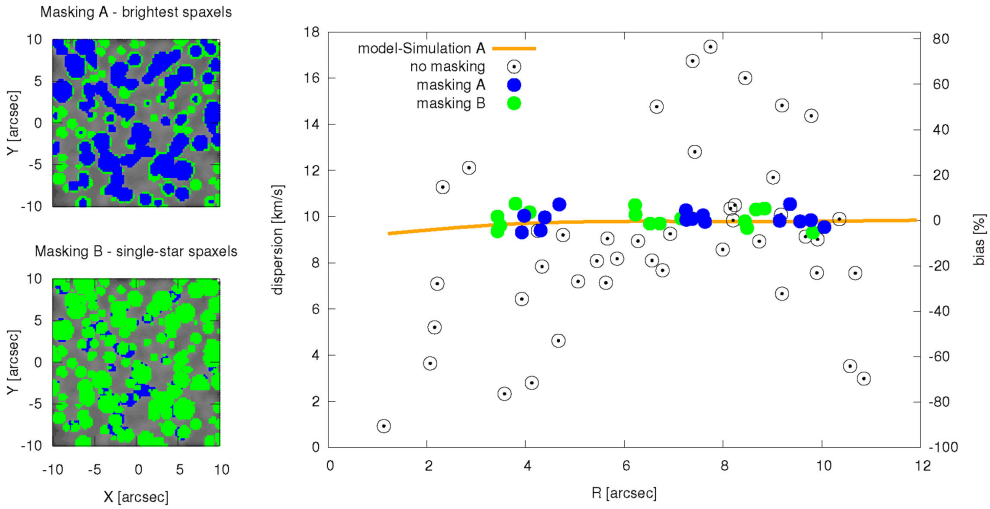

Figure 8. Left panels: luminosity maps in logarithmic scale with masked spaxels indicated in blue for masking strategy A (masking of the 30 per cent brightest spaxels in the FoV) and in green for masking B (masking of the spaxels dominated by a single bright star), applied to an IFU observation with 1 arcsec seeing, and S/N $\simeq$ 10 per Å (Simulation A). Right panel: velocity dispersion profiles for the five IFU observations without masking (open circles) and after masking according to strategy A (blue points) and B (green points). The orange line indicates the expected model velocity dispersion profile (see Fig. 5) and the vertical axis on the right indicates the bias with respect to the expected velocity dispersion, in percentage. The two masking strategies discard approximately the same 'bad spaxels' (30–40 per cent of the total number of spaxels) and yield velocity dispersion profiles fully consistent with each other. Both masking strategies allow for an efficient recovery of the expected model velocity dispersion profile, and significantly reduce the stochastic scatter (from a scatter of $\simeq$38 per cent around the central velocity dispersion value to $\simeq$3 per cent).

Moreover, we wish to stress that the high S/N spaxels dominated by a single star that are rejected with the masking approach still contain important kinematic information that can be used in complementary ways, for example, to determine discrete (i.e. individually resolved) kinematics (see e.g. Kamann, Wisotzki & Roth 2013; Lanzoni et al. 2013; Kamann et al. 2014). Finally, we tested an alternative approach to masking, consisting in performing the kinematic analysis after normalizing the luminosity of each spaxels, so that every spaxel has the same relative contribution in the final kinematic measurements (as performed in Noyola et al. 2010). Our results show that this procedure leads to an effect slightly worse than that obtained with a weak masking (see Fig. 6).

5.3 Shape of the PSF, bad seeing conditions, and misidentification of the centre of the cluster

In this section we discuss the general validity of our results, exploring different parameter configurations for our IFU mock observations. In particular, we explore the changes introduced in case of a different shapes of the PSF, bad seeing conditions and slight mis-identifications of the cluster centre.

First, we test the effect of modelling the shape of the PSF using a Moffat (1969) light distribution instead of a Gaussian PSF. We fix a seeing of 1 arcsec (full width at half maximum) and model the Moffat distribution with a shape-parameter $\beta = 2.5$ (Trujillo et al. 2001). Although the PSF appears now more extended (due to the wings of the distribution), the masking techniques described above still recover the expected values of velocity dispersion.

We then test a case of bad seeing conditions of 2 arcsec, using a Moffat PSF for the high-crowding simulation (Simulation C). Before applying masking, the five independent realizations show a stochastic scatter of 12 per cent. This value is significantly lower than the corresponding case with 1 arcsec seeing (scatter of 21 per cent),[7] since now the light of the stars is distributed over several spaxels because of the more spatially extended PSF shape. When strong masking is applied, the scatter is only slightly reduced to 8 per cent, hinting that masking is not particularly efficient in cases of bad seeing.

As a final test we explore the effect of changing the identification of the centre of our simulation (using Simulation A). We shift the centre by 2 or 5 arcsec along the x-axis, or 2 arcsec along the y-axis, and we construct the velocity dispersion profile with and without applying the masking procedure outlined. The adopted shifts correspond to 7–20 per cent the value of the core radius of $R_c \simeq 1.3$ pc. The result is shown in Fig. 9, where it is clear that even a small change of the centre causes a strong variation of the velocity dispersion profile: we estimate a scatter of $\simeq$37 per cent around the expected value of velocity dispersion. This is due to the changed position of the few bright stars with respect to the binning used. However, after masking (right panel Fig. 9) we are able to recover the expected velocity dispersion profile, since we remove the bright stars that were biasing our result, reducing significantly the scatter to $\simeq$5 per cent. Note that the issues connected to the misidentification of the centre may change when considering a simulation with a central IMBH.

6 CONCLUSIONS

We have constructed realistic integral field spectroscopic mock observations of the central region of GCs. Our software SISCO produces

[7] This does not mean that bad seeing conditions are best suited for integrated-light spectroscopy studies. In fact, the typical FoV of many available IFU spectrographs is of a few arcsec only (i.e. comparable to or slightly larger than the seeing considered here) and if just a couple of bright stars are present, their light would completely dominate the acquired spectra.

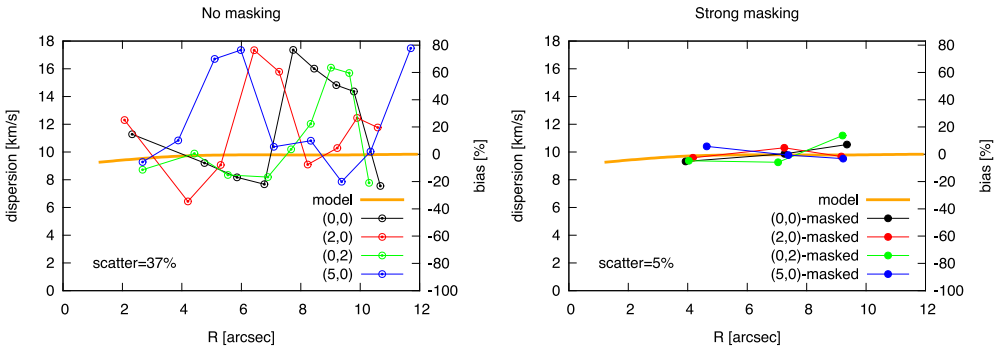

Figure 9. Comparison of the velocity dispersion profiles obtained from one IFU simulated observation using four different centres for the cluster (Simulation A); in particular no offset from the default centre given by the simulation (black line), 2 arcsec offset along the *x*-axis (red line), 2 arcsec offset along the *y*-axis (green line), 5 arcsec offset along the *x*-axis (blue line). The orange line indicates the expected model velocity dispersion (see Fig. 5) and the vertical axis on the right indicates the bias with respect the expected velocity dispersion, in percentage. Left panel: no masking applied. Right panel: masking of 'bad spaxels' has been applied (strong masking A; see Section 5). The shape of the velocity dispersion profiles strongly depends on the choice of the centre; however the correct value of velocity dispersion is recovered after applying masking, since the scatter is significantly reduced from ≃37 to ≃5 per cent.

a data cube with spectra and luminosity information in a given wavelength region (e.g. the Calcium triplet region, 8400–8800 Å) for every spaxel in a desired FoV, with adjustable seeing conditions and S/N. The starting point of our mock observations can be any realistic single stellar population cluster model, for which the stellar parameters are given as an output.

Here we applied SISCO to Monte Carlo cluster simulations in which the stellar initial mass function, stellar evolution, initial binary fraction, a realistic number of stars (up to $N \approx 2\,000\,000$) and realistic concentrations are taken into consideration. No IMBHs are considered in this work. We used the output of our mock observations to extract the internal kinematics of the cluster from the Doppler shift and broadening of the spectra. From these we extract kinematic maps and velocity dispersion profiles in the same manner as observational studies.

With the mock observations we aim to understand the biases resulting from using integrated-light spectroscopy to measure the kinematics of partially resolved stellar systems. This is a first step to understand the discrepancies reported in the literature between resolved discrete kinematics and unresolved luminosity-weighted kinematics, connected to the detection of IMBHs. From the analysis of our specific set of simulations we find the following.

(i) The luminosity-weighted kinematics from IFU observations can be strongly biased by the presence of a few bright stars. The kinematic data are strongly affected by stochasticity, and this prevents reliable measurements of the central velocity dispersion of GCs. Using five independent realizations of a given cluster simulation we estimate that the intrinsic scatter around the expected value of velocity dispersion can be as high as 40 per cent for the less crowded simulations (central luminosity density of $\simeq$60 $L_\odot$ arcsec^{-2}) and 20 per cent for the more crowded ones (central luminosity density of $\simeq$200 $L_\odot$ arcsec^{-2}), in typical seeing conditions. An additional source of stochasticity (quantitatively comparable to the former) is introduced by the particular choice of the centre of the cluster, since changing the centre position has the effect of changing the positions of the bright stars with respect to the radial bins.

(ii) The internal kinematics in the central region of a GC depends on the kinematic tracers involved in the observations. High-mass stars have a lower velocity dispersion than low-mass stars because of mass segregation. We show that the average kinematic tracers of our IFU (and likely most actual) observations have a mass of $\simeq$0.75 $M_\odot$, slightly lower than the typical mass of resolved line-of-sight velocity measurements (giant stars with mass $\simeq$0.85 $M_\odot$). Understanding which tracers are carrying the kinematic information is a necessary step when combining kinematic data sets obtained with different and complementary observational strategies. This conclusion will become particularly important when using proper motions and line-of-sight velocities in the same kinematic analysis. For example, *Hubble Space Telescope* proper motion measurements sample the kinematics for stars with different masses along the main sequence (Bellini et al. 2014; Watkins et al. 2015), while line-of-sight velocities sample bright (and more massive) stars only.

(iii) Given these findings, we are able to assess that luminosity-weighted kinematics is highly dependent on the presence of a few bright stars that can bias (both overestimating and underestimating) the measurements of the central velocity dispersion. This is a first step to explain the discrepancies reported in the literature between resolved discrete kinematics and unresolved luminosity-weighted kinematics. For a sensible comparison of these different measurements, it is necessary to apply a proper treatment to the unresolved integrated-light kinematic measurements, like masking techniques. Note, however, that simulations specifically designed to match particular cases are needed to further understand in details the discrepancies reported in the literature (e.g. see the case of NGC 6388, Lützgendorf et al. 2011, 2015; Lanzoni et al. 2013).

(iv) We show that, for the specific simulations used in this paper, masking of spaxels contaminated by bright stars allows us to recover measurements consistent with the model of the kinematic tracers. Moreover, masking reduces significantly the intrinsic scatter around the expected value of velocity dispersion in the luminosity-weighted data, bringing it down to the value of a few per cent. Reducing the scatter to a low level is essential to allow for a reliable interpretation of the presence/absence of IMBHs. We report that the efficiency of masking depends on the crowding of the FoV and the seeing conditions. In particular, for a highly crowded FoV (luminosity density of $\simeq$200 $L_\odot$ arcsec^{-2}) and bad seeing conditions masking proves to be less efficient. The main limitation of masking is to cause a loss of spatial resolution, typically across the central three to four

PSF elements. Therefore, masking can be used as a complementary approach to the one of extracting the kinematics of only the bright, high S/N spaxels dominated by single stars.

In a subsequent paper we will apply our program SISCO to state-of-the-art dynamical simulations of GCs models in which additional physical ingredients are included. In particular, we will compare mock observations of models with and without IMBHs to help understand if the presence of an IMBH can be inferred with the application of standard dynamical modelling approaches.

ACKNOWLEDGEMENTS

We are grateful to Jonathan Downing for providing the Monte Carlo cluster simulations used in this work. We thank Barbara Lanzoni and Nora Lützgendorf for useful discussions and the referee for constructive remarks that have helped improve the quality of the paper. PB acknowledges financial support from Heidelberg Graduate School for Fundamental Physics.

REFERENCES

Bahcall J. N., Wolf R. A., 1976, ApJ, 209, 214
Bellini A. et al., 2014, ApJ, 797, 115
Bianchini P., Varri A. L., Bertin G., Zocchi A., 2013, ApJ, 772, 67
Cappellari M., Emsellem E., 2004, PASP, 116, 138
den Brok M., van de Ven G., van den Bosch R., Watkins L., 2014, MNRAS, 438, 487
Downing J. M. B., Benacquista M. J., Giersz M., Spurzem R., 2010, MNRAS, 407, 1946
Dubath P., Meylan G., Mayor M., 1997, A&A, 324, 505
Fabbiano G., Zezas A., Murray S. S., 2001, ApJ, 554, 1035
Fabricius M. H. et al., 2014, ApJ, 787, L26
Ferrarese L., Merritt D., 2000, ApJ, 539, L9
Gebhardt K., Pryor C., O'Connell R. D., Williams T. B., Hesser J. E., 2000, AJ, 119, 1268
Giersz M., 1998, MNRAS, 298, 1239
Giersz M., Heggie D. C., Hurley J. R., Hypki A., 2013, MNRAS, 431, 2184
Gustafsson B. et al., 2008, A&A, 486, 951
Hanuschik R. W., 2003, A&A, 407, 1157
Hypki A., Giersz M., 2013, MNRAS, 429, 1221
Kacharov N. et al., 2014, A&A, 567, A69
Kamann S., Wisotzki L., Roth M. M., 2013, A&A, 549, A71
Kamann S. et al., 2014, A&A, 566, A58
Kirsten F., Vlemmings W. H. T., 2012, A&A, 542, A44
Kotulla R., Fritze U., Weilbacher P., Anders P., 2009, MNRAS, 396, 462
Kroupa P., 2001, MNRAS, 322, 231
Lanzoni B. et al., 2013, ApJ, 769, 107
Lardo C. et al., 2015, A&A, 573, A115
Lejeune T., Cuisinier F., Buser R., 1997, A&AS, 125, 229
Lejeune T., Cuisinier F., Buser R., 1998a, A&AS, 130, 65
Lejeune T., Cuisinier F., Buser R., 1998b, VizieR Online Data Catalog, 413, 65
Lützgendorf N. et al., 2011, A&A, 533, A36
Lützgendorf N. et al., 2013, A&A, 552, A49
Lützgendorf N., Gebhardt K., Baumgardt H., Noyola E., Neumayer N., Kissler-Patig M., de Zeeuw T., 2015, preprint (arXiv:1507.02813)
Maccarone T. J., Servillat M., 2008, MNRAS, 389, 379
Magorrian J. et al., 1998, AJ, 115, 2285
Matsumoto H. et al., 2001, ApJ, 547, L25
Miller M. C., Hamilton D. P., 2002, MNRAS, 330, 232
Moffat A. F. J., 1969, A&A, 3, 455
Noyola E. et al., 2010, ApJ, 719, L60
Pasquini L. et al., 2002, The Messenger, 110, 1
Plummer H. C., 1911, MNRAS, 71, 460
Strader J. et al., 2012, ApJ, 750, L27
Trenti M., van der Marel R., 2013, MNRAS, 435, 3272
Trujillo I., Aguerri J. A. L., Cepa J., Gutiérrez C. M., 2001, MNRAS, 328, 977
van den Bosch R., de Zeeuw T., Gebhardt K., Noyola E., van de Ven G., 2006, ApJ, 641, 852
van der Marel R. P., Anderson J., 2010, ApJ, 710, 1063
Watkins L. L., van der Marel R. P., Bellini A., Anderson J., 2015, ApJ, 803, 29

This paper has been typeset from a TEX/LATEX file prepared by the author.

Chapter 4

Measuring internal proper motions of globular clusters with the Hubble Space Telescope

"*Hubble Space Telescope Proper Motion (HSTPROMO) Catalogs of Galactic Globular Clusters. I. Sample Selection, Data Reduction, and NGC 7078 Results*"
Bellini, A.; Anderson, J.; van der Marel, R. P.; Watkins, L. L.; King, I. R.; Bianchini, P.; Chanamé, J.; Chandar, R.; Cool, A. M.; Ferraro, F. R.; Ford, H.; Massari, D.
The Astrophysical Journal, Volume 797, Issue 2, article id. 115, 33 pp. (2014)
`http://adsabs.harvard.edu/abs/2014ApJ...797..115B`

This paper is the result of the work of the ongoing HSTPROMO collaboration of which I am a member. It presents the high-precision proper motion catalog based on *HST* observations for 22 galactic GCs, delivering a median of $\sim 60\,000$ measured proper motions per cluster. My contribution to this work was devoted mainly to the understanding of the quality of the data sets and the developing of criteria to select high-quality subsamples suitable for studies of the internal dynamics of GCs (in particular Section 7 of the paper, referring to the data set of the cluster NGC 7078/M15). The paper presents the data sample for the globular cluster NGC 7078/M15 that will be extensively used in Chapter 5 of this Thesis, together with a set of dynamical cluster simulations, to infer the kinematic effects of unresolved binaries.

The Astrophysical Journal, 797:115 (33pp), 2014 December 20 doi:10.1088/0004-637X/797/2/115

HUBBLE SPACE TELESCOPE PROPER MOTION (HSTPROMO) CATALOGS OF GALACTIC GLOBULAR CLUSTERS. I. SAMPLE SELECTION, DATA REDUCTION, AND NGC 7078 RESULTS*

A. Bellini[1], J. Anderson[1], R. P. van der Marel[1], L. L. Watkins[1], I. R. King[2], P. Bianchini[3], J. Chanamé[4], R. Chandar[5], A. M. Cool[6], F. R. Ferraro[7], H. Ford[8], and D. Massari[7]
[1] Space Telescope Science Institute, 3700 San Martin Drive, Baltimore, MD 21218, USA; bellini@stsci.edu
[2] Department of Astronomy, University of Washington, Box 351580, Seattle, WA 98195, USA
[3] Max Planck Institute for Astronomy, Königstuhl 17, D-69117 Heidelberg, Germany
[4] Instituto de Astrofísica, Pontificia Universidad Católica de Chile, Av. Vicuña Mackenna 4860, Macul 782-0436, Santiago, Chile
[5] Department of Physics and Astronomy, The University of Toledo, 2801 West Bancroft Street, Toledo, OH 43606, USA
[6] Department of Physics and Astronomy, San Francisco State University, 1600 Holloway Avenue, San Francisco, CA 94132, USA
[7] Dipartimento di Fisica e Astronomia, Università di Bologna, via Ranzani 1, I-40127 Bologna, Italy
[8] Department of Physics and Astronomy, The Johns Hopkins University, 3400 North Charles Street, Baltimore, MD 21218, USA
Received 2014 August 27; accepted 2014 October 20; published 2014 December 5

ABSTRACT

We present the first study of high-precision internal proper motions (PMs) in a large sample of globular clusters, based on *Hubble Space Telescope* (*HST*) data obtained over the past decade with the ACS/WFC, ACS/HRC, and WFC3/UVIS instruments. We determine PMs for over 1.3 million stars in the central regions of 22 clusters, with a median number of ∼60,000 stars per cluster. These PMs have the potential to significantly advance our understanding of the internal kinematics of globular clusters by extending past line-of-sight (LOS) velocity measurements to two- or three-dimensional velocities, lower stellar masses, and larger sample sizes. We describe the reduction pipeline that we developed to derive homogeneous PMs from the very heterogeneous archival data. We demonstrate the quality of the measurements through extensive Monte Carlo simulations. We also discuss the PM errors introduced by various systematic effects and the techniques that we have developed to correct or remove them to the extent possible. We provide in electronic form the catalog for NGC 7078 (M 15), which consists of 77,837 stars in the central 2.′4. We validate the catalog by comparison with existing PM measurements and LOS velocities and use it to study the dependence of the velocity dispersion on radius, stellar magnitude (or mass) along the main sequence, and direction in the plane of the sky (radial or tangential). Subsequent papers in this series will explore a range of applications in globular-cluster science and will also present the PM catalogs for the other sample clusters.

Key words: globular clusters: individual (NGC 104 (47 Tuc, NGC 288, NGC 362, NGC 1851, NGC 2808, NGC 5139 (ω Cen, NGC 5904 (M 5, NGC 5927, NGC 6266 (M 62, NGC 6341 (M 92, NGC 6362, NGC 6388, NGC 6397, NGC 6441, NGC 6535, NGC 6624, NGC 6656 (M 22,), NGC 6681 (M 70), NGC 6715 (M 54), NGC 6752, NGC 7078 (M 15), NGC 7099 (M 30)) – proper motions – stars: kinematics and dynamics – stars: Population II – techniques: photometric

Online-only material: color figures, machine-readable tables

1. INTRODUCTION

Globular clusters (GCs) are the oldest surviving stellar systems in galaxies. As such, they provide valuable information on the earliest phases of galactic evolution and have been the target of numerous studies during the past century. Measures of the stellar motions in GCs, for instance, allow us to constrain the structure, formation, and dynamical evolution of these ancient stellar systems and, in turn, that of the Milky Way itself.

Almost all of what is known about the internal motions within GCs is based on spectroscopic line-of-sight (LOS) velocity measurements. Observations of the kinematics of GCs have come a long way since, e.g., Illingworth (1976) measured the velocity dispersions of 10 clusters using the broadening of absorption lines in integrated light spectra and Da Costa et al. (1977) measured the velocities for 11 stars in NGC 6397. The largest published samples today have velocities for a few thousand stars (e.g., Gebhardt et al. 2000; Malavolta et al. 2014; Massari et al. 2014).

Despite the major improvements provided by LOS-based studies on our understanding of the dynamics of GCs, there are some intrinsic limitations. First of all, the need for spectroscopy implies that only the brighter (more massive) stars in a GC can be observed. Moreover, in the crowded central regions of the cluster core, spectroscopy is limited by source confusion. Even integral-field spectroscopy is affected by the shot noise from the brightest sources. Moreover, LOS measurements are limited to measuring only one component of the motion, and therefore several model-dependent assumptions are required to infer the three-dimensional structure of GCs.

A significant improvement in data quality is possible with proper-motion (PM) measurements. Indeed, PMs have the potential to provide several advantages over LOS velocity studies: (1) no spectroscopy is required, so the more plentiful fainter stars can be studied, which yields better statistics on the kinematic quantities of interest; (2) stars are measured individually, in contrast with integrated light measurements, which contain a disproportionate contribution from bright giants; and (3) two components of velocity are measured instead of just one. More importantly, it directly reveals the velocity–dispersion anisotropy of the cluster, thus removing the mass-anisotropy degeneracy (Binney & Mamon 1982).

* Based on proprietary and archival observations with the NASA/ESA *Hubble Space Telescope*, obtained at the Space Telescope Science Institute, which is operated by AURA, Inc., under NASA contract NAS 5-26555.

PMs are small and difficult to measure with ground-based telescopes, where they require an enormous effort to achieve only a modest accuracy, particularly for faint stars in crowded fields (e.g., van Leeuwen et al. 2000; Bellini et al. 2009). On the other hand, the stable environment of space makes the *Hubble Space Telescope* (*HST*) an excellent astrometric tool. Its diffraction-limited resolution allows it to distinguish and measure positions and fluxes for stars all the way to the center of most GCs. Apart from small changes due to breathing, its point-spread function (PSF) and geometric distortion have been extremely stable over the two decades since the repair mission.

HST has the ability to measure PMs of unmatched quality compared with any ground-based facility, even in the most crowded central regions of GCs. Our team has developed methods to do this accurately (e.g., Anderson & King 2003a; Bellini et al. 2011). For instance, for a GC 5 kpc from the Sun, a dispersion of 10 km s^{-1} corresponds to ∼0.42 mas yr^{-1}; with a WFC3/UVIS scale of 40 mas pix^{-1}, this gives ∼0.1 pixel over a 10 year time baseline. Because our measurement techniques reach a precision of ∼0.01 pixel per single exposure for bright, unsaturated sources, a tenth of a pixel is easy game, even for rather faint stars, so large numbers of proper motions depend only on the availability of archival data. To date, detailed *HST* internal PM dynamics of GCs have been studied for only a handful of clusters: NGC 104 (47 Tuc, McLaughlin et al. 2006), NGC 7078 (M 15, McNamara et al. 2003), NGC 6266 (McNamara & McKeever 2011; McNamara et al. 2012), and NGC 5139 (ω Cen, Anderson & van der Marel 2010), but a deluge is now imminent; the project is described by Piotto et al. (2014), and the first result paper has been submitted (Milone et al. 2014).

With high-quality PM catalogs it will be possible to address many important topics for a large number of GCs such as: (1) *cluster-field separation*, for a better identification of bona fide cluster members for luminosity- and mass-function analyses and the study of binaries and exotic stars and to provide clean samples of targets for spectroscopic followup; (2) *internal motions*, to study in detail the kinematics and the dynamics of GCs in general and of each population component in particular (with the aim of looking for fossil signatures of distinct star-formation events); (3) *absolute motions*, by estimating an absolute proper-motion zero point using background galaxies as a reference frame (e.g., the series of papers starting with Dinescu et al. 1997 and continuing as Casetti-Dinescu and Bellini et al. 2010 using ground-based observations, and Bedin et al. 2003, Milone et al. 2006, and Massari et al. 2013 using the *HST*). Absolute PMs, in conjunction with radial velocities, allow calculation of Galactic orbits of GCs; at the same time the orbits that they exhibit are an indicator of the shape of the Galactic potential; (4) *geometric distance*, by comparing the LOS velocity dispersion with that on the plane of the sky (Rees 1995, 1997). This will provide a scale of GC distances that is independent of those based on stellar evolution or RR Lyrae stars; (5) *cluster rotation on the plane of the sky*, from the measure of the stellar velocities as a function of the position angle at different radial distances (e.g., Anderson & King 2003b);[9] (6) *energy equipartition*, from the analysis of stellar velocity dispersion as a function of the stellar mass (e.g., Trenti & van der Marel 2013); (7) *mass segregation*, by studying the stellar velocity dispersion as a function of the distance from the cluster center for different stellar masses; (8) *(an)isotropy*, by comparing tangential and radial components of the stellar motion; (9) *full three-dimensional cluster dynamics*, when LOS velocities are also known. The availability of all three components of the motion will directly constrain the three-dimensional velocity and phase-space distribution functions; and (10) *constraints on the presence of an intermediate-mass black hole*, by looking for both fast-moving individual stars and for a sudden increase in the velocity–dispersion profile near the center (e.g., van der Marel & Anderson 2010).

Unfortunately, the *HST* has executed only a very limited number of programs specifically aimed at the study of internal PM dynamics of GCs. Even so, many GCs have been observed with the *HST* for dozens of different studies, and several of these clusters have been observed on multiple occasions. Motivated by the enormous scientific potential offered by high-precision PM measurements of stars in GCs, we started a project to derive high-precision PM catalogs for all GCs with suitable multiepoch image material in the *HST* archive. This project is part of and uses techniques developed in the context of the *HST* proper-motion (HSTPROMO) collaboration[10], a set of *HST* projects aimed at improving our dynamical understanding of stars, clusters, and galaxies in the nearby universe through the measurement and interpretation of PMs (e.g., van der Marel et al. 2014).

The paper is organized as follows. In Section 2, we present the sample of GCs and data sets used for our study. In Sections 3, 4, and 5, we describe our detailed procedures for raw data reduction, astrometry, and PM measurements, respectively. In Section 6, we test the accuracy of our procedures on simulated data. Section 7 describes the effects of systematic errors and how we mitigate their effects. In Section 8, we discuss some of the kinematic quantities implied by the catalog of PMs for the GC NGC 7078 (M 15). Conclusions are presented in Section 9. Appendices present tables (available electronically) with listings of the *HST* data sets we used for each cluster and the NGC 7078 PM catalog.

This is the first of a series of several papers. Future papers in this series will present the PM catalogs for the other GCs in our sample, discuss the kinematic quantities they imply for these GCs, and address many of the scientific topics listed above.

2. SAMPLE SELECTION

This work is based on archival *HST* images taken with three different cameras: (1) the ultravioletvisible channel of the Wide-Field Camera 3 (WFC3/UVIS), (2) the wide-field channel of the Advanced Camera for Surveys (ACS/WFC), and (3) the high-resolution channel of ACS (ACS/HRC).

The physical characteristics of these cameras are as follows. The WFC3/UVIS camera is made up of two 4096 × 2048-pixel chips, with a pixel scale of about 40 mas pixel^{-1}. The ACS/WFC has the same number of resolution elements as the WFC3/UVIS, but it has a larger sampling of 50 mas pixel^{-1}. The ACS/HRC is the *HST* instrument with the finest resolution, being about 25 mas pixel^{-1}, and it is made up of a single chip of 1024 pixels on each side.

Wide-Field Planetary Camera 2 (WFPC2) exposures were not taken into account because despite the larger time baseline they can generally provide, there would only be a marginal increase in PM accuracy, due primarily to the larger pixel size (larger position uncertainties) and the smaller dynamical range of the

[9] Cluster rotations can also be measured spectroscopically; see, e.g., Peterson & Cudworth (1994); Bianchini et al. (2013).

[10] For details see the HSTPROMO home page at http://www.stsci.edu/∼marel/hstpromo.html.

Table 1
Globular Clusters and Their Parameters

Cluster ID	R.A.[a] ($^{h}.^{m}.^{s}$)	Dec.[a] ($^{\circ}.'.''$)	$D_{\odot}$[b] kpc	[Fe/H][b]	$E(B-V)$[b]	$\sigma_{V_{LOS}}$[b] km s^{-1}	r_c[b] $'$	r_h[b] $'$
NGC 104 (47 Tuc)	00:24:05.71	−72:04:52.7	4.5	−0.72	0.04	11.0 ± 0.3	0.36	3.17
NGC 288	00:52:45.24	−26:34:57.4	8.9	−1.32	0.03	2.9 ± 0.3	1.35	2.23
NGC 362	01:03:14.26	−70:50:55.6	8.6	−1.26	0.05	6.4 ± 0.3	0.18	0.82
NGC 1851	05:14:06.76	−40:02:47.6	12.1	−1.18	0.02	10.4 ± 0.5	0.09	0.51
NGC 2808	09:12:03.10	−64:51:48.6	9.6	−1.14	0.22	13.4 ± 1.2	0.25	0.80
NGC 5139 (ω Cen)	13:26:47.24[c]	−47:28:46.45[c]	5.2	−1.53	0.12	16.8 ± 0.3	2.37	5.00
NGC 5904 (M 5)	15:18:33.22	+02:04:51.7	7.5	−1.29	0.03	5.5 ± 0.4	0.44	1.77
NGC 5927	15:28:00.69	−50:40:22.9	7.7	−0.49	0.45	8.8[d]	0.42	1.10
NGC 6266 (M 62)	17:01:12.78[e]	−30:06:46.0[e]	6.8	−1.18	0.47	14.3 ± 0.4	0.22	0.92
NGC 6341 (M 92)	17:17:07.39	+43:08:09.4	8.3	−2.31	0.02	6.0 ± 0.4	0.26	1.02
NGC 6362	17:31:54.99	−67:02:54.0	7.6	−0.99	0.09	2.8 ± 0.4	1.13	2.05
NGC 6388	17:36:17.23	−44:44:07.8	9.9	−0.55	0.37	18.9 ± 0.8	0.12	0.52
NGC 6397	17:40:42.09	−53:40:27.6	2.3	−2.02	0.18	4.5 ± 0.2	0.05	2.90
NGC 6441	17:50:13.06	−37:03:05.2	11.6	−0.46	0.47	18.0 ± 0.2	0.13	0.57
NGC 6535	18:03:50.51	−00:17:51.5	6.8	−1.79	0.34	2.4 ± 0.5	0.36	0.85
NGC 6624	18:23:40.51	−30:21:39.7	7.9	−0.44	0.28	5.4 ± 0.5	0.06	0.82
NGC 6656 (M 22)	18:36:23.94	−23:54:17.1	3.2	−1.70	0.34	7.8 ± 0.3	1.33	3.36
NGC 6681 (M 70)	18:43:12.76	−32:17:31.6	9.0	−1.62	0.07	5.2 ± 0.5	0.03	0.71
NGC 6715 (M 54)	18:55:03.33	−30:28:47.5	26.5	−1.49	0.15	10.5 ± 0.3	0.09	0.82
NGC 6752	19:10:52.11	−59:59:04.4	4.0	−1.54	0.04	4.9 ± 0.4	0.17	1.91
NGC 7078 (M 15)	21:29:58.33	+12:10:01.2	10.4	−2.37	0.10	13.5 ± 0.9	0.14	1.00
NGC 7099 (M 30)	21:40:22.12	−23:10:47.5	8.1	−2.27	0.03	5.5 ± 0.4	0.06	1.03

Notes.
[a] From Goldsbury et al. (2010), unless stated otherwise.
[b] From Harris 1996 (2010 edition), unless stated otherwise. $D_{\odot}$ is the GC distance from the Sun.
[c] From Anderson & van der Marel (2010).
[d] From Gnedin et al. (2002).
[e] From Beccari et al. (2006).

WFPC2 chips (fewer well-measured stars), particularly in the crowded cores, which is the focus of this study.

Ten GCs were specifically observed with the *HST* by some of us to study their internal motions, namely:

1. NGC 362, NGC 6624, NGC 6681, NGC 7078, NGC 7099 (GO-10401, PI: R. Chandar);
2. NGC 2808, NGC 6341, NGC 6752 (GO-10335 and GO-11801, PI: H. Ford);
3. NGC 6266, (GO-11609, PI: J. Chanamé); and
4. NGC 6715 (GO-12274, PI: R. P. van der Marel).

In 2011 January, we searched through the *HST* archive to look for other suitable data and additional GCs, imaged with the three mentioned cameras and with a total time baseline of at least two yr. Twelve GCs were found that satisfied these two criteria, and we successfully submitted an archival *HST* proposal (AR-12845, PI: A. Bellini) to analyze them. The clusters are NGC 104, NGC 288, NGC 1851, NGC 5139, NGC 5904, NGC 5927, NGC 6362, NGC 6388, NGC 6397, NGC 6441, NGC 6535, and NGC 6656. A summary of the general properties for all 22 GCs is given in Table 1. A complete list of observations used for our analysis of each cluster can be found in Appendices A and B.

3. DATA REDUCTION

3.1. Measuring Stellar Position and Fluxes in Each Exposure

This work is based solely on `_flt` or `_flc` type images. These images are produced by the standard *HST* calibration pipeline *CALWF3* (for WFC3) or *CALACS* (for ACS). Images of type `_flt` are dark- and bias-subtracted and flat-fielded, but not resampled (like the `_drz` type images); `_flc` images are `_flt` exposures that are also corrected for charge-transfer efficiency (CTE) (see below). The choice to use nonresampled images is motivated by the fact that we need to retain information about where exactly a photon hit the detector in order to minimize systematic errors in the PMs.

3.1.1. Charge-transfer Efficiency Corrections

Charge-transfer errors arise from the damaging effects of cosmic rays on the detectors. CTE losses affect both the shape (and therefore position) and the measured flux of stars, and these errors increase over time (see, e.g., Anderson & Bedin 2010). CTE effects are more severe when the image background is low, e.g., for short exposures or when bluer filters are used. It is a crucial step to properly model and correct these CTE losses if we want to measure high-quality PMs.

The CTE correction for ACS is especially important on exposures taken after the camera was repaired in 2009 (seven yr after its installation), whereas CTE damage is only mild or marginal on earlier exposures. For the WFC of ACS, the CTE correction is already included in the *CALACS* pipeline (`_flc` extension). The correction is not available for the HRC of ACS, but this is only a minor issue because the HRC stopped operating in 2006, and it was not repaired during the last *HST* Service Mission 4 (SM4). Moreover, the HRC readout also has a maximum of 1,024 transfers, so at its worst, its CTE losses are only half as bad as the WFC.

An official CTE correction for WFC3/UVIS has recently been made available, but it had not been implemented within the WFC3 calibration pipeline at the time of our reductions, so we manually corrected each individual WFC3/UVIS `_flt`

exposure with the stand-alone CTE correction routine available on the official UVIS Web site[11] to create _flc images.

3.1.2. ACS/WFC

All ACS/WFC _flc images were reduced using the publicly available FORTRAN program img2xym_WFC.09x10, which is described in detail in Anderson & King (2006a).[12] The program does a single pass of finding and measures each star in each exposure by fitting a spatially varying effective PSF, ignoring any contribution from neighbors.

Library PSFs for several filters are provided along with the reduction software. To take into account the variation of the PSF across the field of view (FoV), the library PSFs are made up of an array of 9×10 PSFs across the detector. At any given location on the detector, the local PSF is then obtained through a bilinear interpolation of the four surrounding library PSFs.

During its ∼90 minute orbital period around the Earth, the *HST* is cyclically heated by the Earth and Sun. As a result, the focal length changes slightly during each orbit. This effect, known as "telescope breathing, affects the shape of the PSF in a nonconstant way across the FoV. To take into account the time-dependent variations of the PSFs, for each individual exposure we derived an additional array of up to 5×5 perturbation PSFs by modeling the residuals of library-PSF-subtracted stars across the detector. These perturbation PSFs were then interpolated into the 9×10 array of the library PSFs and added to them. The final set of PSFs (one set for each exposure) was then used to fit stellar profiles.

3.1.3. WFC3/UVIS

Star positions and fluxes on WFC3/UVIS images were measured with the software img2xym_wfc3uv, adapted mostly from img2xym_WFC.09x10. Library spatially varying PSFs are also available for this detector (in an array of 7×8 PSFs). As done for the ACS/WFC, we derived an additional array of perturbation PSFs for each WFC3/UVIS exposure and combined it with the library PSFs to fit stellar profiles. (For a more comprehensive analysis of spatial and time variations of UVIS PSFs, see Sabbi & Bellini 2013).

3.1.4. ACS/HRC

The measurement of stellar fluxes and positions in each ACS/HRC image was performed by using the publicly available routine img2xym_HRC and library PSFs. Because of the small FoV of HRC, there was no need to create spatially varying PSFs, and a constant PSF for each filter is adequate to properly represent stellar profiles all across the detector. We investigated the possibility of taking into account the time-dependent part of the PSFs but found that perturbation PSFs were able to provide only a negligible improvement in modeling stellar profiles.

3.2. Single-exposure Catalogs

The img2xym routine family used here produces a catalog of positions and fluxes of each measured star in each individual exposure, together with some other additional quantities and diagnostics, such as the quality-of-fit (QFIT) parameter, which tells us how well a source has been fit with the PSF model (Anderson et al. 2008).

Neighbor subtraction was not taken into account, so stars were measured as they are on the exposures. Our aim is to measure PMs as precisely as possible, so we decided to focus our attention on relatively isolated stars, for which positions can be reliably measured on individual exposures. The positions of blended stars, or stars for which the profile is impaired by brighter neighbors, would be affected by systematics in any case (see Section 7.5).

The precision with which we are able to measure positions for well-exposed stars on a single image is on the order of $\lesssim$0.01 pixels (see Section 5.2). This level of precision can be achieved thanks to the high quality of the carefully modeled, fully empirical PSFs at our disposal.

3.3. Geometric-distortion Corrections

Stellar positions in each individual exposure were corrected for geometric distortion using the state-of-the-art solutions available for ACS/WFC (Anderson & King 2006a), ACS/HRC (Anderson & King 2006b), and WFC3/UVIS (Bellini & Bedin 2009; Bellini et al. 2011). These corrections are able to provide distortion-free stellar positions with residuals on the order of $\lesssim$0.01 pixel (about the same precision offered by the PSF fitting). This level of precision in the distortion solution depends strongly on the adopted PSFs and cannot be achieved with simple centroid-type approaches, with optics-based PSFs, or even with empirical PSFs that do not adequately treat the spatial variations of the PSFs.

WFC3/UVIS is affected by a chromatic dependence of the geometric distortion, and the effect is larger for the bluer filters (see, e.g., Figure 6 of Bellini et al. 2011). The problem likely resides in the fused-silica CCD windows within the optical system, which refract blue and red photons differently and exhibit a sharp increase in the refractive index in the ultraviolet regime.

We showed in Bellini et al. (2011) that there are negligible color-dependent residuals in the UVIS distortion solutions for filters redward of F275W. A similar chromatic dependence of the distortion solution might also be present for the bluer filters of ACS/HRC. To minimize this subtle systematic effect, we decided to exclude any exposure taken through filters bluer than F336W for UVIS and F330W for HRC.

The bluest filter available for ACS/WFC peaks at 435 nm (F435W), and no chromatic dependence of the distortion solution has been reported for this camera. The ACS/WFC, however, experienced a slight change in the geometric-distortion solution after it was repaired during SM4. Post-SM4 positional residuals obtained with pre-SM4 geometric-distortion solutions can be on the order of 0.05 pixels and therefore need to be corrected. We carefully modeled the post-SM4 deviation of the distortion solution with a look-up table of residuals.[13] The accuracy of the post-SM4 geometric-distortion solutions for the ACS/WFC is comparable with the pre-SM4 solution and is on the order of $\lesssim$0.01 pixels.

4. THE MASTER FRAME

The 22 GCs for which we want to measure PMs all have different apparent size and core density. Moreover, most of the archival data come from projects with scientific goals other than high-precision astrometry. As a result, the data sets at our disposal are extremely heterogeneous in terms of cameras or

[11] http://www.stsci.edu/hst/wfc3/tools/cte_tools.
[12] http://www.stsci.edu/~jayander/ACSWFC_PSFs/.
[13] http://www.stsci.edu/~jayander/ACSWFC_PSFs/POST-SM4/.

filters used, chosen exposure time, dither strategy, number of exposures, and time baseline.

Despite the severe lack of similarity among the data sets, it is important to be able to measure PMs for all 22 clusters in a homogeneous and standardized fashion. This eases subsequent analyses and comparisons of the dynamical properties of each cluster. To obtain a homogeneous set of PM catalogs, we had to address several issues.

The first issue concerns the definition of the reference system (master frame) on which to register the stellar positions. The master frame needs to be defined in a consistent way for each cluster and to have the same properties. Luckily, there is one data set in common between all but one GC (NGC 6266): GO-10775, PI: A. Sarajedini. This data set has been reduced with software tools similar to the ones we employed here (for more details, see Anderson et al. 2008). Its astrophotometric catalogs are publicly available,[14] and their high quality and reliability are supported by several dozens of papers. Moreover, the GO-10775 data were taken in 2006 and usually lie in between the time baseline of the data sets of each cluster, thus limiting bias effects in computing PMs.

The GO-10775 catalogs have stellar positions in equatorial units and in ACS/WFC pixels (rescaled to be exactly 50 mas pixel^{-1}). The pixel-based reference frame has north up and east to the left and places the center of each GC (as defined in Harris 1996) at location (3000, 3000). To better exploit the GO-10775 catalogs as our reference systems, we applied the following three changes.

1. We modified the pixel scale from 50 to 40 mas pixel^{-1}, which is the WFC3/UVIS pixel scale and represents a compromise between the ACS/HRC and ACS/WFC pixel scales).
2. We shifted the cluster center positions to location (5000, 5000), in order to accommodate all overlapping data sets with GO-10775 (which have different pointings and orientations) without having to deal with negative coordinates.
3. We removed from the GO-10775 catalogs those stars for which the position was not well measured, following the prescriptions given in Anderson et al. (2008). In addition, we removed stars belonging to any of the following cases: (1) saturated stars; (2) stars fainter than instrumental magnitude[15] -5.7 in either F606W or F814W; (3) stars with positional error larger than 5 mas in either coordinate; (4) stars with photometric error larger than 0.2 mag in either filter; and (5) stars with o_V or o_I, i.e., the ratio of neighbor versus star light in the aperture greater than one.

Although a GO-10775 catalog is available for ω Cen, we decided instead to base its reference system on the GO-9442 data set (PI: A. Cool). The reason for this is twofold: (1) the GO-9442 field of view is nine times larger than that of GO-10775, and there are other projects (such as GO-10252) that overlap with GO-9442 but not with GO-10775, thus allowing PM measurements at larger radial distances; and (2) the GO-9442 observation strategy was very similar to that of GO-10775 in terms of dithering scheme, number of exposures, and exposure time. Only the chosen filters are different, based on the different scientific goals. Moreover, the data of GO-9442 were reduced by one of us (J. Anderson) with a preliminary version of the same software used to create the GO-10775 database. To transform the GO-9442 catalog into our reference system, we applied the same changes that were applied to the GO-10775 catalogs.

In order to obtain a reference system for NGC 6266, we noted that the data of GO-10210 were taken following an observing strategy very similar to that of GO-9442 for ω Cen. Therefore, we reduced GO-10120 following the prescriptions given in Anderson et al. (2008) to produce a star catalog analogous to those of GO-10775, and we applied the same three changes as for the GO-10775 data sets.

5. PROPER MOTIONS

In the simple situation of repeated observations taken in only two epochs, one can simply measure the average position of stars within each epoch and then obtain PMs as the difference in position between the second and the first epoch, divided by the time baseline. In reality, our data sets generally contain a varying number of epochs, sometimes with one exposure only. Even when there are multiple exposures within a given epoch (which may span several weeks), stars are usually measured through different filters and with different exposure timesand hence different signal-to-noise ratios and it is not trivial to properly determine an average position for them within each epoch. Therefore, we decided to treat each individual exposure as a stand-alone epoch and to measure PMs by fitting a straight line to the data in the position versus epoch space (essentially the so-called *central overlap* method, first proposed by Eichhorn & Jefferys 1971).

Our general strategy for measuring PMs can be summarized in five main steps: (1) measure stellar positions in each individual exposure, (2) cross-identify the same stars in all of the exposures where they can be found, (3) define a reference network of stars with respect to which we can compute PMs, (4) transform stellar positions onto a common reference frame, and (5) fit straight lines to the data for reference-frame position versus epoch to obtain PMs.

Steps (3), (4), and (5) are nested into each other, and each of them requires some iteration in order to reject discrepant observations and improve the PM measurements. The basic scheme of the iterative process is summarized in the flow chart of Figure 1. We have already discussed step (1) in Section 3; the following subsections will provide a comprehensive explanation of the subsequent steps.

5.1. Linking Master-frame to Single-catalog Stellar Positions

First of all, each star in the master-frame list needs to be identified in each individual exposure where it can be found. The cross-identification is performed by means of general six-parameter linear transformations. These allow us to transform stellar positions as measured in the individual exposures onto the reference system and associate them with the closest star in the master-frame list.

We match up stars that have moved in random directions as time has passed. To limit the number of mismatches, we considered only stars for which master-frame matches are within

[14] http://www.astro.ufl.edu/~ata/public_hstgc/databases.html.

[15] The instrumental magnitude is defined as $-2.5 \times \log(\text{flux})$, where the flux in counts is the volume under the PSF that best fits a stellar profile. We will use instrumental magnitudes extensively throughout this paper because they offer an immediate sense of the signal-to-noise ratio of measured sources. As a reference, a typical *HST* central PSF value is ~0.2 (i.e., 20% of the source flux is in its central pixel): this means that saturated stars (central pixel $\geqslant$55,000 counts) will have magnitudes brighter than instrumental magnitude $-2.5 \times \log(55{,}000/0.2) = -13.6$. Moreover, stars with instrumental magnitude -10 will have a signal-to-noise ratio of 100.

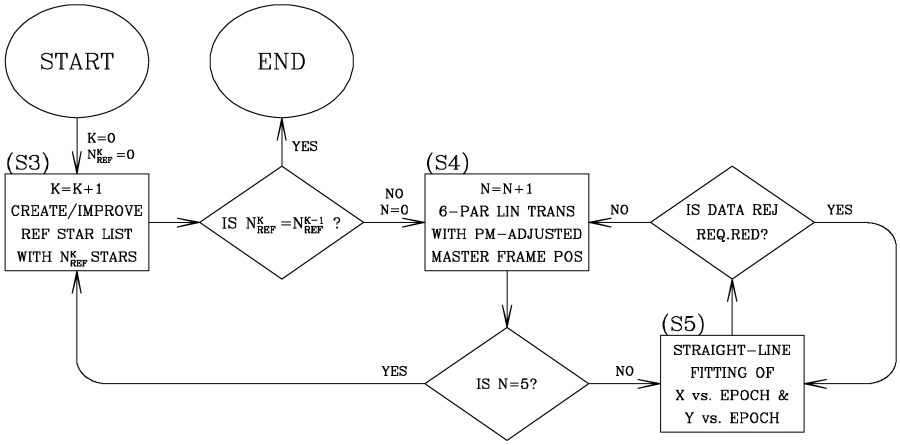

Figure 1. Flow chart illustrating the adopted scheme to compute PMs. The three main steps discussed in the text are marked as (S3), (S4), and (S5). See Sections 5.3, 5.4, and 5.5, respectively, for details.

2.5 pixels (0.″1). This criterion necessarily limits our ability to measure the motion of very fast-moving stars. As an example, let us take the NGC 5927 data set. The time baseline to the reference data set (GO-10775) is 3.87 yr for GO-9453 and about 4.38 yr for GO-11664 and GO-11729. The fastest motion we can measure for stars present only in the GO-10775 and GO-9453 data is $\mu = 2.5 \times 40/3.87$ mas yr^{-1} = 25.84 mas yr^{-1}. This limit is further reduced to 22.83 mas yr^{-1} if stars are measured in the GO-11664 or GO-11729 data sets but not in the GO-9453 one (see also Table 14). These PMs correspond to ∼940 km s^{-1} and 830 km s^{-1} at the distance of NGC 5927, but would correspond to smaller velocities for foreground stars.

At the initial stage, there is no need to fine tune the linear transformations, so long as we are able to identify master-frame stars in each exposure. We will later compute improved transformations to precisely place single-exposure stellar positions onto the master frame.

5.2. Expected Errors

Because each exposure corresponds to a stand-alone epoch, we cannot directly measure stellar positional errors from the rms of the residuals around an epoch-averaged position, as in the case of multiple exposures per epoch. Instead, we need to assign an a priori expected error based on some assumptions.

We reduced thousands of *HST* images and found, as expected, that there is a general trend of increasing positional rms as a function of the instrumental magnitude. This trend is stable over time and has little dependence on the filter used. For this reason, we decided to model this trend for the three *HST* detectors employed here and assign an expected positional error to each star of each individual catalog according to its instrumental magnitude.

To model the ACS/WFC expected-error trend, we chose the exposures of the core of ω Cen, a moderately crowded field containing several thousand stars and imaged through several dithered exposures in the F435W, F606W, and F814W filters (to sample the available wavelength coverage). For each filter, we computed average star magnitudes and positions and measured

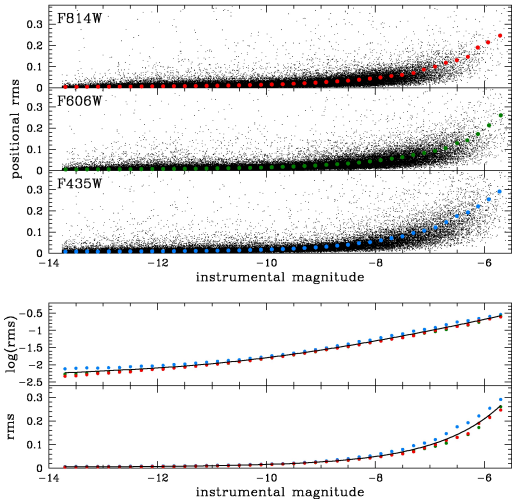

Figure 2. Modeling of the expected errors for the ACS/WFC camera. The top three panels show the one-dimensional positional rms as a function of the instrumental magnitude for three filters of the central field of ω Cen. We computed the 68.27 percentile of these rms in bins of 0.2 mag and fitted a fifth-order polynomial to them. The bottom two panels show the binned rms in linear and logarithmic units, together with the fitted function.
(A color version of this figure is available in the online journal.)

the positional rms of the residuals about the mean. Stars brighter than instrumental magnitude ∼−13.7 are saturated and were not taken into account. Stars fainter than ∼−5.7 are generally close to the shot-noise level for single-exposure measurements and define the faint limit of the model.

The top three panels of Figure 2 show the one-dimensional positional rms as a function of the instrumental magnitude for F814W, F606W, and F435W from top to bottom. We divided each sample of points into bins of 0.2 mag and computed a 3σ clipped 68.27 percentile of the positional rms within

each bin (full colored circles). The bottom two panels of the figure show sampled values of the three filters, in linear and logarithmic units, as a function of the instrumental magnitude. The logarithmic units allow one to better distinguish the sampled values in the bright regime, whereas the linear units work better for the faint regime. A least-squares fifth-order polynomial is fit to the points in the log plane to model the positional rms trend. This model provides our expected errors for the ACS/WFC camera.

For the ACS/HRC and WFC3/UVIS cameras, we used the central fields of 47 Tuc and ω Cen, respectively,[16] and followed the same procedures used for the ACS/WFC camera to model the positional rms, and thus the expected errors, as a function of the instrumental magnitude. For these two detectors, we again modeled the expected errors using three filters: a blue, an intermediate, and a red filter. As for the ACS/WFC, the intermediate and red filters are the F606W and the F814W. As the blue filter for ACS/HRC, we chose F475W instead of the ACS/WFC F435W because F475W exposures are more numerous and have longer exposure times. Because the WFC3/UVIS detector covers bluer wavelengths than the ACS/WFC, the adopted blue filter was the F336W (which is also the bluest filter used to compute PMs). The average modeled curves of the expected errors for the ACS/HRC and the WFC3/UVIS cameras are very similar to those for the ACS/WFC shown in Figure 2.

5.3. The Reference-star List

At this stage in the reduction process, we are ready to start measuring PMs. We want to stress here that we will compute *relative* and not *absolute* PMs. The main reason is that the cores of GCs are so dense that the light of a background galaxy can hardly push itself above the scattered light of the cluster. (One of the few clusters in which there are enough galaxies to actually measure absolute PMs is NGC 6681; see Massari et al. 2013.) Therefore, in general we need to choose a reference set of objects other than background galaxies against which to measure motions. This leaves the cluster stars and the field stars. The cluster stars have a much tighter PM distribution, so they are the obvious choice. Our motions will thus be in a frame that moves and rotates with the cluster.

We want to use only the best-measured, unsaturated master-frame stars in order to minimize transformation residuals. Master-frame magnitudes are zero-pointed with respect to the deep exposures of GO-10775, so the short-exposure saturation limit in instrumental magnitudes is about -16.5, and the long-exposure limit is about -13.5. Stars between -16.5 and -13.5 mag are measured only in the short exposures. Generally, the best-measured stars lie within $\sim$3 mag of the saturation limit. Therefore, in principle, we could consider all stars between instrumental magnitude -16.5 and -10 in our reference list. However, because of the large variety of exposure times in our data sets, it could be that these bright stars are too bright (i.e., saturated) in some exposures. We therefore adopted a compromise by including fainter, less-constrained stars in the reference list to obtain an adequate number of reference stars for the transformations by extending the magnitude range of the reference-list stars to instrumental magnitude -8.

The process of creating the reference-star list is labeled as (S3) on the flow chart of Figure 1. We start by selecting cluster members on the basis of their positions on the color–magnitude diagram (CMD). To make the selection easier, especially for those clusters with high reddening foreground values, we corrected the master-frame photometry for differential reddening as done in Bellini et al. (2013), following prescriptions given in Milone et al. (2012). A few field stars will still be included, but once PMs are computed, we refined our reference-star list by removing from it those stars with PMs that are inconsistent with the cluster's bulk motion. This is an iterative process that ends when, from one iteration to the next, the number of stars in the reference list stops decreasing, meaning that we have computed PMs with respect to a list of bona fide cluster members that is as genuine as we can hope to obtain.

5.4. Positions on the Master Frame

For each exposure, we transformed the distortion-corrected positions of its stars into the master frame using general six-parameter linear transformations. Only bright, unsaturated reference stars in common between the single-exposure catalog and the master-frame catalog were used to compute the transformation parameters (i.e., reference stars that in the single-exposure catalogs are brighter than instrumental magnitude -9.5).

We chose to restrict the use of common reference stars to the same amplifier, to limit the impact of uncorrected geometric-distortion and CTE-mitigation residuals. The ACS/WFC and WFC3/UVIS cameras have four amplifiers each, corresponding to an area of 2048×2048 pixels. On the other hand, the ACS/HRC camera has only one amplifier, so this restriction does not apply.

The geometric distortion has a smooth variation across the detectors, and therefore it can be considered locally flat. If we were to use the local-transformation approach (see, e.g., Anderson et al. 2006; Bellini et al. 2009), we would have minimized the impact of uncorrected geometric-distortion residuals. However, the adopted amplifier-type restriction (a sort of semilocal approach) allows us to limit these effects. We will henceforth refer to the PMs thus obtained as "amplifier based". This is in contrast to "locally corrected" PMs, which are discussed in Section 7.3. Both types of PMs are listed in our catalogs. Which PMs are best depends on the specific scientific application.

Concerning CTE-correction residuals, y-CTE effects (i.e., trails along the Y axis of the detector) vary as a function of their distance from the register. Each amplifier has its own register. To date, there is no pixel-based x-CTE correction (i.e., trails along the X axis) available for *HST*. However, the impact of x-CTE effects is orders of magnitude smaller than that of y-CTE, and to the first order, it should be compensated for by our amplifier-based approach.

Because all of the stars in our reference list are moving in random directions with respect to each other with some dispersion, each and every transformed star position is affected by a systematic error of err $\propto \sqrt{\sigma_{\rm ref}/N_{\rm ref}}$, where $N_{\rm ref}$ is the total number of reference stars used for the transformation and $\sigma_{\rm ref}$ their PM dispersion. This implies that a large number of reference stars is best to minimize this source of error. On the other hand, it is not uncommon to have only a handful of reference stars to use for the transformations, especially in partially overlapping data sets or when the image depth is very different. A good compromise for the used data sets was found by rejecting all transformed stars that had less than 75 reference stars within their amplifier for ACS/WFC and WFC3/UVIS exposures and less than 50 for ACS/HRC exposures. In the vast

[16] No suitable ACS/HRC exposures of the core of ω Cen have been taken, whereas the core of 47 Tuc was used as the ACS/HRC calibration field.

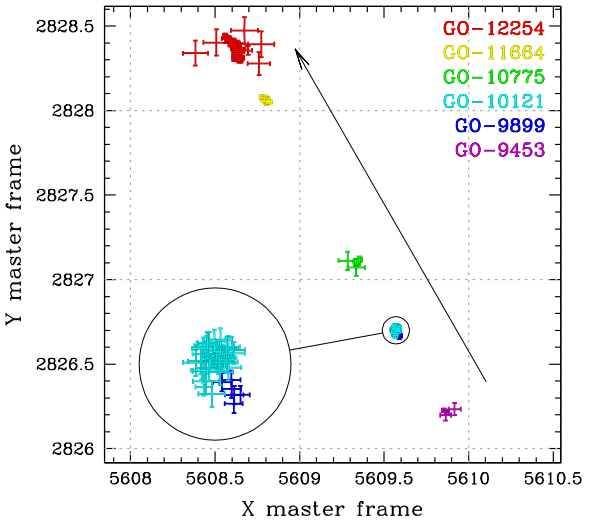

Figure 3. Transformed positions of a single star of the NGC 6752 data set, taken at six different epochs, as they appear on the reference system. Master-frame pixels are highlighted with dashed lines. Star positions and error bars are color-coded according to their program ID. Colors go from violet to green to red, moving from the 2002 to 2006 to 2011 epochs. A zoomed-in region of GO-9899 and GO-10121 positions is enclosed for clarity. An arrow shows the motion of the star during ∼nine yr.

(A color version of this figure is available in the online journal.)

majority of cases, the typical number of reference stars used for the transformations is larger than 300.

As mentioned, the reference stars themselves do also move. As a result, when we transform stellar positions of exposures taken years apart from the master-frame epoch, we will necessarily have to deal with larger transformation residuals. These residuals will in turn translate into larger uncertainties in the transformed positions of stars. We can bypass this problem by correcting the positions of the reference stars to correspond to the epoch of the single-exposure catalog that we want to transform.

Obviously, we need to know the PM of the reference stars to compute their position adjustments. As a consequence, computing positions on the master frame is an iterative process. With improved transformations we will be able to measure more precise PMs, and with them obtain even better transformations. We found that five iterations were enough to minimize the transformation residuals.

Once all of the stars of all of the exposures are transformed into the master frame, each master-frame star will be characterized by several slightly different positions, each of them referring to a different exposure (i.e., a different epoch). In Figure 3, we illustrate this concept for a rapidly moving star in the field of NGC 6752. On the master frame (the pixels of which are highlighted by dashed lines), each point represents a transformed single-exposure position. Error bars are obtained using expected errors (from Section 5.2) so that larger error bars refer to shorter exposure times. For clarity, we color-coded star positions according to their program number. The epochs of the observations go from 2002 (GO-9453, purple data) to 2011 (GO-12254, red data). We recall that the master-frame epoch is defined by the GO-10775 observations (in green). The actual master-frame position of this star lies underneath the green points (not shown). The data of GO-9899 and GO-10121 are separated by less than three months, and their position is magnified in the enclosed circle. An arrow indicates the motion of the star over ∼nine yr.

5.5. Proper Motion Fitting and Data Rejection

Let us suppose that for a given star we have N total positions in the master frame. Each position has an associated expected one-dimensional error and epoch of observation and is therefore characterized by the quadruplet (x_N, y_N, e_N, t_N). To measure the motion of this star along the X and Y axes, we used a weighted least-squares to fit a straight line to the data points (x_N, t_N) and (y_N, t_N). We progressively improved the fit by rejecting outliers or badly measured observations. This iterative straight-line fitting process is marked as (S5) in the flow chart of Figure 1.

We require that a star have at least four data points, with at least six months of time baseline between the second and the second-from-last point, in order for its PM to be measured. These conditions must be satisfied at every stage of the fitting and rejection process.

Before starting with the iterative process, we identify and reject obvious outliers. This task is done by removing one point at a time, then fitting the straight lines to the remaining $N-1$ points. If the distance of a removed point from its associated fitted line is larger than 10 times its expected error, the point is rejected immediately. Such data points generally come from objects with a cosmic-ray event within their fitting radius. As a result, the centroid is shifted toward the cosmic ray, and their measured luminosity is enhanced by the cosmic-ray counts.

Let us suppose that a star still has N data points after these preliminary selections. We fit two weighted straight lines to the points (x_N, t_N) and (y_N, t_N). An example of these fits for the same star used in Figure 3 is illustrated in Figure 4. Data points are color-coded as in Figure 3. Panel (a) of Figure 4 shows the fitted line in the X position versus epoch plane, where the epoch of each point is expressed relative to the master-frame epoch (T = 0, in years). Panel (c) shows the fit for the Y position versus epoch. Panels (b) and (d) show the residuals (dx_N, dy_N) of the points around the straight-line fits.

To identify and reject the marginal outliers, we adopted the one-point-at-a-time approach as follows. We define error-normalized quantities $dx'_N = dx_N/e_N$, $dy'_N = dy_N/e_N$, and their sum in quadrature $r_N = \sqrt{dx'^2_N + dy'^2_N}$. For a Gaussian distribution, the cumulative probability distribution of r_N is $P[r_N] = 1 - \exp(-r_N^2/2)$. Alternatively, if the enclosed probability is p_N, then $r_N = \sqrt{-2 \times \ln(1-p_N)}$. For example, for $p = 0.6$ (the reference value we adopted), $r = 1.3537$. This means that in a two-dimensional Gaussian distribution, 60% of the points should be within 1.3537σ. Let the 60th percentile value of r_N of the data points be M. Then, to ensure that our residuals are consistent with the expected Gaussian, we would need to multiply all of our e_N values by a factor of $1.3537/M$. We let the rescaled, normalized residuals be (sx_N, sy_N).[17]

After the rescaling, to the lowest order the cloud of data points should be consistent with a two-dimensional Gaussian. Panel (e) of Figure 4 shows the distribution of the normalized and rescaled residuals (sx_N, sy_N). A circle of radius 1.3537 encloses 60% of the points (in gray). We now identify the outermost data point, at distance R. The probability that one data point has

[17] The rescaling can be done in principle using any percentile value. Our choice of using $p = 0.6$ is motivated by the fact that p needs to be small enough that the distribution is not sensitive to outliers, but p also needs to be large enough to guarantee good statistics.

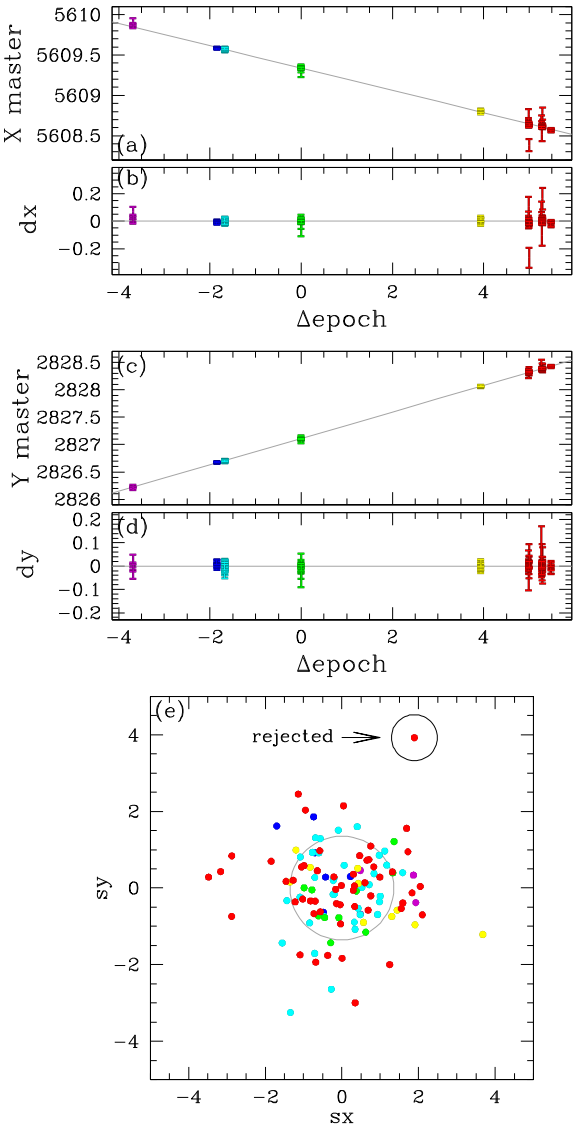

Figure 4. Illustrative example of the least-squares straight-line fitting procedure. The chosen star is the same as shown in Figure 3 (and points are color-coded accordingly). Panel (a) shows the X positions vs. the epoch of the observations with respect to the master-frame epoch, in Julian years. The fitted line is marked in gray. The residuals of the fit are in panel (b). Panels (c) and (d) show the same for the Y positions. Panel (e) illustrates the adopted rejection criterion. In the normalized and rescaled residual plane (sx, sy) (where points resemble a two-dimensional Gaussian), we identify the outermost point and check whether its probability of being that far out is inconsistent with that of a two-dimensional Gaussian distribution at a confidence level of 97.5%. If not, the data point is rejected (as in the example), and the straight-line fitting process is repeated without it.

(A color version of this figure is available in the online journal.)

such a high value of R is $P[1/1] = \exp(-R^2/2)$. Because there are N total points in the distribution, the probability of finding one data point out of N with such a high R is $P[1/N] = 1 - (1 - P[1/1])^N$. For example, if $R = 3$ then $P[1/1] \sim 1\%$, and $P[1/3] \sim N \times P[1/1]$. So, for $N = 10$ data points, there is a 10% chance of having a $\geqslant 3\sigma$ outlier.

We set a confidence threshold Q for accepting data points at 2.5%. If the data point with the highest R has $P[1/N] < Q$, then the data point is rejected and the straight-line fitting process is repeated. The iterations stop when all of the remaining data points are consistent with a two-dimensional Gaussian distribution. At this point, we also compute the errors of the slopes (proper motions) and intercepts of the fitted lines and the reduced χ^2 values. We report the PM errors measured in two distinct ways: (1) using the estimated errors as weights and (2) using the actual residuals of the data points around the fitted lines, as described in Section 6.1. It would also be possible to compute PM errors in a third, independent way, by multiplying the expected errors by the square root of the reduced χ^2 values, because all of these quantities are included in our PM catalogs.

To summarize, our rejection algorithm works as follows.

1. Preliminary rejection of obvious outliers;
2. Straight-line fitting to X and Y positions versus epoch;
3. Rescaling of normalized residuals to be consistent with a two-dimensional Gaussian distribution;
4. Checking whenever the outermost data point has $P[1/N] < Q$:
   (a) YES: reject the outermost data point, return to 2.
   (b) NO: continue.
5. Final straight-line fitting with the final set of acceptable data points to obtain the final straight-line-fit parameters and errors.

6. SIMULATIONS

In order to test the performance, accuracy, and reliability of our PM measurements, we carried out two types of simulations. The first simulation is based on a series of Monte Carlo tests that focus on our ability to reject outliers and obtain accurate values for the PMs and their errors. The second simulation tests our PM measurements in an artificial-star field representing a typical case, with GC stars and several field-star components, each of which has its own spatial density, bulk motion, and velocity dispersion.

6.1. Single-star Monte Carlo Simulations

Our Monte Carlo tests focus on the PM measurement of one single star, in cases where we have 10, 50, or 200 data points. For each case we run 100,000 random realizations in which data points span a time baseline of 5 yr. Two-thirds of the points are at t = 0, and the remaining are either randomly distributed or placed at the ends of the time baseline (±2.5 yr). Most of the data points have an assigned positional displacement that follows a Gaussian distribution with $\sigma = 0.01$ pixel. Five percent of the points are displaced with a dispersion 10 times larger, to mimic a population of outlier measurements, whereas an additional 5% of the points are misplaced by up to ±5 pixels, to mimic possible mismatches.

In each Monte Carlo run, individual observations were rejected based on the procedures described in Section 5.5, but the least-squares fits for the slope (the PM components μ_x and μ_y) and the intercepts (the positions at t = 0: $\overline{x}$ and $\overline{y}$) are computed with weights from the signal-to-noise-based error estimates from Section 5.2. The error estimates from each point are also used to compute errors in the motions and positions. For various reasons (cosmic rays, bad pixels, neighbors, and so on), individual observations can have errors that are larger than the

Table 2
Results of Monte Carlo Simulations[a]

Type	$\mathrm{err}_{\overline{x}}$	$\mathrm{err}_{\overline{y}}$	err_{μ_x}	err_{μ_y}
10 Data Points				
Monte Carlo rms	5.68	5.60	1.61	1.61
Average expected errors	5.09	5.13	1.46	1.47
Average residual-based	5.94	5.92	1.71	1.73
50 Data Points				
Monte Carlo rms	1.89	1.90	0.64	0.64
Average expected errors	1.87	1.86	0.63	0.63
Average residual-based	1.90	1.90	0.66	0.66
200 Data Points				
Monte Carlo rms	0.93	0.93	0.32	0.32
Average expected errors	0.92	0.92	0.32	0.32
Average residual-based	0.92	0.93	0.32	0.32

Notes.
[a] Units of 0.001 pixels for $\mathrm{err}_{\overline{x}}$ and $\mathrm{err}_{\overline{y}}$, and 0.001 pixel yr^{-1} for err_{μ_x} and err_{μ_y}.

expected errors, but not large enough to cause the observation to be rejected. To estimate the influence of these points on the errors in the measurements, we determine a residual for every point (using a fit to the four parameters that excludes that point) and adopt that residual as the estimate for the error in that determination. We then redetermine the errors in the slopes and intercepts using the same procedure as before. Because different observations have different effects on the slope and intercept determinations, this allows us to construct a more empirical estimate of the errors in the derived parameters.

Finally, for each of the three cases, we computed the Monte Carlo rms of the measured−true residual distribution for each of the derived quantities ($\mathrm{err}_{\overline{x}}$, $\mathrm{err}_{\overline{y}}$, err_{μ_x}, and err_{μ_y}) and compared them with the average of the two different error estimates. The results are shown in Table 2. In the case with 10 points, which resembles those data sets with few observations, the expected errors tend to underestimate the true errors, whereas the residual-based error estimates are more consistent with the true errors, although slightly larger. When more data points are available, both ways of computing the errors are in very good agreement with the Monte Carlo rms.

These results suggest that our fitting, rejection, and error-estimation algorithms are working well. Note that here we did not simulate the potential of small systematic errors (such as imperfect CTE corrections) in the bulk of the measurements. In reality, such errors will always be present at some level. The residual-based PM errors should therefore generally be more accurate than the PM errors based on assumed error estimates. The latter propagate only the random error in individual exposures and are unable to take into account small but present systematic errors.

6.2. Comprehensive Data Simulations

In order to test the automated procedure of converging on cluster-member-based PMs, the second simulation concerns the PM measurement and analysis of a field containing ∼19,000 simulated stars resembling cluster stars, field stars, and stars of two Milky Way satellite galaxies. Each star component has its own spatial density, proper motion, and velocity dispersion. We started by setting up the input master frame catalog, and then we extracted from it single-exposure catalogs simulating different exposure times, dithers, roll-angle orientations, cameras, and epochs.

6.2.1. The Input Master Frame

The spatial extension of the input master frame is 8000 × 8000 pixels and allows us to fully populate single-exposure catalogs with different dithers and roll-angle orientations. The CMD of cluster stars resembles that of a real cluster, but it was drawn by hand without aiming to be a reliable, physical representation of the real CMD of any actual GC. Panel (a) of Figure 5 shows the input CMD for cluster stars in instrumental magnitudes that for simplicity are called V and I. As for the real data sets, we run the simulation using instrumental-like magnitudes. All of the main evolutionary sequences are traced. We generated a total of 12,074 cluster stars, divided as follows: 9964 main-sequence (MS) stars (more numerous at increasing magnitudes), 350 subgiant branch (SGB) stars, 651 red giant branch (RGB) stars, 1,078 horizontal branch (HB) stars, and 31 white dwarf (WD) stars.

Cluster stars have a Gaussian-like distribution on the master frame (centered at position (5000, 5000)), to mimic the typical crowding conditions of the center of GCs. Moreover, their positional dispersion is larger at fainter magnitudes, to mimic some sort of mass segregation. The dispersion of MS stars grows from 344 to 600 pixels, while evolved stars have the same 344 pixel spatial dispersion as the bright MS stars.

The cluster's bulk motion is null by construction because all measured proper motions will be computed with respect to the bulk motion of the cluster. To resemble some sort of energy equipartition and test the quality of measured PM errors, we divided the MS into five groups and assigned to each of them an increasing velocity dispersion with fainter magnitudes. Velocity dispersions go from 0.01 pixel yr^{-1} for the brighter MS stars to 0.03 pixel yr^{-1} at the faint end. Evolved stars all have the same velocity dispersion as the bright MS stars. Panels (b1) to (b5) of Figure 5 show the vector point diagrams of cluster stars for the five different values of input velocity dispersion.

Because it is not uncommon to have Milky Way satellite stars superimposed on GC fields (e.g., Small Magellanic Cloud stars in NGC 104 and NGC 362, or Sagittarius dwarf spheroidal stars in NGC 6681 and NGC 6715), we included the presence of two such nearby galaxies. Panel (c) of Figure 5 shows their CMD. Galaxy stars are placed randomly with a flat distribution on the master frame. The brighter galaxy (GAL1) has 1126 stars and a bulk motion of (−0.12, −0.17) pixel yr^{-1}. We set its internal velocity dispersion to be small but still measurable: 5 milli-pixel yr^{-1}(i.e., 0.2 mas yr^{-1}). The faint galaxy (GAL2) has 685 stars and a bulk motion of (−0.25, 0.2) pixel yr^{-1}. We assigned no internal velocity dispersion to its stars: in this way we are able to obtain an external estimate of our measurement errors. Panel (e1) of Figure 5 shows the vector-point diagram of GAL1 stars; the black cross marks the location of the cluster's bulk motion. An arrow in panel (e2) points to the bulk motion of GAL2.

We generated three sets of field stars, named FS1 (1516 stars), FS2 (1273 stars), and FS3 (2057 stars). Each set has its own ridge line on the CMD (see panel (d) of Figure 5). Although cluster and galaxy stars do not have a color spread by construction (mimicking single-stellar populations), we introduced a Gaussian scatter ($\sigma \sim 0.5$ mag) to the color of field stars to resemble the fact that they are not at the same distance or do not have the same chemical composition.

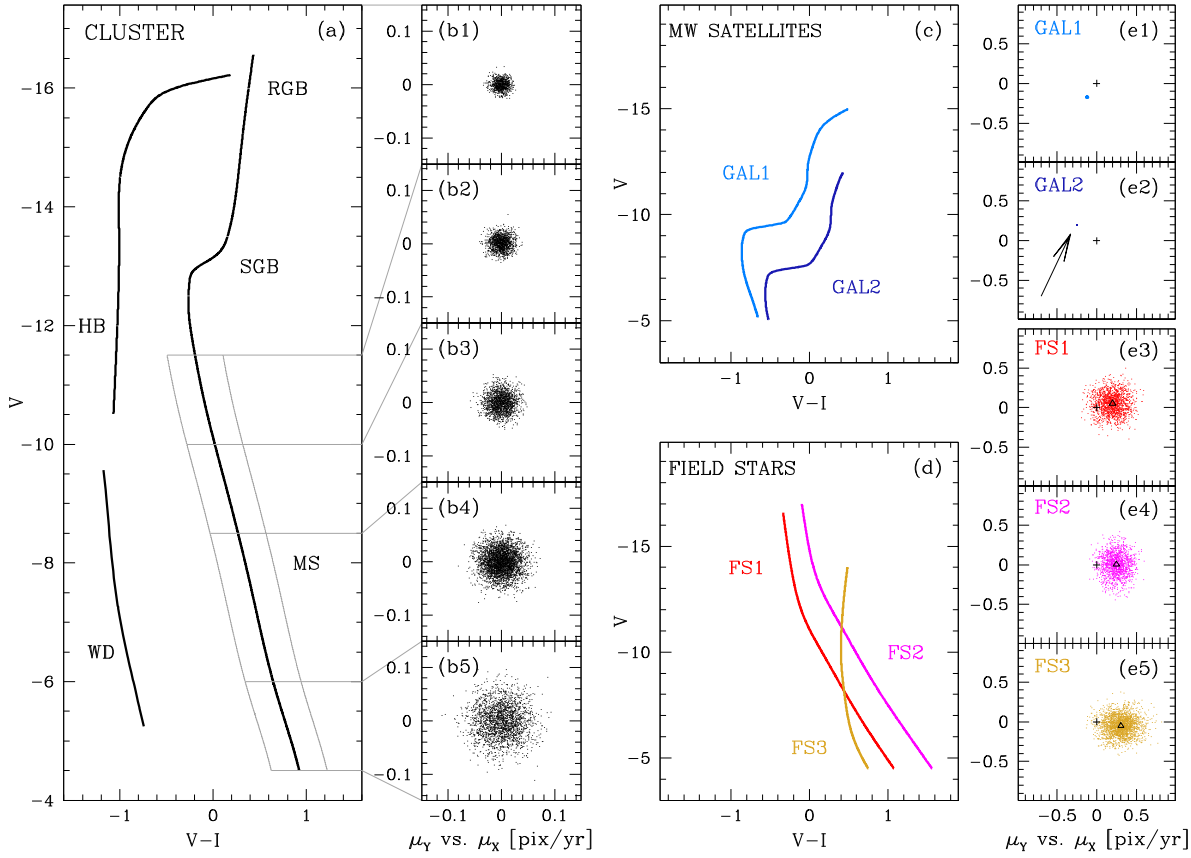

Figure 5. Color–magnitude and vector–point diagrams of the stars used for our comprehensive simulation. The CMD of cluster stars is in panel (a). All of the main evolutionary sequences have been included. We assigned to MS stars an increasing internal velocity dispersion at increasing magnitudes, to mimic some sort of energy equipartition. Panels (b2) to (b5) show the vector point diagrams of MS stars for four different values of the velocity dispersion. Bright MS stars and more evolved stars all have the same (smaller) velocity dispersion, as shown in panel (b1). We also simulated two Milky Way dwarf galaxies (GAL1 and GAL2, in azure and blue) and three components of field stars (FS1, FS2, and FS3 in red, magenta, and yellow, respectively). Their CMDs are in panel (c) and (d), respectively. We assigned a very small velocity dispersion (0.005 pixel yr^{-1}, 0.2 mas yr^{-1}) to GAL1 stars (panel (e1)) and no velocity dispersion at all to GAL2 stars (panel (e2)). Field stars have the largest velocity dispersion. We assigned a bulk motion (black triangle) to field stars in such a way that they partially overlap cluster stars in the vector point diagram (panels (e3), (e4), and (e5)).

(A color version of this figure is available in the online journal.)

The field FS1 has a bulk motion of (0.2, 0.05) pixel yr^{-1}, with a round velocity dispersion of 0.13 pixel yr^{-1}. The bulk motion of field FS2 is (0.25, 0.0) pixel yr^{-1}, with a X-velocity dispersion of 0.12 pixel yr^{-1} and a Y-velocity dispersion of 0.14 pixel yr^{-1}. For the field FS3, these three quantities are, respectively, (0.3, −0.05) pixel yr^{-1}, 0.14 pixel yr^{-1} and 0.12 pixel yr^{-1}. The vector point diagrams of field stars are shown in panels (e3), (e4), and (e5) of Figure 5). The bulk motion of each field component is marked by a triangle.

For clarity, Figure 6 shows the complete simulated vector-point diagram. Each component is color-coded as in Figure 5. The location of the bulk motion of GAL2 stars is highlighted by an open circle.

6.2.2. Single-exposure Catalogs

Now that the input master frame has been defined, we can extract single-exposure catalogs from it as follows. We set up five data sets spanning a total time baseline of 3.18 yr. Each epoch has its own orientation angle, offset (i.e., the center of the cluster is not always at the center of the pointing), dither pattern, magnitude zero point, and pixel scale (to simulate the three cameras (ACS/WFC, ACS/HRC, and WFC3/UVIS). In addition, we added small random variations to all of these quantities: up to 0.2% variation for orientation angle, scale (to mimic focus changes), and observing time (to mimic exposures taken within a few days), and up to ±40 pixels in either direction to resemble a dither pattern.

Table 3 lists the parameters adopted for each data set. The first two data sets mimic ACS/WFC exposures (and the second one is designed to be similar to GO-10775), the third refers to ACS/HRC exposures, and the WFC3/UVIS exposures are in data sets 4 and 5. The magnitude zero point Δmag listed in Table 3 is the difference in instrumental magnitude between input master stars and deep-exposure stars. Stars in the short exposures are 2.2 mag fainter than those in the deep ones. Offsets are in units of pixels in the raw-coordinate system of each catalog. We generated a total of 50 single-exposure catalogs.

Stars of each single-exposure catalog are selected from the input master frame according to their positional parameters (roll angle, scale, offsets), and a magnitude zero point is applied. The positions of the stars are then decorrected for geometric distortion and put into their raw-coordinate system.

Table 3
Simulated Single-exposure Catalog Parameters

Data Set	Δtime (yr)	Filter	Exposures	Δmag	Roll Angle	Scale (mas pixel^{-1})	X offset (pixel)	Y offset (pixel)
1	−1.78	*V*	5 long, 2 short	−0.1	130°	50	2100	1900
		I	5 long, 2 short	+0.1	−190°	50	2200	1800
2	0.0	*V*	5 long, 2 short	+0.05	20°	50	1900	2100
		I	5 long, 2 short	−0.5	85°	50	1800	2200
3	0.7	*V*	4 medium	+1.5	80°	28.27	500	500
		I	4 medium	+1.5	80°	28.27	500	500
4	+1.3	*I*	5 long, 2 short	−0.07	210°	40	2030	2020
5	+1.4	*V*	5 long, 2 short	+0.1	60°	40	2020	2030

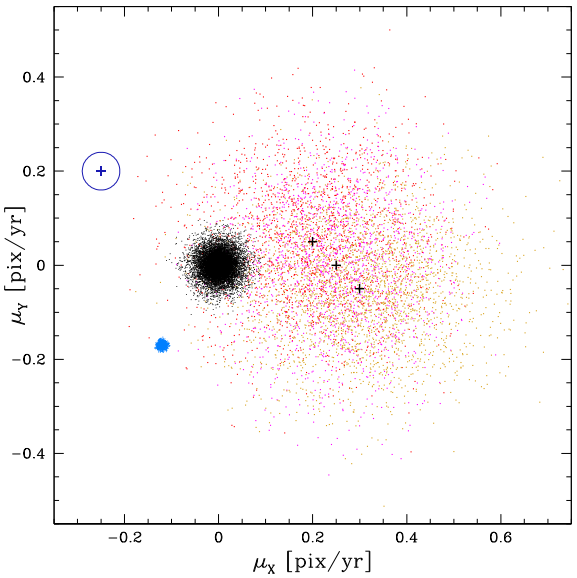

Figure 6. Vector point diagram of all of the population components of our comprehensive simulation, color-coded as in Figure 5. The GAL2 stars have zero PM dispersion, so they fall underneath the cross inside the blue circle. The means of the three field components are marked by black crosses.
(A color version of this figure is available in the online journal.)

Finally, to resemble positional uncertainties, an additional Gaussian-like shift in a random direction is added to each star's position (with a dispersion equal to its expected error; see Section 5.2). A similar method was used to introduce scatter in the magnitudes.

6.2.3. Results of the Full Simulation

We now have at our disposal single-exposure catalogs constructed as if they were the result of reduced images. We derived from them an output master frame using exposures of data set number 2 for positions and using all of the exposures for photometry. The recovered master frame is necessarily different from the input master frame: it contains uncertainties in the transformation parameters (because of the position shift added to each star related to its PM plus measurement error), and it has errors in the average position and errors in the magnitude of its stars. The recovered master frame CMD is shown on panel (a) of Figure 7. It contains only unsaturated stars. Stars measured in deep exposures have a magnitude value up to ∼−13.5, and brighter stars are measured only in short exposures.

Table 4
Measured Velocity Dispersions of Simulated GAL1 and GAL2 stars

Mag Range	GAL1 σ_μ (pixel yr^{-1})	GAL2 σ_μ (pixel yr^{-1})
(−12, −11)	0.0068	0.0029
(−11, −10)	0.0066	0.0034
(−10, −9)	0.0071	0.0048
(−9, −8)	0.0102	0.0062
(−8, −7)	0.0226	0.0087
(−7, −6)	0.0282	0.0252

The input master frame was not used beyond this. The recovered master frame was the one used to compute proper motions. For simplicity, hereafter we refer to the recovered master frame simply as the master frame.

Because of the different pointings and orientation of each data set, there will be master-frame stars present in some but not all of the exposures. As a consequence, the time baseline available for some stars will be shorter than 3.18 yr.

We treated our master frame as if it came from the official GO-10775 release and our simulated single-exposure catalogs as if they were the output of our reduction routines. We measured PMs in the exact same way that we do for real data sets. Panels (b1) to (b5) of Figure 7 show the recovered vector point diagrams for five different magnitude bins, highlighted by gray horizontal lines in panel (a), from the bright bin to the faint one, respectively.

As expected, the velocity dispersion of GAL1 stars is found to be larger than that of GAL2 stars (see, e.g., the different size of the GAL1 and GAL2 clouds of points in panels (b2) to (b5) of Figure 7). The one-dimensional velocity dispersion of GAL2 stars, i.e., the estimate of our internal errors, goes from ∼3 milli-pixel yr^{-1} at $V = -11.5$ to ∼25 milli-pixel yr^{-1} at $V = -6.5$. In the same magnitude interval, GAL1 stars have a measured velocity dispersion (i.e., without subtracting the error in quadrature) ranging from ∼7 milli-pixel yr^{-1} to ∼28 milli-pixel yr^{-1} and is systematically larger than that of GAL2 stars. Table 4 lists velocity–dispersion values for both galaxies in 6 mag ranges.

Panel (c) of Figure 7 illustrates the trend of PM errors as a function of the instrumental magnitude. We can distinguish two tails of errors at fainter magnitudes: a more-populated, smaller error trend, corresponding to stars with motions measured using the full 3.18 yr of time baseline, and a second, less-populated tail that corresponds to stars with a time baseline of 1.78 yr. Moreover, there is an increase in the PM errors for stars brighter than ∼−13.5 mag. These stars are measured only in the short

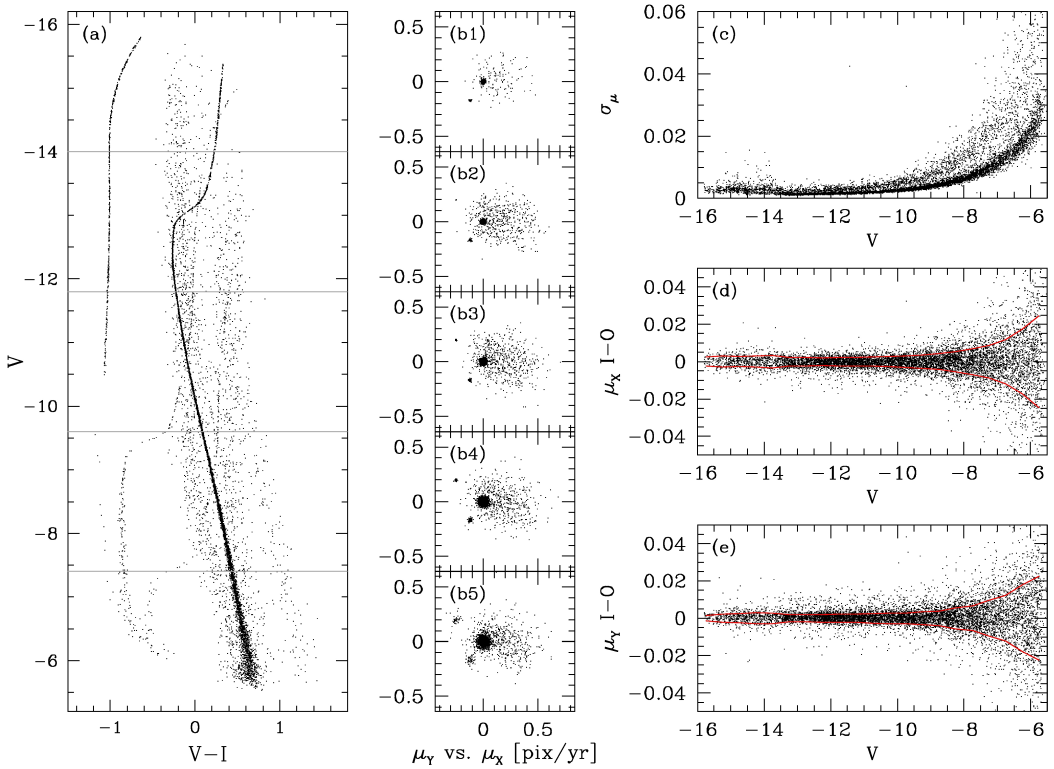

Figure 7. Results of our comprehensive data simulation. The recovered master-frame CMD is shown in panel (a). Proper motions are divided into 5 mag bins (gray horizontal lines) and displayed in panels (b1) to (b5), from the brighter to the fainter bin. Proper-motion errors as a function of the instrumental magnitude are shown in panel (c). The input−output difference of stellar PMs along the X and the Y axes, as a function of the instrumental magnitude, are shown in panels (d) and (e), respectively. Red lines in both panels mark the 68.27 percentile of the residuals around the median values.

(A color version of this figure is available in the online journal.)

exposures (eight out of 50), and therefore their PMs are less well constrained.

Panels (d) and (e) show the difference (defined as input−output, I−O) of each component of the motion. Red lines mark the ±68.27 percentile (rms) of the I–O values around the median values. These two plots provide another way to estimate the internal errors of our procedure. For the particular simulation we set up, the μ_X I−O rms is about 0.0032 pixel yr^{-1} (0.13 mas yr^{-1}) for the short-exposure regime, and it goes from 0.0022 pixel yr^{-1} (0.09 mas yr^{-1}) at $V = -13$ to 0.0024 pixel yr^{-1} (0.10 mas yr^{-1}) at $V = -10$ to 0.006 pixel yr^{-1} (0.24 mas yr^{-1}) at $V = -8$, reaching 0.02 pixel yr^{-1} (0.8 mas pixel^{-1}) at $V = -6$. The rms of μ_Y I−O has a similar behavior. These values are consistent with the velocity dispersion of GAL2 stars.

The comparison of input and output PMs shows that our PM measurement algorithms are highly reliable. There are astrophysical applications for which accurate error estimates are crucial. For instance, when we want to measure the intrinsic velocity dispersion of cluster stars, we have to subtract in quadrature the PM measurement errors from the observed dispersion. When the errors contribute a large fraction of the observed dispersion, a small over- or underestimate of the errors leads to biased results.

To test this, we compute the intrinsic velocity dispersion of cluster stars from the PM catalog (as done in van der Marel & Anderson 2010) and check whether it is in agreement with the input values. The top panel of Figure 8 shows the inferred velocity dispersions (in black, with error bars) as a function of the instrumental magnitude (0.4 mas yr^{-1} corresponds to 0.01 pixel yr^{-1}on the master frame). The real (input) velocity dispersion of cluster stars is represented by red open circles. The agreement between input and output velocity dispersions (bottom panel) shows an absence of clear systematic residuals, meaning that our quoted PM errors are accurate and reliable.

There is perhaps a marginal discrepancy (at the 1.2σ level) at the faint-end magnitude limit, where it seems that the PM errors have been slightly overestimated, with the result that the inferred velocity dispersion is lower than the input one. However, this should not come as a surprise. The input velocity dispersion of faint GC stars is 0.03 pixel yr^{-1}, and their measured PM error is almost as large (∼0.025 pixel yr^{-1}; see panel (c) of Figure 7). One should always be careful in trusting results that come from the quadrature difference of quantities of similar size, especially when one of the quantities is an error estimate. The fact that, even at the faint limit of our simulated measurements, input and output velocity dispersions are still quite consistent (at the 1.2σ level) is a further validation of our methodology.

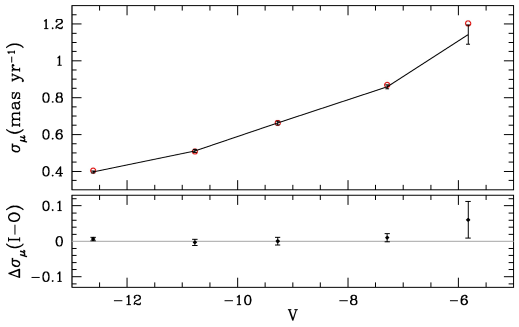

Figure 8. Top panel shows the input (red open circles) and inferred (black with error bars) velocity dispersion of cluster stars in our comprehensive simulation, as a function of the instrumental magnitude. The bottom panel shows the residuals between the input and the output values.

(A color version of this figure is available in the online journal.)

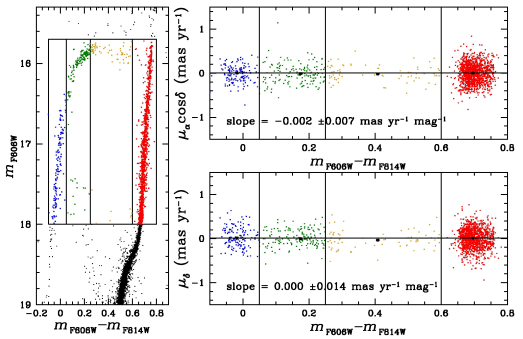

Figure 9. Left panel shows the CMD of NGC 7078 around the HB and RGB regions and the stars used to investigate the presence of chromatic-induced systematic effects. The right panels show the $\mu_\alpha \cos\delta$ and μ_δ components of the motion of selected stars as a function of the star colors (top and bottom panels, respectively). We divided and color-coded the selected stars into four groups according to their color, for clarity. We computed median motion and error for each group of stars and fitted two lines to the median points (the size of the errors are comparable to, or smaller than, the median points). The slopes of the fitted lines, consistent with zero, imply no chromatic-induced systematic errors in our measurements.

(A color version of this figure is available in the online journal.)

7. MITIGATING SOURCES OF SYSTEMATIC ERROR

In the previous section, we demonstrated that our PM-measurement algorithms are reliable when random errors and mild systematic effects are taken into account. Unfortunately, unaccounted for systematic sources of error may also be present in real data. In this section, we describe the methods we have adopted to mitigate their effects on our PM measurements.

In what follows, we will describe as an example the case of NGC 7078 (M 15). This is the cluster for which we will present the PM analysis and catalog in Section 8. NGC 7078 is a typical case among the 22 clusters in our study, in the sense that it has an average time baseline and an average number of data sets.

7.1. Chromatic Effects

A systematic effect that is always present in ground-based PM measurements is the so-called differential-chromatic refraction (DCR; see, e.g., Anderson et al. 2006; Bellini et al. 2009). The DCR effect shifts the photon positions on the CCD, and the displacement is proportional to the photon wavelength and to the zenithal distance of the observations. Space-based telescopes are obviously immune to DCR effects. Nonetheless, as anticipated in Section 3.3, we found a chromatic-dependent shift of blue and red stellar positions when UV filters are used with the WFC3/UVIS camera (Bellini et al. 2011), and for this reason we decided not to include observations taken with filters bluer than 330 nm.

A way to check whether or not our PM measurements are nonetheless affected by some chromatic-induced systematic effects is to analyze the behavior of the single components of the stellar motions as a function of the star colors. The left panel of Figure 9 shows the CMD of NGC 7078 around the HB and RGB regions. We selected stars in the magnitude range $15.7 < m_{F606W} < 18$, in order to cover the largest available color baseline, and divided them into four color bins (blue, green, yellow, and red in the figure). The $\mu_\alpha \cos\delta$ component of their motions is shown in the top right panel, as a function of the star colors. We determined the median color and motion, with error, for each of the four groups of stars (black full squares). The same plot for the μ_δ component of the stellar motions is shown in the bottom right panel.

The median motions in each of the two right-hand panels are fitted with a weighted straight line (in black). Because we are using cluster members for the test, in principle the fitted lines should have no slope. On the other hand, slopes that significantly differ from zero would immediately reveal the possible presence of chromatic-induced sytematic effects. The computed slopes and errors are -0.002 ± 0.007 mas yr^{-1} mag^{-1} for $\mu_\alpha \cos\delta$ and 0.000 ± 0.014 mas yr^{-1} mag^{-1} for μ_δ. These values are consistent with zero well within their errors, and therefore we can rule out any presence of chromatic-induced systematic effects in our PMs.

7.2. CTE Effects

One problem not addressed by our simulations is that the GO-10775 master frame that was used for the real data is not really astrometrically flat. At the time the GO-10775 catalogs were released to the public, the pixel-based CTE correction for the ACS/WFC was not yet available. The stellar positions in the catalog thus suffer from this systematic error. As a result, single-exposure star positions transformed onto the master frame are affected by a systematic shift in position that is a function of both the location of the stars on the master frame and of their master-frame magnitude.

Our PM measurement algorithms produce as output the predicted position $(\overline{x}, \overline{y})$ of each star at the epoch of the master frame ($t = 0$), obtained as the intercept values of the least-squares fits versus time. This predicted position is based on a large number of (CTE-corrected) exposures, and not just those from GO-10775, and thus the new master frame should provide a better estimate of the true star position at $t = 0$. A comparison between the GO-10775 master-frame positions and the PM-based predicted positions $(\overline{x}, \overline{y})$ should therefore reveal the signature of uncorrected CTE effects in the GO-10775 master-catalog positions.

Panel (a) of Figure 10 shows the CMD of NGC 7078 for all of the stars in our PM catalog. We divided the CMD into 4 mag regions, from the brighter to the fainter, labeled R1 to R4. For each star in each magnitude region, we computed the 3σ clipped averaged difference (ΔX, ΔY) (in pixels) between the

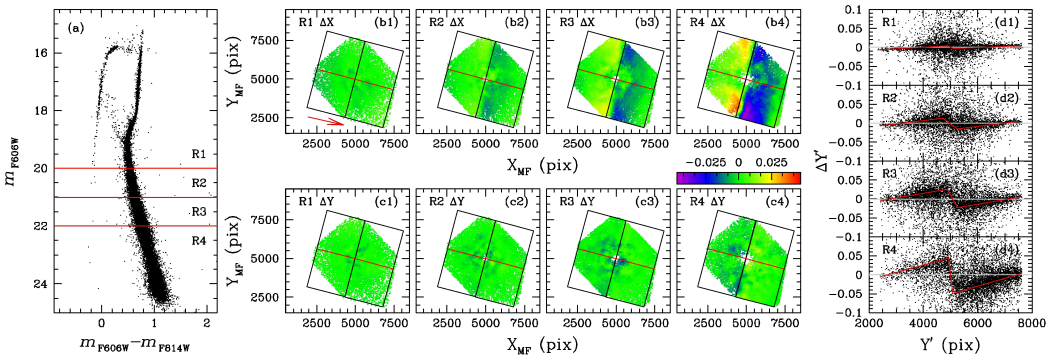

Figure 10. Effect of uncorrected CTE effects on the GO-10775 NGC 7078 master frame. Panel (a) shows the m_{F606W} vs. $m_{F606W} - m_{F814W}$ CMD. We divided the stars into 4 mag regions, labeled R1, R2, R3, and R4. For each region, we computed the locally averaged difference between the GO-10775 master-frame X and Y positions and those predicted by our PM fits at the epoch of the master frame. Panels (b1) to (b4) illustrate these differences for the X positions (ΔX) as a function of the stellar location on the master frame, for the magnitude regions R1 to R4. Panels (c1) to (c4) similarly show the differences in position along the Y axis (ΔY). Points are color-coded according to the size of the differences. A footprint of the typical location of the GO-10775 ACS/WFC chip placements is also shown in black, with individual amplifiers separated by a red line. A strong correlation between the pattern of position differences and the chip layout is evident. Panels (d1) to (d4) illustrate the position differences on a rotated reference system, such that the rotated Y′ axis is parallel to the raw Y direction of the GO-10775 exposures. The averaged ΔY′ residuals are highlighted by a red line. The fact that these residuals are strongly correlated with Y′ and increase at fainter magnitudes is a clear signature of unaccounted-for CTE losses.

(A color version of this figure is available in the online journal.)

master-frame and the PM-predicted positions, locally averaged over its surrounding 200 stars. Panels (b1) to (b4) show the map of the ΔX residuals for the magnitude regions R1 to R4, respectively. Panels (c1) to (c4) show the same for the ΔY residuals. Stars are colored according to the size of the residuals, following the color-coded bar on top of panel (c4). In each of these middle panels, we overplotted the typical GO-10775 layout, in which ACS/WFC single chips are drawn in black, and their amplifier subdivision is in red.

It is clear from panels (b) and (c) of Figure 10 that the pattern of residuals correlates with position on the master frame in the manner expected for a master frame not corrected for CTE losses.

CTE losses occur along the Y-axis direction of the raw GO-10775 exposures, highlighted by a red arrow in panel (b1). By rotating the master frame in such a way that its rotated Y axis Y′ is parallel to the raw Y axis of GO-10775, the position residuals ΔY′ directly reveal the impact of CTE losses. Panels (d1) to (d4) of Figure 10 show the ΔY′ residuals as a function of the Y′ position for the 4 mag regions. The red line in each panel indicates the average residual trend. The results are remarkably similar to, e.g., Figure 15 of Anderson & Bedin (2010) and leave no doubt that the source of the systematic error is CTE losses.

To mitigate the effect of uncorrected CTE losses on the master-frame positions, we remeasured all stellar PMs using the $(\overline{x}, \overline{y})$ values as the new master-frame positions. Figure 11 shows the ΔY′ residuals (not binned in magnitude) as a function of the Y′ positions, obtained by using the original GO-10775 master frame (in black) and the improved master frame (in red). This figure clearly shows that our procedure successfully eliminates most of the impact of uncorrected CTE losses in the GO-10775 master-frame positions. We therefore used this procedure for all final PM calculations.

7.3. Other Residual Systematics

Even in the ideal case of a systematics-free master frame, imperfectly corrected geometric distortion and CTE residuals

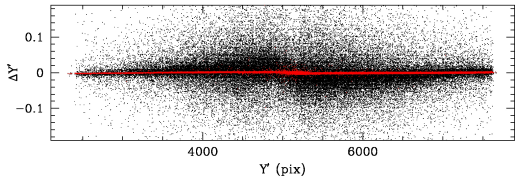

Figure 11. Rotated ΔY′ position offsets as a function of the Y′ position using the original GO-10775 positions as the master frame (black, same as panel (d) of Figure 10, but not binned in magnitude) and using the PM-predicted positions at $t = 0$ (red). The latter are used for all of our final PM catalogs.

(A color version of this figure is available in the online journal.)

are always to be expected in our single-exposure star positions. Depending on how a given data set is oriented and dithered with respect to the master frame, these uncorrected residuals may affect the measured PMs.

To assess the extent of any remaining systematic effects in our catalogs, we considered two-dimensional maps of the mean PM of cluster stars. To the lowest order, no mean PM is expected. In the radial direction, any contraction or expansion due to core collapse or gravothermal oscillations is too slow to induce measurable PMs. The same is true for any apparent contraction or expansion due to a cluster's line-of-sight motion away from or toward us. In the azimuthal direction, there may, in principle, be nonzero mean PMs due to cluster rotation. However, clusters are generally close to spherical, so any rotation is expected to be small. Moreover, our calibration procedure, using six-parameter linear transformations to align frames, removes any inherent solid-body rotation component from the mean PM field (see discussion in van der Marel & Anderson 2010). Therefore, the only mean PM components that may in principle be present in our PM catalogs are small differential-rotation components. Such components should be azimuthally aligned with a well-defined symmetry around the cluster center. Any other mean

Table 5
Amplifier-based, Local Average PM Statistical Quantities

Unit	Minimum	Median	Maximum	Semi-inter.
		$\mu_\alpha \cos\delta$		
pixel yr^{-1}	−0.0049	0.0003	0.0079	0.0011
mas yr^{-1}	−0.2017	0.0119	0.3143	0.0444
km s^{-1}	−9.9487	0.5867	15.495	2.1914
km s^{-1}/$\sigma_{V_{\rm LOS}}$	−0.7368	0.0405	1.1478	0.1623
		μ_δ		
pixel yr^{-1}	−0.0042	0.0003	0.0049	0.0008
mas yr^{-1}	−0.1737	0.0111	0.1948	0.0322
km s^{-1}	−8.5683	0.5472	9.6037	1.5875
km s^{-1}/$\sigma_{V_{\rm LOS}}$	−0.6346	0.0405	0.7114	0.1176

Table 6
Locally Corrected, Local Average PM Statistical Quantities

Unit	Minimum	Median	Maximum	Semi-inter.
		$\mu_\alpha \cos\delta$		
pixel yr^{-1}	−0.0024	0.0000	0.0028	0.0004
mas yr^{-1}	−0.0992	0.0007	0.1100	0.0149
km s^{-1}	−4.8954	0.0345	5.4230	0.7345
km s^{-1}/$\sigma_{V_{\rm LOS}}$	−0.3625	0.0026	0.4017	0.0544
		μ_δ		
pixel yr^{-1}	−0.0026	0.0000	0.0027	0.0004
mas yr^{-1}	−0.1063	0.0010	0.1063	0.0151
km s^{-1}	−5.2454	0.0493	5.2406	0.7444
km s^{-1}/$\sigma_{V_{\rm LOS}}$	−0.3885	0.0037	0.3882	0.0551

PM component inherent in our catalogs is therefore a likely indication of residual systematic errors.

We constructed a two-dimensional (2D) map for each component of the average motion by color-coding each star in our NGC 7078 PM catalog according to the average motion of its surrounding 200 stars. We used 3σ clipping to remove any influence from noncluster members. The top panels of Figure 12 show the so-derived 2D maps for the X (left) and the Y (right) components of the motion. The color scale is shown in the top-right panel of the figure, in units of pixel yr^{-1}. The panels reveal the presence of systematic errors. Transitions between lower and higher average PM values happen in proximity to the detector or amplifier edges of the adopted data sets, namely: GO-10401, GO-10775, GO-11233, and GO-12605 (see Table 27 for the full list of exposures we used). To quantify the size of these systematic trends, we computed for each component of the locally averaged motion the minimum, median, maximum, and semi-interquartile values in four different PM units: mas yr^{-1}, pixel yr^{-1}, km s^{-1} and km s^{-1}/$\sigma_{V_{\rm LOS}}$, where $\sigma_{V_{\rm LOS}}$ is from Table 1. Table 5 collects these values.

In an absolute sense, the systematic trends are generally very small. In fact, 50% of the stars in our catalog have locally averaged PMs smaller than 0.0011 and 0.0004 pixel yr^{-1} for the X and the Y components, respectively. As a reference, we recall that we can measure the position of bright, unsaturated stars in each exposure with an average precision of ∼0.01 pixel. Nevertheless, there are locations on the master frame where the systematic trends are as large as ∼0.008 pixel yr^{-1}. The available time baseline for these locations is about 5.5 yr, giving a total displacement of more than 0.04 pixels.

These systematic trends have the potential to significantly affect specific scientific studies. Even though the systematic trends are typically only as large as ∼15% of the quoted velocity dispersion $\sigma_{V_{\rm LOS}}$ (at least for NGC 7078), there are locations on the master frame where the systematic effects are even larger than $\sigma_{V_{\rm LOS}}$, so this may affect dynamical studies of the spatially dependent kinematics. In contrast, other scientific studies, e.g., those focusing on differences in kinematics between different subpopulations of the cluster, won't be affected by these systematic trends. The PM of stars of different populations will be locally biased in the same way.

The user of the catalogs can decide to simply not include stars in any high-mean PM regions in the analysis, but it can be tricky to carefully choose which stars are good and which stars are not. The choice depends on the specific scientific needs. In order to make our PM catalogs useful for a wide range of scientific investigations, the PMs in our catalogs are offered in two ways: the amplifier-based PM measurements discussed so far, and the locally corrected PM measurements obtained as described in the following section.

7.4. Local Corrections

Local PM corrections can be obtained in two ways: (1) a priori, by using a local sample of reference stars to compute the linear transformations from each single-exposure catalog onto the master frame (the so-called local-transformation approach; see, e.g., Anderson et al. 2006; Bellini et al. 2009); or (2) a posteriori, by locally correcting the PM of each star by the net motion of its surrounding neighbors. Our adopted local PM correction is of the latter kind.

Surrounding neighbors are chosen as follows. For each star in the PM catalog, we identify surrounding cluster stars within 600 pixels and within ± 0.5 $m_{\rm F606W}$ magnitudes from the target star (to mitigate the effect of both uncorrected geometric distortion and uncorrected CTE residuals). Then, we compute the 3.5σ clipped median value of each component of the motion for these neighbors: $\overline{\mu_\alpha \cos\delta}$ and $\overline{\mu_\delta}$. We correct the motion of the target star by subtracting these values. If there are less than 50 neighbor stars, no correction is applied. If there are more than 150 neighbor stars, we compute $\overline{\mu_\alpha \cos\delta}$ and $\overline{\mu_\delta}$ values using only the closest 150 stars.

Panels (c) and (d) of Figure 12 show the locally averaged PMs after our local correction is applied. Points are color-coded in the same way as for the amplifier-based average motions. As expected, all systematic spatial PM trends have been removed. Table 6 collects the same statistical quantities as Table 5, but now for the local-corrected PMs. The improvement offered by the local correction with respect to the amplifier-based PMs is evident in all values listed in Table 6.

Because uncorrected CTE residuals are a function of both stellar positions and magnitudes, a further proof that our local corrections are able to properly remove any systematic-error residual would be the absence of trends in the PM versus magnitude plane. The two panels of Figure 13 show each component of the locally corrected PMs as a function of the stellar magnitude. We computed 3.5σ clipped median motions and errors binning every 0.5 mag (red points; error bars are comparable to, or smaller than, the median points). Rejected points are marked with gray crosses. The red horizontal lines indicate the absence of any systematic trend and are not a fit to the points, which all lie on the lines well within their errors.

It is clear from Figures 12 and 13 that locally corrected proper motions successfully correct any spatially and magnitude-dependent systematic trends. However, users should carefully

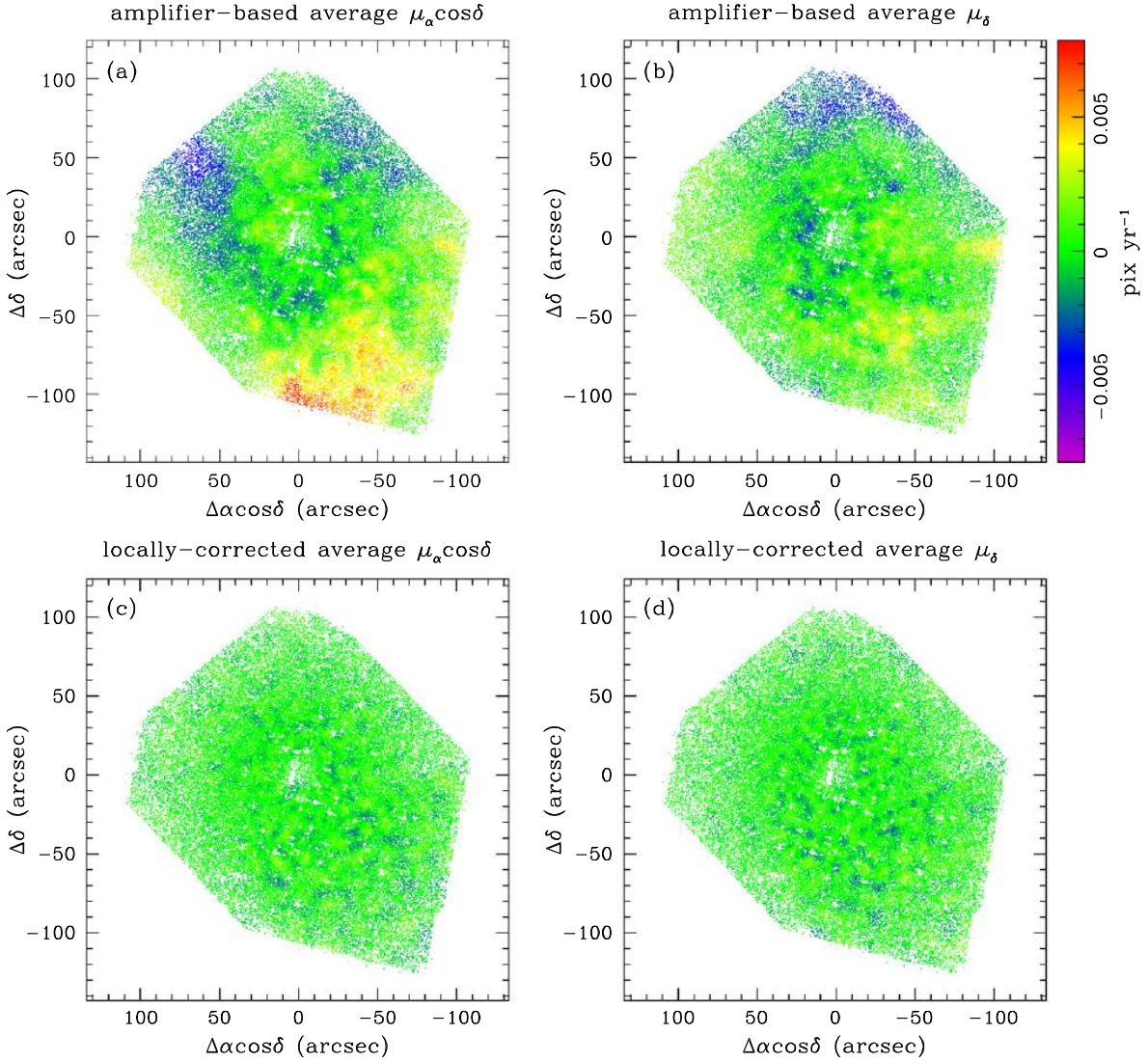

Figure 12. Top panels show two-dimensional maps of the locally averaged $\mu_\alpha \cos\delta$ (a) and μ_δ (b) components of the PM, as a function of positions with respect to the cluster center (in units of arcsec). Stars are color-coded according to their locally averaged PM, according to the color bar on the top right. Bottom panels show the same after we applied our local correction described in Section 7.4.

(A color version of this figure is available in the online journal.)

consider whether it is best to use the amplifier-based PMs or the locally corrected PMs. The latter have fewer systematics, so they may be best for studies of, e.g., cluster velocity dispersion profiles. However, locally corrected PMs have any intrinsic mean motion removed by brute force. Therefore, they are not suitable for studies of, e.g., cluster rotation.

7.5. Selections Based on Data-quality Parameters

In the previous sections, we discussed systematic effects that affect all of our PM catalogs. Other sources of systematic errors, e.g., those caused by crowding, affect some clusters more than others. Moreover, such systematics are relevant to only some of the scientific investigations listed in the Introduction (e.g., internal motions). As part of the PM analysis, we derive several data quality parameters that are reported in our catalogs. These parameters can serve as diagnostics to determine which stars to include or exclude from a particular analysis, depending on the specific scientific needs.

We do not include in our catalogs stars with obvious neighbors (see Section 4). Nonetheless, some stars in our catalogs will be affected by (faint) neighbors, even when not explicitly recognized as such. The resulting crowding-induced systematic effects are among the most subtle sources of error. In clusters with a very dense core, the measured position of sources with neighbors is shifted away from its true position. This causes a systematic PM error if the shift is not the same at different epochs. This can happen if the sources have a high relative motion or if the sources are observed with different filters at

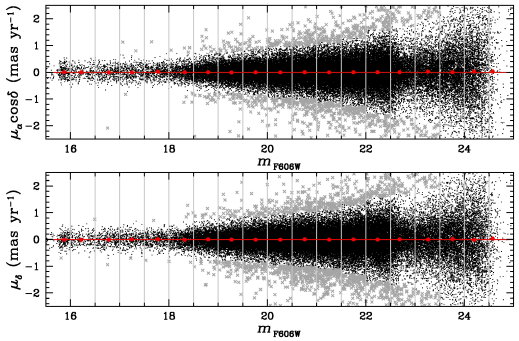

Figure 13. PM components as a function of the $m_{\rm F606W}$ magnitude: $\mu_\alpha \cos\delta$ (top) and μ_δ (bottom). Motions are divided into magnitude bins, and their 3.5σ clipped medians are shown in red, for each bin. The sizes of the median errors are comparable to, or even smaller than, the median points. Rejected points are marked with gray crosses. The red horizontal line shows the absence of any magnitude trend and is not a fit to the points.

(A color version of this figure is available in the online journal.)

different epochs. To illustrate the latter case, consider the case of two close sources: a red and a blue star. When observed through a red filter, the apparent shift induced by one star on the position of the other is different than when observed through a blue filter. If we have only two epochs of observations, one based on red and one based on blue exposures, then this will induce systematic PM errors. The situation is obviously worse the closer the stars are (and especially when dealing with complete blends) or when there are multiple close neighbors of different colors.

The QFIT parameter included in the GO-10775 catalogs (which is also replicated in our PM catalogs) is an important diagnostic to assess crowding effects. This parameter quantifies how well a source has been fit with the PSF model. This, in turn, correlates with the amount of light contamination from neighbor stars that fell within the region over which the stellar profile was fitted. Lower QFIT values correspond to more isolated, less systematicly affected stars.

Another parameter that helps in assessing crowding effects on the PM measurements is the reduced χ^2. For position measurements with only Gaussian random errors, the least-squares linear fits, we used to measure PMs should generate $\chi^2 \approx N$, where N is the number of degrees of freedom. Hence, it should result in a reduced $\chi^2 \approx 1$. Instead, when the position measurements also contain systematic errors, the reduced χ^2 tends to be larger. Rejecting stars with large QFIT or large reduced χ^2 values therefore helps to minimize the effect of crowding-induced systematics on the PM catalog.

A third diagnostic worth mentioning is N_R, defined as the ratio $N_{\rm used}/N_{\rm found}$. Here, $N_{\rm found}$ is the total number of data points initially available for the PM straight-line fits, and $N_{\rm used}$ is the final number of data points actually used after the one-point-at-a-time rejection algorithm (see Section 5.5). If N_R is low, then a high fraction of data points are rejected in the PM fit of a given star, and one should be suspicious about the quality of the resulting PM measurement.

As a practical example, let us again consider NGC 7078. Because this is a post-core-collapse cluster, its level of crowding is very high even at *HST* resolution. Therefore, crowding- or blending-driven systematics are expected to play an important role. When two stars on the MS are blended, their blended sum typically shows up as a source on the red side of the MS (this is because the fainter star that perturbsthe brighter star is redder, owing to the MS slope in the CMD). So to look for a possible signature of systematic PM errors, we studied in NGC 7078 the dependence of the PM kinematics as a function of color within a given magnitude range.

We selected NGC 7078 stars along the MS in the magnitude interval $19 < m_{\rm F814W} < 21$ (panel (a) of Figure 14). We drew by hand two fiducial lines on the blue and on the red side of the MS (in red in the panel) and used them to rectifythe MS so that the blue-side and red-side fiducials have a Δ^N color of zero and one, respectively, on the rectified plane (panel b). We then defined three subsamples of stars: the blue MS (bMS, in blue), the red MS (rMS, in red), and a sample containing very red objects (vrO, in green). The vrO sample should contain mostly blends because the binary fraction of NGC 7078 is less than 4% (Milone et al. 2012) and the photometry is corrected for differential reddening. The velocity–dispersion profiles for the three PM subsamples (determined as described in Section 8.3 below) are shown as a function of the radial distance in panel (c).

It is evident that the velocity dispersion is systematically higher for redder stars. This can be explained by assuming that

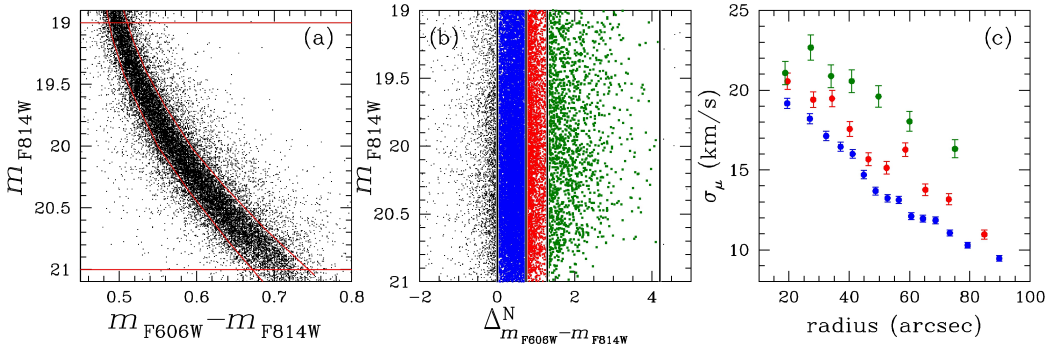

Figure 14. Panel (a): the upper MS of NGC 7078. Stars in the magnitude range $19 < m_{\rm F814W} < 21$ (horizontal red lines) are selected for measurement of the velocity dispersion. The two red lines along the MS are used for the rectification of MS stars shown in panel (b), where we define three samples of stars according to their color: bMS (blue), rMS (red), and very red objects (vrO, in green). The radial velocity–dispersion profile of the three components is shown in panel (c), where we can see the effects of crowding or blending on σ_μ, as described in the text.

(A color version of this figure is available in the online journal.)

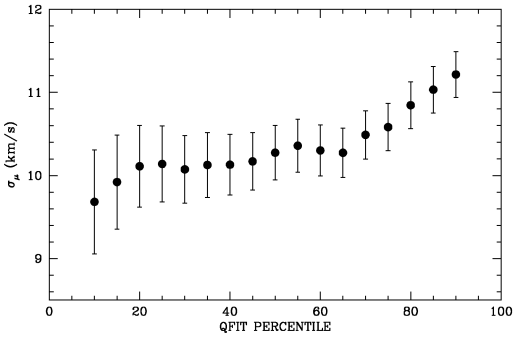

Figure 15. Sensitivity of the inferred velocity dispersion of NGC 7078 stars with similar kinematic properties to different QFIT selection cuts on the PM catalog. NGC 7078 is the prototype of high-central-density clusters with unbalanced filters in the different epochs, for which use of appropriate cuts based on data quality parameters is important.

the redder stars are affected by blending and that this blending induces a systematic component of PM scatter that is observed in addition to the actual random motions of the stars in the cluster. To test this hypothesis, one can repeat the analysis using only stars with smaller values of QFIT and reduced χ^2 and higher N_R. One would expect this to reduce the difference in velocity dispersion between the bMS, rMS, and vrO stars.

Choosing the optimal cuts for the QFIT, reduced χ^2, and N_R selections is a delicate issue. In principle, one can use an iterative approach in which one gradually rejects stars using increasingly stringent cuts and then measures the velocity dispersion for each progressive cut. Convergence in the measured velocity dispersions might occur if at some cut level all blended sources have been removed from the sample. In practice, though, the selections (especially those based on QFIT and reduced χ^2) preferentially remove fainter stars close to the cluster center, and these stars have intrinsically a higher velocity dispersion than other stars because of hydrostatic equilibrium and energy equipartition. This means that every time a sharper cut is applied to the sample, a counteracting bias is also applied to the surviving sample of stars. Hence, there may be no convergence in the inferred velocity dispersions as stronger cuts are applied.

For these reasons, the best way to choose cuts without introducing excessive selection biases is to select stars of similar luminosity (e.g., mass) and distance from the cluster center. As an example, we selected NGC 7078 stars in an annulus between 60 and 70 arcsec from the cluster center and between $m_{\rm F606W} = 20.3$ and 20.6 (about 1 mag below the turnoff).[18] We chose fixed cuts for the reduced χ^2 (<1.25) and N_R (>0.85) and applied various QFIT cuts to show how this affects the measured velocity dispersion. The initial total number of selected stars is 510. We measured the stellar velocity dispersion σ_μ by keeping the best 90, 85, 80, ..., 10 percentile of the QFIT values in both the $m_{\rm F606W}$ and $m_{\rm F814W}$ magnitudes.

Figure 15 shows the velocity dispersions thus derived for different QFIT cuts. Stars with high QFIT values are those with a higher chance of being affected by crowding or blending effects. As expected, going from right to left in the figure, more stringent QFIT cuts produce a smaller velocity dispersion for the surviving sample. Below the 65th percentile, the velocity dispersions converge and stay constant to within the errors. From this we infer that a 65th percentile cut is able to remove most of the blended objects from the sample. The small decrease of σ_μ as a function of the QFIT below the 65th percentile is likely due to the fact that even in the small magnitude and radial range under consideration, progressively stronger cuts induce a kinematic bias in the surviving sample, as described above.

Based on these considerations, we reanalyzed the bMS, rMS, and vrO samples of NGC 7078 as in Figure 14, but now including only stars that have $\chi^2 < 1.25$ and $N_R > 0.85$ and survive a 50th percentile QFIT cut. The results are shown in Figure 16. The velocity dispersions of the three MS components are now comparable. This supports the hypothesis that the kinematic differences evident in Figure 14(c) were entirely due to blending-induced PM systematics. It also supports the notion that the cuts applied here are necessary and sufficient for this particular PM catalog. It should be noted that even for the bMS stars, for which the observed color provides no indication of blending, the velocity dispersion drops significantly after application of the cuts. Therefore, for dynamical studies of clusters such as NGC 7078, it is critical to use the data quality parameters provided in our catalogs to compose an optimal sample. This is due to the combination of several effects,

[18] If we were to use stars that are fainter or closer to the center, then low-number statistics would have become a problem.

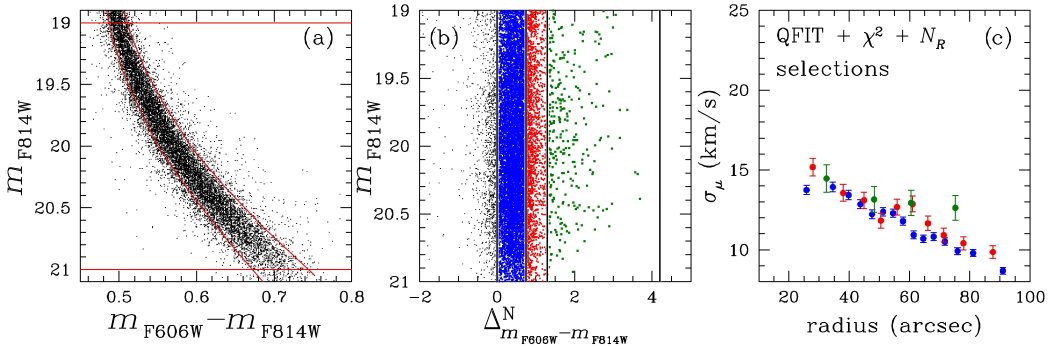

Figure 16. Similar to Figure 14, but for the subset of NGC 7078 catalog stars with high-quality PMs. There is now no disagreement between the velocity dispersions of the three MS samples in panel (c), and the σ_μ values are reduced across the board compared to Figure 14.

(A color version of this figure is available in the online journal.)

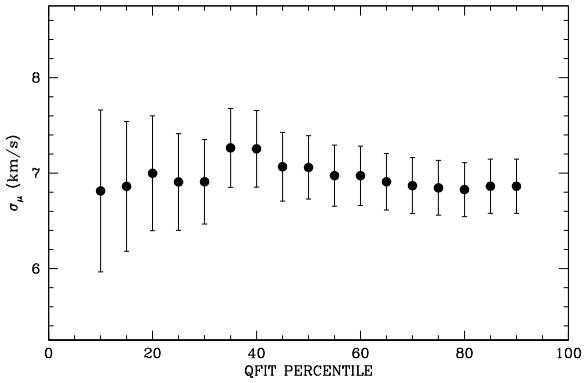

Figure 17. Similar to Figure 15, but for NGC 6752, a closer and less massive cluster and with a more homogeneous filter or epoch coverage than NGC 7078. In this case, cuts based on data quality parameters do not significantly affect the inferred velocity dispersion.

including the fact that NGC 7078 is post-core-collapse, the fact that it is relatively distant, the fact that we only have a few epochs of data for this cluster, and the fact that the data at different epochs were taken in different filters. Faint stars and stars at small radii are the most sensitive to these effects because they tend to be most affected by crowding.

Other less-crowded clusters, or clusters for which a large number of exposures are available (even when taken through a variety of different filters), are far less affected by crowding- or blending-induced PM systematics. As an example, we repeated the same selection test shown in Figure 15 on the PM catalog of NGC 6752. This cluster has nearly 300 exposures of its core taken with nine different filters spanning from F390W to F814W (see Table 25), and it is much closer than NGC 7078 (4.0 kpc instead of 10.4). The test was performed on MS stars with magnitudes $18.3 < m_{\rm F606W} < 18.6$ (about 1 mag below the turnoff) and between 50 and 60 arcsec from the cluster center. Figure 17 shows the results of this second test. In this case, the measured velocity dispersions all agree within the uncertainties, regardless of the applied `QFIT` cut.

7.6. Caveats

In Section 6, we showed that the techniques we developed to measure high-precision PMs with the *HST* are highly reliable, and our PM errors are a very good representation of the true errors. In this section, we showed that we are able to identify and correct systematic errors introduced by the use of nonoptimal master frames (Section 7.2), by uncorrected geometric distortion and uncorrected CTE residuals in the single-exposure catalogs (Sections 7.3 and Section 7.4), and by crowding and blending (Section 7.5). We believe that with the corrections described in these sections, our PM measurements are as good as they can be, given the limitations of the data available in the *HST* archive (which are extremely heterogeneous and were rarely obtained for the purpose of astrometry). Nevertheless, several more issues need to be kept in mind when using our PM catalogs.

Our catalogs are necessarily incomplete, and in different ways for different clusters. For instance, in the most-crowded central regions of each cluster, we can measure PMs for only the brightest stars. Specific dynamical studies, like the search for intermediate-mass black holes, require a large number of stars with high-quality PMs in the very proximity of the cluster center. This does not mean that our PM catalogs are not suitable for these kinds of studies in general, but some clusters will be more appropriate than others, and it depends on the crowding conditions of their centers. A better way to measure high-quality PMs for a large number of stars in the cluster centers would be to have used a master frame based on higher spatial resolution ACS/HRC exposures (when available) rather than on the ACS/WFC data, but this goes beyond the scope of the present work.

We saw in Section 6.2.3 that at the faint limit, there might be some nonnegligible systematic errors in the measured velocity dispersion. Estimation of the velocity dispersion requires, in essence, that the PM-measurement uncertainties be subtracted in quadrature from the observed PM scatter. At the faint end, the PM uncertainties become comparable to (or exceed) the velocity dispersion of the cluster. Very accurate estimates of the PM-measurement uncertainties are then required in order to obtain reliable results. In our somewhat idealized simulations of Figure 8, PM uncertainties can be fairly reliably estimated at all magnitudes. In practice, there is always the potential of low-level unidentified systematic errors. The random errors estimated by our algorithms are then at best only an approximation to the true uncertainties. For this reason, it is advised to restrict any dynamical analysis to stars for which the PM uncertainties are well below the cluster velocity dispersion. This is particularly important for studies of energy equipartition (e.g., Anderson & van der Marel 2010; Trenti & van der Marel 2013), which rely on quantifying the increase of the velocity dispersion with decreasing stellar mass. It is then particularly important to reliably understand how the PM-measurement errors increase toward fainter magnitudes.

The errors in our catalogs are not homogeneously distributed. Some locations of the master frame will have larger time baselines or more single-exposure measurements. Taking special care in selecting high-quality PMs is therefore always crucial and a delicate matterregardless of the specific scientific needs (unless PMs are only used to select a cleaned sample of cluster stars for photometric studies).

8. PROPER-MOTION KINEMATICS OF NGC 7078

Our PM catalog for NGC 7078 is described in Appendix B and is distributed electronically as part of this paper (Table 30).

8.1. Overview

Figure 18 provides a visual overview of the information contained in the catalog. Panel (a) shows the GO-10775 CMD, corrected for differential reddening, for all stars with a PM measurement. We measured PMs from just above the HB region down to ~5 mag below the MS turnoff. The total spatial coverage of the catalog is shown in panel (b), with respect to the cluster center. We added two circles of radius $1'$ and $2'$ for reference. The histogram of the time baseline used to compute each star's motion is shown in panel (c). The Y axis of the plot is in logarithmic units, to properly show all histogram bins using the same scale. Panel (d) shows the PM vector point diagram, in units of mas yr^{-1}. Histograms of the PM distribution for each component of the motion and for each time baseline bin are also shown, again on a logarithmic Y-axis scale. Finally, PM errors as a function of the $m_{\rm F606W}$ magnitude are shown in panel (e). In each panel, stars are color-coded according to their time baseline. The figure gives an immediate sense of the PM distribution, quality, and respective magnitude range in each location of the available FoV. Proper motion errors are smaller than 30 μas yr^{-1} for the brightest stars with the longest time

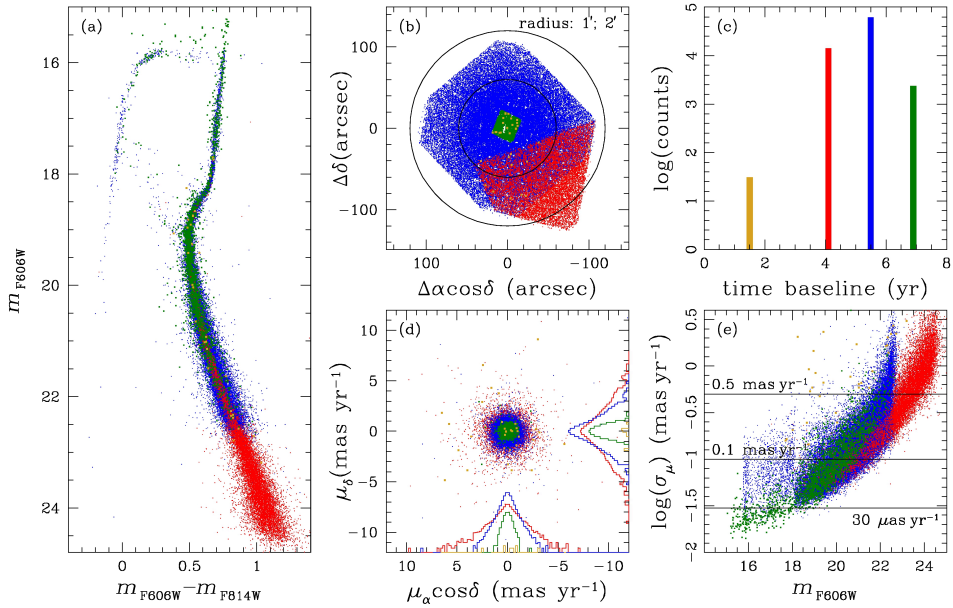

Figure 18. Panel (a): the CMD of all stars in the NGC 7078 PM catalog. Panel (b): stellar spatial distribution with respect to the cluster center, in arcsec. Two circles at 1′ and 2′ are shown for reference. Panel (c): logarithmic histogram of the time baseline used to compute PMs. The counts refer to the number of stars. Panel (d): PM diagram, together with histograms of the two PM components for each available time baseline. Panel (e): PM errors as a function of the m_{F606W} magnitude. In each panel, stars are color-coded according to their time baseline.

(A color version of this figure is available in the online journal.)

baseline and increase up to ∼3 mas yr^{-1} for the faintest stars in the catalog. There are 32 stars in the catalog with a time baseline of less than 2 yr. Although the PM of these stars is poorly constrained, they are included in the catalog for completeness.

8.2. Comparison with Other Published PM Catalogs

The internal PM dispersion of NGC 7078, based on 210 bright RGB stars, was first (barely) detected by Cudworth (1976), using photographic plates spanning over 70 yr of time baseline. The first high-quality PM catalog of NGC 7078 was published by McNamara et al. (2003, hereafter McN03) for 1764 stars in the core, obtained with the *HST* WFPC2 detector. The authors computed proper motions using four first-epoch and 12 s epoch exposures taken ∼8 yr apart. Their catalog includes positions in the geometric-distortion-corrected frame of their first exposure, in pixels, and proper motions as displacements in pixels over the available time baseline.[19]

We applied general six-parameter linear transformations to translate the McN03 WFPC2 positions into our master frame and cross-identified their stars with the closest stars in our catalog within 2.5 pixels. A total of 686 stars were found in common, 323 of which were used in their internal PM analysis. Among them, there are 26 stars in the proximity of McN03 FoV edges that exhibit a significant offset in position with respect to our master frame, probably due to unaccounted for WFPC2 geometric distortion residuals. These 26 stars are not included

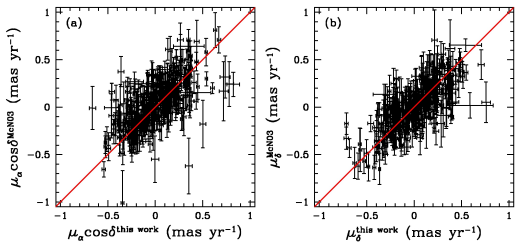

Figure 19. PM component-to-component comparison between our catalog and that of McN03. Most of the scatter is due to the larger error bars of the McN03 catalog.

(A color version of this figure is available in the online journal.)

in the PM comparison. Finally, we transformed quoted McN03 PMs and errors into ($\mu_\alpha \cos\delta$, μ_δ) units.[20]

In Figure 19, we illustrate the comparison between our PMs and those of McN03, with $\mu_\alpha \cos\delta$ in panel (a) and μ_δ in panel (b). Most of the scatter is due to the uncertainties of the McN03 PM measurements, which are significantly larger than those in our catalog (our catalog is also superior in that it has 40 times as many stars). The fact that the points are mostly aligned along the red line implies that our PMs are consistent with those of McN03. The scatter of the points along the direction

[19] Note that McN03 quoted displacements are to be intended as first-epoch positions minus second-epoch positions and not vice versa.

[20] In order to convert McN03-quoted PMs into mas yr^{-1} units, we applied a scaling factor of 5.69 instead of their suggested 5.75 (a 1% difference). This difference is due to the different pixel scale adopted for WFPC2: they use a 46 mas pixel^{-1} scale value, while we directly measured their plate scale on our master frame to be 45.46 mas pixel^{-1}.

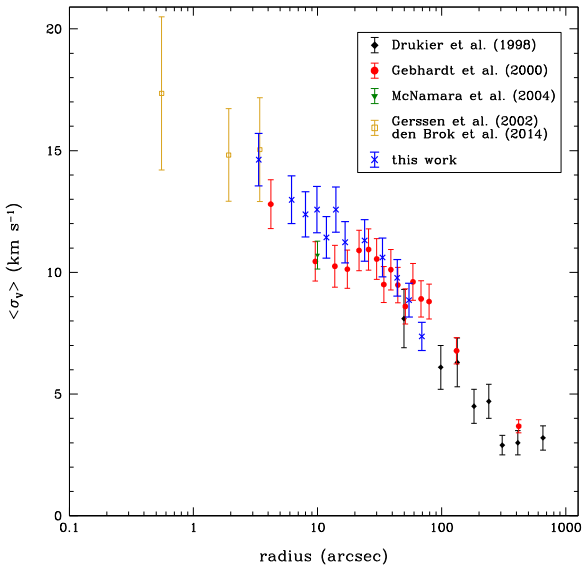

Figure 20. Velocity–dispersion profiles in the literature (black, red, and green points) and that obtained with RGB stars in our catalog (in blue), assuming a cluster distance of 10.4 kpc (see Table 1).

(A color version of this figure is available in the online journal.)

perpendicular to the red line (which is not a fit to the data but just the plane bisector) reveals a small but marginal (within the errors) disagreement. The fact that our PMs are consistent with those of McN03 is a further indication of the reliability of our measurements.

8.3. Velocity–dispersion Profiles

In 1989, Peterson et al. (1989) first measured the line-of-sight velocity–dispersion profile of NGC 7078, based on 120 spectra of individual stars in the centermost 4.′6. In subsequent years, many authors have analyzed the line-of-sight velocity–dispersion profile of NGC 7078 with various telescopes and techniques. High signal-to-noise spectra are generally obtained from only the brightest stars in a GC (i.e., RGB stars). In Figure 20, we therefore compare literature high-quality velocity–dispersion profiles (in black, red, green, and yellow for Drukier et al. 1998, Gebhardt et al. 2000, McNamara et al. 2004, and Gerssen et al. 2002/den Brok et al. 2014, respectively[21]) with that obtained from the stars in our catalog brighter than the SGB (in blue), using 10.4 kpc as the cluster distance (see Table 1). There is excellent agreement between our values and those obtained from spectra, as expected for a cluster with an isotropic velocity distribution and a correctly estimated distance. This once again confirms the high quality and reliability of our PM catalog.

Here and henceforth, velocity dispersions were estimated from the PM catalog using the same method as in van der Marel & Anderson (2010). This corrects the observed scatter for the individual stellar PM uncertainties. Unless stated otherwise, we quote the average one-dimensional velocity dispersion σ_μ, based on the combined x and y PM measurements. Moreover, we adopted an appropriate sample of high-quality PM stars for the analysis.

Satisfied that our PM measurements appear to be solid both internally (see Section 6) and externally (see Section 8.2), we proceed by analyzing more in detail the MS velocity–dispersion profile of NGC 7078. In order to select the best-measured stars, we proceeded as follows. First, we selected likely cluster members on the basis of their positions on the CMD. In addition, we kept only those stars with QFIT-percentile values below 50%, reduced χ^2 values below 1.25, and $N_R > 0.85$ that proved to remove crowding or blending as a source of systematic effects (see Section 7.5).

Then we adopted an iterative procedure that further identifies and rejects stars for which the measurement error is larger than F times the local σ_μ, where F is a certain threshold value, and the local σ_μ is computed for each star using the 100 stars closest in radial distance and magnitude to the target star. We iterated this procedure until we obtained convergence of the dispersion profiles. We found that F = 0.5 provides the best compromise between accuracy and sample size. After these procedures were applied, there were no remaining candidate field stars with highly discrepant ($>5\sigma$) PMs. Our final sample consists of 18 136 stars, of which 15 456 are MS stars with $m_{\rm F606W}$ magnitudes between 19.15 (which here defines the turnoff) and 22.7, and between 11.′6 and 136.′6 from the cluster center.

We divided this sample into 8 mag bins each having approximately the same number of stars, and into 10 radial intervals, again each having approximately the same number of stars. These subdivisions define 80 regions in the magnitude–radius space, with each containing on average 193 stars. Obviously, the innermost radial intervals have fewer faint stars on average than the outermost ones because of crowding-driven incompleteness. The number of stars in each region ranges from 72 to 342. For each region we computed the velocity dispersion σ_μ and its error for both amplifier-based and locally corrected PMs.

Figure 21 collects the results of the velocity–dispersion analysis. We show the results in two ways: (1) σ_μ as a function of the magnitude for different radial intervals (top panels) and (2) σ_μ as a function of the radial distance for different magnitude bins (bottom panels). Panels (a) and (e) show the CMD of selected stars around the MS of NGC 7078. Horizontal lines delimit the magnitude bins. Panels (b) and (f) show the spatial distribution of the selected stars. The circles define the radial intervals. Panels (c) and (d) show the σ_μ profiles as a function of the $m_{\rm F606W}$ magnitude for locally corrected and amplifier-based PMs, respectively. Points and error bars are color-coded according to their radial intervals. Panels (g) and (h) show the σ_μ profiles as a function of the radial distance from the cluster center, with points and error bars color-coded according to their magnitude bin.

Figure 21 reveals a complex behavior of σ_μ as a function of both magnitude and radius. Bright, more massive stars are kinematically colder than faint, less massive stars at all radii. This behavior is a direct consequence of the effects of energy equipartition. Moreover, stars at larger radii are colder than stars closer to the cluster center for each magnitude bin, which is a direct consequence of hydrostatic equilibrium. There is little (a statistically insignificant) difference between amplifier-based and locally corrected velocity–dispersion profiles, with the latter being on average only slightly lower than the former. Figure 21

[21] Gerssen et al. (2002) published individual star velocities and unparameterized profiles of V and σ_V of stars in the core of the NGC 7078, obtained with the *HST* STIS spectrograph; den Brok et al. (2014) combined Gerssen et al. (2002) velocities with those of Gebhardt et al. (2000) to compute radial-binned profiles. Here we consider only the innermost three data points of the den Brok et al. (2014) profile (their Figure 1), which are mostly (if not completely) derived using the Gerssen et al. (2002) data.

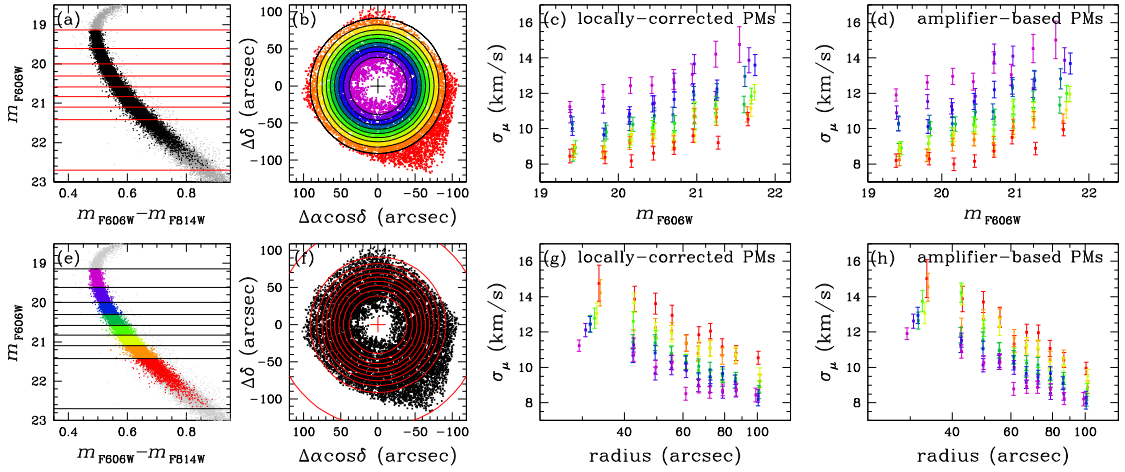

Figure 21. Top panels show the velocity–dispersion profiles σ_μ of MS stars in different radial intervals as a function of the m_{F606W} magnitude. (a) The CMD of NGC 7078 around its MS for all selected stars (gray) and for those with PM errors smaller than half the local velocity dispersion (black). The red lines define 8 mag bins with the same number of stars. (b) The spatial distribution of high-quality-PM MS stars. The black circles define 10 radial intervals with the same number of stars. Panels (c) and (d) show σ_μ values as a function of m_{F606W} for the locally corrected and amplifier-based PMs, respectively. Points and error bars are color-coded according to their radial interval. Bottom panels show the σ_μ profiles for the same stars in different magnitude intervals as a function of their distance from the cluster center. The magnitude and radial bins are the same as in the top panels. These time points are color-coded according to their magnitude bin.

(A color version of this figure is available in the online journal.)

also tells us that the LOS velocity dispersions quoted in the literature based on RGB stars are to be considered as lower limits. The vast majority of stars are less massive than RGB stars and move faster.

8.4. Anisotropy

A direct estimate of the degree of velocity anisotropy of the cluster is obtained by studying the ratio between tangential and radial proper motion dispersions as a function of the radial distance. We measured the velocity dispersion in each direction, using the full sample of 15,546 high-quality stars, in order to map the velocity–anisotropy profile. Moreover, velocity dispersions are computed using both amplifier-based and locally corrected PM values.

The results are summarized in Figure 22, using amplifier-based PMs in the top panel and locally corrected PMs in the bottom panel. As before, there is only a small difference between the two ways of computing PMs. The velocity distribution of NGC 7078 in the central $\sim 45''$ (comparable to the half-light radius $r_h = 60''$; Harris 1996, 2010 edition) is close to isotropic. This is consistent with what might be expected given the short two-body relaxation time of NGC 7078. There is evidence of motions that are preferably oriented radially rather than tangentially at distances greater than $45''$.

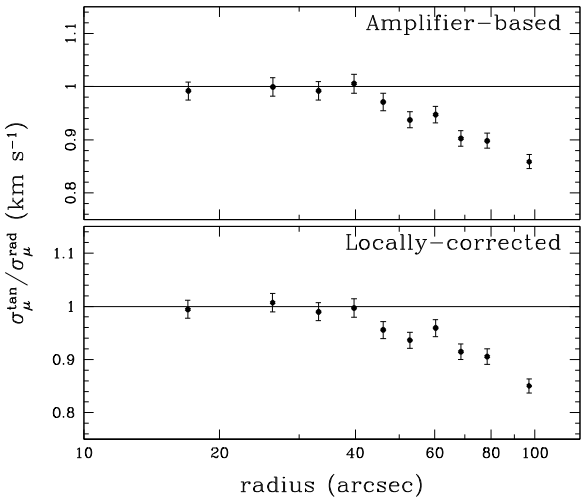

Figure 22. Anisotropy in the proper motion velocity dispersion as a function of the radial distance. Amplifier-based PMs are in the top panel, and locally corrected PMs are in the bottom one.

9. CONCLUSIONS AND DISCUSSION

Our understanding of the internal kinematics of GCs is based largely on studies of modest samples of stellar LOS velocities. PM studies with the *HST* have the potential to significantly advance our understanding, by extending the measurements to two- or three-dimensional velocities, lower stellar masses, and larger sample sizes. We have presented here the first study of *HST* PMs for a large sample of GCs, based on heterogenous data assembled from the *HST* archive. This first paper in a series has focused on the data reduction procedures, data quality, and new kinematic quantities inferred for NGC 7078 (M 15). Subsequent papers will explore a range of applications, including the many scientific topics of interest highlighted in Section 1.

We identified clusters in the *HST* archive with suitable exposures spread over multiple epochs, resulting in a sample of 22 clusters. For these clusters we analyzed a total of 2510 different exposures, obtained over the past decade with the ACS/WFC, ACS/HRC, and WFC3/UVIS instruments. We created photometric, astrometric, and PM catalogs from these data. For this, we used and extended the software developed in the context of our previous GC studies and in the context of our HSTPROMO collaboration. The data reduction also folded in and improved many of the single-epoch catalogs previously obtained in the context of the *HST* Globular Cluster Treasury

Table 7
List of Observations of NGC 104

GO	PI	Intr./Cam.	Filter	$N \times$Exp. Time	Epoch
9019	Bohlin	ACS/HRC	F330W	18 × 66s	2002 Apr
			F435W	2 × 5s, 2 × 20s, 17 × 60s, 2×300s	
			F475W	10 × 60s	
			F555W	14 × 60s	
			F606W	10 × 60s	
			F625W	10 × 60s	
			F775W	13 × 60s	
			F814W	2 × 5s, 2 × 20s, 14 × 60s, 2 × 300s	
			F850LP	10 × 60s	
9028	Meurer	ACS/HRC	F475W	40 × 60s	2002 Apr
		ACS/WFC	F475W	20 × 60s	
9281	Grindlay	ACS/WFC	F435W	1 × 10s, 6 × 100s, 3 × 115	2002 Sep-Oct
			F625W	2 × 10s, 20 × 65s	
			F658N	6 × 350s, 6 × 370s, 8 × 390s	
9575	Sparks	ACS/WFC	F475W	3 × 700s	2002 Apr
			F775W	1 × 578s, 5 × 700s	
			F850LP	6 × 700s	
9443	King	ACS/HRC	F330W	1 × 350s	2002 Jul
			F435W	1 × 350s	
			F475W	20 × 60s, 1 × 350s	
			F555W	1 × 350s	
			F606W	1 × 350s	
			F814W	1 × 350s	
		ACS/WFC	F435W	1 × 150s	
			F475W	5 × 60s, 1 × 150s	
			F555W	1 × 150s	
			F606W	1 × 100s	
			F814W	1 × 150s	
9453	Brown	ACS/WFC	F606W	1 × 6s, 1 × 70s	2002 Jul
			F814W	1 × 5s, 1 × 72s	
9662	Gilliland	ACS/HRC	F606W	2 × 1s	2002 Sep
9503	Nagar	ACS/WFC	F475W	1 × 60s	2003 Jan
			F658N	1 × 340s	
10055	Biretta	ACS/HRC	F330W	2 × 40s, 6 × 150s	2004 Feb
			F435W	2 × 20s, 6 × 60s	
			F606W	2 × 10s	
			F775W	2 × 10s	
10375	Mack	ACS/HRC	F435W	4 × 60s	2004–2005
			F475W	4 × 60s	
			F555W	4 × 60s	
			F606W	4 × 60s	
			F625W	4 × 60s	
			F775W	4 × 60s	
			F814W	4 × 60s	
			F850LP	4 × 60s	
10737	Mack	ACS/HRC	F330W	2 × 66s	2005–2006
			F435W	6 × 60s	
			F475W	6 × 60s	
			F555W	6 × 60s	
			F606W	6 × 60s	
			F625W	6 × 60s	
			F775W	6 × 60s	
			F814W	6 × 60s	
			F850LP	6 × 60s	
10775	Sarajedini	ACS/WFC	F606W	1 × 3s, 4 × 50s	2006 Mar
			F814W	1 × 3s, 4 × 50s	
11664	Brown	WFC3/UVIS	F390W	2 × 10s, 2 × 348s, 2 × 940s	2010 Sep
			F555W	1 × 1s, 1 × 30s, 2 × 665s	
			F814W	1 × 30s, 2 × 565s	
11729	Holtzman	WFC3/UVIS	F336W	1 × 30s, 2 × 580s	2010 Sep
			F390W	1 × 10s	
			F467M	1 × 40s, 2 × 450s	
12116	Dalcanton	ACS/WFC	F475W	2 × 7s	2012 Jul

Table 8
List of Observations of NGC 288

GO	PI	Intr./Cam.	Filter	$N\times$Exp. Time	Epoch
10120	Anderson	ACS/WFC	F435W	1 × 60s, 2 × 340s	2004 Sep
			F625W	1 × 10s, 1 × 75s, 1 × 115s, 1 × 120s	
			F658N	2 × 340, 2 × 540x	
10775	Sarajedini	ACS/WFC	F606W	2 × 10s, 8 × 130s	2006 Jul
			F814W	2 × 10s, 8 × 150s	
12193	Lee	WFC3/UVIS	F467M	1 × 964s, 1 × 1055s	2010 Nov

Table 9
List of Observations of NGC 362

GO	PI	Intr./Cam.	Filter	$N\times$Exp. Time	Epoch
10005	Lewin	ACS/WFC	F435W	4 × 340s	2003 Dec
			F625W	2 × 110s, 2 × 120s	
			F658N	2 × 440s, 2 × 500s	
10401	Chandar	ACS/HRC	F435W	17 × 85s	2004 Dec
10615	Anderson	ACS/WFC	F435W	5 × 70s, 30 × 340s	2005 Sep
10775	Sarajedini	ACS/WFC	F606W	1 × 10s, 4 × 150s	2006 Jun
			F814W	1 × 10s, 4 × 170s	

Table 10
List of Observations of NGC 1851

GO	PI	Intr./Cam.	Filter	$N\times$Exp. Time	Epoch
10458	Biretta	ACS/HRC	F555W	12 × 10s, 4 × 100s, 2 × 500s	2005 Aug
10775	Sarajedini	ACS/WFC	F606W	1 × 20s, 5 × 350s	2006 May
			F814W	1 × 20s, 5 × 350s	
12311	Piotto	WFC3/UVIS	F814W	7 × 100s	2010–2011

Table 11
List of Observations of NGC 2808

GO	PI	Intr./Cam.	Filter	$N\times$Exp. Time	Epoch
9899	Piotto	ACS/WFC	F475W	6 × 340s	2004 May
10335	Ford	ACS/HRC	F435W	24 × 135s	2006 Jun
			F555W	4 × 50s	
10775	Sarajedini	ACS/WFC	F606W	1 × 23s, 4 × 360s	2006 Mar
			F814W	1 × 23s, 4 × 370s	
10922	Piotto	ACS/WFC	F475W	1 × 20s, 2 × 350s, 2 × 360s	2006 Aug–Nov
			F814W	1 × 10s, 3 × 350s, 4 × 360s	
11801	Ford	WFC3/UVIS	F438W	7 × 20s, 9 × 160s	2009 Dec

Program GO-10775. Significant effort was invested to develop a reduction procedure that can be used in a homogeneous way for all clusters to obtain high-quality PM measurements, despite the very heterogeneous nature of the archival data (which were not generally obtained for high-precision astrometry).

We demonstrated the quality of the PM measurements through extensive Monte Carlo simulations for single stars and comprehensive data sets. These show that input PM distributions and dispersions can be reliably recovered for realistic observational setups and random errors. In practice, we also have to contend with various sources of systematic errors. We have discussed in detail the effects on the PM measurements that are due to charge-transfer-inefficiency effects, uncorrected geometric-distortion residuals, and crowding and blending. We have developed and discussed techniques to remove systematic PM errors that are due to these effects to the extent possible.

Table 12
List of Observations of NGC 5139

GO	PI	Intr./Cam.	Filter	$N \times$Exp. Time	Epoch
9442	Cool	ACS/WFC	F435W	9 × 12s, 27 × 340s	2002 Jun
			F625W	8 × 8s, 27 × 340s	
			F658N	36 × 440s	
10252	Anderson	ACS/WFC	F606W	1 × 15s, 5 × 340s	2004 Dec
			F814W	1 × 15s, 5 × 340s	
10775	Sarajedini	ACS/WFC	F606W	1 × 4s, 4 × 80s	2006 Mar–Jul
			F814W	1 × 4s, 4 × 80s	
11452	Kim Quijano	WFC3/UVIS	F336W	9 × 350s	2009 Jul
			F606W	1 × 35s	
			F814W	1 × 35s	
11911	Sabbi	WFC3/UVIS	F336W	19 × 350s	2010 Jan–Jul
			F390W	15 × 350s	
			F438W	25 × 350s	
			F555W	18 × 40s	
			F606W	22 × 40s	
			F775W	16 × 350s	
			F814W	24 × 40s	
			F850LP	17 × 60s	
12094	Petro	WFC3/UVIS	F606W	9 × 40s	2010 Apr
12339	Sabbi	WFC3/UVIS	F336W	9 × 350s	2011 Feb–Mar
			F438W	9 × 350s	
			F555W	9 × 40s	
			F606W	9 × 40s	
			F814W	9 × 40s	
			F850LP	9 × 60s	
12353	Kozhurina-Platais	WFC3/UVIS	F606W	11 × 40s	2010–2011
12694	Long	WFC3/UVIS	F467M	3 × 400s, 3 × 450s	2012 Feb–Apr
12700	Riess	WFC3/UVIS	F775W	2 × 450s	2012 Jun
12714	Kozhurina-Platais	WFC3/UVIS	F606W	4 × 40s	2012 Mar
13100	Kozhurina-Platais	WFC3/UVIS	F606W	6 × 48s	2012–2013

Table 13
List of Observations of NGC 5904

GO	PI	Intr./Cam.	Filter	$N \times$Exp. Time	Epoch
10120	Anderson	ACS/WFC	F435W	1 × 70s, 2 × 340s	2004 Aug
			F625W	1 × 10s, 1 × 70s, 2 × 110s	
			F658N	2 × 340s, 2 × 540s	
10615	Anderson	ACS/WFC	F435W	1 × 130s, 3 × 215s, 25 × 240s	2006 Feb
10775	Sarajedini	ACS/WFC	F606W	1 × 7s, 4 × 140s	2006 Mar
			F814W	1 × 7s, 4 × 140s	
11615	Ferraro	WFC3/UVIS	F390W	6 × 500s	2010 Jul
			F606W	4 × 150s	
			F814W	4 × 150s	

We have presented various tests that have shown that with these corrections, our PM data quality is excellent.

From our analyses we were able to measure the PM of over 1.3 million stars in the central regions of the target clusters, with a median number of ∼60,000 stars per cluster. Most of the PM catalogs will be disseminated as parts of future papers in this series. Here we focus on, and release, the catalog for NGC 7078, which consists of 77,837 stars. The number of stars with measured velocities is ∼40 times larger than in the best catalogs of NGC 7078 PMs and LOS velocities previously available (Gebhardt et al. 2000; McNamara et al. 2004). Our measurements are consistent with these previous catalogs in the areas of overlap. For the PMs, we demonstrated this on a star-by-star basis, and for the LOS velocities, we demonstrated this by comparison of the velocity–dispersion profiles for bright stars under the assumption of isotropy.

Table 14
List of Observations of NGC 5927

GO	PI	Intr./Cam.	Filter	$N\times$Exp. Time	Epoch
9453	Brown	ACS/WFC	F606W	1×2s, 1×30s, 1×500s	2002 Aug
			F814W	1×15s, 1×340s	
10775	Sarajedini	ACS/WFC	F606W	1×30s, 5×350s	2006 Apr
			F814W	1×25s, 5×360s	
11664	Brown	WFC3/UVIS	F390W	2×40s, 2×348s, 2×800s	2010 Aug
			F555W	1×50s, 2×665s	
			F814W	1×50s, 2×455s	
11729	Holtzman	WFC3/UVIS	F336W	2×475s	2010 Sep
			F467M	2×365s	

Table 15
List of Observations of NGC 6266

GO	PI	Intr./Cam.	Filter	$N\times$Exp. Time	Epoch
10120	Anderson	ACS/WFC	F435W	1×200s, 2×340s	2004 Aug
			F625W	1×30s, 1×120s, 3×340s	
			F658N	1×340s, 3×350s, 3×365s, 3×375s	
11609	Chanamé	WFC3/UVIS	F390W	4×35s, 5×393s, 5×421s	2010 Jun

Table 16
List of Observations of NGC 6341

GO	PI	Intr./Cam.	Filter	$N\times$Exp. Time	Epoch
9453	Brown	ACS/WFC	F606W	1×5s, 1×90s	2002 Aug
			F814W	1×6s, 1×100s	
10120	Anderson	ACS/WFC	F435W	1×90s, 2×340s	2004 Aug
			F625W	1×10s, 3×120s	
			F658N	2×350s, 2×555s	
10335	Ford	ACS/HRC	F435W	36×85s	2004–2006
			F435W	15×40s	
10443	Biretta	ACS/HRC	F330W	8×100s, 4×500s	2005 Feb
			F555W	78×10s, 33×100s, 18×500s	
			F606W	14×357	
10455	Biretta	ACS/HRC	F555W	12×10s, 41×100s, 2×500s	2005 Feb
10505	Gallart	ACS/WFC	F475W	1×3s, 1×20s, 1×40s	2006 Jan
			F814W	1×7s, 1×10s, 1×20s	
10615	Anderson	ACS/WFC	F435W	30×340s	2006 Jan
10775	Sarajedini	ACS/WFC	F606W	1×7s, 5×140s	2006 Apr
			F814W	1×7s, 5×150s	
11664	Brown	WFC3/UVIS	F390W	2×348s, 2×795s	2009 Oct
			F555W	1×30s, 2×665s	
			F814W	1×30s, 2×415s	
11801	Ford	WFC3/UVIS	F438W	6×10s, 11×110s	2009 Nov
11729	Holtzman	WFC3/UVIS	F336W	1×30s, 2×425s	2010 Oct
			F390W	1×10s	
			F467M	1×40s, 2×350s	

Table 17
List of Observations of NGC 6362

GO	PI	Intr./Cam.	Filter	$N\times$Exp. Time	Epoch
10775	Sarajedini	ACS/WFC	F606W	1×10s, 4×130s	2006 May
			F814W	1×10s, 4×150s	
12008	Kong	WFC3/UVIS	F336W	1×368s, 5×450s	2010 Aug

Table 18
List of Observations of NGC 6388

GO	PI	Intr./Cam.	Filter	$N \times$Exp. Time	Epoch
9821	Pritzl	ACS/WFC	F435W	6 × 11s	2003–2004
			F555W	6 × 7s	
			F814W	6 × 3s	
9835	Drukier	ACS/HRC	F555W	48 × 155s	2003 Oct
			F814W	5 × 25s, 2 × 469s, 10 × 505s	
10350	Cohn	ACS/HRC	F330W	2 × 1266s, 4 × 1314s	2006 Apr
			F555W	3 × 155s	
10474	Drukier	ACS/HRC	F555W	48 × 155s	2006 Apr
			F814W	4 × 25s, 8 × 501s, 4 × 508s	
10775	Sarajedini	ACS/WFC	F606W	1 × 40s, 5 × 340s	2006 Apr
			F814W	1 × 40s, 5 × 350s	
11739	Piotto	WFC3/UVIS	F390W	6 × 880s	2010 Jun–Jul

Table 19
List of Observations of NGC 6397

GO	PI	Intr./Cam.	Filter	$N \times$Exp. Time	Epoch
10257	Anderson	ACS/WFC	F435W	5 × 13s, 5 × 340s	2004–2005
			F625W	5 × 10s, 5 × 340s	
			F658N	20 × 390s, 20 × 395s	
10775	Sarajedini	ACS/WFC	F606W	1 × 1s, 4 × 15s	2006 May
			F814W	1 × 1s, 4 × 15s	
11633	Rich	WFC3/UVIS	F336W	6 × 620s	2010 Mar
			F606W	6 × 360s	

Table 20
List of Observations of NGC 6441

GO	PI	Intr./Cam.	Filter	$N \times$Exp. Time	Epoch
9835	Drukier	ACS/HRC	F555W	36 × 240s	2003 Sep
			F814W	5 × 40s, 2 × 413s, 10 × 440s	
10775	Sarajedini	ACS/WFC	F606W	1 × 45s, 5 × 340s	2006 May
			F814W	1 × 45s, 5 × 350s	
11739	Piotto	WFC3/UVIS	F390W	2 × 880s, 2 × 884s, 8 × 885s	2010–2011

Table 21
List of Observations of NGC 6535

GO	PI	Intr./Cam.	Filter	$N \times$Exp. Time	Epoch
10775	Sarajedini	ACS/WFC	F606W	1 × 12s, 4 × 130s	2006 Mar
			F814W	1 × 12s, 4 × 150s	
12008	Kong	ACS/WFC	F625W	1 × 100s, 1 × 148s	2010 Sep
			F658N	1 × 588s, 1 × 600s	
		WFC3/UVIS	F336W	1 × 253s, 5 × 400s	

Table 22
List of Observations of NGC 6624

GO	PI	Intr./Cam.	Filter	$N \times$Exp. Time	Epoch
10401	Chandar	ACS/HRC	F435W	20 × 200s	2005 Feb
10775	Sarajedini	ACS/WFC	F606W	1 × 15s, 5 × 350s	2006 Apr
			F814W	1 × 15s, 5 × 350s	
10573	Mateo	ACS/WFC	F435W	1 × 360s	2006 Jun
			F555W	1 × 160s	
			F814W	1 × 65s	

We present a preliminary analysis of the PM kinematics of NGC 7078 that demonstrates the potential of our data. The large number of measurements allows detailed studies of the velocity dispersion as a function of radius, as a function of stellar magnitude (or mass) along the main sequence, and as a function of direction in the plane of the sky (radial or tangential). The velocity dispersion increases toward the center as expected from hydrostatic equilibrium, and it increases toward lower masses as expected from energy equipartition. The velocity dispersion is isotropic near the center, as expected from two-body relaxation. There is evidence of motions that are preferably oriented radially rather than tangentially outside the half-light radius.

Although this work represents the most detailed study of GC PMs to date, there continues to be room for significant

Table 23
List of Observations of NGC 6656

GO	PI	Intr./Cam.	Filter	$N\times$Exp. Time	Epoch
10775	Sarajedini	ACS/WFC	F606W	1 × 3s, 4 × 55s	2006 Apr
			F814W	1 × 3s, 4 × 65s	
11558	De Marco	ACS/WFC	F502N	2 × 441s, 1 × 2102x, 1 × 2322s	2010 Mar
12311	Piotto	WFC3/UVIS	F814W	4 × 50s	2010–2011

Table 24
List of Observations of NGC 6681

GO	PI	Intr./Cam.	Filter	$N\times$Exp. Time	Epoch
9019	Bohlin	ACS/HRC	F330W	4 × 170s	2002 Apr
9010	Tran	ACS/HRC	F330W	6 × 70s	2002 May–June
9565	De Marchi	ACS/HRC	F330W	16 × 70s	2002 Jun-Sep
9566	De Marchi	ACS/HRC	F330W	17 × 70s	2003 Feb
9655	Giavalisco	ACS/HRC	F330W	16 × 70s	2003 Feb–Sep
10047	Giavalisco	ACS/HRC	F330W	6 × 70s	2004 Mar–Sep
10401	Chandar	ACS/HRC	F435W	26 × 125s	2005 Feb
10373	Giavalisco	ACS/HRC	F330W	4 × 70s	2005–2006
10736	Maiz-Apellaniz	ACS/HRC	F330W	8 × 20s	2006 Mar
			F435W	4 × 2s	
			F555W	4 × 2s	
			F625W	4 × 1s	
			F814W	4 × 1s	
10775	Sarajedini	ACS/WFC	F606W	1 × 10s, 4 × 140s	2006 May
			F814W	1 × 10s, 4 × 150s	
12516	Ferraro	WFC3/UVIS	F390W	12 × 348s	2011 Nov
			F555W	2 × 127s, 8 × 150s	
			F814W	13 × 348s	

Table 25
List of Observations of NGC 6752

GO	PI	Intr./Cam.	Filter	$N\times$Exp. Time	Epoch
9453	Brown	ACS/WFC	F606W	1 × 4s, 1 × 40s	2002 Sep
			F814W	1 × 4s, 1 × 45s	
9899	Piotto	ACS/WFC	F475W	6 × 340s	2004 Jul
10121	Bailyn	ACS/WFC	F555W	12 × 80s, 11 × 435s	2004 Sep
			F814W	12 × 40s	
10335	Ford	ACS/HRC	F435W	24 × 35s	2004–2006
			F555W	13 × 10s	
10458	Biretta	ACS/HRC	F555W	12 × 10s, 4 × 100s, 2 × 500s	2005 Aug
			F606W	2 × 357s	
10459	Biretta	ACS/WFC	F606W	8 × 450	2005 Oct
10335	Ford	ACS/HRC	F435W	24 × 35s	2004 Jun
			F555W	13 × 10s	
10775	Sarajedini	ACS/WFC	F606W	1 × 2s, 4 × 35s	2006 May
			F814W	1 × 2s, 4 × 40s	
11801	Ford	WFC3/UVIS	F438W	4 × 5s, 18 × 45s	2009 Nov
11664	Brown	WFC3/UVIS	F390W	2 × 348s, 2 × 880s	2010 May
			F555W	1 × 30s, 2 × 665s	
			F814W	1 × 30s, 2 × 495s	
11904	Kalirai	WFC3/UVIS	F555W	15 × 550s	2010 Jul–Aug
			F814W	15 × 550s	
12254	Cool	ACS/WFC	F435W	6 × 10s, 12 × 380s	2011 May–Nov
			F625W	18 × 10s, 12 × 360s	
			F658N	12 × 724s, 12 × 820s	
12311	Piotto	WFC3/UVIS	F814W	2 × 50s	2011 Mar–Apr

Table 26
List of Observations of NGC 6715

GO	PI	Intr./Cam.	Filter	$N\times$Exp. Time	Epoch
10775	Sarajedini	ACS/WFC	F606W	2 × 30s, 10 × 340s	2006 May
			F814W	2 × 30s, 10 × 350s	
12274	van der Marel	WFC3/UVIS	F438W	10 × 30s, 5 × 234s, 5 × 256s	2011 Sep

Table 27
List of Observations of NGC 7078

GO	PI	Intr./Cam.	Filter	$N\times$Exp. Time	Epoch
10401	Chandar	ACS/HRC	F435W	13 × 125s	2004 Dec
10775	Sarajedini	ACS/WFC	F606W	1 × 15s, 4 × 130s	2006 May
			F814W	1 × 15s, 4 × 150s	
11233	Piotto	WFC3/UVIS	F390W	6 × 827s	2010 May
12605	Piotto	WFC3/UVIS	F336W	6 × 350s	2011 Oct
			F438W	6 × 65s	

Table 28
List of Observations of NGC 7099

GO	PI	Intr./Cam.	Filter	$N\times$Exp. Time	Epoch
10401	Chandar	ACS/HRC	F435W	13 × 125s	2004 Dec
10775	Sarajedini	ACS/WFC	F606W	1 × 7s, 4 × 140s	2006 May
			F814W	1 × 7s, 4 × 140s	

improvement in the observations and measurements. New observations of the cores of GCs are taken in each *HST* observing cycle. This makes it possible to construct PM catalogs for more clusters and to extend the time baselines (and reduce the uncertainties) for clusters with existing PM catalogs. Also, the measurements presented here were not optimized to deal with very crowded fields. Some clusters have deep ACS/HRC observations of their cores. These have higher spatial resolution than the ACS/WFC observations that were used to build the GO-10775 master frames used for our analysis. Moreover, these ACS/HRC observations are often taken in bluer filters, which will yield less crowding (because the brightest stars tend to be *red* giants). New photometric reduction techniques for the WFC3 detector (J. Anderson et al., in preparation) can measure stellar positions and fluxes after subtraction of surrounding neighbors (deblending; see Anderson et al. 2008 for ACS/WFC). Master frames based on the ACS/HRC observations, combined with data reduction techniques that explicitly deblend, have the potential to yield catalogs with more stars with more accurately measured PMs and better characterized errors. This is especially relevant close to the cluster centers, which are dominated by crowding and blending issues. These central regions are crucial for studies of intermediate-mass black holes in GCs.

We thank the anonymous referee for comments that helped improve the presentation of our results. Support for this work was provided by grants for *HST* programs GO-9453, GO-10335, GO-10401, GO-11664, GO-11801, GO-12274, AR-12656, and AR-12845, provided by the Space Telescope Science Institute, which is operated by AURA, Inc., under NASA contract NAS 5-26555. F.R.F. and D.M. acknowledge the support from the Cosmic-Lab project (Web site: http://www.cosmic-lab.eu) funded by the European Research Council (under contract ERC-2010-AdG-267675). P.B. acknowledges financial support from the International Max Planck Research School for Astronomy and Cosmic Physics (IMPRS) at the University of Heidelberg and travel support from the Heidelberg Graduate School for Fundamental Physics (HGSFP). The authors are grateful to Laura Ferrarese, Rodrigo Ibata, and Carlton Pryor for help with the proposal preparation for some of these projects and to Michele Trenti for helpful discussions.

APPENDIX A

COMPLETE LIST OF THE DATA SETS USED FOR EACH CLUSTER

Tables 7–28 provide the full list of used exposures for each cluster, ordered by program number, camera, and filter. These tables are available only in the electronic version of the article.

APPENDIX B

PROPER-MOTION CATALOG OF NGC 7078

Our procedures generate a large number of parameters for each star, but most users will need only the high-level data. The PM catalog of NGC 7078 contains 91 lines of header information, followed by one line for each star with a PM measurement, for a total of 77,837 stars. Stars in the catalog are sorted according to their distance from the cluster center, as given in Table 1.

The header starts with some general information about the cluster, such as the reference time of the master frame and the adopted cluster center position, in both equatorial and master-frame units. Then follows a column-by-column description of the catalog. The columns contain the reference-frame positions and distance from the cluster center, calibrated and differential-reddening-corrected F606W and F814W magnitudes with errors and some photometric-quality information, PMs with errors derived using both the expected errors as a weight and the actual residuals around the PM least-squares fits (see Section 6.1), some additional astrometric-quality information, and finally the differences between local-corrected and amplifier-based PMs (see Section 7.4). A description of each column of the catalog is given in Table 29, and the first 10 lines of the NGC 7078 PM catalog are shown in Table 30.

Table 29
Column-by-column Information Contained in the Catalog

Col	Name (unit)	Explanation
		Astrometric information
1	r ($''$)	Distance from the cluster center
2	Δx_0 ($''$)	GO-10775 x-position in the rectified Cartesian system with respect to the adopted center
3	Δy_0 ($''$)	GO-10775 y-position in the rectified Cartesian system with respect to the adopted center
4	$\mu_\alpha \cos\delta$ (mas yr^{-1})	PM along the x-axis (parallel to and increasing as R.A.)
5	μ_δ (mas yr^{-1})	PM along the y-axis (parallel to and increasing as Dec.)
6	$\sigma_{\mu_\alpha \cos\delta}$ (mas yr^{-1})	1σ uncertainty in $\mu_\alpha \cos\delta$ computed using actual residuals
7	σ_{μ_δ} (mas yr^{-1})	1σ uncertainty in μ_δ computed using actual residuals
8	$x_{\rm M}$ (pixel)	x-position on the master frame
9	$y_{\rm M}$ (pixel)	y-position on the master frame
10	Δx (pixel)	Difference between $x_{\rm M}$ and the PM-predicted position at the reference time ($\overline{x}$)
11	Δy (pixel)	Difference between $y_{\rm M}$ and the PM-predicted position at the reference time ($\overline{y}$)
12	$\mathrm{err}_{\mu_\alpha \cos\delta}$ (mas yr^{-1})	1σ uncertainty in $\mu_\alpha \cos\delta$ computed using expected errors
13	$\mathrm{err}_{\mu_\delta}$ (mas yr^{-1})	1σ uncertainty in μ_δ computed using expected errors
		Photometric information
14	$m_{\rm F606W}$ (mag)	Differential-reddening-corrected GO-10775 F606W Vega-mag photometry
15	$m_{\rm F814W}$ (mag)	Differential-reddening-corrected GO-10775 F814W Vega-mag photometry
16	$\sigma_{m_{\rm F606W}}$ (mag)	Photometric error in F606W (from GO-10775)
17	$\sigma_{m_{\rm F814W}}$ (mag)	Photometric error in F814W (from GO-10775)
18	$\mathtt{QFIT}_{\rm F606W}$	Quality of F606W PSF-fit (from GO-10775)
19	$\mathtt{QFIT}_{\rm F814W}$	Quality of F814W PSF-fit (from GO-10775)
		Proper-motion quality information
20	$\chi^2_{\mu_\alpha \cos\delta}$	Reduced χ^2 of the fit of the x-component of the motion
21	$\chi^2_{\mu_\delta}$	Reduced χ^2 of the fit of the y-component of the motion
22	$\sigma_{\overline{x}}$ (pix)	1σ uncertainty in the intercept of the PM fit for the x-component using actual residuals
23	$\sigma_{\overline{y}}$ (pix)	1σ uncertainty in the intercept of the PM fit for the y-component using actual residuals
24	time (yr)	Time baseline, in Julian years
25	$\mathrm{err}_{\overline{x}}$ (pix)	1σ uncertainty in the intercept of the PM fit for the x-component using expected errors
26	$\mathrm{err}_{\overline{y}}$ (pix)	1σ uncertainty in the intercept of the PM fit for the y-component using expected errors
27	$\mathrm{U_{ref}}$	Flag: 1 if used as reference bona fide cluster star for the linear transformations, 0 otherwise
28	$\mathrm{N_{found}}$	Initial number of data points for the PM fits
29	$\mathrm{N_{used}}$	Final number of data points used for the PM fits
30	ID	ID number for each star (not the GO-10775 ID)
		Local PM corrections
31	$\Delta\mu_\alpha \cos\delta$ (mas yr^{-1})	Difference in $\mu_\alpha \cos\delta$ between locally corrected and amplifier-based PMs. Add to column 4 to obtain locally corrected PMs.
32	$\Delta\mu_\delta$ (mas yr^{-1})	Difference in μ_δ between locally corrected and amplifier-based PMs. Add to column 5 to obtain locally corrected PMs.

Table 30
First 10 Lines of the NGC 7078 PM Catalog

r ($''$) (1)	Δx_0 ($''$) (2)	Δy_0 ($''$) (3)	$\mu_\alpha \cos\delta$ (4)	μ_δ (5)	$\sigma_{\mu_\alpha \cos\delta}$ (6)	σ_{μ_δ} (7)	x_M (8)	y_M (9)	Δx (10)	Δy (11)	$\mathrm{err}_{\mu_\alpha \cos\delta}$ (12)	$\mathrm{err}_{\mu_\delta}$ (13)	m_{F606W} (14)	m_{F814W} (15)	$\sigma_{m_{F606W}}$ (16)	→
0.22148	0.19883	0.09756	−0.203	0.249	0.039	0.030	4984.312	5019.940	0.024	0.014	0.032	0.030	17.015	16.276	9.900	...
0.50339	0.24141	0.44172	−3.057	9.266	0.367	2.021	4983.246	5028.540	−0.078	−0.241	0.418	0.957	18.253	17.774	9.900	...
1.13357	0.84530	0.75528	0.201	0.245	0.045	0.054	4968.149	5036.379	0.030	0.003	0.042	0.037	15.508	15.113	9.900	...
1.24526	1.18454	0.38412	−0.283	0.055	0.020	0.038	4959.674	5027.097	−0.014	0.052	0.021	0.034	15.985	15.801	9.900	...
1.32849	0.86993	1.00404	0.001	−0.192	0.023	0.021	4967.535	5042.601	0.012	−0.008	0.024	0.018	16.974	16.193	9.900	...
1.33293	0.59227	1.19412	0.321	−0.101	0.027	0.031	4974.479	5047.344	0.004	−0.013	0.027	0.035	17.419	16.724	9.900	...
1.46104	−1.44918	0.18576	0.176	−0.084	0.022	0.023	5025.506	5022.140	0.016	0.012	0.018	0.028	16.686	15.977	9.900	...
1.62112	−0.24352	1.60272	0.054	−0.045	0.034	0.019	4995.371	5057.557	−0.030	0.022	0.029	0.023	15.478	15.406	9.900	...
1.77721	−1.39604	−1.09980	−0.403	0.109	0.025	0.046	5024.188	4990.005	0.022	0.005	0.024	0.036	17.375	16.719	9.900	...
1.90239	−1.31299	1.37664	0.387	−0.474	0.015	0.031	5022.109	5051.913	0.021	−0.021	0.019	0.029	17.443	16.765	9.900	...
...	...	...	...	...	...	...	...	...	...	...	...	...	...	...	...	...

→	$\sigma_{m_{F814W}}$ (17)	QFIT$_{F606W}$ (18)	QFIT$_{F814W}$ (19)	$\chi^2_{\mu_\alpha \cos\delta}$ (20)	$\chi^2_{\mu_\delta}$ (21)	$\sigma_{\bar{x}}$ (22)	$\sigma_{\bar{y}}$ (23)	time (24)	$\mathrm{err}_{\bar{x}}$ (25)	$\mathrm{err}_{\bar{y}}$ (26)	U_{ref} (27)	N_{found} (28)	N_{used} (29)	ID (30)	$\Delta\mu_\alpha \cos\delta$ (31)	$\Delta\mu_\delta$ (32)
...	9.900	0.080	0.056	2.412	2.116	0.0018	0.0017	6.96206	0.0018	0.0016	1	30	24	86023	0.004	0.005
...	9.900	0.331	0.347	2.328	11.882	0.0134	0.0749	1.48741	0.0153	0.0350	0	26	15	86021	0.023	−0.079
...	9.900	0.084	0.049	3.502	2.750	0.0020	0.0022	6.96206	0.0019	0.0017	0	20	18	86020	0.047	0.013
...	9.900	0.062	0.043	1.706	4.652	0.0011	0.0019	6.96206	0.0011	0.0018	0	25	23	86022	0.049	0.014
...	9.900	0.118	0.063	1.279	0.796	0.0014	0.0011	6.96206	0.0013	0.0010	1	24	21	86019	0.017	−0.002
...	9.900	0.115	0.117	1.475	2.553	0.0016	0.0021	6.96206	0.0015	0.0020	1	25	23	86018	−0.006	0.017
...	9.900	0.080	0.084	1.045	2.306	0.0010	0.0017	6.96206	0.0010	0.0016	1	27	26	86483	0.022	−0.028
...	9.900	0.046	0.042	1.746	1.067	0.0015	0.0011	6.96195	0.0014	0.0011	0	16	14	86228	0.033	0.001
...	9.900	0.098	0.068	1.140	2.624	0.0013	0.0020	6.96206	0.0013	0.0021	1	25	25	86481	−0.010	0.011
...	9.900	0.146	0.096	0.895	2.024	0.0013	0.0016	6.96206	0.0012	0.0018	1	27	26	86485	−0.010	0.005
...	...	...	...	...	...	...	...	...	...	...	...	...	...	...	...	...

(This table is available in its entirety in a machine-readable form in the online journal. A portion is shown here for guidance regarding its form and content.)

REFERENCES

Anderson, J., & Bedin, L. R. 2010, PASP, 122, 1035
Anderson, J., Bedin, L. R., Piotto, G., Yadav, R. S., & Bellini, A. 2006, A&A, 454, 1029
Anderson, J., & King, I. R. 2003a, PASP, 115, 113
Anderson, J., & King, I. R. 2003b, AJ, 126, 772
Anderson, J., & King, I. R. 2006a, ACS/ISR 2006-01 (Baltimore, MD: STScI), available online at http://www.stsci.edu/hst/acs/documents/isrs
Anderson, J., & King, I. R. 2006b, ACS/ISR 2004-15 (Baltimore, MD: STScI), available online at http://www.stsci.edu/hst/acs/documents/isrs
Anderson, J., Sarajedini, A., Bedin, L. R., et al. 2008, AJ, 135, 2055
Anderson, J., & van der Marel, R. P. 2010, ApJ, 710, 1032
Beccari, G., Ferraro, F. R., Possenti, A., et al. 2006, AJ, 131, 2551
Bedin, L. R., Piotto, G., King, I. R., & Anderson, J. 2003, AJ, 126, 247
Bellini, A., Anderson, J., & Bedin, L. R. 2011, PASP, 123, 622
Bellini, A., & Bedin, L. R. 2009, PASP, 121, 1419
Bellini, A., Bedin, L. R., Pichardo, B., et al. 2010, A&A, 513, A51
Bellini, A., Piotto, G., Bedin, L. R., et al. 2009, A&A, 493, 959
Bellini, A., Piotto, G., Milone, A. P., et al. 2013, ApJ, 765, 32
Bianchini, P., Varri, A. L., Bertin, G., & Zocchi, A. 2013, ApJ, 772, 67
Binney, J., & Mamon, G. A. 1982, MNRAS, 200, 361
Cudworth, K. M. 1976, AJ, 81, 519
Da Costa, G. S., Freeman, K. C., Kalnajs, A. J., Rodgers, A. W., & Stapinski, T. E. 1977, AJ, 82, 810
den Brok, M., van de Ven, G., van den Bosch, R., & Watkins, L. 2014, MNRAS, 438, 487
Dinescu, D. I., Girard, T. M., van Altena, W. F., Mendez, R. A., & Lopez, C. E. 1997, AJ, 114, 1014
Drukier, G. A., Slavin, S. D., Cohn, H. N., et al. 1998, AJ, 115, 708
Eichhorn, H., & Jefferys, W. H. 1971, PMcCo, 16, 267
Gebhardt, K., Pryor, C., O'Connell, R. D., Williams, T. B., & Hesser, J. E. 2000, AJ, 119, 1268
Gerssen, J., van der Marel, R. P., Gebhardt, K., et al. 2002, AJ, 124, 3270
Gnedin, O. Y., Zhao, H., Pringle, J. E., et al. 2002, ApJL, 568, L23
Goldsbury, R., Richer, H. B., Anderson, J., et al. 2010, AJ, 140, 1830
Harris, W. E. 1996, AJ, 112, 1487 (2010 edition)
Illingworth, G. 1976, ApJ, 204, 73
Malavolta, L., Sneden, C., Piotto, G., et al. 2014, AJ, 147, 25
Massari, D., Bellini, A., Ferraro, F. R., et al. 2013, ApJ, 779, 81
Massari, D., Mucciarelli, A., Ferraro, F. R., et al. 2014, ApJ, 791, 101
McLaughlin, D. E., Anderson, J., Meylan, G., et al. 2006, ApJS, 166, 249
McNamara, B. J., Harrison, T. E., & Anderson, J. 2003, ApJ, 595, 187 (McN03)
McNamara, B. J., Harrison, T. E., & Baumgardt, H. 2004, ApJ, 602, 264
McNamara, B. J., Harrison, T. E., Baumgardt, H., & Khalaj, P. 2012, ApJ, 745, 175
McNamara, B. J., & McKeever, J. 2011, AJ, 142, 163
Milone, A. P., Piotto, G., Bedin, L. R., et al. 2012, A&A, 540, A16
Milone, A. P., Villanova, S., Bedin, L. R., et al. 2006, A&A, 456, 517
Peterson, R. C., & Cudworth, K. M. 1994, ApJ, 420, 612
Peterson, R. C., Seitzer, P., & Cudworth, K. M. 1989, ApJ, 347, 251
Piotto, G., Milone, A. P., Bedin, L. R., et al. 2014, arXiv:1410.4564
Rees, R. F., Jr. 1995, PhD thesis, Univ. Chicago, IL, USA
Rees, R. F., Jr. 1997, in ASP Conf. Ser. 127, Proper Motions and Galactic Astronomy, ed. R. M. Humphreys (San Francisco, CA: ASP), 109
Sabbi, E., & Bellini, A. 2013, WFC3/ISR 2013-11 (Baltimore, MD: StscI), available online at http://www.stsci.edu/hst/wfc3/documents/ISRs
Trenti, M., & van der Marel, R. 2013, MNRAS, 435, 3272
van der Marel, R. P., & Anderson, J. 2010, ApJ, 710, 1063
van der Marel, R. P., Anderson, J., Bellini, A., et al. 2014, in ASP Conf. Ser. 480, Structure and Dynamics of Disk Galaxies, ed. M. S. Seigar & P. Treuthardt (San Francisco, CA: ASP), 43
van Leeuwen, F., Le Poole, R. S., Reijns, R. A., Freeman, K. C., & de Zeeuw, P. T. 2000, A&A, 360, 472

Chapter 5

The effect of binaries on kinematic profiles from proper motions

"*The Effect of Unresolved Binaries on Globular Cluster Proper-motion Dispersion Profiles*"
Bianchini, P.; Norris, M. A.; van de Ven, G.; Schinnerer, E.; Bellini, A.; van der Marel, R. P.; Watkins, L. L.; Anderson, J.
The Astrophysical Journal Letters, Volume 820, Issue 1, article id. L22, 7 pp. (2016)
`http://adsabs.harvard.edu/abs/2016ApJ...820L..22B`

The advent of high-precision proper motion data sets demands for a deep understanding of all sources of contamination that can be present. In this Chapter, I investigate the so-far unexplored effect of unresolved binary stars on proper motions data sets. Since binaries are more massive stellar systems than average stars, their velocity dispersion will be lower due to the effect of energy equipartition (see also the following Chapter 6). Using a suite of Monte Carlo cluster simulations treated as realistic *HST* proper motion data sets, I quantify the subtle color-dependent biases that this effect can introduce in the kinematic measurements. A comparison to HSTPROMO data set of the GC M15 (see Chapter 4) shows that unresolved binaries do not significantly affect the proper motion kinematics and no color-dependency is observed. This analysis can also be interpreted in the context of multiple stellar populations as an indication of the lack of significant kinematic differences amongst the stellar populations of M15.

The Astrophysical Journal Letters, 820:L22 (7pp), 2016 March 20 doi:10.3847/2041-8205/820/1/L22

THE EFFECT OF UNRESOLVED BINARIES ON GLOBULAR CLUSTER PROPER-MOTION DISPERSION PROFILES

P. Bianchini[1,4], M. A. Norris[1,2], G. van de Ven[1], E. Schinnerer[1], A. Bellini[3], R. P. van der Marel[3], L. L. Watkins[3], and J. Anderson[3]
[1] Max-Planck Institute for Astronomy, Königstuhl 17, D-69117 Heidelberg, Germany; bianchini@mpia.de
[2] University of Central Lancashire, Preston, PR1 2HE, UK
[3] Space Telescope Science Institute, 3700 San Martin Drive, Baltimore, MD 21218, USA
Received 2015 November 12; accepted 2016 March 3; published 2016 March 18

ABSTRACT

High-precision kinematic studies of globular clusters (GCs) require an accurate knowledge of all possible sources of contamination. Among other sources, binary stars can introduce systematic biases in the kinematics. Using a set of Monte Carlo cluster simulations with different concentrations and binary fractions, we investigate the effect of unresolved binaries on proper-motion dispersion profiles, treating the simulations like *Hubble Space Telescope* proper-motion samples. Since GCs evolve toward a state of partial energy equipartition, more-massive stars lose energy and decrease their velocity dispersion. As a consequence, on average, binaries have a lower velocity dispersion, since they are more-massive kinematic tracers. We show that, in the case of clusters with high binary fractions (initial binary fractions of 50%) and high concentrations (i.e., closer to energy equipartition), unresolved binaries introduce a color-dependent bias in the velocity dispersion of main-sequence stars of the order of 0.1–0.3 km s^{-1} (corresponding to 1%−6% of the velocity dispersion), with the reddest stars having a lower velocity dispersion, due to the higher fraction of contaminating binaries. This bias depends on the ability to distinguish binaries from single stars, on the details of the color–magnitude diagram and the photometric errors. We apply our analysis to the HSTPROMO data set of NGC 7078 (M15) and show that no effect ascribable to binaries is observed, consistent with the low binary fraction of the cluster. Our work indicates that binaries do not significantly bias proper-motion velocity-dispersion profiles, but should be taken into account in the error budget of kinematic analyses.

Key words: binaries: general – globular clusters: general – globular clusters: individual (NGC 7078 (M15)) – proper motions – stars: kinematics and dynamics

1. INTRODUCTION

Globular clusters (GCs) are some of the oldest stellar systems in the universe and provide crucial information on the early phases of galaxy formation and assembly. In order to constrain their formation, a growing focus has been devoted to the study of their internal kinematics, which provides a long-lasting fossil record of their formation and dynamical evolution.

Typical kinematic studies of Galactic GCs are based on line-of-sight velocities, from spectroscopic measurements either of resolved stars, or of (partially) unresolved stars through integrated-light spectroscopy. These measurements are limited by the fact that only one component of the velocity-vector is observed and only for the brightest sources, i.e., giant stars all with similar masses. However, a significant improvement was recently made possible thanks to high-precision *Hubble Space Telescope* (*HST*) proper motions (HSTPROMO, Bellini et al. 2014; Watkins et al. 2015a, 2015b), providing velocity measurements on the plane of the sky for 22 GCs, with a median of ∼60,000 stars per cluster, and thanks to other proper-motion samples dedicated to single GCs (e.g., McLaughlin et al. 2006; Richer et al. 2013 for NGC 104, McNamara et al. 2003 for NGC 7078, McNamara & McKeever 2011; McNamara et al. 2012 for NGC 6266, and Anderson & van der Marel 2010 for NGC 5139).

Proper-motion samples provide two-dimensional velocity information (the two components on the plane of the sky) and sample both bright giant and fainter stars along the main sequence, allowing us to measure the motion of stars with different masses. Moreover, since they provide large samples of stars, they are ideal to study the detailed internal kinematics of a GC, reaching low levels of random errors, and possibly allowing the coupling of the kinematics with color and chemical information.

An accurate kinematic analysis requires that any bias present in the observed kinematics should be well understood. A common source of contamination is binaries. Binaries can contaminate line-of-sight measurements, due to the motions of the stellar components around their mutual barycenter adding to the systemic motion of the binary system (e.g., Minor et al. 2010). Unidentified binaries can cause an overestimate of the measured line-of-sight velocity dispersion. Unfortunately, their identification is challenging, even for bright stars, since it requires repeated spectroscopic measurements. The resulting bias is negligible in typical GCs, characterized by a low binary fraction (lower than that of field stars, Milone et al. 2012), but it can be crucial for faint stellar systems (e.g., ultra-faint dwarf galaxies) with low velocity dispersion and small data samples (McConnachie & Cote 2010; Bradford et al. 2011).

In the case of proper motions, binaries can affect the data in three ways. First, the internal binary motion can produce an effect on the astrometric measurements, adding scatter to the

[4] Member of the International Max Planck Research School for Astronomy and Cosmic Physics at the University of Heidelberg, IMPRS-HD, Germany.

Table 1
Properties of the Simulations for an 11 Gyr Snapshot Observed at 5 kpc

Simulation Name	Initial Concentration	$f_{\rm initial}$	$f_{\rm final}$	$f_{\rm FOV}$	f_{R_c}	R_c		R_h		c
						(pc)	(arcmin)	(pc)	(arcmin)	
Simulation 1	intermediate	10%	2.9%	5.5%	7.3%	3.15	2.16	4.92	3.38	1.45
Simulation 2	intermediate	50%	16.2%	28.5%	30.8%	3.89	2.68	6.06	4.16	1.34
Simulation 3	low	10%	5.5%	9.6%	9.5%	6.07	4.17	9.05	6.22	1.16
Simulation 4	low	50%	20.2%	32.6%	31.5%	6.47	4.45	10.92	7.51	1.12
Simulation 5	high	10%	3.4%	6.8%	16.4%	0.75	0.51	2.69	1.85	2.06
Simulation 6	high	50%	11.5%	21.1%	32.0%	1.34	0.92	3.05	2.09	1.79

Note. The name of the simulation is followed by the primordial binary fraction $f_{\rm initial}$, the global binary fraction at 11 Gyr $f_{\rm final}$, the binary fraction within the FOV of 4 arcmin and magnitude cut between 17 and 24 r-band mag, and the binary fraction within the core radius R_c. The concentration $c = \log(R_t/R_c)$, the core radius R_c, and the half-light radius R_h are also provided.

proper-motion determination; this is, however, negligible.[5] Second, semi-resolved binaries seen as astrometric blends, can be characterized by poor-quality astrometry (because of the difficulties in centroiding the point-spread function), that translates to biased proper-motion measurements. This effect can be reliably mitigated using quality selection criteria on the proper-motion samples (see the discussion for NGC 7078; Bellini et al. 2014). Third, unresolved binaries can bias the kinematics since they are more-massive kinematic tracers than single stars at a given magnitude. In fact, due to two-body interactions, GCs evolve toward a state of partial energy equipartition (Trenti & van der Marel 2013; Bianchini et al. 2016). This means that while more-massive stars lose energy and sink toward the center, less massive stars gain energy and move outward, leading to a mass-dependent kinematics.

Unresolved binaries, being more-massive kinematic tracers, will be characterized by a lower velocity dispersion.[6] The effect of binaries on proper-motions samples would therefore be to systematically decrease the velocity dispersion otherwise measured from single stars alone. Moreover, since unresolved binaries are seen as a single star with flux given by the sum of the fluxes of the two components, they are redder in color along the main sequence. Their kinematic effect could therefore introduce a subtle color-dependence on the kinematics, that must be disentangled from any other possible color-dependent kinematic effects (e.g., the kinematic differences expected from different multiple stellar population scenarios, Henault-Brunet et al. 2015 and the observations presented in Richer et al. 2013 for NGC 104 and Bellini et al. 2015 for NGC 2808).

The aim of this Letter is to understand and quantify the kinematic effect of unresolved binaries connected to partial energy equipartition. We use a two step approach: first, we analyze a set of Monte Carlo cluster simulations (Downing et al. 2010) spanning a realistic range of concentrations and binary fractions, treating them as mock *HST* proper-motion samples to look for the kinematic effects of binaries (Sections 2 and 3). Second, we apply the same analysis to the HSTPROMO data of NGC 7078 (M15) for a comparison to observations (Section 4).

[5] The effect is proportional to $a/(\sigma\, T)$, with a major axis of the binary, σ typical velocity dispersion, T time-baseline of the proper-motion measurements; this effect is maximum for face-on orbits and epochs separated by a half-integer of the orbital period.

[6] Such mass-dependent kinematics can also be observed by comparing blue straggler stars against evolved stars (Baldwin et al. 2016).

2. SIMULATIONS

We consider a set of Monte Carlo cluster simulations, developed by Downing et al. (2010) with the Monte Carlo code by Giersz (1998). The simulations have an initial number of particles of $N = 500{,}000$, an initial mass function (IMF), stellar evolution, and primordial binaries, providing a realistic description of the long-term evolution of GCs with a single stellar population.

All simulations have initial conditions drawn from a Plummer (1911) model, a Kroupa (2001) IMF, [Fe/H] $= -1.3$, and an initial tidal cut-off at 150 pc (making them relatively isolated). We consider six simulations, characterized by three values of initial concentration with binary fractions of 10% or 50%. The initial binary parameters are described in Downing et al. (2010) and are based on the eigenvalue evolution and feeding algorithms of Kroupa (1995). These prescriptions use birth mass ratios drawn at random from the Kroupa et al. (1993) IMF. After 11 Gyr of dynamical evolution, the distribution of the mass-ratio q is flat for $q > 0.5$ (consistent with observations, e.g., Milone et al. 2016), decreasing for $q < 0.5$, and with an excess of binaries at $q \approx 1$. The output of each simulation consists of the three-dimensional position and velocity vectors, the stellar mass and the magnitude for each star (in r and i Sloan bands).

We treat our simulations similarly to real observations (in particular to HSTPROMO proper motions, Bellini et al. 2014), considering the properties of an 11 Gyr snapshot, projected along the line of sight at 5 kpc distance (typical of a Galactic GC). Furthermore, we consider stars in a field of view (FOV) of 4 arcmin around the center of the cluster, and within the magnitude range of $m_r = 17$ (just below the turnoff) to $m_r = 24$. The properties of our simulations are reported in Table 1.

The simulations span a range of concentrations[7] $c =$ 1.12–2.06 similar to typical Galactic GCs, with a range of final binary fractions from $\simeq$5% to $\simeq$30% (consistent with observations, e.g., Sollima et al. 2007; Milone et al. 2012). Note that we aim to explore a significant range of the parameter space without tuning our simulations to any specific GC.

Since the binary fraction is a radially dependent quantity, in Table 1, we report three values for the 11 Gyr snapshots: the global binary fraction, the one within the FOV of 4 arcmin and with a magnitude cut between 17 and 24 r-band magnitudes, and the one within the core radius R_c. Note that, interestingly,

[7] Defined as $c = \log(R_t/R_c)$, with R_t as the tidal and R_c as the core radius.

The Astrophysical Journal Letters, 820:L22 (7pp), 2016 March 20 Bianchini et al.

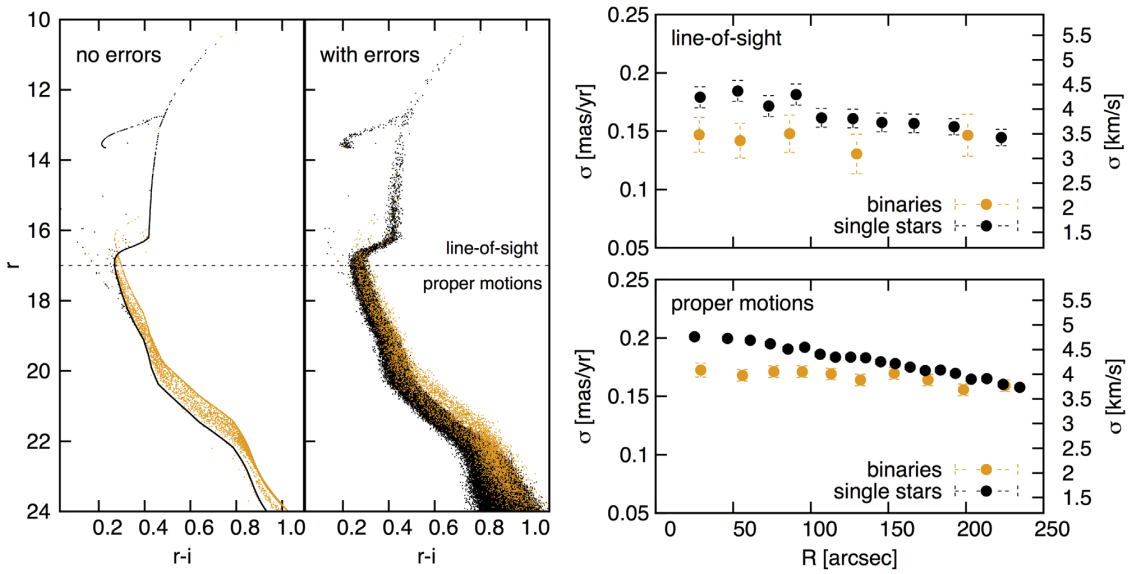

Figure 1. Left: color–magnitude diagrams of Simulation 1, with and without artificial errors. Binaries (orange) are in a redder sequence parallel to the main sequence. Note that the simulated r vs. r–i diagram does not match the typical observed r vs. r–i diagram closely. Right: velocity-dispersion profiles for single stars and binaries separately. The top panel refers to bright stars only, for which typical measurements of line-of-sight velocities are available, while the bottom panel refers to a typical magnitude range sampled by proper motions. Binaries show a lower velocity-dispersion profile (globally, 8% lower than single stars) because of the effect of partial energy equipartition.

the binary fraction within the core radius for the simulations with 50% primordial binaries settles to the value of ≃30%, independent of the concentration of the cluster.

In a separate paper (Bianchini et al. 2016), we investigate in detail the state of partial energy equipartition reached by our simulations and its relation to the clusters properties. Here we focus on the fact that all the simulations display mass-dependent kinematics.

2.1. Incorporating Errors in the Simulation Output

To enable a comparison with observations, we add realistic errors to the simulations. The errors for each star are selected to reproduce the trends of the errors in HSTPROMO data (e.g., Figure 18 from Bellini et al. 2014). For both proper motions and magnitudes, the errors are modeled to be magnitude dependent by assigning larger errors to fainter stars.[8] The errors are drawn at random from a Gaussian distribution[9] with standard deviation increasing with stellar magnitude, following a growth of $a/(b - \mathrm{mag})$, where a and b are such that the errors increase asymptotically for mag = 25.5 in the i band, and produce an average magnitude error (average for all of the stars) of ≈0.02 and of ≈0.1 mas yr^{-1} for proper motions (corresponding to ≈2 km s^{-1} at the distance[10] of 5 kpc). Figure 1, shows an example of a color–magnitude diagram with and without errors. Note that the detailed shape of the color–magnitude diagram does not reproduce the typical observed r versus r–i diagram.

2.2. Construction of Kinematic Profiles

We construct kinematic profiles by dividing the projected data into concentric radial bins each containing an equal number of stars. For every bin, a maximum-likelihood estimator (Pryor & Meylan 1993) is used to obtain the velocity dispersion and the associated error, taking into account the individual measurement errors. The proper motions are decomposed into radial and tangential components on the plane of the sky and the average dispersion $\sigma = \sqrt{(\sigma_R^2 + \sigma_T^2)/2}$ is used.

3. THE EFFECT OF UNRESOLVED BINARIES ON KINEMATICS

We analyze the differences in kinematics between binaries and single stars, using the proper-motion samples extracted from our simulations, restricted within the FOV of 4 arcmin with added velocity errors.

First, we assume that we are able to distinguish single stars from binaries and separately construct their velocity-dispersion profiles. In the right panel of Figure 1, we show the result for Simulation 1, where binaries show a lower velocity-dispersion profile than single stars. For completeness, we show the velocity dispersion calculated for the magnitude range typically measured in line-of-sight velocity samples (bright stars), and for typical proper-motion samples. Note that, for line-of-sight measurements, the main bias introduced by binaries is an overestimate of the velocity due to the motions of the stellar components around their mutual barycenter (e.g., Minor et al. 2010). Here we focus only on the effect on proper-motion samples, which so far has remained unexplored.

[8] In real *HST* proper-motion observations, the errors are also radial dependent, with higher errors for stars in the crowded center; this effect is not considered here.

[9] In the observations, photometric errors are non-symmetric; this can make some main-sequence stars appear as red as binaries. In our simulations, we do not consider this possibility, assuming that these apparent binaries are reliably rejected from observations (Bellini et al. 2014).

[10] The proper motions are reported in mas yr^{-1}; assuming a distance d in kiloparsec, a multiplication of $4.74d$ yields the values in km s^{-1}.

Table 2
Velocity Dispersions for Single Stars and Binaries within the FOV and the Corresponding Percentage Difference and Binary Fraction and Velocity Dispersion as a Function of Color Bin for the Simulations with Errors Included

Simulation	Velocity Dispersion (mas yr^{-1}) Single Stars	Velocity Dispersion (mas yr^{-1}) Binary Stars	Difference (%)	Binary Fraction (%) Left	Binary Fraction (%) Center	Binary Fraction (%) Right	Velocity Dispersion (mas yr^{-1}) Left	Velocity Dispersion (mas yr^{-1}) Center	Velocity Dispersion (mas yr^{-1}) Right
Simulation 1	0.1804 ± 0.0004	0.166 ± 0.002	8.0	1.4	2.4	12.5	0.180 ± 0.001	0.180 ± 0.001	0.180 ± 0.001
Simulation 2	0.1995 ± 0.0005	0.183 ± 0.001	8.2	12.7	18.4	54.4	0.196 ± 0.001	0.196±0.001	0.193±0.001
Simulation 3	0.1488 ± 0.0005	0.137 ± 0.001	7.9	4.3	5.0	19.6	0.148 ± 0.001	0.148 ± 0.001	0.148 ± 0.001
Simulation 4	0.1670 ± 0.0006	0.158 ± 0.001	5.4	16.1	22.7	59.0	0.165 ± 0.001	0.164 ± 0.001	0.164 ± 0.001
Simulation 5	0.2110 ± 0.0004	0.199 ± 0.002	5.7	2.0	3.0	15.5	0.211 ± 0.001	0.210 ± 0.001	0.210 ± 0.001
Simulation 6	0.2255 ± 0.0004	0.205 ± 0.001	9.1	6.4	11.3	45.7	0.223 ± 0.001	0.224 ± 0.001	0.220 ± 0.001

Note. Binaries have a lower velocity dispersion due to the effect of energy equipartition. The global values of velocity dispersion are consistent for different color bins, except for the more concentrated simulations with high binary fractions (Simulation 2 and 6).

For each simulation, we calculate the global value of velocity dispersion for binaries and single stars within the FOV and their percentage difference. The differences range between $\simeq$5% and $\simeq$9%. The values are reported in Table 2.

We now consider the more realistic case in which we cannot distinguish binaries from single stars. Since unresolved binaries are seen as single stars with fluxes given by the sum of two stellar components, we expect them to be located preferentially on the redder side of the main sequence (see Figure 1). We divide the main sequence into three color bins restricted to the FOV of 4 arcmin and with r-band magnitudes between 17 and 24 mag. We label them as left, center, and right bins, each containing one-third of the stars ($\approx$20,000–50,000 stars each, depending on the simulation). We calculate the fraction of binaries contaminating each color bin and the corresponding velocity dispersion without distinguishing binaries from single stars. We report the values in Table 2.

As expected, the right (redder) bins have a higher contamination of binaries, up to $\simeq$60%. However, the velocity dispersions for the different color bins are consistent with each other, except for Simulation 2 and Simulation 6. These two simulations are, in fact, characterized by high binary contamination in the right color bin (54.4% and 45.7%, respectively) and show a small ($\simeq$0.1 km s^{-1}, 1.5% of the velocity dispersion) but significant difference in the global velocity dispersion at the 2σ level. In contrast, Simulation 4, even though characterized by a 59.0% binary contamination in the right bin, does not display color-dependent kinematic differences. This is explained by the fact that this simulation is the least concentrated ($c = 1.12$) and reaches a low level of partial energy equipartition, and hence displays a weak kinematic dependence on stellar mass (see Bianchini et al. 2016).

We note that the differences obtained in the velocity dispersion depend on the assumption for the photometric errors: assuming a more accurate photometry would enable us to distinguish binaries from single stars more efficiently. This would allow us to measure larger differences in velocity dispersion between the color bins.

Figure 2 shows a comparison between the velocity-dispersion profiles of the three color bins, and the corresponding profiles for single stars and binaries only. For Simulations 2 and 6, the kinematic difference becomes larger in the central region, where the binary fraction increases. In particular, in the central region of Simulation 6, the right color bin differs from the left and the center bins by $\approx$0.015 mas yr^{-1} (0.35 km s^{-1} at 5 kpc, corresponding to $\approx$6% of the central velocity dispersion), with a significance of 3.5σ.

4. APPLICATION TO *HST* PROPER MOTIONS OF NGC 7078

We apply the analysis described above to the HSTPROMO proper motions of NGC 7078 (M15, Bellini et al. 2014), consisting of 74,831 stars in a field of $\approx$180 × 195 arcsec^2 around the center of the cluster, for which color information from the F606W and F814W bands are available. We choose NGC 7078, since a detailed understanding of the sample's quality is already available and discussed in Bellini et al. (2014).

We perform the analysis on a high-quality subsample of the data in which the contaminant stars and mismatched proper motions are rejected, and only highly accurate proper motions are considered. We follow the selection criteria outlined in Section 7.5 of Bellini et al. (2014) and restrict our analysis to the main-sequence stars between 19.5 and 22.5 F606W magnitude. The final sample consists of 12,027 stars with an average proper-motion error of 0.07 mas yr^{-1} (corresponding to 3.4 km s^{-1} at 10.4 kpc, Harris 1996, 2010 edition).

Figure 3 shows the velocity-dispersion profiles for the color bins. The global velocity dispersions are 0.214 ± 0.003, 0.207 ± 0.003, and 0.213 ± 0.003 mas yr^{-1}, for the left, central, and right bins respectively, measured with an accuracy of $\sim$1.5%. The maximum difference is found between the central and left bins, corresponding to 2% of the velocity dispersion, and the velocity dispersions are still consistent within less than 2σ. Therefore, we do not detect any significant difference between the profiles, ascribeble to the presence of binaries. This is consistent with the low binary fraction of 3 ±1% measured in NGC 7078 (Milone et al. 2012) similar to our Simulation 1, where binaries do not lead to any kinematic signatures.

Finally, we note that NGC 7078 is known to host at least three stellar populations (e.g., Piotto et al. 2015) differing in helium abundances (and therefore main-sequence colors). The lack of velocity dispersion differences between the color bins (Figure 3) can be interpreted in the context of multiple stellar populations as an indication of the absence of significant kinematic differences among them, in the inner $\simeq$2 arcmin.

5. CONCLUSIONS

We investigated and quantified the effect of unresolved binaries on GC proper-motion dispersion profiles using Monte

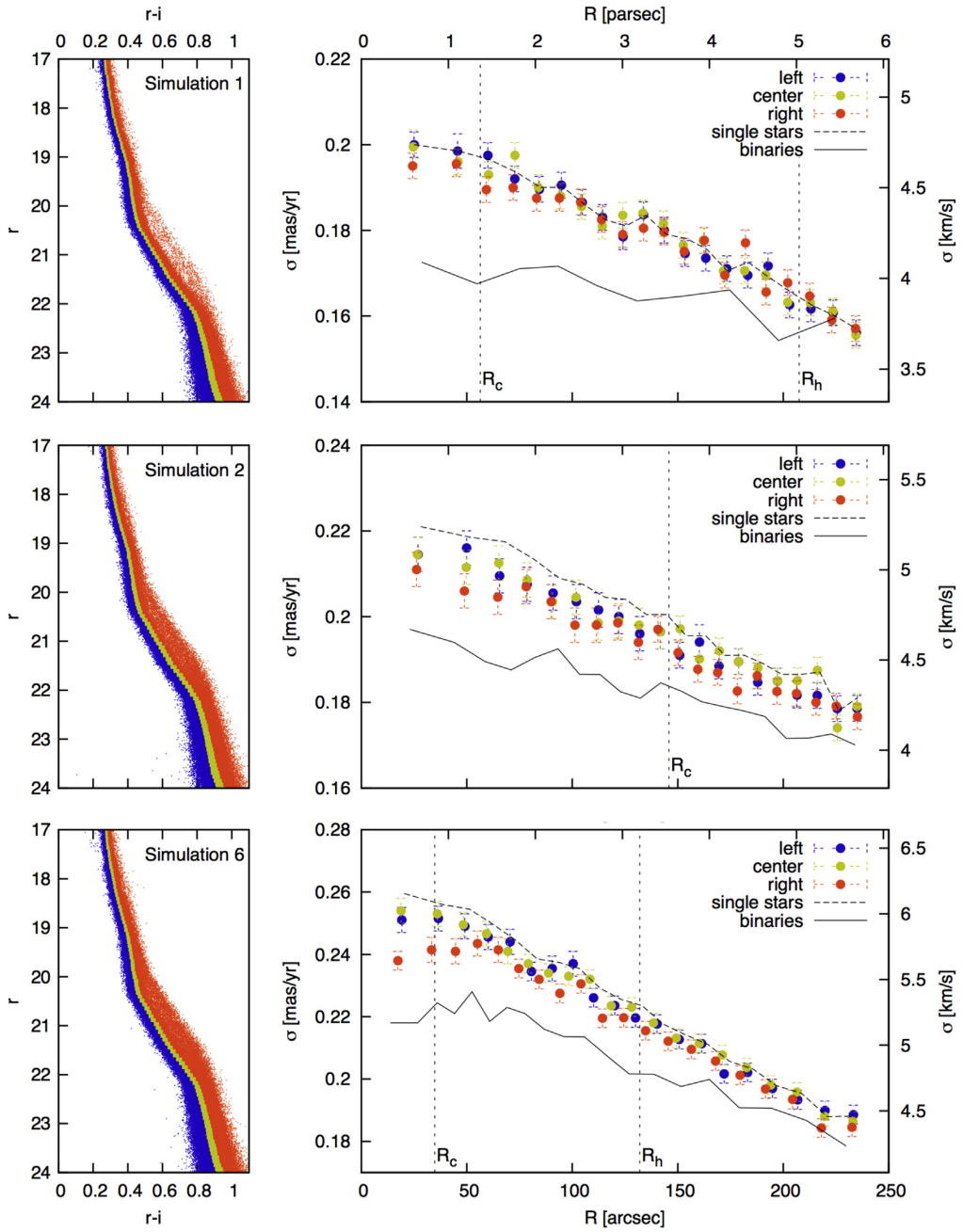

Figure 2. Left: color–magnitude diagrams for the main sequence of our simulated data divided into three color bins, each containing one-third of the stars. Right: velocity-dispersion profiles for the left, center, and right color bins (blue, yellow, red, respectively). The profiles are constructed without distinguishing between single stars and binaries. The velocity-dispersion profiles for single stars and for binaries are shown by dashed and solid black lines, respectively. The vertical dotted lines indicate the core radii R_c and the half-light radii R_h. Simulations 1, 2, and 6 are shown. The first shows no difference in velocity dispersion with color, while the second and the last, characterized by a high binary contamination $\simeq$50% in the right bins (see Table 2), show significant kinematic differences (up to 0.35 km s^{-1}, corresponding to 6% of the central velocity dispersion) that become more pronounced in the center due to increasing binary fractions due to mass segregation.

Carlo cluster simulations. The simulations cover a large range of concentrations and binary fractions (from $\simeq$5% to $\simeq$30%) and reach a state of partial energy equipartition that imprints a lower velocity dispersion on binary stars (that are, on average, more-massive kinematic tracers than the single stars). From the analysis of the simulations, treated similarly to *HST* proper-motion samples, we conclude the following.

1. Binaries can introduce a color-dependent bias in the velocity dispersion calculated for the main sequence, with

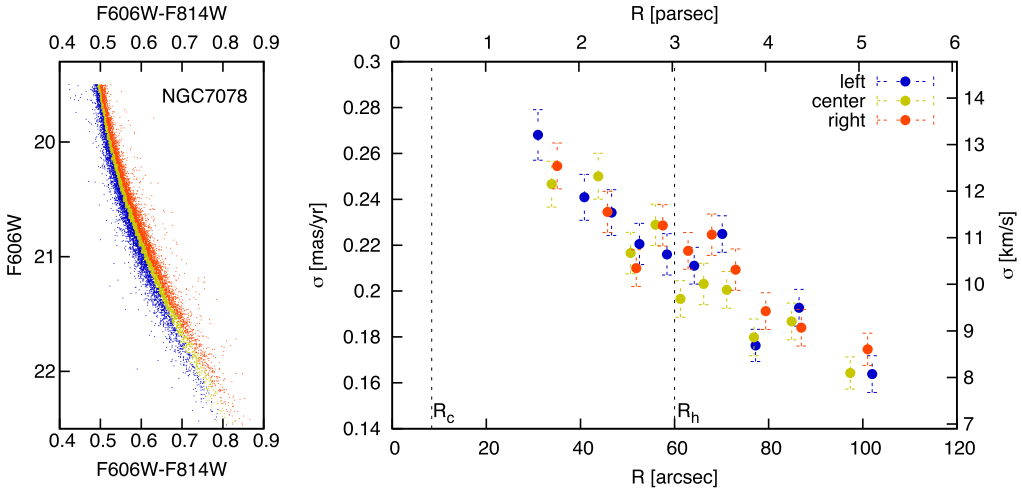

Figure 3. Left: color–magnitude diagram for the main-sequence stars of NGC 7078 with high-quality measured HSTPROMO proper motions from Bellini et al. (2014; photometry from Anderson et al. 2008). Each color bin contains ≈4000 stars. Right: velocity-dispersion profiles for each of the color bins as in Figure 2. The three profiles are consistent with each other and do not show any kinematic signature ascribable to the presence of binary stars, consistent with the low binary fraction measured for NGC 7078 of 3 ± 1% in the observed field of view (Milone et al. 2012).

the reddest stars showing a lower velocity dispersion, due to the higher fraction of contaminating binaries. Only simulations with a high binary fraction (an initial binary fraction of 50%) and a high concentration (i.e., more efficient in reaching a state closer to energy equipartition, hence displaying a stronger mass-dependence of their kinematics, Bianchini et al. 2016) show a significant difference in velocity dispersion, of the order of 0.1–0.3 km s^{-1} (Simulation 2 and Simulation 6), corresponding to 1%–6% of the velocity dispersion. The effect is larger in the center where the binary fraction increases. The low level of the bias indicates that proper-motion data are less affected by binaries than typical line-of-sight samples. Note that the color-dependent bias due to the presence of binaries is a generic result, merely due to the presence of a stellar component more massive than average on the red side of the main sequence; however, the quantitative details could depend on the specific initial conditions adopted, in particular, on the ability of efficiently distinguish binaries from single stars, the shape of the color–magnitude diagram, and the photometric errors.

2. With state-of-the-art *HST* proper-motion data (Bellini et al. 2014; Watkins et al. 2015a, 2015b) it is possible to measure such low kinematic differences since sufficient stars are available to achieve low random errors. However, at this very low error level, other systematic effects can influence the measurements (e.g., contaminant stars, mismatched proper motions, or astrometric blends, Bellini et al. 2014), making the detection of the kinematic effects of binaries challenging. This suggests that the kinematic impact of binaries, quantified in our work, must be taken into account in the error budget of any proper-motion analysis of *HST* data. This is particularly important in the context of multiple stellar populations, where different color bins could contain different stellar populations, with possible intrinsically different kinematics (see Richer et al. 2013; Bellini et al. 2015; Henault-Brunet et al. 2015).
3. We applied our analysis to the high-quality HSTPROMO data set of NGC 7078. The velocity dispersions are measured with an accuracy ∼1.5% and we confirm that no kinematic effects due to unresolved binaries is detectable, consistent with the predictions from our simulations for a low binary fraction GC (<5%). This analysis can be interpreted in the context of multiple stellar populations as an indication of the lack of significant kinematic differences among the stellar populations of NGC 7078.

We are grateful to Jonathan M. B. Downing for providing the Monte Carlo simulations used in this work. P.B. thanks Anna Sippel for interesting comments and discussions. A.B. acknowledges support from HST grant AR-12845, provided by the Space Telescope Science Institute, which is operated by AURA, Inc., under NASA contract NAS 5-26555. This work was supported by Sonderforschungsbereich SFB 881 "The Milky Way System" (subproject A7 and A8) of the German Research Foundation (DFG). We thank the referee for helping to improve the quality of our manuscript.

REFERENCES

Anderson, J., Sarajedini, A., Bedin, L. R., et al. 2008, AJ, 135, 2055
Anderson, J., & van der Marel, R. P. 2010, ApJ, 710, 1032
Baldwin, A., Watkins, L. L., van der Marel, R. P., et al. 2016, ApJ, submitted
Bellini, A., Anderson, J., van der Marel, R. P., et al. 2014, ApJ, 797, 115
Bellini, A., Vesperini, E., Piotto, G., et al. 2015, ApJL, 810, L13
Bianchini, P., van de Ven, G., Norris, M. A., Schinnerer, E., & Varri, A. L. 2016, MNRAS, in press
Bradford, J. D., Geha, M., Munoz, R. R., et al. 2011, ApJ, 743, 167
Downing, J. M. B., Benacquista, M. J., Giersz, M., & Spurzem, R. 2010, MNRAS, 407, 1946
Giersz, M. 1998, MNRAS, 298, 1239
Harris, W. E. 1996, AJ, 112, 1487
Henault-Brunet, V., Gieles, M., Agertz, O., & Read, J. I. 2015, MNRAS, 450, 1164

Kroupa, P. 1995, MNRAS, 277, 1491
Kroupa, P. 2001, MNRAS, 322, 231
Kroupa, P., Tout, C. A., & Gilmore, G. 1993, MNRAS, 262, 545
McConnachie, A. W., & Cote, P. 2010, ApJL, 722, L209
McLaughlin, D. E., Anderson, J., Meylan, G., et al. 2006, ApJS, 166, 249
McNamara, B. J., Harrison, T. E., & Anderson, J. 2003, ApJ, 595, 187
McNamara, B. J., Harrison, T. E., Baumgardt, H., & Khalaj, P. 2012, ApJ, 745, 175
McNamara, B. J., & McKeever, J. 2011, AJ, 142, 163
Milone, A. P., Marino, A. F., Bedin, L. R., et al. 2016, MNRAS, 455, 3009
Milone, A. P., Piotto, G., Bedin, L. R., et al. 2012, A&A, 540, A16
Minor, Q. E., Martinez, G., Bullock, J., Kaplinghat, M., & Trainor, R. 2010, ApJ, 721, 1142
Piotto, G., Milone, A. P., Bedin, L. R., et al. 2015, AJ, 149, 91
Plummer, H. C. 1911, MNRAS, 71, 460
Pryor, C., & Meylan, G. 1993, in ASP Conf. Ser. 50, Structure and Dynamics of Globular Clusters, ed. S. G. Djorgovski, & G. Meylan (San Francisco, CA: ASP), 357
Richer, H. B., Heyl, J., Anderson, J., et al. 2013, ApJL, 771, L15
Sollima, A., Beccari, G., Ferraro, F. R., Fusi Pecci, F., & Sarajedini, A. 2007, MNRAS, 380, 781
Trenti, M., & van der Marel, R. 2013, MNRAS, 435, 3272
Watkins, L. L., van der Marel, R. P., Bellini, A., & Anderson, J. 2015a, ApJ, 803, 29
Watkins, L. L., van der Marel, R. P., Bellini, A., & Anderson, J. 2015b, ApJ, 812, 149

Chapter 6

Energy equipartition in globular clusters

"*A novel look at energy equipartition in globular clusters*"
Bianchini, P.; van de Ven, G.; Norris, M. A.; Schinnerer, E.; Varri, A. L.
Monthly Notices of the Royal Astronomical Society, Volume 458, Issue 4, p.3644-3654
`http://adsabs.harvard.edu/abs/2016MNRAS.458.3644B`

This Chapter focuses on the onset of energy equipartition in GCs, resulting from their long-term evolution driven by two-body interactions. The main question that is addressed here is how the degree of energy equipartition can be quantified using kinematic data only. This work is motivated by the comprehensive kinematic observations of GCs now available, sampling a large number of stars in a mass range between $\simeq 0.4 - 0.9\ M_{\odot}$ (line-of-sight velocities coupled with proper motions). These data will allow the direct measurements of the kinematics, that is the direct consequence of the onset of partial energy equipartition. With the analysis of a set of Monte Carlo cluster simulations, I will introduce a novel way to quantify the mass dependence of the kinematics and correlate it to the relaxation state of a cluster. This tight relation between the degree of energy equipartition and the relaxation condition will serve as a tool to measure the dynamical state of a cluster, setting the first step to disentangle those clusters that underwent a standard evolution from those that experienced a peculiar dynamical evolution.

Monthly Notices of the ROYAL ASTRONOMICAL SOCIETY

MNRAS **458,** 3644–3654 (2016) doi:10.1093/mnras/stw552
Advance Access publication 2016 March 8

A novel look at energy equipartition in globular clusters

P. Bianchini,[1]★† G. van de Ven,[1] M. A. Norris,[1,2] E. Schinnerer[1] and A. L. Varri[3]

[1]*Max-Planck Institute for Astronomy, Koenigstuhl 17, D-69117 Heidelberg, Germany*
[2]*University of Central Lancashire, Preston PR1 2HE, UK*
[3]*School of Mathematics and Maxwell Institute of Mathematical Sciences, University of Edinburgh, King's Buildings, Edinburgh EH9 3JZ, UK*

Accepted 2016 March 2. Received 2016 March 2; in original form 2015 December 21

ABSTRACT

Two-body interactions play a major role in shaping the structural and dynamical properties of globular clusters (GCs) over their long-term evolution. In particular, GCs evolve towards a state of partial energy equipartition that induces a mass dependence in their kinematics. By using a set of Monte Carlo cluster simulations evolved in quasi-isolation, we show that the stellar mass dependence of the velocity dispersion $\sigma(m)$ can be described by an exponential function $\sigma^2 \propto \exp(-m/m_{\rm eq})$, with the parameter $m_{\rm eq}$ quantifying the degree of partial energy equipartition of the systems. This simple parametrization successfully captures the behaviour of the velocity dispersion at lower as well as higher stellar masses, that is, the regime where the system is expected to approach full equipartition. We find a tight correlation between the degree of equipartition reached by a GC and its dynamical state, indicating that clusters that are more than about 20 core relaxation times old, have reached a maximum degree of equipartition. This equipartition–dynamical state relation can be used as a tool to characterize the relaxation condition of a cluster with a kinematic measure of the $m_{\rm eq}$ parameter. Vice versa, the mass dependence of the kinematics can be predicted knowing the relaxation time solely on the basis of photometric measurements. Moreover, any deviations from this tight relation could be used as a probe of a peculiar dynamical history of a cluster. Finally, our novel approach is important for the interpretation of state-of-the-art *Hubble Space Telescope* proper motion data, for which the mass dependence of kinematics can now be measured, and for the application of modelling techniques which take into consideration multimass components and mass segregation.

Key words: stars: kinematics and dynamics – globular clusters: general.

1 INTRODUCTION

The apparent simplicity of Galactic globular clusters (GCs) is the result of their >10 Gyr evolution driven by the complex interplay of gravitational encounters (dynamical two-body interactions between stars), interactions with the host galaxy and internal stellar astrophysical processes. The deep understanding of these evolutionary ingredients is the key to interpret their current internal properties and to reveal their formation during the earliest epochs of galaxy formation.

In particular, gravitational encounters, over the two-body relaxation time-scale, are crucial in shaping the internal structural and dynamical properties of GCs. One of the effects of two-body interactions is to bring a system towards a state of thermalization, where stars with different masses approach the same energy (Spitzer 1987). This is known as energy equipartition: massive stars lose kinematic energy sinking towards the centre of the cluster, while, vice versa, low-mass stars gain kinetic energy and move towards the outer parts. This produces a mass dependence of the kinematics with massive stars displaying a lower velocity dispersion than low-mass stars, and furthermore induces mass segregation.

Starting from the early work of Spitzer (1969), studies have been devoted to the understanding of how the process of energy equipartition takes place in GCs, pointing out that in a simple two-mass component system, energy equipartition is not always reached. Depending on the mass ratio of the particles of different species (m_1/m_2), as well as their contribution to the total mass of the system (M_1/M_2), the self-gravity of the heavier stars can dominate the potential in the core, and create a sub-system which is dynamically separated from the lighter components. Such a sub-system will no longer be in energy equipartition with the rest of the system, and it may even undergo gravothermal collapse, while the light stars will not ('Spitzer instability'). This result was later generalized by Vishniac (1978) for the case of a continuous mass spectrum.

★ E-mail: bianchini@mpia.de
† Member of the International Max Planck Research School for Astronomy and Cosmic Physics at the University of Heidelberg, IMPRS-HD, Germany.

Even in the Spitzer-stable case, many additional elements should be taken into account, in particular the fact that the distribution of the velocities of the stars in the system is affected also by the change of the potential itself, due to the change of the spatial distribution of the stars. Calculations have been performed with various models for the density-potential pairs, usually for the simple case of a two-component system (e.g. see Lightman & Fall 1978 the case of homogeneous spheres, or Inagaki & Wiyanto 1984 for Fokker–Planck models). Relatively fewer studies have considered the evolution of multimass systems, but the lack of energy equipartition emerged very emphatically especially in the Fokker–Plank study by Inagaki & Saslaw (1985).

This issue has been explored also by means of multimass *N*-body simulations, which have offered convincing evidence that collisional systems reach a state of only partial energy equipartition, especially in the outer regions (e.g. see Baumgardt & Makino 2003, section 3.5; Khalisi, Amaro-Seoane & Spurzem 2007). More recently, Trenti & van der Marel (2013) performed a systematic *N*-body study to characterize the dependence of the velocity dispersion on mass $\sigma(m)$, in terms of the scaling $\sigma \propto m^{-\eta}$ (where $\eta = 0.5$ corresponds to full equipartition). They find that $\eta < 0.5$, i.e. corresponding to only partial energy equipartition. Moreover, the lack of energy equipartition has also been tested with direct *N*-body simulations in the regime of open clusters (Spera, Mapelli & Jeffries 2016). Finally, an additional confirmation of the lack of energy equipartition in GCs comes also from the side of distribution function-based models, especially lowered isothermal multimass equilibria (see the appendix).

Even though GCs are not in full energy equipartition, the mass dependence of kinematics represents an additional complication to take into consideration for a complete understanding of the current internal dynamics of GCs. In fact, traditional modelling techniques that do not take into consideration this mass dependence present limitations that in general should be fully explored (Shanahan & Gieles 2015; Sollima et al. 2015). Secondly, the evidence of mass-dependent kinematics should motivate the development and the application of multimass models, which could provide a more comprehensive and realistic description of the internal dynamics of GCs (e.g. the multimass generalization of the classic King models, proposed by Da Costa & Freeman (1976) or the recently developed family of multimass lowered isothermal models by Gieles & Zocchi 2015).

Mass-dependent kinematics is now within reach of our observational capabilities, thanks to the combination of traditional spectroscopic-based line-of-sight velocities and high-precision *Hubble Space Telescope* (*HST*) proper motions studies. In particular, the latter provide samples up to 100 × larger than the traditional line-of-sight velocity data sets, and allow us to measure the velocities for both giant stars and less-massive main sequence stars (see HSTPROMO data sets for 22 GCs, Bellini et al. 2014; Watkins et al. 2015a,b; Baldwin et al. 2016; Bianchini et al. 2016; and references therein for other proper motion samples for specific GCs).

We therefore wish to introduce a novel approach for the analysis of energy equipartition in GCs suitable for applications to *both simulations and observations*. Traditionally, the mass-dependent kinematics have been analysed using the simple power-law dependence of the velocity dispersion on mass, $\sigma \propto m^{-\eta}$, that strictly is only valid for restricted stellar mass ranges (Trenti & van der Marel 2013). Fitting this function to simulations showed that the η parameter is higher at the higher mass end (stellar remnants) than for the lower mass stars, indicating that a mass dependence of η is, in fact, needed. Moreover, the analysis of the simulations has been limited to studies of clusters with fixed relaxation conditions (Trenti & van der Marel 2013), not allowing a direct comparison with real GC systems, characterized by a variety of relaxation conditions.

For this reason our work will be based on two premises. (1) The analysis of energy equipartition will be performed on a set of simulations all observed at a fixed time-snapshot. This gives us the advantage of creating a similarity to what we can actually observe, that is the Milky Way (MW) GCs that can be considered roughly coeval (Meylan & Heggie 1997) and characterized by systems with a variety of relaxation states. (2) Extend the simple power-law $\sigma \propto m^{-\eta}$, introducing a more flexible function that can provide a fit to the mass-dependent velocity dispersion $\sigma(m)$ in the entire stellar mass range with a mass-dependent slope $\eta = \eta(m)$. Additionally, the function should provide a quantitative measure of the degree of energy equipartition reached by a system. The combination of the two points above will allow us to study the variety of mass dependence of kinematics that we could expect for the MW GC system and to find possible correlations of the degree of partial equipartition with cluster properties.

In Section 2 we introduce the set of Monte Carlo cluster simulations used in this work and describe the construction of the $\sigma(m)$ profiles. In Section 3 the new fitting function is introduced and applied to the simulations. Section. 4 is devoted to the analysis of the results of the fits to the simulations and the study of how the degree of partial equipartition relates to cluster properties. In Section 5, we discuss the implication of our findings and, finally we summarize our conclusions in Section 6.

2 SIMULATIONS

We consider a set of Monte Carlo cluster simulations, developed by Downing et al. (2010) with the Monte Carlo code of Giersz (1998) (see also Hypki & Giersz 2013). The simulations include an initial mass function, stellar evolution, primordial binaries, and a relatively high number of particles, providing a realistic description of the long-term evolution of GCs with a single stellar population.[1] No internal rotation is considered.

All simulations have their initial conditions drawn from a Plummer (1911) model, a Kroupa (2001) initial mass function, a metallicity of [Fe/H] = −1.3, and an initial tidal cut-off at 150 pc (making the simulations relatively isolated, comparable to halo clusters at 9–10 kpc from the centre of the MW). We consider a total of six simulations with 500 000 initial particles, characterized by three values of initial concentrations and two values for the initial binary fraction (either 10 per cent or 50 per cent). We also consider an additional simulation with 2 000 000 particles and 10 per cent initial binary fraction. All the snapshots that we will consider here are pre-core collapse[2] and are indicative of typical metal poor GC spanning a large range of initial concentrations, binary fractions, and relatively high number of particles. The details of the initial conditions of the simulations are summarized in Table 1 and described in Downing et al. (2010), expect Sim 7 (10low75-2M), not present in the original work. The quantities used to characterized the

[1] Note that Monte Carlo simulations provide a high degree of realism achievable at low computational costs; moreover, they are consistent with direct *N*-body simulations (Wang et al. 2016).

[2] We restrict our investigations to pre-core collapsed systems since the interplay between mass segregation and core collapse is highly non-trivial; moreover, the majority of MW GCs are expected to be in a pre-core collapsed phase Harris 1996 (2010 edition).

Table 1. Initial conditions of our set of simulations. The original name of the simulations from Downing et al. (2010) are given in parentheses. We report the initial binary fraction $f_{\rm binary}$, the initial ratio of the intrinsic three-dimensional tidal to half-mass radius r_t/r_m, the initial number of particles N, and the initial mass M. Simulations from Downing et al. (2010), except Sim 7, 10low75-2M, Downing (private communication).

	$f_{\rm binary}$	r_t/r_m	N	M [$M_\odot$]
Sim 1 (10low75)	10 per cent	75	5×10^5	3.62×10^5
Sim 2 (50low75)	50 per cent	75	5×10^5	5.07×10^5
Sim 3 (10low37)	10 per cent	37	5×10^5	3.62×10^5
Sim 4 (50low37)	50 per cent	37	5×10^5	5.07×10^5
Sim 5 (10low180)	10 per cent	180	5×10^5	3.63×10^5
Sim 6 (50low180)	50 per cent	180	5×10^5	5.07×10^5
Sim 7 (10low75-2M)	10 per cent	75	20×10^5	7.26×10^5

initial conditions of the simulations are all intrinsic three-dimensional quantities. The simulations were kindly shared by J. M. B. Downing.

We report in Table 2 the properties of the simulations typically assessed by observations, specifically for the time-snapshots at 4, 7, 11 Gyr. We report the concentration c defined as $c = \log(R_t/R_c)$, with R_t the projected tidal radius[3] and R_c the projected core radius; the projected core radius R_c, defined as the radius where the surface density is half of the central surface density;[4] the projected half-light radius R_h, containing half of the luminosity of the cluster; the logarithm of the half-mass relaxation time $T_{\rm rh}$ and the logarithm of the core relaxation time $T_{\rm rc}$. For the relaxation times, we follow the approach of the Harris 1996 (2010 edition) catalogue, that is equation 10 of Djorgovski (1993) for the core relaxation time:

$$T_{\rm rc} = \frac{8.3377 \times 10^6\ {\rm yr}}{\ln(0.4\,N)} \left(\frac{{\rm M}_\odot}{\langle m \rangle}\right) \left(\frac{\rho_0}{{\rm M}_\odot/{\rm pc}^3}\right)^{1/2} \left(\frac{R_c}{\rm pc}\right)^3, \quad (1)$$

with N the number of stars in the cluster, M the mass of the cluster, $\langle m \rangle$ the average stellar mass, and ρ_0 the central density of the cluster.[5] For the half-mass relaxation time we use equations (8–72) of Binney & Tremaine (2008):

$$T_{\rm rh} = \frac{6.5 \times 10^8\ {\rm yr}}{\ln(0.4\,N)} \left(\frac{M}{10^5\,{\rm M}_\odot}\right)^{1/2} \left(\frac{{\rm M}_\odot}{\langle m \rangle}\right) \left(\frac{R_h}{\rm pc}\right)^{3/2}. \quad (2)$$

2.1 Construction of velocity dispersion-mass profiles

In order to quantify the mass dependence of the kinematics of our simulations, we construct the *projected* velocity dispersion profile as a function of stellar mass, $\sigma(m)$. We restrict the analysis to stars within the projected half-light radius[6] R_h (considering a cylinder of radius R_h around the *za*-axis as the line-of-sight direction) and include all the stars of our simulations within the mass range 0.1–1.8 $M_\odot$ (the effect of different stellar objects such as binary stars and stellar remnants is separately discussed in Section 2.2).[7] For every 0.1 $M_\odot$ mass interval, we calculate the projected one-dimensional velocity dispersion and the associated errors, averaging the velocity dispersions of the three spatial coordinates. We point out that we consider projected quantities in order to enable a direct comparison with observations.

2.2 Role of binary stars and stellar remnants

In order to understand the role of different stellar objects in shaping the mass dependence of the velocity dispersion, we analyse separately the $\sigma(m)$ profile for binary stars and for stellar remnants. When considering binaries, we use the kinematics of their centre-of-mass.

Fig. 1 shows the result of our analysis: in the left-hand panels the comparison between all stars and binary stars is reported, while in the right-hand panels the comparison between the profiles with all stars, excluding dark remnants and excluding all remnants. From this we conclude that, for all the time-snapshots analysed, binary stars and stellar remnants follow the same $\sigma(m)$ relation of single stars. However it is worth noting that around 0.6 $M_\odot$ the shape of $\sigma(m)$ shows a systematic dip. The right-hand panels of Fig. 1 indicate that white dwarfs could be responsible for this feature, since the $\sigma(m)$ profile excluding all remnants does not show this dip around 0.6 $M_\odot$.

We investigate the effect of white dwarfs, by plotting in Fig. 2 separately all stars with and without white dwarfs and white dwarfs alone. White dwarfs that have recently formed and with masses around 0.6 $M_\odot$ underwent a severe mass-loss. Their kinematics are not consistent with the one of other stellar objects with comparable mass, since they did not have time to dynamically relax. Therefore they are characterized by a lower velocity dispersion, in agreement with their original higher mass (see also Heyl et al. 2015). As the cluster evolves, two-body interactions slowly reduce this difference, as observed for the more evolved snapshots at 7 and 11 Gyr.

In the following analysis we will construct $\sigma(m)$ profiles excluding white dwarfs, in order to avoid any bias.

3 FITTING THE VELOCITY DISPERSION–MASS PROFILE

We wish to find a parametrization for the $\sigma(m)$ profile that describes the mass dependence of kinematics in the entire stellar mass range sampled and quantifies how close/far from energy equipartition the systems are. Traditionally a power-law $\sigma \propto m^{-\eta}$ has been used for limited ranges of masses, showing that the best-fitting parameter η is higher for the higher mass end (stellar remnants) than for the lower mass stars (Trenti & van der Marel 2013). This indicates the differential behaviour of equipartition that is reached more efficiently in the higher stellar mass regime ($\gtrsim$1 $M_\odot$) than in the lower stellar mass regime, where the $\sigma(m)$ profile flattens ($\lesssim$0.3 $M_\odot$). It is therefore evident that a single η value is not able to describe the entire trend of the $\sigma(m)$ profile and a fitting function with $\eta = \eta(m)$ is needed.

3.1 Exponential fitting function

We propose a simple exponential function, suitable for the entire stellar mass range sampled, and able to reproduce both the flat behaviour in the limit of low stellar masses and the steepening towards higher masses. A physical justification of the asymptotic

[3] Note that the projected tidal radius does not significantly differs from the three-dimensional tidal radius, r_t.
[4] Calculated from number count surface density profiles.
[5] We define the central mass density of the cluster as the density enclosed within $R_h/10$.
[6] GCs kinematics are typically observed within the half-light radius.
[7] The upper limit of 1.8 $M_\odot$ is chosen to guarantee a high enough number of stars per bin, since only a few stars have masses greater than that.

Table 2. Projected properties of the set of simulations for the 4, 7,11 Gyr snapshots. We report the concentration $c = \log(R_t/R_c)$, with R_t and R_c as projected tidal radius and projected core radius, respectively, the half light radius R_h in parsec, core radius R_c in parsec, the logarithm of the half-light relaxation time $T_{\rm rh}$ in yr, and the logarithm of the core relaxation time $T_{\rm rc}$ in yr. All simulations have an initial number of particles of $N = 500\,000$, except for simulation 7 with $N = 2\,000\,000$.

	c			R_h			R_c			$\log T_{\rm rh}$			$\log T_{\rm rc}$		
	4 Gyr	7 Gyr	11 Gyr	4 Gyr	7 Gyr	11 Gyr	4 Gyr	7 Gyr	11 Gyr	4 Gyr	7 Gyr	11 Gyr	4 Gyr	7 Gyr	11 Gyr
Sim 1	1.52	1.46	1.45	4.01	4.23	4.92	2.74	3.12	3.15	9.382	9.487	9.543	9.151	9.172	9.123
Sim 2	1.42	1.38	1.34	4.89	5.92	6.06	3.42	3.62	3.89	9.474	9.579	9.655	9.345	9.287	9.286
Sim 3	1.26	1.21	1.16	7.04	8.16	9.05	4.92	5.52	6.07	9.658	9.755	9.820	9.647	9.656	9.645
Sim 4	1.21	1.16	1.12	8.84	8.96	10.92	5.54	6.11	6.47	9.705	9.803	9.877	9.757	9.776	9.744
Sim 5	1.81	1.95	2.06	1.53	1.90	2.69	1.33	0.96	0.75	9.171	9.263	9.349	8.437	8.033	7.740
Sim 6	1.73	1.74	1.79	2.96	3.10	3.05	1.64	1.56	1.34	9.249	9.347	9.417	8.598	8.472	8.262
Sim 7	1.52	1.52	1.51	2.57	2.62	2.90	1.73	1.87	1.85	9.415	9.498	9.565	9.040	8.965	8.991

limits is described in the Appendix. The function is characterized by a velocity scale parameter σ_0 and one mass scale parameter $m_{\rm eq}$:

$$\sigma(m) = \begin{cases} \sigma_0 \, \exp\left(-\frac{1}{2}\frac{m}{m_{\rm eq}}\right) & \text{if } m \leq m_{\rm eq}, \\ \sigma_{\rm eq} \left(\frac{m}{m_{\rm eq}}\right)^{-1/2} & \text{if } m > m_{\rm eq}. \end{cases} \quad (3)$$

Here, σ_0 indicates the value of velocity dispersion at $m = 0$, while $\sigma_{\rm eq}$ corresponds to the value of velocity dispersion at $m_{\rm eq}$, so that $\sigma_{\rm eq} = \sigma_0 \exp(-\frac{1}{2})$. The parameter $m_{\rm eq}$ quantifies the level of partial energy equipartition reached by the systems. For $m > m_{\rm eq}$ the system is characterized by constant full energy equipartition ($\sigma \propto m^{-1/2}$).

In accordance with the used power-law assumption ($\sigma \propto m^{-\eta}$; Trenti & van der Marel 2013), the slope of our function is

$$\eta(m) = -\frac{d\ln\sigma}{d\ln m} = \begin{cases} \frac{1}{2}\frac{m}{m_{\rm eq}} & \text{if } m \leq m_{\rm eq}, \\ \frac{1}{2} & \text{if } m > m_{\rm eq}. \end{cases} \quad (4)$$

The truncation of the exponential function for $m > m_{\rm eq}$ was introduced in equation (3) in order to avoid values of the slope $\eta > 1/2$ that would unphysically exceed energy equipartition as well as to match the asymptotic limits described in the appendix, based on analytical multimass distribution function-based models (Gieles & Zocchi 2015).

The mass parameter $m_{\rm eq}$ will be used to quantify the degree of equipartition throughout our work: a system has reached equipartition in the stellar mass regime $m \gtrsim m_{\rm eq}$. Systems characterized by *lower* values of $m_{\rm eq}$ are thus *closer* to full energy equipartition.

3.2 Application to the simulations

We apply equation (3) to our set of simulations and quantify, through the parameter $m_{\rm eq}$, the degree of partial equipartition reached by the systems. We perform two fits: one using all stars in the mass range 0.1–1.8 $M_\odot$ (excluding white dwarfs, as explained in Section 2.2) and one restricting to only observable stars in the mass range 0.4–1.0 $M_\odot$ (i.e. we exclude all stellar remnants) in order to match the typical observations.[8]

[8] Kinematic observations are now able to sample both bright (massive) stars and lower-mass stars along the main sequence. In particular, traditional spectroscopic line-of-sight measurements observe giant stars with masses 0.8–0.9 $M_\odot$ (for ∼10 Gyr clusters) and proper motions provide the additional kinematic information for less massive main-sequence stars, down to ∼0.4 $M_\odot$ (Bellini et al. 2014; Watkins et al. 2015a,b); these could be complemented by the state-of-the-art line-of-sight velocities observations by MUSE@VLT, able to sample stars down to ∼0.5 $M_\odot$ (Kamann et al. 2016).

The fit to all the stars is performed to the binned profiles (described in Section 2.1) and will be used to demonstrate the performance of our fitting function. In the case restricted to observable stars only, we use a discrete fitting approach, which is particularly convenient and flexible for an application to real data, where errors or additional sources of contamination need to be included in the fit to the data. In this latter case, we define a likelihood function as

$$L_i = \prod_{i=1}^{N} \frac{1}{\sqrt{2\pi\sigma^2(m_i)}} \exp\left[-\frac{1}{2}\frac{v_i^2}{\sigma^2(m_i)}\right], \quad (5)$$

where $\sigma(m_i)$ is given by equation (3), m_i and v_i are the stellar mass and the velocity of the observed stars, and the free parameters are σ_0 and $m_{\rm eq}$. Note that here we assume a Gaussian velocity distribution with zero mean velocity. The parameter space is explored using EMCEE, an affine-invariant Markov Chain Monte Carlo (MCMC) sampler (Foreman-Mackey et al. 2013) and the mean and associated 1σ errors are returned.

Fig. 3 shows the fit to the entire stellar mass range for one of the simulations. The left-hand panel shows the $\sigma(m)$ profile in a log–log plot, while the right-hand panel in a log-linear plot. The horizontal line intersects the $\sigma(m)$ profile at $m = m_{\rm eq}$, the mass above which the system is in equipartition. In Fig. 4, we show the fits for all our simulations for the different time-snapshots and demonstrate that our fitting function provides an excellent description of the mass dependence of the kinematics in all cases. Minor deviations are observed exclusively in the high stellar mass regime of the most concentrated cluster model, which is likely about to reach the condition of core collapse (see bottom panel, dark orange line).

Table 3 summarizes the results of our fits to both the entire stellar mass range and to the restricted mass range. The two sets of fits give results consistent with each other, as also visualized in Fig. 5. This indicates that using only a stellar mass range restricted to the current observations, it is still possible to obtain a good global description of the entire $\sigma(m)$ profile. In turn, this implies that we can also predict the mass dependence of the kinematics for both low-mass and high-mass stars for which the kinematics are not measurable (including non-observable dark remnants).

The values of $m_{\rm eq}$ obtained from the fits indicate that the systems are, as expected, only in partial energy equipartition, since the typical value of $m_{\rm eq} \gtrsim 1.5$ $M_\odot$ indicates that all the stars sampled below this mass are characterized by a $\sigma(m)$ profile with a local slope $\eta < 1/2$ (see equation 4). In the following section we investigate in detail the relation between the degree of partial energy equipartition reached by a system and its global properties.

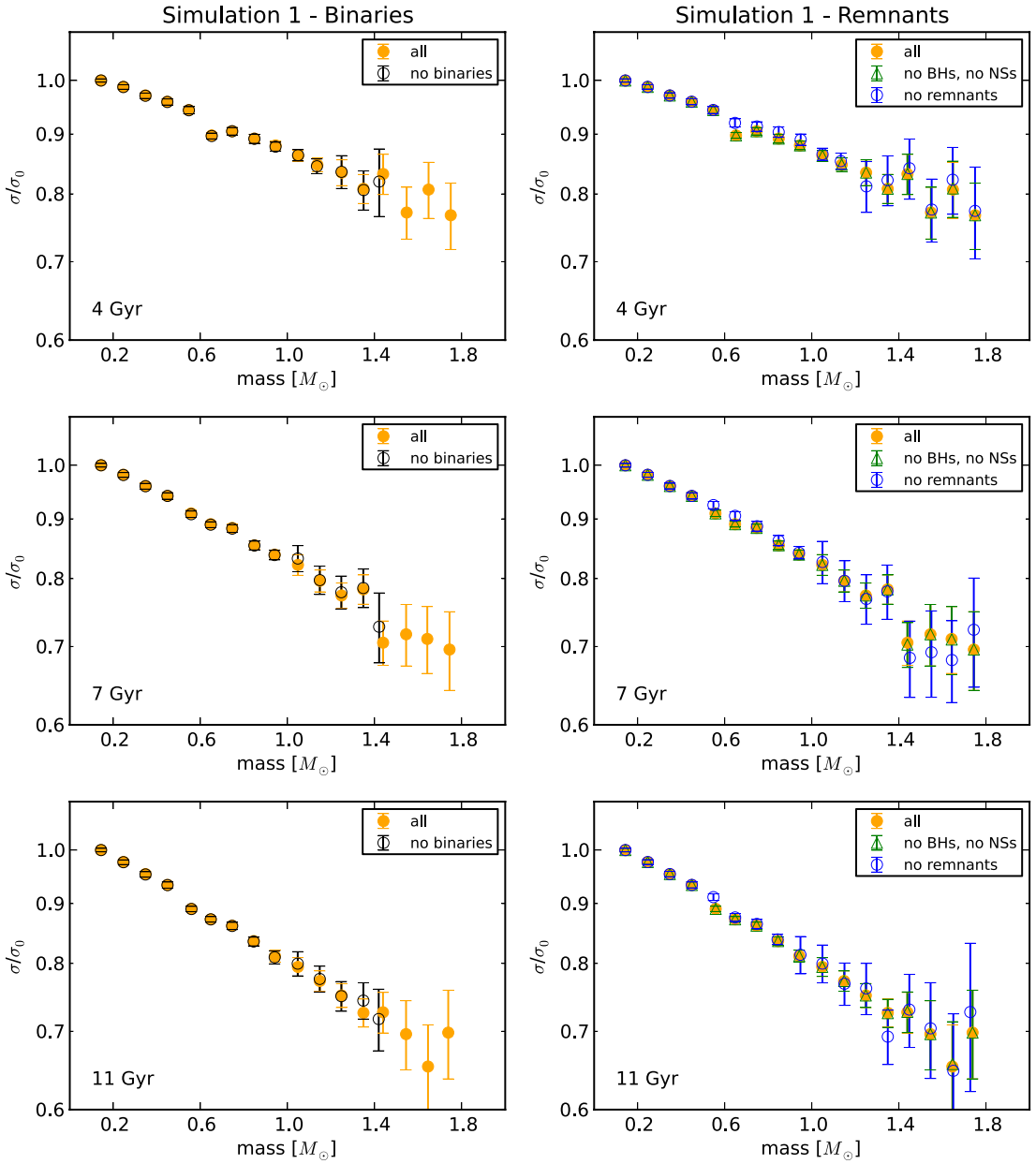

Figure 1. Velocity dispersion as a function of stellar mass for the 4, 7, 11 Gyr snapshots of simulation 1 (from top to bottom), restricted to the stars within the projected half-light radius. The profiles are normalized to the first bin, denoted as σ_0. Left column: velocity dispersions for all stars within the half-light radius (orange circles) and when excluding binary stars only (open black circles). The binaries do not show an offset from the entire sample. Right column: velocity dispersions for all stars within the half-light radius (orange circles), excluding dark stellar remnants (black holes and neutron stars; open green triangles), and excluding all stellar remnants (open clue circles). Stellar remnants do not introduce any significant bias in the velocity dispersions, except for white dwarfs around 0.6 $M_\odot$ (for details, see Fig. 2).

4 DEGREE OF EQUIPARTITION VERSUS CLUSTER PROPERTIES

The fitting function introduced in the previous section allows us to characterize the degree of partial equipartition reached by a cluster through the parameter $m_{\rm eq}$. We now analyse how this parameter correlates with structural properties of the GC simulations.

The first panel of Fig. 6 shows the relation between $m_{\rm eq}$ and the cluster concentration c, for the three time snapshots of 4, 7, 11 Gyr indicated by the different colours and symbols. More concentrated

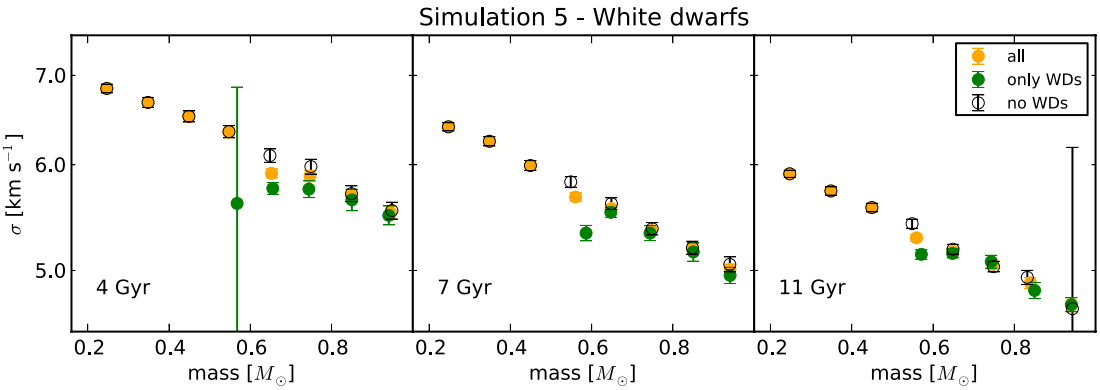

Figure 2. Velocity dispersion as a function of stellar mass for the 4, 7, 11 Gyr snapshots of simulation 5, for all stars within the half-light radius (orange circles), only white dwarf (green circles), and excluding white dwarfs (open black circles). The lowest mass white dwarfs (≈0.6 $M_\odot$) show a lower velocity dispersion than the other stars with similar mass, biasing the velocity dispersion of the sample with all stars towards lower values. The lower velocity dispersion of low-mass white dwarfs can be explained by the fact that they have not reached the same equipartition level as they recently underwent severe mass-loss. The large error bars in the first and last panels are due to low number statistics.

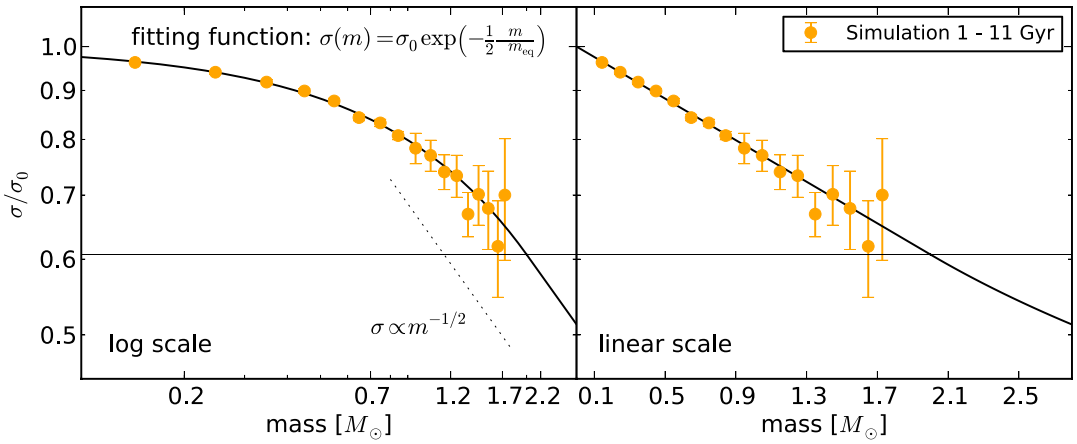

Figure 3. Fit to the projected velocity dispersion as a function of the stellar mass $\sigma(m)$ using the exponential fitting function introduced with equation (3). The free parameter m_{eq} indicates the degree of equipartition reached by the system. The fit is shown for simulation 1 in both a log–log scale (left-hand panel) and in a linear-log scale (right-hand panel) and it is performed on all stars within the half-mass radius. The profiles are normalized at $m = 0$, using the best-fitting parameter σ_0 (see equation 3). The dotted line shows the power-law function $\sigma \propto m^{-1/2}$ indicating full energy equipartition. The horizontal line intersects the fitting function at $m = m_{eq}$; beyond this mass the slope of the fitting function is kept constant at $\sigma \propto m^{-1/2}$ (solid line). The exponential fitting function provides an excellent fit on all the sampled mass range.

clusters are characterized by a lower value of m_{eq}, corresponding to a steeper slope of the $\sigma(m)$ profile and, hence, are closer to energy equipartition (the increase of slope with concentration was already evident in Fig. 4). The plot also shows that the equipartition–concentration relation depends on the age of the cluster: older clusters have reached a state closer to energy equipartition than younger clusters. This explains the three distinct relations, one for each time snapshot in the plot. Note, however, that in view of an application to MW GCs, any age dependence would only be marginally relevant, since all GCs can be safely considered as coeval.

In order to explain this relation between a purely photometric quantity (concentration) and a purely kinematic quantity (the degree of equipartition), we further investigate the role of the relaxation condition of the systems. For this reason, in the second panel of Fig. 6, we plot m_{eq} against the current core relaxation time T_{rc} calculated from equation (1), for the particular time snapshot considered.[9] Clusters with shorter relaxation times show lower values of m_{eq}, indicating that two-body interactions have been more effective in establishing a higher degree of partial energy equipartition, since they have been acting for more relaxation times. However, a small dependence on the cluster age is still noticeable.

In the bottom panel of Fig. 6, we introduce the quantity $n_{rel} = T_{age}/T_{rc}$, with T_{age} the age of the cluster. This quantity indicates the numbers of relaxation times that a cluster has experienced,

[9] We use the core relaxation time since it provides a better description of the relaxation conditions for the central regions, in contrast with the half-light relaxation time that represents an average quantity suitable to describe the system globally.

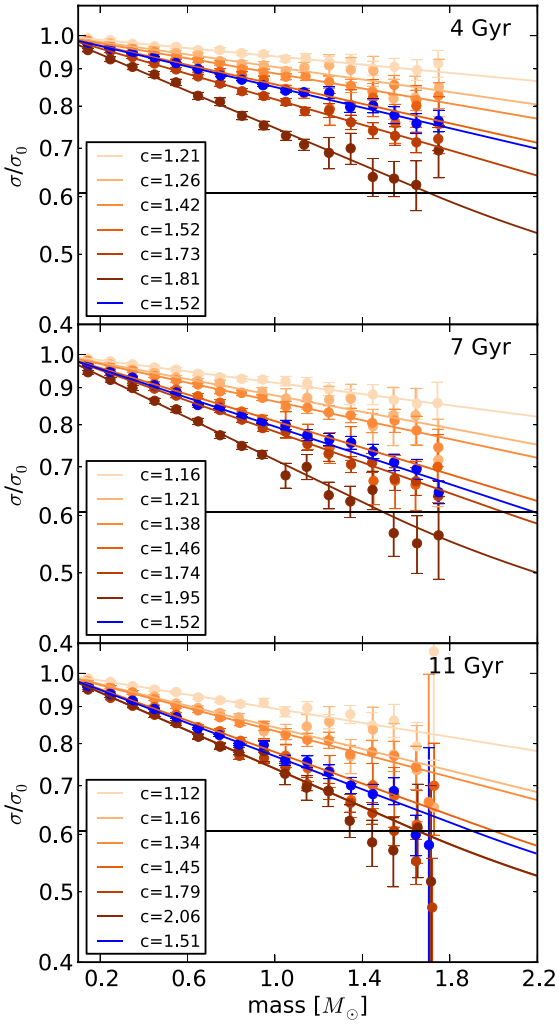

Figure 4. Fit to the projected velocity dispersion as a function of stellar mass for the 4, 7, 11 Gyr snapshots of all our simulations. See Fig. 3 for details on the fit. The simulations are colour coded according to their concentration (orange scale) with the exception of simulation 7 (blue dots), the only simulation with an initial number of particles of 2 000 000. The horizontal line intersects the fitting function at $m = m_{\rm eq}$. The simple exponential function fits well all our simulations in the entire mass range sampled. Minor deviations are observed exclusively in the high-mass regime of the most concentrated cluster model, which is likely about to reach the condition of core collapse (see bottom panel, $c = 2.06$). Given a time snapshot, more concentrated clusters display a steeper velocity dispersion−mass profile. Older snapshots have also steeper relation than younger ones, reflecting the dynamical evolution of the clusters.

with higher $n_{\rm rel}$ corresponding to more relaxed stellar systems. A tight correlation is obtained for $m_{\rm eq} - n_{\rm rel}$, indicating clearly that the establishment of energy equipartition depends on the units of relaxation time experienced by a cluster. Interestingly, clusters with $n_{\rm rel} > 20$ seem to reach an asymptotic maximum value of degree of equipartition, characterized by $m_{\rm eq} \simeq 1.5$ M$_\odot$. These clusters have $\log T_{\rm rc} < 8.5$, and are usually referred to as relaxed GCs, according to the classification of Zocchi, Bertin & Varri (2012).

Table 3. Results of the exponential fit to the 4, 7, 11 Gyr snapshots of all our simulations. The concentration c and the fitted parameters σ_0 and $m_{\rm eq}$ are reported with the associated 1σ errors. For every simulations two fits are performed: one for entire stellar mass range (0.1–1.8 M$_\odot$) and the other for only observable stars in a mass range similar to the one for which kinematic observations are available (0.4–1.0 M$_\odot$). The latter fit is performed to discrete data (see equation 5). Both fits give results consistent with each other.

	c	σ_0 km s^{-1}	$m_{\rm eq}$ M$_\odot$	σ_0 km s^{-1}	$m_{\rm eq}$ M$_\odot$
4 Gyr		all		observable	
Sim 4	1.21	4.50 ± 0.01	7.63 ± 0.28	4.48 ± 0.04	7.36 ± 1.37
Sim 3	1.26	4.17 ± 0.01	5.03 ± 0.18	4.17 ± 0.05	4.59 ± 0.85
Sim 2	1.42	5.82 ± 0.01	4.18 ± 0.08	5.77 ± 0.07	4.36 ± 0.65
Sim 1	1.52	5.46 ± 0.01	3.24 ± 0.08	5.41 ± 0.07	3.42 ± 0.46
Sim 6	1.73	7.28 ± 0.01	2.48 ± 0.03	7.28 ± 0.08	2.35 ± 0.20
Sim 5	1.81	7.38 ± 0.03	1.71 ± 0.04	7.30 ± 0.13	1.76 ± 0.18
Sim 7	1.52	12.42 ± 0.01	3.07 ± 0.04	13.23 ± 0.08	2.43 ± 0.11
7 Gyr		all		observable	
Sim 4	1.16	4.22 ± 0.01	5.58 ± 0.14	4.15 ± 0.05	6.23 ± 1.34
Sim 3	1.21	3.83 ± 0.01	3.84 ± 0.11	3.81 ± 0.05	3.71 ± 0.54
Sim 2	1.38	5.34 ± 0.01	3.36 ± 0.06	5.31 ± 0.06	3.25 ± 0.35
Sim 1	1.46	5.09 ± 0.01	2.37 ± 0.06	5.05 ± 0.07	2.44 ± 0.25
Sim 6	1.74	6.83 ± 0.01	2.04 ± 0.03	6.74 ± 0.08	2.13 ± 0.17
Sim 5	1.95	6.94 ± 0.03	1.50 ± 0.03	6.95 ± 0.12	1.47 ± 0.11
Sim 7	1.52	11.99 ± 0.03	2.19 ± 0.05	12.73 ± 0.08	1.78 ± 0.06
11 Gyr		all		observable	
Sim 4	1.12	3.89 ± 0.01	4.46 ± 0.15	3.86 ± 0.05	4.47 ± 0.84
Sim 3	1.16	3.62 ± 0.01	2.92 ± 0.11	3.63 ± 0.05	2.72 ± 0.36
Sim 2	1.34	5.12 ± 0.01	2.73 ± 0.04	4.99 ± 0.06	3.22 ± 0.44
Sim 1	1.45	4.88 ± 0.01	2.00 ± 0.04	4.97 ± 0.07	1.75 ± 0.14
Sim 6	1.79	6.63 ± 0.02	1.65 ± 0.03	6.55 ± 0.10	1.69 ± 0.13
Sim 5	2.06	6.34 ± 0.03	1.66 ± 0.05	6.43 ± 0.12	1.51 ± 0.13
Sim 7	1.51	11.42 ± 0.02	1.90 ± 0.03	12.20 ± 0.09	1.54 ± 0.06

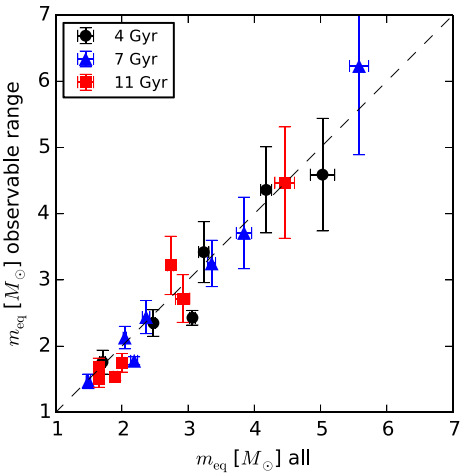

Figure 5. Comparison of the $m_{\rm eq}$ parameter of our simulations obtained from the fits to the entire stellar mass range 0.1–1.8 M$_\odot$ and from the fits (on discrete data, see equation 5) restricted to the observable mass range 0.4–1.0 M$_\odot$. The fits to the observable mass range still allow for a good global description of the entire $\sigma(m)$ profile.

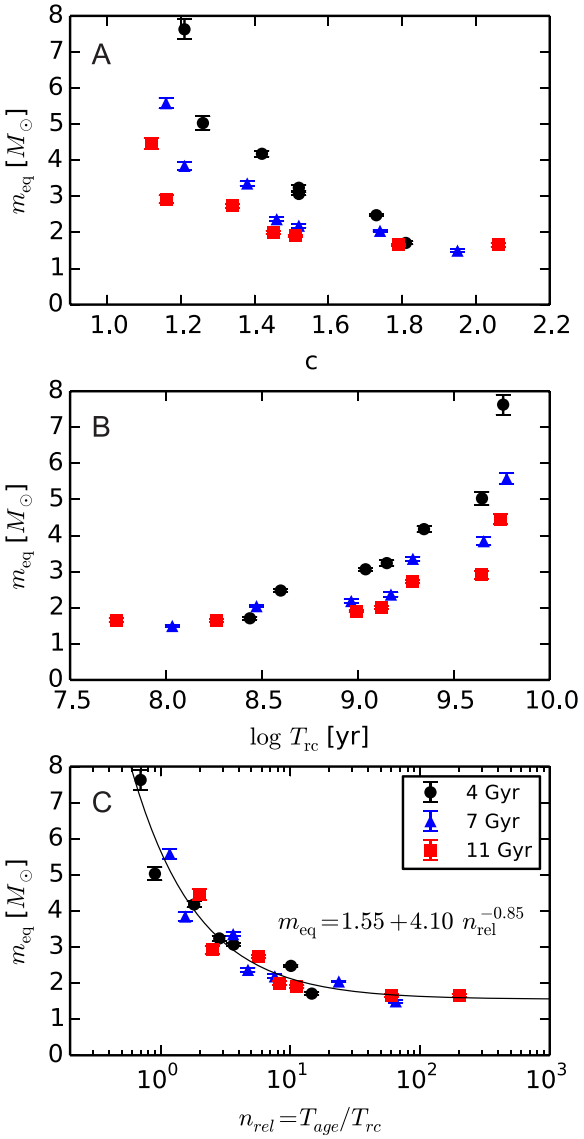

Figure 6. Correlation between different cluster properties and the parameter m_{eq} obtained from the fits to the simulations. From top to bottom: the cluster concentration $c = \log(R_t/R_c)$ (panel A), the logarithm of the current core relaxation time T_{rc} (panel B), and the numbers of relaxation times experienced by a cluster $n_{rel} = T_{age}/T_{rc}$, with T_{age} the age of the cluster (panel C). These plots demonstrate that the level of energy equipartition reached by a cluster depends on its relaxation condition. Well-relaxed clusters (characterized by $n_{rel} > 20$) reach a maximum value for the degree of energy equipartition. The solid line in panel C is the best fit for the $m_{eq} - n_{rel}$ correlation, see Section 5.

A further discussion of the implications of the $m_{eq} - n_{rel}$ is presented in Section 5.

5 THE DYNAMICAL STATE OF A CLUSTER

We have shown that the degree of partial equipartition primarily correlates with the relaxation condition of the clusters (number of relaxation times that a cluster has experienced). Additionally, a dependence on concentration and age is also visible.

The cluster simulations used in this work are all initialized with the same tidal cut-off that sets them into a relatively isolated initial condition, suitable for halo clusters at 9–10 kpc from the Galactic Center (see Downing et al. 2010 for details). Moreover, note that the simulations did not undergo core collapse. Our work therefore does not take into consideration such a particularly complex phase of star clusters dynamical evolution. However, the homogeneity of our set of simulations still allows us to investigate the fundamental effects that are solely connected to the internal dynamical processes.

Here, we focus primarily on the implications of the correlation between the relaxation condition of the cluster and the degree of energy equipartition. In fact, this is a more sound relation between two well connected internal dynamical properties of the clusters. It provides also a straightforward interpretation: more relaxed clusters have reached a higher degree of partial energy equipartition.

This relation can provide a fundamental tool to measure the relaxation condition of a cluster. Relaxation time, as used in this work, is a quantity accessible observationally from solely photometric quantities and it is already available for MW GCs Harris 1996 (2010 edition). The degree of partial energy equipartition can be efficiently determined using the parameter m_{eq} of the fitting function defined in equation (3), applied to a combination of line-of-sight velocities and state-of-the-art *HST* proper motion data sets.

We fit a power-law to the $m_{eq} - n_{rel}$ relation in the bottom panel of Fig. 6 and obtain

$$m_{eq} = (1.55 \pm 0.23) + (4.10 \pm 0.31)\, n_{rel}^{-0.85\pm0.12}, \quad (6)$$

and the corresponding inverse function

$$n_{rel} = 5.28 \pm 1.35\, (m_{eq} - 1.55 \pm 0.23)^{-1.18\pm0.17}. \quad (7)$$

Given the $m_{eq} - n_{rel}$ relation, with a measure of $n_{eq} = T_{age}/T_{rc}$ is possible to predict the m_{eq} parameter, hence the mass dependence of the kinematics for a given GC. In this way, the $m_{eq} - n_{rel}$ relation can be used to predict the dynamics of dark stellar remnants or of other stars for which the kinematics are not easily available (see Baldwin et al. 2016 for an application to blue straggler stars, and Bianchini et al. 2016 for binary stars). This is fundamental since it can allow us to carry out a complete dynamical analysis without neglecting the effect of partial energy equipartition and mass dependent kinematics. In addition, it offers a reference framework for a direct comparison with multimass modelling techniques (e.g. Gieles & Zocchi 2015). Interestingly, Gieles & Zocchi (2015) also find a correlation between the degree of energy equipartition and concentration (defined as the central depth of the potential) for their recently developed multimass distribution function models (see first panel Fig. 6 and the appendix).

Inversely, with a kinematic measure of m_{eq}, one can predict the n_{rel} for a given cluster and therefore characterize its relaxation condition and provide a dynamical age, indicating at which stage of evolution the system is. Therefore, the correlation between energy equipartition and relaxation time found here offers an additional dynamical age estimator to be added to those introduced in the literature. In particular, Ferraro et al. (2012) introduced a dynamical clock calibrated on the radial distribution of blue stragglers stars (see also Alessandrini et al. 2014). This is based on the fact that the radial distribution of blue stragglers stars is determined by mass segregation (as a consequence of two-body relaxation leading to partial energy equipartition) and therefore it depends on the dynamical age of the cluster. Our approach, purely based on kinematics, allows one to

look at the same problem from an independent and complimentary perspective.

Finally, the relations shown in this work can potentially be used as a tool to highlight the complexity of the evolutionary path of a cluster. In fact, any deviations from the tight $m_{\rm eq} - n_{\rm rel}$ relation determined here for the non-rotating quasi-isolated clusters, could be used to infer a complex dynamical evolution of a particular cluster, highlighting for example post-core collapse clusters, presence of intermediate-mass black holes, clusters with a peculiar orbit around the MW, accretion versus *in situ* formation, or other peculiar formation environments (e.g. nucleus of dwarf galaxies). In parallel, also the relation between degree of equipartition and concentration (first panel Fig. 6) can be used to single out complex evolutionary paths.

6 CONCLUSIONS

Two-body interactions shape the internal structure and dynamics of GCs over their long-term evolution, bringing the systems in a state of partial energy equipartition characterized by mass-dependent kinematics. In this work, we introduced a novel approach to characterize the degree of partial energy equipartition reached by GCs suitable for both simulations and observations, and we investigated its correlation with GCs properties.

We analysed a set of Monte Carlo cluster simulations spanning a large range of concentrations and binary fractions, and considered them at the *same time-snapshots* (in line with the MW GC system which is characterized by coeval clusters). For these simulations, we constructed the projected $\sigma(m)$ profile, describing the mass dependence of the velocity dispersion, in the region within the half-light radius. We summarize our findings here.

(i) Different stellar objects (single stars, binary stars, stellar remnants) follow the same $\sigma(m)$ profile, with the exception of recently formed white dwarfs that underwent rapid severe mass-loss. These white dwarfs are characterized by lower velocity dispersion than the one expected for their current mass.

(ii) *Fitting function for mass-dependent kinematics.* We introduce a simple exponential fitting function able to match the mass dependence of the velocity dispersion in the entire stellar mass range sampled. This function is able to reproduce the flattening of the slope of the $\sigma(m)$ profile towards low stellar masses and the steepening at the higher mass regime. The fitted parameter is the mass parameter $m_{\rm eq}$ that is physically well motivated as it indicates the degree of partial equipartition reached by the cluster. For $m \geq m_{\rm eq}$ the slope of the function corresponds to that of full energy equipartition; while for $m < m_{\rm eq}$ only partial equipartition is achieved. The exponential fitting function provides excellent fits to the mass-dependent kinematics of our simulations, showing that the systems are only in partial energy equipartition. Note that our function can be considered an extension of the commonly used power-law function $\sigma \propto m^{-\eta}$ that is instead only valid for restricted mass ranges.

(iii) *Applicability to observations.* We tested our fitting function on different mass ranges. Using a discrete fitting technique, we showed that, even for the restricted mass range 0.4–1.0 $M_\odot$ accessible from state-of-the-art observations from combination of *HST* proper motions and line-of-sight velocities, it is still possible to reliably characterize the degree of partial equipartition with the parameter $m_{\rm eq}$. This indicates that, once the $\sigma(m)$ profile is characterized, it can be used to predict the mass dependence of kinematics also for the non-observable low-mass regime and stellar remnant mass regime (see Baldwin et al. 2016 for an application to blue straggler stars). This will be particularly useful to carry out comprehensive dynamical modelling for those clusters for which the kinematics is restricted to only a limited stellar mass range.

(iv) *Measuring the dynamical state of a cluster.* We looked for correlations of the degree of energy equipartition given by the parameter $m_{\rm eq}$ with different cluster properties. In particular, we find that more concentrated clusters are closer to energy equipartition than less concentrated ones and that younger clusters are further away from energy equipartition than older ones. We showed that these relations are due to the correlation of the degree of energy equipartition with the relaxation state of the cluster, which we quantified by $n_{\rm eq} = T_{\rm age}/T_{\rm rc}$ with $T_{\rm age}$ the age of the cluster and $T_{\rm rc}$ the current core relaxation time. The tight relation obtained for $m_{\rm eq} - n_{\rm rel}$ can serve as a tool to investigate the dynamical condition of a GC. In fact, given a relaxation state of a cluster (easily accessible from photometric quantities), it is possible to predict the $m_{\rm eq}$ parameter, and therefore the mass dependence of the kinematics. Vice versa, measuring the equipartition parameter $m_{\rm eq}$ from kinematics, it is possible to retrieve the internal dynamical state of a cluster. Finally, the validity of this relation is restricted to quasi-isolated clusters, so that any deviations from it could potentially be used as a simple tool to unveil a peculiar dynamical history of a given cluster (e.g. post-core collapse, presence of intermediate-mass black hole, disc shocking, *in situ* versus accreted formation, peculiar formation environments). We plan to undertake a specific analysis in order to quantify these effects in a follow-up work.

A natural consequence of energy equipartition is the sinking of massive stars into the central regions of a clusters (mass segregation). This causes a radial variation of the mass-to-light ratio, M/L, in a cluster. We therefore anticipate a dependence of *M/L* on the dynamical state of a cluster and hence on its degree of energy equipartition. We will address this point further in a forthcoming paper. Finally, we point out that the approach introduced in this work to describe energy equipartition in GCs can serve as an optimal tool not only to characterize simulations and state-of-the-art kinematic observations, but also for testing dynamical models in which multimass components (i.e. a realistic mass function) are taken into consideration (e.g. Gieles & Zocchi 2015).

ACKNOWLEDGEMENTS

We are grateful to Jonathan M. B. Downing for providing the Monte Carlo simulations used in this work. We wish to thank Giuseppe Bertin, Roeland van der Marel, Anna Sippel and Laura Watkins for useful comments and discussions. ALV is grateful to Douglas Heggie for many interesting discussions, and acknowledges financial support from the 1851 Royal Commission. We thank the referee for helping improving the clarity of our paper. This work was supported by Sonderforschungsbereich SFB 881 'The Milky Way System' (subproject A7 and A8) of the German Research Foundation (DFG).

REFERENCES

Alessandrini E., Lanzoni B., Miocchi P., Ciotti L., Ferraro F. R., 2014, ApJ, 795, 169
Baldwin A., Watkins L. L., van der Marel R. P., Bianchini P., Bellini A., Anderson J., 2016, ApJ, in press
Baumgardt H., Makino J., 2003, MNRAS, 340, 227
Bellini A. et al., 2014, ApJ, 797, 115

Bianchini P., Norris M. A., van de Ven G., Schinnerer E., Bellini A., van der Marel R. P., Watkins L. L., J. A., 2016, ApJ, 820, L22
Binney J., Tremaine S., 2008, Galactic Dynamics, 2nd edn. Princeton Univ. Press, Princeton, NJ
Da Costa G. S., Freeman K. C., 1976, ApJ, 206, 128
Djorgovski S., 1993, in Djorgovski S. G., Meylan G., eds, ASP Conf. Ser. Vol. 50, Structure and Dynamics of Globular Clusters. Astron. Soc. Pac., San Francisco, p. 373
Downing J. M. B., Benacquista M. J., Giersz M., Spurzem R., 2010, MNRAS, 407, 1946
Ferraro F. R. et al., 2012, Nature, 492, 393
Foreman-Mackey D., Hogg D. W., Lang D., Goodman J., 2013, PASP, 125, 306
Gieles M., Zocchi A., 2015, MNRAS, 454, 576 (GZ15)
Giersz M., 1998, MNRAS, 298, 1239
Gomez-Leyton Y. J., Velazquez L., 2014, J. Stat. Mech.: Theory Exp., 4, 6
Gunn J. E., Griffin R. F., 1979, AJ, 84, 752
Harris W. E., 1996, AJ, 112, 1487 (2010 edition)
Heyl J., Richer H. B., Antolini E., Goldsbury R., Kalirai J., Parada J., Tremblay P.-E., 2015, ApJ, 804, 53
Hypki A., Giersz M., 2013, MNRAS, 429, 1221
Inagaki S., Saslaw W. C., 1985, ApJ, 292, 339
Inagaki S., Wiyanto P., 1984, PASJ, 36, 391
Kamann S. et al., 2016, preprint (arXiv:1602.01643)
Khalisi E., Amaro-Seoane P., Spurzem R., 2007, MNRAS, 374, 703
King I. R., 1966, AJ, 71, 64
Kroupa P., 2001, MNRAS, 322, 231
Lightman A. P., Fall S. M., 1978, ApJ, 221, 567
Merritt D., 1981, AJ, 86, 318
Meylan G., 1987, A&A, 184, 144
Meylan G., Heggie D. C., 1997, A&AR, 8, 1
Miocchi P., 2006, MNRAS, 366, 227
Plummer H. C., 1911, MNRAS, 71, 460
Shanahan R. L., Gieles M., 2015, MNRAS, 448, L94
Sollima A., Bellazzini M., Lee J.-W., 2012, ApJ, 755, 156
Sollima A., Baumgardt H., Zocchi A., Balbinot E., Gieles M., Hénault-Brunet V., Varri A. L., 2015, MNRAS, 451, 2185
Spera M., Mapelli M., Jeffries R. D., 2016, preprint (arXiv:e-prints)
Spitzer L., Jr, 1969, ApJ, 158, L139
Spitzer L., 1987, Dynamical Evolution of Globular Clusters. Princeton Univ. Press, Princeton, NJ
Trenti M., van der Marel R., 2013, MNRAS, 435, 3272
Vishniac E. T., 1978, ApJ, 223, 986
Wang L. et al., 2016, MNRAS, 458, 1450
Watkins L. L., van der Marel R. P., Bellini A., Anderson J., 2015a, ApJ, 803, 29
Watkins L. L., van der Marel R. P., Bellini A., Anderson J., 2015b, ApJ, 812, 149
Wilson C. P., 1975, AJ, 80, 175
Woolley R. V. D. R., 1954, MNRAS, 114, 191
Zocchi A., Bertin G., Varri A. L., 2012, A&A, 539, A65

APPENDIX A

The exponential fitting function proposed in Section 3.1 is physically motivated by two asymptotic behaviours of the central value of the velocity dispersion profile $\sigma(m)$, in the limit of low and high mass, respectively. Such behaviours can be studied in detail by taking advantage of the analytical framework provided by appropriate distribution function-based equilibria. Previous dynamical studies have indeed showed that multimass, lowered isothermal models (e.g. Woolley 1954; King 1966; Wilson 1975, and more recently Gomez-Leyton & Velazquez 2014; Gieles & Zocchi 2015, hereafter GZ15) offer a successful description of Galactic GCs, even in different relaxation conditions (e.g. see Da Costa & Freeman 1976; Gunn & Griffin 1979; Meylan 1987; Sollima, Bellazzini & Lee 2012). These equilibria are characterized by multiple mass components, which are traditionally defined in terms of a set of relations between the velocity scales s_j and the masses m_j of the different components, such that $m_j\, s_j^2 = m_i\, s_i^2$. As previously noted (Merritt 1981; Miocchi 2006, GZ15), we emphasize that such a prescription does *not* enforce a condition of full energy equipartition in the resulting configurations, neither locally nor globally.

This class of models allow us to derive the velocity dispersion profile in closed analytical form (i.e. as a function of the potential), which may be expressed in terms of appropriate special functions. For the reader's convenience, here we will adopt the same notation used by GZ15, in which the central value of the dimensionless velocity dispersion of the component j is given by

$$\hat{\sigma}_{1d\,j\,0} = \frac{1}{\mu_j^{\delta}} \frac{E_\gamma(g+5/2;\mu_j^{2\delta}\hat{\phi}_0)}{E_\gamma(g+3/2;\mu_j^{2\delta}\hat{\phi}_0)}, \tag{A1}$$

where $\hat{\phi}_0 = \hat{\phi}(\hat{r}=0)$ is the depth of the central potential well (i.e. a measure of the central concentration), $\mu_j = m_j/\bar{m}$ is the dimensionless mass of component j, and its normalization is given by the central density weighted mean-mass $\bar{m} = \Sigma_j\, m_j \rho_{0j} / \Sigma_j \rho_{0j}$. The function E_γ is a convenient piecewise definition of the modified lowered incomplete Gamma function, introduced by Gomez-Leyton & Velazquez (2014) (see also equation 2 and appendix D1 of GZ15). The parameter g sets the continuity properties of the truncation prescription of the distribution function (see equation 1 of GZ15), in such a way that, in the isotropic limit, $g = 0, 1, 2$ correspond to the usual Woolley (1954), King (1966), and non-rotating Wilson (1975) multimass models, respectively. Finally, the parameter δ is defined so that $m_j s_j^{1/\delta} = m_i\, s_i^{1/\delta}$; for $\delta = 1/2$, such a relation reduces to the condition usually adopted in the literature.

By considering the regime $\mu_j \ll 1$ (i.e. $m_j \ll \bar{m}$), the asymptotic behaviour of the function indicated in equation (A1) can be easily calculated up to the order $\mathcal{O}(\mu_j^{4\delta})$ (i.e. second order in μ_j, for $\delta = 1/2$):

$$\begin{aligned}\hat{\sigma}_{1d\,j\,0} \sim & \left[\frac{(g+3/2)\Gamma(g+3/2)}{(g+5/2)\Gamma(g+5/2)}\right]^{1/2} \hat{\phi}_0^{1/2} \\ & \left[1 - \frac{1}{2(g+5/2)(g+7/2)}\,\hat{\phi}_0\,\mu_j^{2\delta}\right. \\ & \left. + \frac{6+3(g+5/2)-4(g+5/2)^2}{8(g+5/2)^2(g+7/2)^2(g+9/2)}\,\hat{\phi}_0^2\mu_j^{4\delta}\right]\end{aligned} \tag{A2}$$

where Γ denotes the Gamma function. We stress that, in the limit $\mu_j \to 0$, the central velocity dispersion (for a chosen value of the truncation parameter g) tends to a constant value, which depends only on the central concentration $\hat{\phi}_0$. The limiting values for the traditional Woolley, King, and isotropic Wilson models are recovered as $\hat{\sigma}_{1d\,j\,0} \sim A(g)^{1/2}\hat{\phi}_0^{1/2}$, with $A(g) = 2/(5+2g)$ for $g = 0, 1, 2$ (to be compared, e.g. with the central values of the models depicted in fig. 9 of GZ15). Such an asymptotic behaviour in the regime of low stellar masses informed our choice for the expression of the fitting function introduced in equation (1), which, for $m \ll m_{\rm eq}$, may be expressed as

$$\sigma \sim \sigma_0 \left[1 - \frac{1}{2}\frac{m}{m_{\rm eq}} + \frac{1}{8}\left(\frac{m}{m_{\rm eq}}\right)^2\right], \tag{A3}$$

which is the first terms of a Taylor expansion of $\sigma = \sigma_0 \exp(-1/2\, m/m_{\rm eq})$.

Similarly, by considering the regime $\mu_j \gg 1$ (i.e. $m_j \gg \bar{m}$), the asymptotic behaviour of the function indicated in equation (A1) is simply given by $\hat{\sigma}_{1d\,j\,0} \sim 1/\mu_j^{\delta}$. For the typical value $\delta = 1/2$, this corresponds to the traditional scaling $\hat{\sigma}_{1d\,j\,0} \sim m_j^{-1/2}$ (see also Section 3.2.1 of GZ15), with a coefficient, $\bar{m}^{1/2}$, which is, once again, a function of the central concentration alone (for a chosen value of the parameter g). Such a behaviour motivates the piecewise definition of our fitting function in the regime of higher masses (i.e. $m \gg m_{\rm eq}$).

This paper has been typeset from a TEX/LATEX file prepared by the author.

Chapter 7

Conclusions and future prospects

The simplistic textbook picture of GCs has in the recent years rapidly fallen apart. The discovery of a larger degree of complexity in the structure, morphology, stellar populations and internal dynamics of GCs has opened up fundamental questions on the origin of these stellar systems. How did GCs form in the early epochs of galaxy formation? Which GC formed in-situ and which is instead an accreted stellar system? What is the mechanism of formation of the multiple stellar populations observed ubiquitously in MW GCs? What is the contribution of MW GCs to the Galactic halo?

This Thesis contributed in unveiling the complexity in the internal kinematics of GCs and exploiting it in order to *find a link between the current dynamical state of a cluster and its formation and evolution.* In particular, the starting point of this work was motivated by the need of finding robust signatures that could trace GCs properties and their dynamical history. In Chapter 2, I showed that the use of morphology alone is not enough to have a sound indicator of the formation or evolution on a cluster: clusters that underwent an accretion event are morphologically similar to clusters that evolved in isolation and formed in-situ. This motivated the detailed exploration of the internal kinematics, that is a long lasting "fossil record" of the dynamical processes that a GC has experienced during its long-term evolution.

The feasibility of the study of the kinematics was boosted from the observational side, since detailed observations recently became available and can now deliver the comprehensive data necessary to undertake a thorough kinematic investigation of MW GCs. Another key aspect further needed to unveil the complexity of the internal kinematics of GCs, is the combined use of dynamical models and kinematic observations. Bridging the gap between models and observations is the strategy used throughout my work in order to make an improvement in our understanding of both the data and the physical processes described by the models. All of this allowed us to robustly study the internal kinematics of GCs, focusing on signatures of the presence of IMBHs, of binary stars, the effects of energy equipartition and to set up a first step to trace the evolution of GCs, based on their current kinematic state.

In the following Sections, I will summarize the lessons learned from the detailed study of the internal kinematics of MW GCs carried out in this Thesis; I will then point out the open problems that still remain unanswered and outline the possible direction to follow in order to solve them.

7.1 Conclusions

7.1.1 The importance of understanding the data

The large amount of kinematic data now available for MW GCs consists in a variety of samples collected in different field-of-views and with different observational methodology, namely velocities along the line-of-sight with spectroscopy and velocities on the plane of the sky with proper motions. In order to build a comprehensive picture of the current state of GCs it is necessary to use all of these data sets in combination to deliver a three-dimensional kinematic view of a GC. This unavoidably poses the challenge of first reaching a deep understanding of the data, before attempting any physical interpretation of the observations.

The two main questions that I investigated in this Thesis consisted in the understanding of the biases involved in the central kinematic measurements using integrated-light IFU spectroscopy (Chapter 3), and the biases concerning *HST* proper motion data sets (Chapter 4 and 5). The problems that can occur with IFU measurements are connected to the application of integrated-light measurements to MW GCs that are resolved or partially resolved stellar systems. This can produce very dramatic biases in the measurements because of shot noise due to the presence of few very bright stars (see for example the discussion about the possible detection of IMBHs in the center of GCs, Chapter 3). Moreover, the very high crowding of the field-of-view further makes the measurements around a few arcsec of the centers of GCs very challenging.

For *HST* proper motion data sets, the focus was twofold: first, understanding the quality of the data in order to select a subsample suitable for the study of the internal dynamics of GCs (i.e., high quality measurements with low associated errors); second, exploring the possible systematics introduced by the presence of unresolved binary stars. Given the novelty of *HST* proper motions, the challenge was to explore for the first time the effects connected for example to luminosity-dependent and color-dependent systematics, blended stars, and the identification of mismatched proper motions.

The strategy adopted to reach a deeper understanding of the data and to devise techniques to mitigate systematics was the *extensive use of mock observations*. This strategy gives the direct advantage of disentangling the physical effects from the effects of biases, in order to reach an accurate interpretation of the observations. Moreover, it can serve as the optimal tool to plan for the observability of fingerprints predicted by the models. The construction of mock observations is carried out starting from state-of-the-art dynamical models of GCs, where the most relevant physical ingredients responsible of their dynamical evolution are taken into considerations. These models are then "translated" into the observational-space incorporating a number of observational effects, to reach the desired degree of realism.

The most complete tool created in this Thesis to translate models into mock observations has been presented in Chapter 3 (see also Appendix). This code, `SISCO`, allows one to obtain a realistic simulation of an IFU observation of a GC, including all the relevant observational effects: to every star in the dynamical simulation is assigned a stellar spectrum, then a field-of-view with a given spaxel scale is assigned, the luminosity-weighted spectra are convolved with a PSF given a seeing condition and accordingly summed in each spaxel. Then a signal-to-noise is assigned and the three-

dimensional data cube is produced, consisting of a spectrum for every spatial element in the the field-of-view, ready to be analyzed in the same manner as observers.

`SISCO` was applied to study the effects of the use of integrated-light spectroscopy to measure the central kinematics of GCs connected to the presence of IMBHs (see following Section), but it is a flexible tool that can be applied to any given realistic dynamical simulation of dense stellar systems (GCs but also nuclear star clusters or open clusters), in order to unveil their kinematic state and test predictions from the models.

The work carried out in this Thesis and the approach of using mock observations to understand the data will be even more fundamental in the upcoming years when the necessity of coupling information form different data sets will become stronger. As an example, the large amount of Gaia data that will soon be available, will pose a question methodologically similar to the one tackled here. Only starting from a deep understanding of the data it will be possible to create the most comprehensive picture of the current dynamical state of GCs.

7.1.2 Unveiling the complex kinematics of globular clusters

The dual approach based on the combined use of models and observations employed throughout my work revealed to be crucial for the study of the internal kinematics of GCs. This work has contributed significantly in highlighting the fact that GCs are not the simple stellar systems previously thought of, but contain instead a high degree of complexity also in their internal kinematics. Amongst others, the three physical ingredients that I have studied in details in this Thesis are: 1) the signatures of IMBHs (Chapter 3), 2) the effect of binary stars (Chapter 5) and 3) the effect of the onset of energy equipartition (Chapter 6). I will here briefly summarize the results achieved from this investigation.

The debate on the presence/absence of IMBHs in the center of MW GCs has been so far inconclusive, as different kinematic observations often delivered different results. The work presented here, has contributed to this discussion by introducing a new approach, namely starting from the understanding of the discrepancy between the different data sets. Specifically, the focus was given on how to robustly measure the central value of the velocity dispersion profile using integrated-light measurements. A correct accounting of the biases and stochasticity due to the presence of a few bright stars together with the accounting of the uncertainties on the measurement of the center of the cluster led to the conclusion that the velocity dispersion measurements can have an intrinsic scatter of up to 40%. This can potentially prevent any sound assessment of the presence/absence of an IMBH. A number of solutions to mitigate this scatter have therefore been proposed (such as masking of bright pixels) and shown to efficiently recover unbiased measurements.

Binary stars are a fundamental ingredient for the evolution of GCs, as their formation and destruction can significantly contribute in the overall energy budget of the clusters. Moreover, their presence in GCs can significantly affect the kinematic measurements both along the line-of-sight and the proper motions. In this Thesis, I

investigated for the first time the effect of unresolved binaries in *HST* proper motion data sets. Since binaries are more massive systems than the average stars in a cluster, they are expected to sink towards the center and acquire lower velocity dispersion, due to the effect of two-body interaction causing the onset of energy equipartition. Therefore, a high number of unidentified unresolved binaries can contribute in lowering the measured value of velocity dispersion. Moreover, since binaries are located on the red side of the stellar main sequence, they can introduce a color dependence in the velocity dispersion. We quantified that this effect is observable only for GCs with a high binary fraction of $\simeq$30% and it is of the order of 1%-6% of the velocity dispersion. This indicates that the effect of unresolved binaries should be taken into account in the error budget of proper motion kinematic analysis. This is particularly important in the context of multiple stellar populations, where different color stars can correspond to different stellar populations, with possible intrinsically different kinematics.

Two-body interactions shape the internal structure and dynamics of GCs over their long-term evolution, bringing the systems toward a state of energy equipartition, where massive stars display lower velocity dispersions than low-mass stars. This mass-dependence of the kinematics has so far been mostly neglected, since the traditional data sampled only the bright stars, all in the same mass range of $0.8 - 0.9\ M_{\odot}$. In this Thesis, a new approach to characterize the mass dependence of kinematics was introduced, suitable to both simulations and state-of-the-art observations (a combination of *HST* proper motions and line-of-sight velocities). An exponential fitting function was used to describe the velocity dispersion as a function of the stellar mass. This function gives a single parameter indicating the degree of equipartition attained by a cluster and provides excellent fits to the mass-dependent kinematics of the simulations analyzed, showing that GCs are expected to be only in partial energy equipartition. Moreover, once the mass dependence of the velocity dispersion is uniquely determined, it can be used to predict the kinematics also for the stars in a non-observable low-mass regime, stellar remnants or exotic objects for which the kinematics cannot yet be directly measured.

7.1.3 Linking the current state of globular clusters to their formation and evolution

The internal kinematic properties of GCs evolve during their > 10 Gyr lifetime, because of the cumulative effect of gravitational encounters between stars. The kinematic properties that we see today are however also dependent on the formation properties of a cluster and its subsequent peculiar evolution, therefore they can be exploited to gain insights into their past history. How can we exploit the large amount of data and the detailed information on present day GCs to unveil their formation and evolution? In Chapter 6 of this Thesis, I presented a first fundamental step to link the current kinematic properties of GCs to their formation and evolution, using the effects connected to energy equipartition and studying in details the mass-dependence of the kinematics.

In particular, using a set of realistic dynamical simulations, I showed that the mass-dependence of kinematics measured in a cluster can be used as a dynamical age estimator to trace its relaxation condition. In fact, the degree of energy equipartition reached by a cluster correlates tightly with its relaxation conditions: more relaxed clus-

ters are closer to full energy equipartition. Therefore, with a measure of the degree of equipartition from the mass-dependent kinematics, it is possible to retrieve the internal dynamical state of a cluster.

This tight relation presented here is strictly valid only for GCs evolved in isolation. Hence, GCs that underwent a different dynamical evolution will deviate from this relation, offering a probe to single out GCs with a peculiar dynamical history. This can include clusters in post-core collapse phase, clusters that underwent disk shocking, clusters formed in a different environment such as a nucleus of a dwarf galaxy, clusters accreted onto the MW, or clusters that host a central IMBH. All of these processes are expected to leave a significant fingerprint in the kinematics of GCs and tailored simulations will provide insights on the detailed expectations. Since the degree of equipartition reached by a system is now measurable using *HST* proper motion data and line-of-sight observations, this approach provides a viable tool to disentangle the evolution process experienced by a GC, on the sole basis of kinematics.

7.2 Open questions and outlook

Throughout this Thesis, I showed how the combined use of the recently available state-of-the-art kinematic observations and detailed dynamical simulations made it possible to start a deep investigation of the internal kinematic of GCs to unveil their formation and evolution. In this final Section, I will summarize the issues that still remain unanswered, the open questions triggered by this work and the path to follow to solve them.

Accreted vs. in-situ globular clusters. Despite the many lines of argument on the existence of both GCs formed in-situ in the MW and GCs later accreted, to date, there is no unambiguous signature that allows us to distinguish these two categories of GCs. A possible procedure to look for definite signatures of accreted formation could come from the study of the internal properties of clusters and their relation with their host galaxy. In fact, if accreted GCs are the final product of stripped dwarf galaxies, they are the "living fossils" of the consecutive merger events of smaller galaxies that built up the MW through cosmological time. Therefore, a detailed study of the accretion processes and of the expected contribution of accreted clusters to the Galactic halo will give clear insights on this issue. Moreover, the capacity of this approach can be significantly augmented coupling the dynamical expectations to the chemical information: since GCs display the peculiar multiple stellar population abundances, they can be used as ideal chemical tags.

Another important piece of information to disentangle clusters formed in-situ and accreted clusters, could come from the detailed study of the internal properties of those clusters suspected to be stripped nuclei of dwarf galaxies. The use of all the available three-dimensional kinematic data and dynamical modeling can lead to the identification of the signatures expected for stripped nuclei, including signatures in orbital anisotropy, internal rotation, energy equipartition, presence of IMBH and presence of residual dark matter. Finally, the study of GC systems in external galaxies could deliver further fundamental and complimentary insights, exploiting the larger number

statistics available and the possibility to study the correlation of GCs properties with different environments.

IMBHs: are they there? Understanding in a definite way whether IMBHs exist in the centers of GCs is still one of the fundamental questions that needs to be answered. The search for unique fingerprints of the existence of IMBHs should follow a twofold approach: 1) continue on the path of mock observations presented in this Thesis, using realistic simulations that include the presence of an IMBH to understand its detectability using different instrumentations and observational setups; 2) use comprehensive dynamical modeling that includes all the possible physical ingredients that could be degenerate with the signature of an IMBH, to assess their contribution and to disentangle it from the one of an IMBH only. The combination of the points above will allow to detect in a definite way the presence of an IMBH in the center of a cluster, using the available data. Moreover, when future instruments provided by the upcoming Extremely Large Telescopes will be available, it will be possible to push our limits further measuring the motions of stars within the sphere of influence of the central black hole (in analogy of what has been done around the super massive black hole of our Galaxy) and also extend the hunt for IMBHs to extragalactic GCs.

Multiple stellar populations. The phenomenon of multiple stellar populations in Galactic GCs still remains an unsolved puzzle that questions our understanding of the processes of star formation responsible for the origin of GCs. In order to advance in our understanding, a parallel effort from both the observational and theoretical side need to be pursued. From the observational side, one could extend the studies of the presence of multiple stellar populations to extragalactic GCs (see e.g., Peacock et al., 2013). This will help in understanding to which extent this is a general property and whether it could be connected for example to galactic environmental effects. From the theoretical side, multiple stellar populations need to be included in direct N-body simulations in order to be able to understand consistently their dynamical evolution.

Going beyond dynamics alone. Dynamics has been the main focus of this Thesis and its study has proved essential for the understanding of the internal properties of GCs. Our ability to interpret and unveil the formation and evolution of GCs relies on the construction of realistic models that are able to encompass all the relevant physical ingredients. The study of energy equipartition reported here calls explicitly for the need of dynamical modeling characterized by multiple mass components with different kinematic behavior. Moreover, our understanding of the internal properties of GCs can enormously be improved if dynamics is coupled with other available information, such as chemical abundances. The construction of chemo-dynamical models, where stars characterized by different chemical composition are allowed to have different dynamical behaviors, could represent the turning point in the understanding of phenomena such as the existence of multiple stellar populations in the context of GC formation and evolution.

The childhood of GCs. The origin of GCs is deeply interweaved with the physical processes that took place at the early stage of galaxy formation. This includes the

presence of gas as well as the structure formation in a cosmological context. Hence, in order to unveil the early life of GCs, it is necessary to consider these processes all together. One direction could be the one of coupling dynamical simulations of GCs with cosmological simulations of structure formation from the early universe until today. This will give us new insights on the environments of formation of GCs, and their effect on the evolution of these stellar systems. Another approach consists in adding to the dynamical studies of GCs the physical effects connected to the presence of gas during the early phases of their lives. This will be possible, for example, exploiting the software AMUSE (Pelupessy et al., 2013), in which the coupling of gravitational dynamics, stellar evolution, hydrodynamics and radiative transfer is possible.

The work carried out in this Thesis has shown the roadmap to unveil the internal dynamics of GCs, bringing together state-of-the-art dynamical modeling and observations. This synergy between models, observations and detailed analysis of the kinematics will be the starting point for exploiting at full power the amount of data that will be delivered in the approaching era of Extremely Large Telescopes and of James Webb Space Telescope, to continue to pursue the goal of understanding the formation of GCs.

Bibliography

Aarseth S. J., 1999, PASP, 111, 1333

—, 2003, Gravitational N-Body Simulations

Anderson J., King I. R., 2003, AJ, 126, 772

Anderson J., van der Marel R. P., 2010, ApJ, 710, 1032

Baldwin A., Watkins L. L., van der Marel R. P., Bianchini P., Bellini A., Anderson J., subm

Bastian N., Cabrera-Ziri I., Salaris M., 2015a, MNRAS, 449, 3333

—, 2015b, MNRAS, 449, 3333

Bastian N., Lamers H. J. G. L. M., de Mink S. E., Longmore S. N., Goodwin S. P., Gieles M., 2013, MNRAS, 436, 2398

Bechtol K., Drlica-Wagner A., Balbinot E., Pieres A., Simon J. D., Yanny B., Santiago B., Wechsler R. H., Frieman J., Walker A. R., Williams P., Rozo E., Rykoff E. S., Queiroz A., Luque E., Benoit-Lévy A., Tucker D., Sevilla I., Gruendl R. A., da Costa L. N., Fausti Neto A., Maia M. A. G., Abbott T., Allam S., Armstrong R., Bauer A. H., Bernstein G. M., Bernstein R. A., Bertin E., Brooks D., Buckley-Geer E., Burke D. L., Carnero Rosell A., Castander F. J., Covarrubias R., D'Andrea C. B., DePoy D. L., Desai S., Diehl H. T., Eifler T. F., Estrada J., Evrard A. E., Fernandez E., Finley D. A., Flaugher B., Gaztanaga E., Gerdes D., Girardi L., Gladders M., Gruen D., Gutierrez G., Hao J., Honscheid K., Jain B., James D., Kent S., Kron R., Kuehn K., Kuropatkin N., Lahav O., Li T. S., Lin H., Makler M., March M., Marshall J., Martini P., Merritt K. W., Miller C., Miquel R., Mohr J., Neilsen E., Nichol R., Nord B., Ogando R., Peoples J., Petravick D., Plazas A. A., Romer A. K., Roodman A., Sako M., Sanchez E., Scarpine V., Schubnell M., Smith R. C., Soares-Santos M., Sobreira F., Suchyta E., Swanson M. E. C., Tarle G., Thaler J., Thomas D., Wester W., Zuntz J., DES Collaboration, 2015, ApJ, 807, 50

Bedin L. R., Piotto G., Anderson J., Cassisi S., King I. R., Momany Y., Carraro G., 2004, ApJ, 605, L125

Bekki K., Freeman K. C., 2003, MNRAS, 346, L11

Bellazzini M., Bragaglia A., Carretta E., Gratton R. G., Lucatello S., Catanzaro G., Leone F., 2012, A&A, 538, A18

Bellini A., Anderson J., van der Marel R. P., Watkins L. L., King I. R., Bianchini P., Chanamé J., Chandar R., Cool A. M., Ferraro F. R., Ford H., Massari D., 2014, ApJ, 797, 115

Bellini A., Piotto G., Bedin L. R., Anderson J., Platais I., Momany Y., Moretti A., Milone A. P., Ortolani S., 2009, A&A, 493, 959

Bellini A., Vesperini E., Piotto G., Milone A. P., Hong J., Anderson J., van der Marel R. P., Bedin L. R., Cassisi S., D'Antona F., Marino A. F., Renzini A., 2015, ApJ, 810, L13

Belokurov V., Irwin M. J., Koposov S. E., Evans N. W., Gonzalez-Solares E., Metcalfe N., Shanks T., 2014, MNRAS, 441, 2124

Bertin G., 2014, Dynamics of Galaxies

Bianchini P., Renaud F., Gieles M., Varri A. L., 2015, MNRAS, 447, L40

Bianchini P., Varri A. L., Bertin G., Zocchi A., 2013, ApJ, 772, 67

Binney J., Mamon G. A., 1982, MNRAS, 200, 361

Brodie J. P., Larsen S. S., 2002, AJ, 124, 1410

Brodie J. P., Romanowsky A. J., Strader J., Forbes D. A., 2011, AJ, 142, 199

Cannon R. D., Croke B. F. W., Bell R. A., Hesser J. E., Stathakis R. A., 1998, MNRAS, 298, 601

Carretta E., Bragaglia A., Gratton R. G., Lucatello S., Catanzaro G., Leone F., Bellazzini M., Claudi R., D'Orazi V., Momany Y., Ortolani S., Pancino E., Piotto G., Recio-Blanco A., Sabbi E., 2009, A&A, 505, 117

Chen C. W., Chen W. P., 2010, ApJ, 721, 1790 (CC10)

Cohn H., 1980, ApJ, 242, 765

Da Costa G. S., 2015, ArXiv e-prints

Da Costa G. S., Freeman K. C., 1976, ApJ, 206, 128

de Vita R., Bertin G., Zocchi A., 2016, ArXiv e-prints

Decressin T., Meynet G., Charbonnel C., Prantzos N., Ekström S., 2007, A&A, 464, 1029

den Brok M., van de Ven G., van den Bosch R., Watkins L., 2014, MNRAS, 438, 487

D'Ercole A., Vesperini E., D'Antona F., McMillan S. L. W., Recchi S., 2008, MNRAS, 391, 825

Einsel C., Spurzem R., 1999, MNRAS, 302, 81

Fabricius M. H., Noyola E., Rukdee S., Saglia R. P., Bender R., Hopp U., Thomas J., Opitsch M., Williams M. J., 2014, ApJ, 787, L26

Ferrarese L., Merritt D., 2000, ApJ, 539, L9

Fiestas J., Spurzem R., Kim E., 2006, MNRAS, 373, 677

Forbes D. A., Bridges T., 2010, MNRAS, 404, 1203

Freeman K. C., 1993, in Astronomical Society of the Pacific Conference Series, Vol. 48, The Globular Cluster-Galaxy Connection, G. H. Smith & J. P. Brodie, ed., pp. 608–+

Gaburov E., Harfst S., Portegies Zwart S., 2009, New Astronomy, 14, 630

Gebhardt K., Pryor C., O'Connell R. D., Williams T. B., Hesser J. E., 2000, AJ, 119, 1268

Georgiev I. Y., Hilker M., Puzia T. H., Goudfrooij P., Baumgardt H., 2009, MNRAS, 396, 1075

Geyer E. H., Nelles B., Hopp U., 1983, A&A, 125, 359

Gieles M., Zocchi A., 2015, MNRAS, 454, 576

Giersz M., Heggie D. C., Hurley J. R., Hypki A., 2013, MNRAS, 431, 2184

Giersz M., Leigh N., Hypki A., Lützgendorf N., Askar A., 2015, MNRAS, 454, 3150

Gratton R. G., Carretta E., Bragaglia A., 2012, 20, 50

Harris W. E., 2010, arXiv:1012.3224

Heggie D., Hut P., 2003, The Gravitational Million-Body Problem: A Multidisciplinary Approach to Star Cluster Dynamics. Cambridge University Press, Cambridge UK

Heggie D. C., 2011, Bulletin of the Astronomical Society of India, 39, 69

Hénault-Brunet V., Gieles M., Agertz O., Read J. I., 2015, MNRAS, 450, 1164

Hénon M. H., 1971, Ap&SS, 14, 151

Hut P., 2010, New Astronomy Reviews, 54, 163

Huxor A. P., Mackey A. D., Ferguson A. M. N., Irwin M. J., Martin N. F., Tanvir N. R., Veljanoski J., McConnachie A., Fishlock C. K., Ibata R., Lewis G. F., 2014, MNRAS, 442, 2165

Hypki A., Giersz M., 2013, MNRAS, 429, 1221

Ibata R. A., Gilmore G., Irwin M. J., 1995, MNRAS, 277, 781

Jennings Z. G., Romanowsky A. J., Brodie J. P., Janz J., Norris M. A., Forbes D. A., Martinez-Delgado D., Fagioli M., Penny S. J., 2015, ApJ, 812, L10

Jordi K., Grebel E. K., 2010, A&A, 522, A71+

Kacharov N., Bianchini P., Koch A., Frank M. J., Martin N. F., van de Ven G., Puzia T. H., McDonald I., Johnson C. I., Zijlstra A. A., 2014, A&A, 567, A69

Kamann S., Husser T.-O., Brinchmann J., Emsellem E., Weilbacher P. M., Wisotzki L., Wendt M., Krajnović D., Roth M. M., Bacon R., Dreizler S., 2016, ArXiv e-prints

Keller S. C., Mackey D., Da Costa G. S., 2012, ApJ, 744, 57

King I. R., 1966, AJ, 71, 64

Koposov S. E., Belokurov V., Torrealba G., Evans N. W., 2015, ApJ, 805, 130

Kraft R. P., 1994, PASP, 106, 553

Laevens B. P. M., Martin N. F., Bernard E. J., Schlafly E. F., Sesar B., Rix H.-W., Bell E. F., Ferguson A. M. N., Slater C. T., Sweeney W. E., Wyse R. F. G., Huxor A. P., Burgett W. S., Chambers K. C., Draper P. W., Hodapp K. A., Kaiser N., Magnier E. A., Metcalfe N., Tonry J. L., Wainscoat R. J., Waters C., 2015, ApJ, 813, 44

Laevens B. P. M., Martin N. F., Sesar B., Bernard E. J., Rix H.-W., Slater C. T., Bell E. F., Ferguson A. M. N., Schlafly E. F., Burgett W. S., Chambers K. C., Denneau L., Draper P. W., Kaiser N., Kudritzki R.-P., Magnier E. A., Metcalfe N., Morgan J. S., Price P. A., Sweeney W. E., Tonry J. L., Wainscoat R. J., Waters C., 2014, ApJ, 786, L3

Lanzoni B., Mucciarelli A., Origlia L., Bellazzini M., Ferraro F. R., Valenti E., Miocchi P., Dalessandro E., Pallanca C., Massari D., 2013, ApJ, 769, 107

Lardo C., Pancino E., Bellazzini M., Bragaglia A., Donati P., Gilmore G., Randich S., Feltzing S., Jeffries R. D., Vallenari A., Alfaro E. J., Allende Prieto C., Flaccomio E., Koposov S. E., Recio-Blanco A., Bergemann M., Carraro G., Costado M. T., Damiani F., Hourihane A., Jofré P., de Laverny P., Marconi G., Masseron T., Morbidelli L., Sacco G. G., Worley C. C., 2015, A&A, 573, A115

Leaman R., 2012, AJ, 144, 183

Leaman R., VandenBerg D. A., Mendel J. T., 2013, MNRAS, 436, 122

Lützgendorf N., Gebhardt K., Baumgardt H., Noyola E., Neumayer N., Kissler-Patig M., de Zeeuw T., 2015, A&A, 581, A1

Lützgendorf N., Kissler-Patig M., Gebhardt K., Baumgardt H., Noyola E., de Zeeuw P. T., Neumayer N., Jalali B., Feldmeier A., 2013, A&A, 552, A49

Lynden-Bell D., 1967, MNRAS, 136, 101

Mackey A. D., Gilmore G. F., 2004, MNRAS, 355, 504

Mackey A. D., Huxor A. P., Ferguson A. M. N., Irwin M. J., Tanvir N. R., McConnachie A. W., Ibata R. A., Chapman S. C., Lewis G. F., 2010, ApJ, 717, L11

Mackey A. D., Huxor A. P., Martin N. F., Ferguson A. M. N., Dotter A., McConnachie A. W., Ibata R. A., Irwin M. J., Lewis G. F., Sakari C. M., Tanvir N. R., Venn K. A., 2013, ApJ, 770, L17

Magorrian J., Tremaine S., Richstone D., Bender R., Bower G., Dressler A., Faber S. M., Gebhardt K., Green R., Grillmair C., Kormendy J., Lauer T., 1998, AJ, 115, 2285

Makino J., Fukushige T., Koga M., Namura K., 2003, PASJ, 55, 1163

Marín-Franch A., Aparicio A., Piotto G., Rosenberg A., Chaboyer B., Sarajedini A., Siegel M., Anderson J., Bedin L. R., Dotter A., Hempel M., King I., Majewski S., Milone A. P., Paust N., Reid I. N., 2009, ApJ, 694, 1498

McLaughlin D. E., Anderson J., Meylan G., Gebhardt K., Pryor C., Minniti D., Phinney S., 2006, ApJS, 166, 249

McLaughlin D. E., van der Marel R. P., 2005, ApJS, 161, 304 (MLvdM05)

McNamara B. J., Harrison T. E., Anderson J., 2003, ApJ, 595, 187

McNamara B. J., Harrison T. E., Baumgardt H., Khalaj P., 2012, ApJ, 745, 175

McNamara B. J., McKeever J., 2011, AJ, 142, 163

Meylan G., Heggie D. C., 1997, A&A Rev., 8, 1

Meylan G., Sarajedini A., Jablonka P., Djorgovski S. G., Bridges T., Rich R. M., 2001, AJ, 122, 830

Milone A. P., Piotto G., Bedin L. R., Aparicio A., Anderson J., Sarajedini A., Marino A. F., Moretti A., Davies M. B., Chaboyer B., Dotter A., Hempel M., Marín-Franch A., Majewski S., Paust N. E. Q., Reid I. N., Rosenberg A., Siegel M., 2012, A&A, 540, A16

Misgeld I., Hilker M., 2011, MNRAS, 414, 3699

Nitadori K., Aarseth S. J., 2012, MNRAS, 424, 545

Norris M. A., Escudero C. G., Faifer F. R., Kannappan S. J., Forte J. C., van den Bosch R. C. E., 2015, MNRAS, 451, 3615

Norris M. A., Kannappan S. J., Forbes D. A., Romanowsky A. J., Brodie J. P., Faifer F. R., Huxor A., Maraston C., Moffett A. J., Penny S. J., Pota V., Smith-Castelli A., Strader J., Bradley D., Eckert K. D., Fohring D., McBride J., Stark D. V., Vaduvescu O., 2014, MNRAS, 443, 1151

Noyola E., Gebhardt K., Kissler-Patig M., Lützgendorf N., Jalali B., de Zeeuw P. T., Baumgardt H., 2010, ApJ, 719, L60

Peacock M. B., Zepf S. E., Finzell T., 2013, ApJ, 769, 126

Pelupessy F. I., van Elteren A., de Vries N., McMillan S. L. W., Drost N., Portegies Zwart S. F., 2013, A&A, 557, A84

Peng E. W., Jordán A., Côté P., Blakeslee J. P., Ferrarese L., Mei S., West M. J., Merritt D., Milosavljević M., Tonry J. L., 2006, ApJ, 639, 95

Pfeffer J., Baumgardt H., 2013, MNRAS, 433, 1997

Piotto G., Bedin L. R., Anderson J., King I. R., Cassisi S., Milone A. P., Villanova S., Pietrinferni A., Renzini A., 2007, ApJ, 661, L53

Pota V., Forbes D. A., Romanowsky A. J., Brodie J. P., Spitler L. R., Strader J., Foster C., Arnold J. A., Benson A., Blom C., Hargis J. R., Rhode K. L., Usher C., 2013, MNRAS, 428, 389

Richer H. B., Heyl J., Anderson J., Kalirai J. S., Shara M. M., Dotter A., Fahlman G. G., Rich R. M., 2013, ApJ, 771, L15

Seth A. C., van den Bosch R., Mieske S., Baumgardt H., Brok M. D., Strader J., Neumayer N., Chilingarian I., Hilker M., McDermid R., Spitler L., Brodie J., Frank M. J., Walsh J. L., 2014, Nature, 513, 398

Sollima A., Bellazzini M., Smart R. L., Correnti M., Pancino E., Ferraro F. R., Romano D., 2009, MNRAS, 396, 2183

Spitzer L., 1987, Dynamical evolution of globular clusters. Princeton University Press, Princeton

Spitzer Jr. L., 1969, ApJ, 158, L139

Spurzem R., 1999, Journal of Computational and Applied Mathematics, 109, 407

Strader J., Chomiuk L., Maccarone T. J., Miller-Jones J. C. A., Seth A. C., Heinke C. O., Sivakoff G. R., 2012, ApJ, 750, L27

Tiongco M. A., Vesperini E., Varri A. L., 2016, MNRAS, 455, 3693

Tonini C., 2013, ApJ, 762, 39

Trenti M., van der Marel R., 2013, MNRAS

Usher C., Forbes D. A., Brodie J. P., Foster C., Spitler L. R., Arnold J. A., Romanowsky A. J., Strader J., Pota V., 2012, MNRAS, 426, 1475

van de Ven G., van den Bosch R. C. E., Verolme E. K., de Zeeuw P. T., 2006, A&A, 445, 513

van den Bergh S., 2008, AJ, 135, 1731

van den Bosch R., de Zeeuw T., Gebhardt K., Noyola E., van de Ven G., 2006, ApJ, 641, 852

van der Marel R. P., Anderson J., 2010, ApJ, 710, 1063

van Leeuwen F., Le Poole R. S., Reijns R. A., Freeman K. C., de Zeeuw P. T., 2000, A&A, 360, 472

Varri A. L., Bertin G., 2012, A&A, 540, A94 (VB12)

Vesperini E., Varri A. L., McMillan S. L. W., Zepf S. E., 2014, MNRAS, 443, L79

Wang L., Spurzem R., Aarseth S., Giersz M., Askar A., Berczik P., Naab T., Kouwenhoven R. S. M. B. N., 2016, MNRAS

Wang L., Spurzem R., Aarseth S., Nitadori K., Berczik P., Kouwenhoven M. B. N., Naab T., 2015, MNRAS, 450, 4070

Watkins L. L., van de Ven G., den Brok M., van den Bosch R. C. E., 2013, MNRAS, 436, 2598

Watkins L. L., van der Marel R. P., Bellini A., Anderson J., 2015a, ApJ, 803, 29

—, 2015b, ApJ, 812, 149

White R. E., Shawl S. J., 1987, ApJ, 317, 246 (WS87)

Wilson C. P., 1975, AJ, 80, 175

Zocchi A., Bertin G., Varri A. L., 2012, A&A, 539, A65

Appendix A

The code SISCO

In this Appendix, I report the code SISCO developed in this Thesis (see Chapter 3) and presented in details in Bianchini et al. (2015) to simulate IFU observations of GCs. A scheme of the code is provided in Figure A.1. The code is divided into two parts. The first part associates to every star a stellar spectrum, based on the stellar parameters. The second part, defines the observational setup of the IFU instrument (field-of-view, pixel scale, shape of the PSF, seeing condition, signal-to-noise) and the relevant properties of the observed GC (distance, position of the center, direction of the line-of-sight).

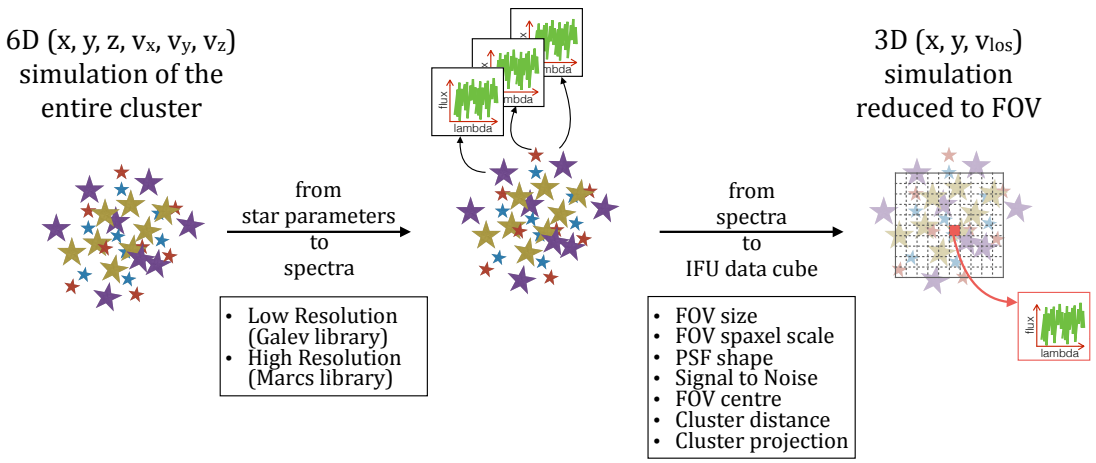

Figure A.1: Scheme of the code SISCO translating a dynamical GC simulation to a mock IFU observation. Graph shared by Ruggero de Vita.

```
//*************************************************************************
// Created by Paolo Bianchini, Updated 04/16 by Ruggero de Vita and Paolo
    Bianchini

// SISCO/FoV
//
// Produces a mock observation of a given 3D simulation (output of SISCO/FIRST).
// To execute FoV, pass as arguments the observational setup: (a) CENTRE, (b)
    DISTANCE, (c) PROJECTION.
//
// ARGUMENTS:
// 1.2.      (X,Y) offset for the FoV centre (in arcsec) (tip: choose value from
    0 to 7-8)
// 3.        distance (in kpc) (tip: choose value from 0.5 to 20)
// 4.5.6.    (ux,uy,uz) versor that defines the cluster rotation with respect to
    the default 3D simulation
// 7.        angle of rotation (in deg)
//
// INPUTS:
// 1.High resolution spectra from MARCS models
// 2.PSF (Moffat)
// 3.Output FIRST, "3Dsim_kin+mag+xyz+spec.dat" : for each star
//       |Teff|M|lum|met|bin|x|y|z|vx|vy|vz|imag|rmag|name_spectrum|resc.factor|
//
// OUTPUTS in outputFoV:
//
// 1. Kinematics in FoV without passing through spectra (model)
//       mod_kin.dat:
//       01- nx
//       02- ny
//       03- x
//       04- y
//       05- average velocity dispersion
//       06- average velocity
//       07- average velocity dispersion luminosity weighted
//       08- average velocity luminosity weighted
//       09- number of stars in the pixel
//       10- sumw
//       11- total luminosity (solar units)
//       12- flux counts
//       13- average velocity dispersion luminosity and psf weighted
//       14- average velocity luminosity and psf weighted
//       15- average mass luminosity and psf weighted
//       16- average mass
//
// 2. PSF out
//       psf_out.dat
//
// 3. Flux average (file important for adding SN)
//       fluxave.dat
//
// 4. MaskB : for each pixel it gives the contribution of each star to the tot.
    luminosity of the pixel. (file important for
//       adding a masking B to the data).
//       maskbis.dat:
//       01- star
//       02- nx
//       03- ny
//       04- counts
//
// 5. Spectra: spectrum for each pixel (file "spec_sumX+Y.dat": lambda|counts)
//
//
//*************************************************************************
```

```
#include <iostream>
#include <fstream>
#include <time.h>
#include <stdlib.h>
#include <stdio.h>
#include <math.h>
#include <time.h>
#include <sstream>
#include <string>
#include <gsl/gsl_errno.h>
#include <gsl/gsl_spline.h>
#include <gsl/gsl_interp.h>

//DEFINITION OF IFU FIELD OF VIEW AND PIXEL SCALE
#define VELSYS 300.0    //systematic velocity
#define FOV 20.0        //Field of view in arcsec
#define PIXSCALE 0.25   //pixel scale in arcsec
#define FOV_PSF 20.25   //field for psf

using namespace std;
int main(int argc, char** argv){

    // CONTROL THE ARGUMENTS FOR A PROPER OBSERVATIONAL SETUP
    double X_C,Y_C,dist,ux,uy,uz,th;
    double factor;
    if (argc!=8) {
        X_C=0.0;
        Y_C=0.0;
        dist=10.0;
        ux=0.0;
        uy=0.0;
        uz=1.0;
        th=0.0;
        cout << "FoV - ERROR: more arguments needed for a proper observational
            setup!!" << endl;
        cout << "Default observational setup: " << endl;
        cout << "(X,Y) offset in arcsec: (0,0)" << endl;
        cout << "distance in kpc: 10" << endl;
        cout << "Rotation (versor u and angle theta): (0,0,1) , 0 " << endl;
    }
    else {
        X_C=atof(argv[1]);
        Y_C=atof(argv[2]);
        dist=atof(argv[3]);
        ux=atof(argv[4]);
        uy=atof(argv[5]);
        uz=atof(argv[6]);
        th=atof(argv[7])*M_PI/180.0;
        cout << "Observational setup: " << endl;
        cout << "(X,Y) offset in arcsec: (" << X_C << "," << Y_C << ")\n";
        cout << "distance in kpc: " << dist << "\n";
        if (ux==0.0 && uy==0.0 && uz==0.0) { //a null vector
            ux=0.0;
            uy=0.0;
            uz=1.0;
            th=0.0;
            cout << "The versor you typed is wrong! Default rotation (versor u
                and angle theta): (";
            cout << ux << "," << uy << "," << uz << ") , " << th << " deg \n";
        }
        else { //normalize the vector
                factor=sqrt(ux*ux+uy*uy+uz*uz);
                ux=ux/factor;
```

```
            uy=uy/factor;
            uz=uz/factor;
            cout << "Rotation (versor u and angle theta): ";
            cout << ux << "," << uy << "," << uz << ") , " << th << " deg \n
                ";
    }

}


// CONTANTS
double G=6.67300e-11; // m^3/(kg s^2)
double sigB=5.67037e-8; //W m,âí2 K,âí4
double M_o=1.988550e30; //kg
double L_o=3.83900e26; //Watt
double r_o=6.95500e8; //m

//DEFINITIONS OF VARIABLES
clock_t t1,t2,t3;
t1=clock();
int nspectrum=0,nspectrumHR=0,ndim_tot=0,numHR=0,num=0,N=1200000;
double*** fluxsum=new double** [200];
for (int i=0;i<200;i++){
    fluxsum[i]=new double*[200];
    for (int j=0;j<200;j++){
        fluxsum[i][j]=new double [5000];
    }
}
double D=4,texp=1,eff=0.3; //mirror radius, exposure time, efficiency
    parameter for losses
double* flux=new double[N];
double* fluxinterp=new double[N];
double* fluxinterp_quality=new double[N];
double* lamb=new double[N];
double* lambHR=new double[N];
double* fluxHR=new double[N];
double* lambsum=new double[N];
double* lamb_new=new double[N];
double* lamb_ref=new double[N];
double* temp=new double[N];
double* mass=new double[N];
double* lum=new double[N];
double* z=new double[N];
double* bin=new double[N];
double* vel=new double[N];
double* x=new double[N];
double* y=new double[N];
double* rmag=new double[N];
double* imag=new double[N];
double* MAG=new double[11];
double* logg=new double[N];
double* rescaling=new double[N];
int k=0,nstars=0,nrealiz=0,ndim=0,l2=0,k2=0,name[N];
double velsys,fov,pixscale,fluxtot;
double zz,uu;
double* psfy=new double [1000000];
double* psfx=new double [1000000];
double sigma,FWHM,fov_psf;
double** fluxpsf=new double* [100];
for (int i=0;i<100;i++) fluxpsf[i]=new double[100];
double** fluxcounts=new double* [200];
for (int i=0;i<200;i++) fluxcounts[i]= new double[200];
double** fluxcountssingle=new double* [200];
for (int i=0;i<200;i++) fluxcountssingle[i]=new double[200];
```

```
double** avewpsf=new double* [200];
for (int i=0;i<200;i++) avewpsf[i]=new double[200];
double** sumwpsf=new double* [200];
for (int i=0;i<200;i++) sumwpsf[i]=new double[200];
double** avew2psf = new double* [200];
for (int i=0;i<200;i++) avew2psf[i]=new double[200];
double** masstot=new double* [200];
for (int i=0;i<200;i++) masstot[i]=new double[200];
double** masspsf=new double* [200];
for (int i=0;i<200;i++) masspsf[i]=new double[200];
double** fluxpsftot=new double* [200];
for (int i=0;i<200;i++) fluxpsftot[i]=new double[200];
double** avev2=new double* [200];
for (int i=0;i<200;i++) avev2[i]=new double[200];
double** avev=new double* [200];
for (int i=0;i<200;i++) avev[i]=new double[200];
double** avew=new double* [200];
for (int i=0;i<200;i++) avew[i]=new double[200];
double** sumw=new double* [200];
for (int i=0;i<200;i++) sumw[i]=new double[200];
double** avew2=new double* [200];
for (int i=0;i<200;i++) avew2[i]=new double[200];
double** lumtot=new double* [200];
for (int i=0;i<200;i++) lumtot[i]=new double[200];
double** ndimpix=new double* [200];
for (int i=0;i<200;i++) ndimpix[i]=new double[200];
double fluxtotave=0;
char identita [200];
std::string kkk;
std::string lll;
std::ostringstream convert;
string filename,filenamename;
fstream fin,foutsum,fout,finlambda,fspecHRin,foutpsf,foutavflux,foutmaskbis,
    fmoffat;
//INPUTS
fin.open("../01_FIRST/outputFIRST/3Dsim_kin+mag+xyz+spec.dat", ios::in); //
    GC SIMULATION PROCEESED BY "FIRST"
finlambda.open ("../01_FIRST/MARCS_models/flx_wavelengths.vac",ios::in); //
    spectra template (wavelength coulumn)
fmoffat.open("./PSF_moffat/psf_moffat_1arcsec_20.dat",ios::in); //TAKE THE
    FILE FOR THE PSF (MOFFAT FUNCTION)
if(fin.fail()) cout << "file 1 does not exist\n";
if(finlambda.fail()) cout << "file 2 does not exist\n";
if(fmoffat.fail()) cout << "file 3 does not exist\n";
//OUTPUTS
fout.open ("./outputFoV/mod_kin.dat",ios::out);
foutpsf.open ("./outputFoV/psf_out.dat",ios::out);
foutavflux.open ("./outputFoV/fluxave.dat",ios::out);
foutmaskbis.open ("./outputFoV/maskbis.dat",ios::out);
fout.precision(10);

velsys=VELSYS;
fov=FOV;
pixscale=PIXSCALE;
fov_psf=FOV_PSF;
double x0,y0,z0,vx0,vy0,vz0;
double x1,y1,z1,vx1,vy1,vz1;
double ux2,uy2,uz2;
double uxy,uyz,uxz;
ux2=ux*ux;
uy2=uy*uy;
uz2=uz*uz;
uxy=ux*uy;
uyz=uy*uz;
```

```
uxz=ux*uz;


for (int j=0; ;j++) { //until the file is over
    //LOAD THE INFORMATION OF THE STAR
    fin >>temp[j]>>mass[j]>>lum[j]>>z[j]>>bin[j]>>x0>>y0>>z0>>vx0>>vy0>>vz0
        >>imag[j]>>rmag[j]>>identita>>rescaling[j];
    //CHANGE ITS POSITION ACCORDING TO A ROTATION OF th RELATIVE TO THE
        VERSOR (ux,uy,uz)
        //change only the coordinates of interest: x,y,vz(=v_los);
    x1=(ux2+(1.0-ux2)*cos(th))       *x0 + (uxy*(1.0-cos(th))-uz*sin(th))*y0
         + (uxz*(1.0-cos(th))+uy*sin(th))*z0;
    y1=(uxy*(1.0-cos(th))+uz*sin(th))*x0 + (uy2+(1.0-uy2)*cos(th))       *y0
         + (uyz*(1.0-cos(th))-ux*sin(th))*z0;
    //z1=(uxz*(1.0-cos(th))-uy*sin(th))*x0 + (uyz*(1.0-cos(th))+ux*sin(th))*
        y0 + (uz2+cos(th)*(1.0-uz2))       *z0;

    //vx1=(ux2+(1.0-ux2)*cos(th))       *vx0 + (uxy*(1.0-cos(th))-uz*sin(th)
        )*vy0 + (uxz*(1.0-cos(th))+uy*sin(th))*vz0;
    //vy1=(uxy*(1.0-cos(th))+uz*sin(th))*vx0 + (uy2+(1.0-uy2)*cos(th))
              *vy0 + (uyz*(1.0-cos(th))-ux*sin(th))*vz0;
    vz1=(uxz*(1.0-cos(th))-uy*sin(th))*vx0 + (uyz*(1.0-cos(th))+ux*sin(th))*
        vy0 + (uz2+cos(th)*(1.0-uz2))       *vz0;
    x[j]=x1; //pc
    y[j]=y1; //pc
    vel[j]=vz1; //km/s
    //DEFINE DISTANCE (TRANSFORM FROM pc TO arcmin)
    x[j]=x[j]/(dist*1000.)*180*60./M_PI;
    y[j]=y[j]/(dist*1000.)*180*60./M_PI;
    //REDEFINE THE CENTER
    x[j]=x[j]-X_C/60.;
    y[j]=y[j]-Y_C/60.;

    ndim_tot++; //increase the number of stars in the sample
    name[j]=ndim_tot; //nominate each star
    if(fin.eof())break;
}
fin.close();
cout<<"Number of the stars in the simulation: ";
cout<<ndim_tot<<endl; //print the number of stars
srand(time(NULL));

//calculate a PSF - MOFFAT PSF
double aaa; //temporary variable
double fluxpsffluxpsf;
int llll,kkkk;
for(int i=0;i<((fov_psf/pixscale)*(fov_psf/pixscale));i++){
    fmoffat>>llll>>kkkk>>aaa>>aaa>>fluxpsffluxpsf;
    fluxpsf[llll][kkkk]=fluxpsffluxpsf;
    if(fmoffat.eof())break;
}
for (int l=0;l<(fov_psf/pixscale);l++) {
    for (int k=0;k<(fov_psf/pixscale);k++) {
        foutpsf<<k<<" "<<l<<" "; //nx, ny
        foutpsf<<-fov_psf/2.+(k+1/2.)*pixscale<<" "<<-fov_psf/2.+(l+1/2.)*
            pixscale<<" "; //x, y
        foutpsf<<fluxpsf[l][k]<<endl;
    }
}
cout<<"Moffat psf calculated"<<endl;
fmoffat.close();


//START DIVISION IN PIXELS. PER EVERY PIXEL IT CREATES A SUMMED SPECTRUM
```

```
fin.open("../01_FIRST/outputFIRST/3Dsim_kin+mag+xyz+spec.dat", ios::in);
double abc; //temporary variable for irrelevant columns
for (int j=0; ;j++) {
    fin>>abc>>abc>>abc>>abc>>abc>>abc>>abc>>abc>>abc>>abc>>abc>>abc>>
        identita>>abc;
    for (int l=0; l<(fov/pixscale);l++) {  //start from bottom left of FoV,
        row by row (from bottom row to top row)
        for (int k=0; k<(fov/pixscale);k++) {
            if(x[j]>(-fov/2./60.+k*pixscale/60.) && x[j]<(-fov/2./60.+(k+1)*
                pixscale/60.)){ //DEFINE PIXELS
                if(y[j]>(-fov/2./60.+l*pixscale/60.) && y[j]<(-fov/2./60.+(l
                    +1)*pixscale/60.)){ //DEFINE PIXELS
                    ndimpix[l][k]++; //increase the number of stars in a
                        pixel
                    ndim++; //increase the number of stars

                    //FIND HIGH RESOLUTION SPECTRA MATCHING THE PARAMETERS
                    filename.clear();
                    filename.append(identita);
                    fspecHRin.open(filename.c_str(),ios::in);

                    //OPEN THE SELECTED HIGH RESOLUTION SPECTRUM AND WRITE
                        INTO ARRAYS
                    nspectrumHR=0.0;
                    for (int i=0; ;i++) {
                        fspecHRin>>fluxHR[i];
                        finlambda>>lambHR[i];
                        fluxHR[i]=rescaling[j]*fluxHR[i];   //rescale the
                            spectrum to the low
                        //resolution spectrum (now the spectra are in erg/s/
                            cm^2/A)
                        if(fspecHRin.eof())break;
                        nspectrumHR++;
                    }
                    fspecHRin.clear();
                    fspecHRin.close();
                    //DOPPLER SHIFT THE HR SPECTRUM
                    vel[j]=vel[j]+velsys; //this is the velocity given by
                        the simulation + the imposed systematic vel
                    avev2[l][k]=avev2[l][k]+vel[j]*vel[j];
                    avev[l][k]=avev[l][k]+vel[j];
                    avew[l][k]=avew[l][k]+vel[j]*lum[j];
                    avew2[l][k]=avew2[l][k]+vel[j]*vel[j]*lum[j];
                    sumw[l][k]=sumw[l][k]+lum[j];
                    masstot[l][k]=masstot[l][k]+mass[j];
                    for (int i=0; i<nspectrumHR ;i++) {
                        lamb_new[i]=lambHR[i]*(vel[j]/300000.+1.);
                    }

                    //INTERPOLATION HR SPECTRUM (ALREADY RESCALED)
                    gsl_interp *interp=gsl_interp_alloc (gsl_interp_linear,
                        nspectrumHR-1); //linear
                    gsl_interp_init (interp, lamb_new, fluxHR, nspectrumHR
                        -1);
                    gsl_interp_accel *acc = gsl_interp_accel_alloc ();

                    for (int i=0; i<4000; i++) { //interpolate in 4000
                        points the spectra for lambda in 8400-8800
                        lamb_ref[i]=8400+i*(8800-8400)/4000.;
                        //find value of flux in the lambda of reference
                        fluxinterp[i] = gsl_interp_eval (interp,lamb_new,
                            fluxHR, lamb_ref[i], acc); //linear

                        //CONVERT EVERYTHING IN PHOTON COUNTS
```

```
        fluxinterp[i]=fluxinterp[i]*lamb_ref[i]/(1.988E-14)
            /10.*
        (D*D*3.1415926)*eff*texp*(10*10)/
        (dist*dist*1000*1000)/10./10.;      //dist*dist is
            to put
        //everythin at 10kpc (originally at 10)
        //the result should be in [photons/A]
    }

    for (int ll=0; ll<(fov_psf/pixscale);ll++) {  // apply
        the psf and relative weight to create summed spectra
        for (int kk=0; kk<(fov_psf/pixscale);kk++) {
            l2=l+(int)(-fov_psf/pixscale/2)+ll;
            k2=k+(int)(-fov_psf/pixscale/2)+kk;
            if(l2>=0 && k2>=0 && l2<(fov/pixscale) && k2<(
                fov/pixscale)){
                // make sure i'm inside the field of view
                lumtot[l2][k2]=lumtot[l2][k2]+lum[j]*fluxpsf
                    [ll][kk];       //total luminosity per
                    pixel with PSF
                //(bolometric luminosity)
                fluxcountssingle[l2][k2]=0;
                for (int i=0; i<4000; i++) { //sum 4000
                    values for the flux with lambda in
                    8400-8800
                    //sum fluxes at a given lambda of
                        reference
                    fluxsum[l2][k2][i]=fluxsum[l2][k2][i]+
                        fluxinterp[i]*fluxpsf[ll][kk];
                    fluxcounts[l2][k2]=fluxcounts[l2][k2]+
                        fluxinterp[i]*fluxpsf[ll][kk];
                    //total "counts" per pixel with PSF
                    fluxcountssingle[l2][k2]=
                        fluxcountssingle[l2][k2]+fluxinterp[
                        i]*fluxpsf[ll][kk];
                    //single contribution of a star
                }

                //print on a file useful for future masking
                if(fluxcountssingle[l2][k2]!=0){
                    foutmaskbis<<name[j]<<" "<<k2<<" "<<l2<<
                        " "<<fluxcountssingle[l2][k2]<<endl;
                    //flux of each star after the PSf,
                    //spreaded around the different pixels
                }
                avewpsf[l2][k2]=avewpsf[l2][k2]+vel[j]*
                    fluxcountssingle[l2][k2];
                //kinematics "luminosity" weighted after PSF
                avew2psf[l2][k2]=avew2psf[l2][k2]+vel[j]*vel
                    [j]*fluxcountssingle[l2][k2];
                sumwpsf[l2][k2]=sumwpsf[l2][k2]+
                    fluxcountssingle[l2][k2];
                masspsf[l2][k2]=masspsf[l2][k2]+mass[j]*
                    fluxcountssingle[l2][k2];
                fluxpsftot[l2][k2]=fluxpsftot[l2][k2]+
                    fluxpsf[ll][kk];
            }
        }
    }
    gsl_interp_free (interp);
    gsl_interp_accel_free (acc);
    if(ndim==100)cout<<"100"<<endl;
    if(ndim==500)cout<<"500"<<endl;
    if(ndim==1000)cout<<"1,000"<<endl;
```

```
                    if(ndim==5000)cout<<"5,000"<<endl;
                    if(ndim==7000)cout<<"7,000"<<endl;
                    if(ndim==10000)cout<<"10,000"<<endl;
                    if(ndim==13000)cout<<"13,000"<<endl;
                    if(ndim==15000)cout<<"15,000"<<endl;
                    if(ndim==17000)cout<<"17,000"<<endl;
                    if(ndim==20000)cout<<"20,000"<<endl;
                    if(ndim==25000)cout<<"25,000"<<endl;
                    if(ndim==30000)cout<<"30,000"<<endl;
                    if(ndim==35000)cout<<"35,000"<<endl;
                    if(ndim==40000)cout<<"40,000"<<endl;
                    if(ndim==45000)cout<<"45,000"<<endl;
                    if(ndim==50000)cout<<"50,000"<<endl;
                }
            }
        }
    }
    if (fin.eof()) break;
}
fin.close();
finlambda.close();
cout<<"Number of stars in FoV: "<<ndim<<endl;

double v_ave_mod,v_ave_mod_lw,v_ave_mod_lpsfw,disp_mod,disp_mod_lw,
    disp_mod_lpsfw,m_ave,m_ave_lpsfw;
for (int l=0; l<(fov/pixscale);l++) {  //start from bottom left of FoV, row
    by row (from bottom row to top row)
    for (int k=0; k<(fov/pixscale);k++) {
        // write final summed spectrum
        convert<<k;
        kkk=convert.str(); //write int into string kk
        convert.str("");
        convert.clear();
        convert<<l;
        lll=convert.str();
        // write final summed spectrum
        filename.clear();
        filenamename.clear();
        filename.append(kkk);

        filenamename.append("./outputFoV/spec_sum");
        filenamename.append(kkk);
        filenamename.append("+");
        filenamename.append(lll);
        filenamename.append(".dat");
        foutsum.open(filenamename.c_str(),ios::out);
        foutsum.precision(10);

        convert.str("");
        convert.clear();

        for (int i=0; i<4000; i++) {
            foutsum<<lamb_ref[i] <<" "<<fluxsum[l][k][i]<<endl;
        }

        foutsum.close();

        v_ave_mod=avev[l][k]/(1.*ndimpix[l][k]);
        v_ave_mod_lw=avew[l][k]/(sumw[l][k]);
        v_ave_mod_lpsfw=avewpsf[l][k]/(sumwpsf[l][k]);
        disp_mod=sqrt(avev2[l][k]/(1.*ndimpix[l][k])-avev[l][k]*avev[l][k
            ]/(1.*ndimpix[l][k]*ndimpix[l][k]));
        disp_mod_lw=sqrt(avew2[l][k]/(sumw[l][k])-avew[l][k]*avew[l][k]/(
            sumw[l][k]*sumw[l][k]));
```

```
            disp_mod_lpsfw=sqrt(avew2psf[l][k]/(sumwpsf[l][k])-avewpsf[l][k]*
                avewpsf[l][k]/(sumwpsf[l][k]*sumwpsf[l][k]));
            m_ave=masstot[l][k]/(1.*ndimpix[l][k]);
            m_ave_lpsfw=masspsf[l][k]/sumwpsf[l][k];
            if (ndimpix[l][k]==0.0){
                v_ave_mod=0.0;
                disp_mod=0.0;
                m_ave=0.0;
            }
            if (sumw[l][k]==0.0) {
                v_ave_mod_lw=0.0;
                disp_mod_lw=0.0;
            }
            if (sumwpsf[l][k]==0.0){
                v_ave_mod_lpsfw=0.0;
                disp_mod_lpsfw=0.0;
                m_ave_lpsfw=0.0;
            }
            fout<<k<<" "<<l<<" "; //nx, ny
            fout<<-fov/2./60.+(k+1/2.)*pixscale/60.<<" "<<-fov/2./60.+(l+1/2.)*
                pixscale/60.<<" "; //x, y
            fout<<disp_mod<<" "<<v_ave_mod<<" ";
            fout<<disp_mod_lw<<" "<<v_ave_mod_lw<<" ";
            fout<<ndimpix[l][k]<<" "<<sumw[l][k]<<" ";
            fout<<lumtot[l][k]<<" "<<fluxcounts[l][k]<<" ";
            fout<<disp_mod_lpsfw<<" "<<v_ave_mod_lpsfw<<" ";
            fout<<m_ave_lpsfw<<" "<<m_ave<<endl;

            fluxtotave=fluxtotave+fluxcounts[l][k];
        }
    }

    foutavflux<<fluxtotave/6400.<<endl;
    foutavflux.close();
    fout.close();
    foutpsf.close();
    foutmaskbis.close();
    t2=clock();
    float diff((float)t2-(float)t1);
    cout<<diff/CLOCKS_PER_SEC<<endl;

    return 0;
}
```

Acknowledgements

I would like to thank the people that followed me through this exciting journey, in particular Glenn van de Ven, Eva Schinnerer and Mark Norris, for their constant scientific advice, guidance and priceless support. A special thanks goes to Rainer Spurzem for agreeing to review this work, to Anna Sippel for her exceptional help during the writing of this Thesis and the number of collaborators that contributed in shaping my scientific growth. Thanks to Office 217 and the people orbiting around it for the generous contributions of all sorts, thanks to Arianna for enhancing my calm and creativity and thanks to my constantly expanding family for the support even from far away.